5-2019

Free Electron Sources and Diffraction in Time

Eric R. Jones
University of Nebraska-Lincoln, eric.ryan.jones@huskers.unl.edu

FREE ELECTRON SOURCES AND DIFFRACTION IN TIME

by

Eric Ryan Jones

A DISSERTATION

Presented to the Faculty of

The Graduate College at the University of Nebraska

In Partial Fulfilment of Requirements

For the Degree of Doctor of Philosophy

Major: Physics and Astronomy

Under the Supervision of Professor Herman Batelaan

Lincoln, Nebraska

May, 2019

FREE ELECTRON SOURCES AND DIFFRACTION IN TIME

Eric Ryan Jones, Ph.D.

University of Nebraska, 2019

Advisor: Herman Batelaan

The quantum revolution of the last century advanced synergistically with technology, for example, with control of the temporal and spatial coherence, and the polarization state of light. Indeed, experimental confirmation of the quirks of quantum theory, as originally highlighted by Einstein, Podolsky, and Rosen, through Bohm, and then Bell, have been performed with photons, i.e., electromagnetic wave packets prepared in the same quantum states. Experimental tests of quantum mechanics with matter wave packets have been limited due to challenges in preparing all of the packets with similar quantum states. While great strides have been made for trapped atoms and Bose-Einstein condensates, the technology for electron matter waves has not kept pace. In other words, electron sources typically have a low quantum degeneracy. As new techniques to control the coherence of electron wave packets are developed, new avenues to test quantum theory become available.

To better understand the temporal coherence of a pulsed electron source, we have studied electron emission from metallic and semiconductor structures. Ultrafast electron emission was obtained by focusing femtosecond laser pulses on metallic nanotips and nanoribbons, as well as semiconductor shards. The various emission mechanisms from these sources were investigated in efforts to control the coherence of the emitted electron wave packets. The electronic band structure of semiconductor materials provides an additional feature in that the spin state of emitted electrons can be optically controlled. Controlling the spin polarization in a pulsed electron source

could lead to a source with the highest quantum degeneracy yet achieved.

The development of a quantum degenerate source of matter waves is a step toward realizing fundamental tests of quantum mechanics with electron wave packets. As quantum degenerate electron sources do not yet exist, their potential and utility remains to be explored. An ultrafast spin-polarized source of electrons is itself intriguing for studying nanoscale magnetic systems with unprecedented temporal resolution. These advancements suggest that an entirely new field of free electron quantum optics may be within our reach, with all of its possibilities open for exploration. The quantum revolution may yet have some surprises in store.

FREE ELECTRON SOURCES AND DIFFRACTION IN TIME

Eric Ryan Jones, Ph.D.

University of Nebraska, 2019

Lay Abstract

Advisor: Herman Batelaan

The development of the first compound microscopes around the 17th century revealed an entirely unseen world for discovery, the world of the very small. Microscopic anatomy was first reported in Giambattista Odierna's *L'occhio della mosca* (*The Fly's Eye*) in 1644. For the first time, individual cells and new lifeforms were discovered, which lead to new fields of inquiry. Using polarized light revealed hidden structures of what was being imaged; however, the ultimate magnification was limited by the size of the wavelength of light used. To see further into the world of the very small then required smaller wavelengths or new methods.

A breakthrough was realized amidst the quantum revolution in 1924, when physicist Louis de Broglie hypothesized that all matter in motion has a wavelength. De Broglie's hypothesis was confirmed through the electron scattering experiments of Davisson and Germer between 1921 and 1925. The first electron microscopes were developed over the next decade by Ernst Ruska and Max Knoll, with the first images obtained by Ernst Lübke in 1932. Resolution was refined to the atomic scale by the 1980's with the development of scanning probe microscopes by Gerd Binnig and Heinrich Rohrer. The 1986 Nobel Prize was shared among Ruska, Binnig, and Rohrer. The famous image of the quantum corral was taken in 1993 at IBM using a scanning probe microscope. Further advancements would come with the development of ultrafast electron microscopy, pioneered in the group of Nobel laureate Ahmed Zewail, which

has lead to the possibility of visualizing objects at the atomic scale in motion.

This dissertation focuses on studying sources that produce short flashes of electrons that can also be spin-polarized. These sources might be used in electron microscopes to provide imaging in time, and, when polarized, could reveal the hidden magnetic structure of objects at these short time scales. The behavior of the electrons produced from these sources could also provide insight into how quantum mechanics works at very short time scales. As technology improves, the world of the very small becomes even larger.

DEDICATION

"... you must dare to dream, but ... there's no substitute for perseverance and hard work. And teamwork, because no one gets there alone."

For Joe H. and Jillian.

ACKNOWLEDGMENTS

First, thank you to Prof. Herman Batelaan, my academic adviser. Herman made the case so that I could begin this journey in the first place. Thank you Herman, for allowing me the space to develop my ideas and apparatus, even in the cases when we didn't necessarily agree. I could not have done this without your support.

I would like to thank the members of my graduate committee, Profs. Timothy J. Gay, Kees Uiterwaal, and Christos Argyropoulos, for their time and support. I would like to especially thank my readers Kees and Tim, who also made the experimental work presented in this dissertation possible. Kees shared his laboratory space and the use of his femtosecond laser system, and was always open for excellent physics discussions. Tim provided me with a challenging collaborative project, as well as support while that work was finished. Tim's discussions on physics, sartorial choices, life, and rock 'n' roll have been invaluable.

Part of my work was possible through the collaboration with Bret N. Flanders and his graduate student, Gobind Basnet, at Kansas State University. Thank you both for your help and patience with my terrible tweezer skills.

The Physics department here at UNL is fortunate to have an excellent support staff. Thank you Kay Haley, Theresa Sis, Marjorie Wolfe, Cyndy Peterson, Amanda Lager Gleason, Kelcey Gabriel, and Jenny Becic. I will always appreciate the help and cat/dog chats.

The staff in our Machine Shop and Student Shop provided constant help in getting my designs to actually work the way I intended, so I would like to thank Les Marquart and Mike Thompson, as well as Bob Rhynalds, Pat Pribil, Keith Placek, and Andrew Kehm, who provided both guidance and tools when I couldn't find the right ones. Bob Kelty, Brian Farleigh, and Anatoly Mironov have helped me solve more electronics

issues than I could list here.

Thank you also to Dan Claes, for helping with resurrecting experiments in the Advanced Teaching Lab, and for guidance and moral support.

Thank you to my mentors, previous group members Wayne Huang, Roger Bach, and Scot McGregor, who not only helped me keep my experiments and code working, but also showed me the value of a coffee break and a good beer. To our current and former group members, Maria Becker, Zilin Chen, Sam Keramati, and Bret Gergely, I wish you all the best. To the undergraduates who worked with me on the oil droplet projects, Adam Lif, Christian Laney, Gabriel Gauthier, Zebulon Cooper, Karissa Goosic, Taylor Morgan, and Greg Hubbard, thank you for all of your efforts.

From the Gay Group, thanks to Joan Dreiling, Evan Brunkow, Nathan Clayburn, Keith Foreman, Karl Ahrendsen, and William Newman. I would also like to thank the undergraduate researchers Samantha Burtwistle, Will Brunner, Jesse Kruse, and especially Zachary Rohde, for priceless technical assistance and being a pretty good guy.

From the Uiterwaal Group, I would like to thank Collin McAcy and Josh Beck, for not only keeping things running in the lab but keeping me running as well.

I would like to thank the NSF for funding that has allowed me to complete my research while still enjoying a burrito now and then.

To my increasingly growing family, thank you for your support (and coffee and terrible movie viewing). Thank you to Nicole Replogle, for your friendship and mutual clowder support. Joe and Ang, Mario and Jenna, Kara and Brian, Josh, Nan, Chris, and Scott, you have been in my corner since the beginning and I love you all.

To my parents, Robin and Howard, I could not have done this without your love and support in everything I've done. I am proud to be your son and I love you both.

Lastly, to my favorite person, Wendy: here's to the future.

PREFACE

Chapter 2 contains figures and results that have been published in *Applied Physics Letters.* Reproduced from E. R. Jones, W. C. Huang, G. Basnet, B. N. Flanders, and H. Batelaan, "Laser-induced electron emission from Au nanowires: A probe for orthogonal polarizations" (Appl. Phys. Lett. **112**, 263104 (2018); `https://doi-org/10.1063/1.5031440`), with the permission of AIP Publishing.

Chapter 3 has been published in *European Journal of Physics* (E. R. Jones, R. A. Bach, and H. Batelaan, "Path integrals, matter waves, and the double slit," Eur. J. Phys. **36**, 065048 (2015).), and was selected by the editors to be included in the "Highlights of 2015" collection.

Chapter 4 includes results that have been published in *Journal of Physics: Conference Series* (H. Batelaan, E. Jones, W. C. Huang, and R. Bach, "Momentum exchange in the electron double-slit experiment," J. Phys.: Conf. Ser. **701**, 012007 (2016).), as well as unpublished results for a future publication.

Chapter 5 contains figures and results that have been published in *Applied Physics Letters.* Reproduced from E. Brunkow, E. R. Jones, H. Batelaan, and T. J. Gay, "Femtosecond-laser-induced spin-polarized electron emission from a GaAs tip" (Appl. Phys. Lett. 114, 073502 (2019); `https://doi.org/10.1063/1.5070059`), with the permission of AIP Publishing. Work related to subadditive emission from GaAs s still in progress and will hopefully be submitted for publication by August 2019.

Table of Contents

List of Figures

List of Tables

Chapter 1

Introduction

1.1 Motivation for research

The motivation for the work presented in this dissertation is to further develop our understanding of the creation and evolution of electron matter wave pulses in space and time. The creation of electron matter waves has proceeded following the independent electron diffraction experiments of Davisson and Germer,[1] and Thompson and Reid,[2] which confirmed de Broglie's hypothesis that electrons in motion possess a characteristic wavelength dependent on their velocity.[3] Electron matter wave pulses became available after the realization of the first femtosecond- and nanometer-scale tip sources, produced by illuminating metallic nanostructures with femtosecond laser pulses.[4–6] Ultrashort, multiple electron bunches have been have been used practically in ultrafast electron diffraction and ultrafast electron crystallography.[7–9] Recently, pulsed tip sources were used for the first time to obtain ultrafast low-energy electron diffraction from polymers and graphene.[10,11] Tip sources have been used in ultrafast electron microscopy,[12,13] in particular, to image the plasmonic near-fields excited in metallic nanostrucures, in a technique referred to as photon-induced near field electron microscopy (PINEM).[14–16] The technique of optically gating electron pulses by utilizing their interactions with plasmonic near-fields in the PINEM arrangement has recently

produced electron pulses having a duration of 30 fs, with the possibility of further gating into the attosecond regime.[17,18] While electrons produced from tip sources are often used to probe a sample target, the electrons produced at the source can give insight into dynamics occurring within the source itself.[19] Owing to their spatial and temporal coherence,[20] such sources have also been used in fundamental tests of quantum mechanics.[21–23] The nanometer spatial confinement provided by the source structure and temporal confinement provided by the exciting laser pulses suggest the possibility for the on-demand production of electrons with the highest possible quantum degeneracy.[24,25] We have attempted to characterize and control various emission processes by making use of unique source geometries other than standard field emission tips, and to increase the degeneracy of our source by considering different materials. The possibilities for unique sources are made available by new methods of growing or shaping tailored nanostructures in a variety of materials.[26] For our purposes, we obtained gold nanoribbons, whose growth can be tuned by various controls,[27] and developed electrochemical etching for several materials, including gold[28–30] and p-doped gallium arsenide (GaAs).[31,32] Electron emission from a nanoribbon source, provided for us by our collaborators Professor Bret N. Flanders and Gobind Basnet at Kansas State University, is presented in Ch. 2.[33] Emission from GaAs, studied through a collaboration with Professor Timothy J. Gay and his former graduate students Evan Brunkow and Nathan Clayburn,[34] is presented later, in Ch. 5, after the presentation of a basic quantum-mechanical model of degenerate electron sources. Ultrafast, nanometer-scale electron sources can therefore illuminate processes both within and outside of the source.

Once electron pulses are created, understanding how they propagate in space and time informs both experimental results and experimental pursuits. The propagation of electron matter waves generally proceeds with the well-established connection between

quantum mechanics and the optics of electromagnetic waves.[35] This connection is made by identifying similar terms in the time-independent solutions of both the Schrödinger and Maxwell wave equations. Indeed, matter wave interferometers have generally confirmed the expectations from optics,[36] and experiments as fundamental as Young's double-slit interference[37] have been repeatedly verified. However, beams of matter waves also experience various interactions with matter optics elements, such as van der Waals forces[38,39] or simple charging effects.[40] Matter waves, unlike electromagnetic waves, are dispersive in free space. Treating matter wave propagation in the same manner as electromagnetic waves can therefore lead to incorrect predictions. In our research group, we have often used the path integral formulation of quantum mechanics,[41,42] informed by the matter-optics analogy, to successfully describe experiments performed with electrons illuminating material gratings and interacting with electromagnetic fields.[37,40,43–47] In order to proceed with our goals of theoretically modeling our quantum degenerate sources, it was necessary to test the limits of the matter-optics analogy, and then use the appropriate theoretical description to determine what results were possible. In Ch. 3, the path integral formalism for electron matter waves interfering in a Young's double slit arrangement is presented. The difficulty of associating elements of the correct theoretical formalism with representations of the physical system in order to make predictions is discussed in detail.[48]

A valuable tool in presenting the matter/optics analogy would be a system where the analogy could be easily visualized. The classic system that has demonstrated wave evolution, developed by Thomas Young himself, is the ripple tank.[49] The advantage of the ripple tank is that unlike electromagnetic waves, water waves are easily visualized, and are thus an invaluable system of demonstrating wave behavior. The disadvantage is that the presentation provided by the ripple tank demonstration can lead to conceptual

difficulties in considering the evolution of matter waves. This conceptual difficulty is highlighted in Ch. 3. The connection between the ripple tank demonstration and matter is further complicated because matter in motion is more often intuitively associated with particles. It seemed an improved system was demonstrated in 2005, when researchers lead by fluid physicist Yves Couder showed that a vertically shaking dish of oil could support bouncing droplets of the same oil. The bouncing droplets were accompanied by parametrically forced macroscopic waves that form spontaneously on the surface of vertically oscillated cells of shallow fluid, which are known as Faraday waves.[50,51] When the frequency and amplitude of the shaking are within a particular range, the drops will interact with their associated Faraday wave at the surface, and will march in step at 1/2 the driving frequency of the dish.[52] An intriguing feature of this system is that while the action of the particle bouncing on the fluid surface initiates the Faraday wave, the Faraday wave locally surrounding the droplet guides the motion of the marching droplets. Disturbances in the local environment that affect the boundary conditions of the wave will change the trajectory of a marching droplet. Similarly intriguing is that the Faraday wave, which is supported by the near-resonance shaking of the fluid, retains information regarding the state of the wave at previous times until that component of the wave damps away.[53–55] The system therefore demonstrates a kind of path memory of previous interactions. Thus, the droplet/wave system is a unique hydrodynamic analog to particle/wave duality,[56] and could then be used to demonstrate the behavior of matter waves. This analogy was studied in the Young's single- and double-slit configuration, and seemed to demonstrate a wave interference pattern generated one marching droplet at a time.[57] This system was reproduced in our research group, and our results are presented in Chapter 4. We further study an arrangement that has features analogous to a particle trapped in an infinite square well potential, and show that system entails research that can be

aimed toward high school students.

The importance of understanding how matter waves propagate in space and time from their appropriate source distributions is an essential component of modeling how multiple-electron wave packets will evolve. The physics describing the creation and evolution of multiple-electron wave packets is studied in Hanbury Brown-Twiss type anticorrelation experiments.[58] The original experiments performed by Hanbury Brown and Twiss, which measured correlations of the detection of photons from independent sources,[59] are often noted as the motivation for the development of quantum optics.[58,60–63] While their methods were developed to measure the angular width of distant stars,[64,65] they demonstrated that photons emitted from seemingly random sources was in fact bunched in time.[59,66] A statistical argument supporting their results was quickly published by Purcell,[67] and a fully quantum mechanical description of their results developed by Fano followed a few years later.[68] Their methods were further utilized to determine the size of the reaction regions of high energy physics collision experiments.[58,69] Similarly, the development of a quantum degenerate electron source could motivate an entirely new field of free electron quantum optics.[70,71] A description of quantum degenerate sources, as well as a quantum mechanical treatment of pairs of electron pulses propagating in time, is presented in Chapter 5.

1.2   Ultrafast electron sources

Electron emission from cathode sources can be obtained from a number of different mechanisms. Typical electron sources are made by biasing a sharp metallic tip at a high voltage. The local electric field at the tip modifies the work function experienced by electrons in two ways: first, the barrier obtains a linear negative slope proportional to the electric field strength at the tip, and second, the barrier is

lowered due to the Schottky effect.[72] Electrons can then be emitted from the metal into the vacuum by tunneling through the modified barrier. Thermionic sources can be obtained by applying a current to a cathode, which in most practical cases is a hairpin filament.[73] For sufficiently low electric fields at the filament apex ($<$ $5\,\mathrm{GV/m}$), electron emission follows a Richardson-Schottky model, and depends on the temperature of the emitter and the applied voltage that lowers the material work function.[74] From semiconductors, electrons can be emitted from the conduction band after being promoted from the valence band.[75] For direct band gap semiconductors like GaAs, this can be accomplished by shining light resonant with the band gap energy on the cathode. The energy difference between the conduction band and vacuum, sometimes referred to as the ionization energy,[76] can be modified by layering materials on the surface of the cathode. This layering process is generally referred to as surface activation. For example, GaAs photocathodes are typically activated by layering Cs and O_2 onto a clean crystal surface.[75,77] The band structure of GaAs allows electrons to be pumped from the valence band to the conduction band with a preferential spin population determined by the helicity of light used to pump the photocathode.[75] The spin polarization obtained during optical pumping can survive transport through the activation layer, and thus electrons emitted from the surface will be spin-polarized. To our knowledge, all of these sources emit electrons at random times. When they do so with a well-defined energy, they are referred to here as continuous wave (CW) sources.

The essential ultrafast electron source requires focusing femtosecond laser pulses onto a photocathode material. Typically, the photocathode of choice is a metallic field emission tip having a radius of curvature on the order of $10\,\mathrm{nm}$–$100\,\mathrm{nm}$; however, since the observation of ultrafast emission from tungsten and gold tips,[4–6] fast electron emission has also been observed by focusing femtosecond laser pulses onto ion-milled grating structures which couple the laser pulses into surface plasmon pulses that

propagate toward a sharp apex,[78–80] and from flat surface unactivated GaAs photo-cathodes attributed to a multiphoton process.[81] The emission process of an ultrafast source results from a number of different mechanisms and depends on the material, the intensity of laser used, and the applied voltage. So far, fast electron emission has been attributed to multiphoton processes, above threshold photoemission, optical field emission, thermally-assisted photoemission, and plasmonic field emission.[19,79,82] Ultrafast electron sources have so far been implemented successfully in a number of schemes.

It is important to define precisely what we mean by "fast" when describing the emission process. When we refer to a fast source of electrons, we mean that the time scale of the emission process is comparable to duration of the laser pulses that cause the emission.[5,33,34] This characterization has only an indirect bearing on the duration of emitted electron pulses, in that temporally short electron pulses can be obtained from fast emission processes, while long electron pulses are expected from slow emission processes. This characterization also does not determine how promptly electron emission follows excitation with the laser pulse, although it is expected that fast emission processes ought to be prompt.

Characterizing how fast an emission process is can be accomplished through pump/probe techniques. When the emission process is found to be additive, electron emission from probe pulses is no longer affected by processes initiated by pump pulses. In this work, pump/probe measurements were performed for a number of samples, including annealed tungsten tips, annealed gold tips, and gold nanoribbons in Ch. 2,[33] and GaAs shards in Ch. 5.[34] The gold nanoribbons, named as such due to their square cross-sectional profile and high aspect ratios, were prepared for us in the research lab of Professor Bret N. Flanders with his graduate student, Gobind Basnet, at Kansas State University, using the method of directed electrochemical nanowire assembly

(DENA).[26,27,83] Comparing emission data among the metallic samples showed that emission from gold nanoribbons can proceed from thermally-assisted processes. The signature of thermal processes depends on the thermal conductivity of the sample being considered. Gold nanoribbons, which have fairly low thermal conductivity and thus retain heat for relatively long times, have been shown to take up to 5 µs to cool to 20 % of their peak temperature in a laser focus.[84] At high source temperatures, one emission signature is therefore enhanced additive electron emission for delays longer than the incident pump and probe pulse durations due to thermally enhanced emission. A second signature, in cases where the laser heating is sufficient, can be observed in the extended tails of the detected time-of-flight spectra taken for single beam illumination. This thermal energy is likely acquired due to laser heating of the samples, and is shown to scale with the incident intensity and polarization used. The time-of-flight spectra can be modeled with a Richardson-Schottky mechanism, which is used to determine the temperature of the source in the laser focus, as well as the material work function and emitter radius of curvature.[74] For GaAs, the multiphoton emission process is more complicated as it can be additive similar to metallic field emission tips, or in an unexpected twist can be subadditive for long delays. The mechanism for subadditive emission is currently under investigation, but a model is presented here that shows that the emission process from GaAs is nonetheless due to a fast process. It was determined by measurements performed by Evan Brunkow and Nathan Clayburn in the lab of Professor Timothy J. Gay here at the University of Nebraska-Lincoln that electron emission from GaAs shards can be spin-polarized, but it remains to be seen if the spin-polarized emission from GaAs shards is due to a fast process.

1.3   Using Feynman's path integrals to describe matter waves

The subject of Richard M. Feynman's own graduate dissertation was the development of the path integral formalism for quantum mechanics.[41,42] Feynman followed Dirac's work that showed the phase evolution of a quantum state between two space and time coordinates was related to the action functional.[85] In Feynman's path integral solution to the Schrödinger equation, a source probability amplitude is propagated in space and time over discrete time steps, where the phase of the amplitude evolves by the value of the action integral along the path taken in the limit of infinitesimal time steps. The path integral propagator, or kernel, is itself a solution of the time-dependent Schrödinger equation.[86] The final probability amplitude is determined by taking the sum of the amplitudes obtained over all possible paths that could exist in the system, and a final probability distribution function is then obtained as the square modulus of the final probability amplitude. Practically, as it is impossible to sum over infinitely many paths in a simulation, it suffices to use paths that result in values of the accumulated phase that are similar to the semiclassical paths in the system, that is, the phase difference between neighboring paths should be smaller than π. The density of spatial or temporal steps necessary for a calculation can then be determined then by observing numerical convergence of the final result.

In our research group, we have used the path integral propagator to describe various scenarios, including the free propagation of electrons through material gratings and slits, as well as through potentials.[37,40,43–47] When appropriate, the propagator phase can be computed using only the path lengths between propagation points and the de Broglie wavelength of particles considered. This computation method is possible in steady-state systems when the matter-optics analogy holds, that is, when a variation in propagation time does not affect the differences in the accumulated phase along

neighboring paths. In situations where the propagation times must be considered, such as passing from one side of a slit to the other in a near-field configuration, the full time-dependence of the propagator must be used.[48] This behavior is explored in detail in Ch. 3. The time-dependent path integral propagator is used to show when one can expect deviation from the matter-optics analogy. As the position of slits acts as a gate to the possible free-space paths at particular times, it is shown that diffraction of matter waves from spatial slits can also demonstrate effects due to diffraction in time. What is perhaps not expected is that the effects of diffraction in time manifest themselves as differences in the spatial diffraction pattern. These effects make matter wave diffraction distinct from optics, as light in free space does not experience dispersion. This means that although the matter/optics analogy generally holds, as is the case for far-field diffraction experiments, care must be taken in the situations where matter wave propagation differs from light wave propagation, and the correct time-dependent formalism must then be used to describe matter waves. The methods obtained and established in Ch. 3 will be applied later in Ch. 5 to the case of the temporal evolution of electron wave packets between two points in space.

The path integral method is also explored for its pedagogic value. The elements of the path integral method, that is, the paths connecting source distributions to screens, and the phases accumulated along the paths, can be used to describe a picture of constructive and destructive interference. In contrast, the usual description of wave interference from slits involves drawing waves along "paths," where interference at a detection point is determined by how much the path lengths differ by fractional multiples of a wavelength.[87–91] These waves could either be interpreted as stationary, e.g., as solutions to the time-independent Schrödinger equation, or as a snapshot of waves evolving in time, i.e., the waves demonstrated by a ripple tank. The distinction is subtle and not usually made. If one considers the stationary wave, the correct

phase difference between waves can be obtained by counting the wavefronts between points. However, if the waves pictured are considered to be evolving in time, the phase difference will be incorrect by a factor of 2, despite the fact that matter and light of the same wavelength are taught to result in the same diffraction pattern. The picture, that uses stationary waves with the same wavelength, is related to the time-independent solution to the problem. It is shown that the discrepancy in the factor of 2 difference between the phase obtained from the time-independent picture and the phase obtained from the application of time evolution to the time-independent picture is due to dispersion, or that the group velocity and the phase velocity describing a matter wave also differ by a factor of 2. Invoking the path integral formalism from the start of the discussion avoids this conceptual difficulty and also justifies the use of paths, as paths are a physical element in the path integral solution and not in the solution of the time-independent wave equation. Thus, the accumulated phase along a single path of a propagating matter wave is half the value expected from optics. This may come as a surprise as it could lead to incorrect predictions. Nevertheless, the phase difference for neighboring paths in the far field agrees with the value expected from optics.

1.4   Visualizing wave-particle duality

One of the difficulties in presenting quantum mechanics is in finding appropriate demonstrations by analogy to aid in visualizing abstract concepts. The physical elements of nonrelativistic quantum theory are waves, so it is natural to present certain phenomena, such as electrons diffracting from slits or scattering from crystals, by presenting other wave systems, such as surface waves excited in a ripple tank, or by analogy in microwave or laser apparatus.[92–94] These systems reinforce the matter/optics analogy, but are missing a key element of experimental observation.

In quantum systems, the observed phenomena are localized "clicks" or "lumps." [95] That is, flashes of fluorescent light or electronic pulses that are well-localized are often identified with particle-like behavior. Rigorous treatments of quantum mechanics will illuminate this issue, as it is an essential step toward describing the quantum measurement problem. [96] For visualizing quantum effects by analogy, it would appear only the wave element of the theory has been accessible thus far. Beginning in 2005, a series of remarkable experiments performed in the research group of Yves Couder developed a system capable of demonstrating quantum analogues which appeared to exhibit both the wave and the particle element of the theory. [51] In short, the system exhibited an intriguing new form of wave-particle duality. [54]

A system consisting of a dish filled with silicone oil (dimethicone), shaken vertically at frequencies near $50\,\mathrm{Hz}$, was shown to support a bouncing droplet with diameter on the order of $1\,\mathrm{mm}$ of the same oil without the droplet coalescing into the fluid. [51] This behavior was found to be due to the existence of a thin layer of air that forms between the droplet and the fluid surface. As the droplet falls, momentum is transferred between the drop and the fluid surface. This causes a circular ripple to form on the surface of the fluid. When the shaking conditions are appropriately tuned, this surface ripple will persist for many oscillations of the dish as a result of the Faraday instability. The Faraday instability is the spontaneous formation of waves on the surface of a shallow fluid under the influence of vertical shaking, which was originally explored by Michael Faraday. [50] This Faraday wave, with a wavelength λ_F of approximately $5\,\mathrm{mm}$, can impart momentum to the drop in the plane of the dish as the fluid surface obtains a slope. In the regime where the droplet bouncing period is twice as long as the shaking period, the droplet will fall on approximately the same fluid height and slope on each bounce, and will march in step with the driving frequency. The oil droplets exhibiting this behavior were originally dubbed *marcheurs*, or "walkers." [52]

Single walkers in a level and barrier-free cell tend to move in straight trajectories with fixed velocities, until they approach a boundary or disturbance in the surface of the fluid.[97] As a walker approaches a cell boundary, the Faraday wave of the walker interacts with the boundary, and the trajectory of the droplet is diverted away from the disturbance. This behavior allows walkers to be pushed around the surface of a fluid with a toothpick, or whatever thin stick happens to be available, without touching the droplet. It was found from this behavior, that while the droplet causes the formation of the Faraday wave, it is the state of the Faraday wave at each bounce that controls where the droplet will bounce. In essence, the Faraday wave maintains a kind of "memory" of previous bounces, and the state of the Faraday wave at any time is in effect a sum of all the prior configurations of the wave which have not yet damped away.[55] Instead of a solid wall, parallel strips were placed under the surface of the fluid, with a narrow (15 mm) opening. The trajectories of walkers passing through this opening were deflected by angles that appeared to be independent of what part of the opening the walkers crossed. After sending many single walkers through this opening, it was reported that an approximate Fraunhofer diffraction distribution of could be obtained. A similar result was obtained for a pair of openings, with each opening being 8 mm wide.[57] It would seem that the challenge of visualizing wave-particle duality found an answer.

Since the presentation of macroscopic single-particle diffraction, a number of other analogues with single walkers demonstrating quantum behavior were developed. These systems included tunneling through a barrier,[98] Bohr orbit quantization,[53] and tracing the distribution of the quantum corral.[99] The orbits of pairs of walkers interacting through their Faraday waves were found to exhibit an analogous effect to Zeeman level splitting.[100] Droplets have been injected with ferrofluid so that they could be affected by magnetic fields configured into a harmonic potential, and thus demonstrated

behavior analogous to the harmonic oscillator.[101]

While these analogues were being explored, we attempted to recreate Couder's single- and double-slit results. Before our results were published,[102] we learned that the research group of Thomas Bohr, grandson of Niels Bohr, had the same goals. His group published results that would seem to contradict Couder's findings, and claimed that they were outright falsified by the new data and a quantum mechanical *Gedankenexperiment.*[103] Our results similarly did not demonstrate single- or double-slit diffraction. Research published from the group of John M. Bush at MIT did not replicate the original results either, but demonstrated the importance of initial conditions and experimental controls in the results that can be obtained.[104] It would appear that we found ourselves in a developing controversy that was even reported in a popular science publication.[105]

The results we obtained for single- and double-slit diffraction of walkers is shown in Ch. 4. A number of students, both graduate and undergraduate, made contributions to the development of the working system over time. The design of coupling a magnetic shaker (in our case, a subwoofer) to a dish that could be externally leveled was my own, and was picked up by other groups.[106] The system we built is highlighted, along with the features it was able to demonstrate. The overall apparatus we built was at considerably less to no cost in comparison to other rigs, which makes our apparatus viable as a tool for demonstration as well as for use in introductory research projects. To show this, data obtained by high school students who worked on the apparatus during the summer of 2018 is presented. We conclude that it is entirely possible to contribute to scientifically controversial research on a low budget, and that this apparatus can aide in visualizing analogues of quantum behavior in a manner that is appropriate for a broad audience.

1.5 Degenerate sources for free-electron quantum optics

The field of quantum optics is generally thought to have begun with the stellar measurements of Hanbury Brown and Twiss (HBT).[64,65] They developed a radio telescope that made use of the spatial correlations of the *intensity* of radio waves emanating from stars, in contrast to methods using Michelson interferometry to obtain correlations of the optical wave field *amplitude*.[58] As Michelson interferometers depend on wave amplitudes, the methods of the time were sensitive to random phase differences introduced between the two input ports that collected light from the object to be measured. The intention of HBT was to develop an intensity interferometer for optical wavelengths, as an intensity interferometer would reduce the sensitivity of the interferometer on phase shifts caused by atmospheric disturbances, and optical wavelengths reduced the baseline necessary to resolve the small angular width of distant objects. Intensity interferometry was understood in the context of radio waves, but there was considerable doubt that employing photomultiplier tubes as detectors for optical wavelengths would give the same results. The method would be proven and tested in a series of fascinating articles published to *Nature* between 1955 and 1957. In order to verify that the intensity interferometer worked in principle for optical sources, HBT performed a table-top experiment using a split beam from a thermal source that was detected by separate photomultipliers to show that indeed, the intensity of coherent sources, and for what was at the time most surprising, the number of detected photons, will be correlated for short time delays between the detectors.[59] That is, photons emitted from a chaotic source were shown for the first time to bunch in time. Their methods and results received immediate criticism from Brannen and Ferguson, who reported an experiment where it was claimed that the original HBT results could not in principle be reproduced.[107] The response from HBT was to build

and demonstrate their optical intensity interferometer to measure the angular width of Sirius A, which they found agreed well with theoretical predictions.[66] In a short article published on the same day as the HBT measurement of Sirius A that demonstrated their optical intensity interferometer, the earlier results showing photon correlations were further justified by a statistical argument made by Purcell, who explained that one would expect to see bunching for a source of bosons prepared in the same state.[67] Purcell also remarked, that one would expect no such bunching for a beam of electrons. He wrote,[67]

> Were we to carry out a similar experiment with a beam of electrons, we should, of course, find a slight suppression of the normal fluctuations instead of a slight enhancement; the accidentally overlapping wave trains are precisely the configurations excluded by the Pauli principle. Nor would we be entitled in that case to treat the wave function as a classical field.

It would seem that this discussion would also then also anticipate the field of free-electron quantum optics.

Such an experiment as described by Purcell was carried out for a beam of free electrons emitted by a sharp tungsten cathode by Kiesel, Renz, and Hasselbach, in 2002.[70] They reported a decrease in coincidence detections of electrons produced by their field emission tip source when they compared incoherent detector illumination to coherent illumination. However, this change in signal was small ($\sim 10^{-4}$) due to their source's low quantum degeneracy, which is a measure of the occupation of electron states produced by the source. Further, it was found that their measurements were consistent with Coulomb effects, as electrons placed in spatial proximity will experience a mutual Coulomb repulsion.[71,108,109] A necessary development to settle the debate over whether quantum degeneracy or Coulomb repulsion was in effect would be an on-demand electron source that can produce electrons in nearly the same quantum state, within Heisenberg uncertainty. Ultrafast electron sources are the ideal

candidates to accomplish this goal, as they confine electron states both spatially and temporally. However, as electrons also have a spin degree of freedom, the typical metallic tip may not be sufficient to distinguish quantum degeneracy from Coulomb repulsion.

In Chapter 5, the quantum degeneracy of an ultrafast source is described. It is shown that with our current experimental apparatus, it is possible to approach a quantum degeneracy of ~ 1, which is 4 orders of magnitude greater than that reported by Hasselbach. A Hanbury Brown-Twiss experiment for a pulsed source of completely spin-polarized electrons is modeled using the path integral methods developed in Ch. 3 to describe the evolution of electron wave packets. These path integral methods are compared to a semi-classical time-of-flight method described by former graduate student Brett Barwick.[110] From these considerations, I conclude that our current detector apparatus should have the necessary temporal resolution to observe effects caused entirely by quantum degeneracy at the source. I designed a split detector consisting of a pair of Dr. Sjuts channel electron multipliers, which has been assembled and is currently being studied by graduate student Sam Keramati. Finally, the last element needed to test quantum degeneracy, a spin-polarized source, is described. Through collaboration with Professor Timothy J. Gay and his graduate students Nathan Clayburn and Evan Brunkow, we have developed an ultrafast source of spin-polarized electrons by illuminating a GaAs shard with femtosecond laser light. The possibility of illuminating our sources with femtosecond laser light was provided by collaboration with Professor Kees Uiterwaal and his graduate student Joshua Beck. Such a source has the potential for broad applications similar to ultrafast metallic tip sources, as well as the possibility of producing an on-demand quantum degenerate electron beam. A quantum degenerate beam is a vital component of experiments in quantum optics, but the analogous element has not yet been realized for electrons.

The range of capabilities and utility of such a beam remain to be explored, but one possibility is that a quantum degenerate beam could be used to finally distinguish Pauli from Coulomb repulsion for free electrons.

Chapter 2

Laser-induced electron emission from Au nanowires: a probe for orthogonal polarization

Photoelectron field emission, induced by femtosecond laser pulses focused on metallic nanotips, provides spatially coherent and temporally short electron pulses. Properties of the photoelectron yield, such as the arrival time of photoelectrons and pump/probe behavior, give insight into both the material properties of the nanostructure and the exciting laser focus. Ultralong nanoribbons, grown as a single crystal attached to a metallic taper as characterized by transmission electron microscope (TEM) measurements performed by our collaborators at Kansas State University, are sources of electron field emission that have not yet been characterized. In the following, photoemission from gold nanoribbon samples is studied and compared to emission from tungsten and gold tips. We observe that the emission from sharp tips generally depends on one transverse component of the exciting laser field, while the emission of a blunted nanoribbon is found to be sensitive to both components. We propose that this property makes photoemission from nanoribbons a candidate for position-sensitive detection of the longitudinal field component in a tightly focused beam.

2.1   Introduction

A consequence of tightly focusing a beam of light is that the beam will become partly longitudinally polarized near the focus.[111–114] The concept of a longitudinally polarized electric field is perhaps familiar in the context of field modes confined to metallic wave guides, in particular, as in the case for transverse magnetic field modes propagating in a rectangular guide.[115] The notion of longitudinal polarization is less familiar in the propagation of beams in free space. The propagation of beams generally follows from the paraxial approximation to Maxwell's equations, which assumes that the complex electric field $\vec{E}$ admits plane-polarized solutions, that is, $\vec{E}$ is transversely polarized to the direction of propagation, and also satisfies $\nabla \cdot \nabla \cdot \vec{E} = 0$. It was shown by Lax, Louisell, and McKnight that these two conditions are generally incompatible with the complete form of Maxwell's equations, but if an expansion of Maxwell's equations in powers of the ratio of the beam waist to the Rayleigh length is considered, the familiar paraxial solution is obtained as the zeroth-order term of the expansion, while the first-order correction includes a longitudinal field component.[112] Tight focusing, which occurs when the size of the focal waist is comparable to the Rayleigh length, therefore results in a component of longitudinal polarization within the focus. A schematic of the transverse and longitudinal polarizations of a tightly focused beam with a focused waist w_0 and Rayleigh length z_R is shown in Fig. 2.1.
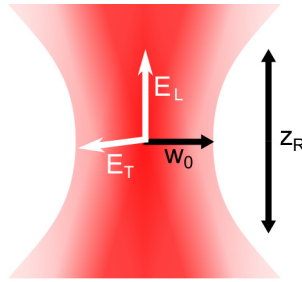
Figure 2.1: Schematic of a tightly focused beam. When the beam waist w_0 is comparable to the Rayleigh length z_R, a longitudinal component of the electric field will be present in the laser focus, denoted by E_L, along with the expected transverse component, E_T.

Longitudinally polarized laser beams are desirable because their focal widths can be below the diffraction limit, and the longitudinal component of the electric field does not contribute to the energy flow along the direction of beam propagation.[116,117] These features find applications in high-resolution optical microscopy,[118,119] optical data storage,[120] particle trapping,[121,122] charged particle acceleration,[123] material ablation,[124] and pushing the high-intensity frontier. The longitudinal field component of a laser focus has been characterized *in situ* by atomic fluorescence[125] and near-field microscopy,[117] and *ex situ* via imaging of material damage[124] and atomic force microscopy of thin film deformation.[126] As the *in situ* methods of characterizing the longitudinal field are limited by intensity or to a resonant wavelength, a flexible alternative would be preferable.

Photoelectron field emission, induced by focusing femtosecond laser pulses onto sharp metallic tapers with nanometer-scale radii of curvature,[4–6] has a broad range of applications. Temporally short electron wave packets[22] with high spatial coherence[20,127] can be achieved with moderate intensities. Tip sources have thus been integrated into electron microscopes to obtain sub-micron spatial resolution with femtosecond timing.[11,14,15] Femtosecond electron pulses have been used to study fundamental quantum mechanics, as in testing the existence of forces in the Aharonov-Bohm

effect,[21] and observing diffraction in time.[22,23] Electron emission from nanotips has been obtained for a range of laser intensities and wavelengths.[128–130] Nanotip emission might then provide an alternative for characterizing the longitudinal component of a laser focus. However, as nanotip emission is dominated by a single transverse component of the polarization of the exciting field, it has not yet been utilized of longitudinal fields.

Ultralong gold nanoribbons,[27] grown by the method of directed electrochemical nanowire assembly (DENA),[26,83] were previously unstudied sources for ultrafast electron photoemission. The DENA method results in single-crystalline samples, as confirmed by electron diffraction, with a uniform rectangular cross-section along the sample length. The samples can also be grown with a considerably large aspect ratio of the length compared to the cross-sectional widths, hence why they are referred to as ultralong nanoribbons in order to distinguish them from standard nanowires. Previous studies into the optical damage threshold of similar nanowire samples indicated that single-crystalline gold nanowires could tolerate high laser pulse peak intensities before melting, but that they exhibited long cooling times on the order of $5\,\mu s$.[84] From these studies, the exchange and dissipation of heat between the nanowire electrons and the crystalline lattice could be modeled. A logical next step would then be to characterize electrons emitted from nanoribbons in response to ultrashort pulse illumination. Photoelectron emission is known to carry information on material effects, such as plasmonic dynamics and laser heating.[19,79] Temporally short electron pulses have been observed from plasmonic nanostructures,[131,132] and the photoemission yield has been used as a sensitive probe of the plasmonic field enhancement from nanostructures.[133] We measured photoelectron emission from nanoribbons in an attempt to determine their plasmonic or thermal properties.[19,79,133] In the following, nanoribbon samples are characterized by photoelectron emission and compared to standard single-crystalline

gold and tungsten samples. The resulting photoelectron emission spectra reveal that nanoribbons can be employed as position- and polarization-sensitive detectors within a laser focus. As the transverse dimensions of nanoribbon samples can have a thickness of 40 nm, and widths ranging from 130 nm–360 nm along the length of the sample, with an apex radius of curvature of 10 nm,[27] these nanoribbon samples could provide a potential *in situ* sub-wavelength probe for longitudinal polarization of pulsed beams having a typical wavelength of 800 nm.

2.2 Experimental apparatus

A schematic for the system used to characterize tip samples is given in Fig. 2.2.
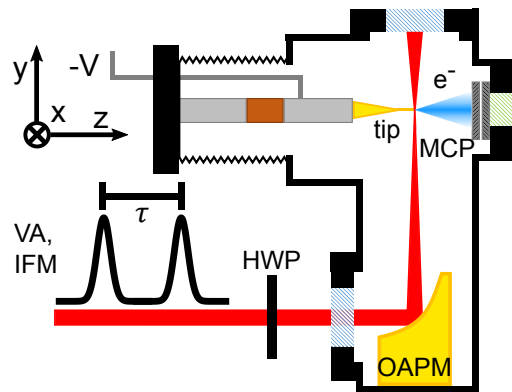
Figure 2.2: Experimental schematic showing pump/probe configuration for tip and nanoribbon photoelectron emission (see text for description).
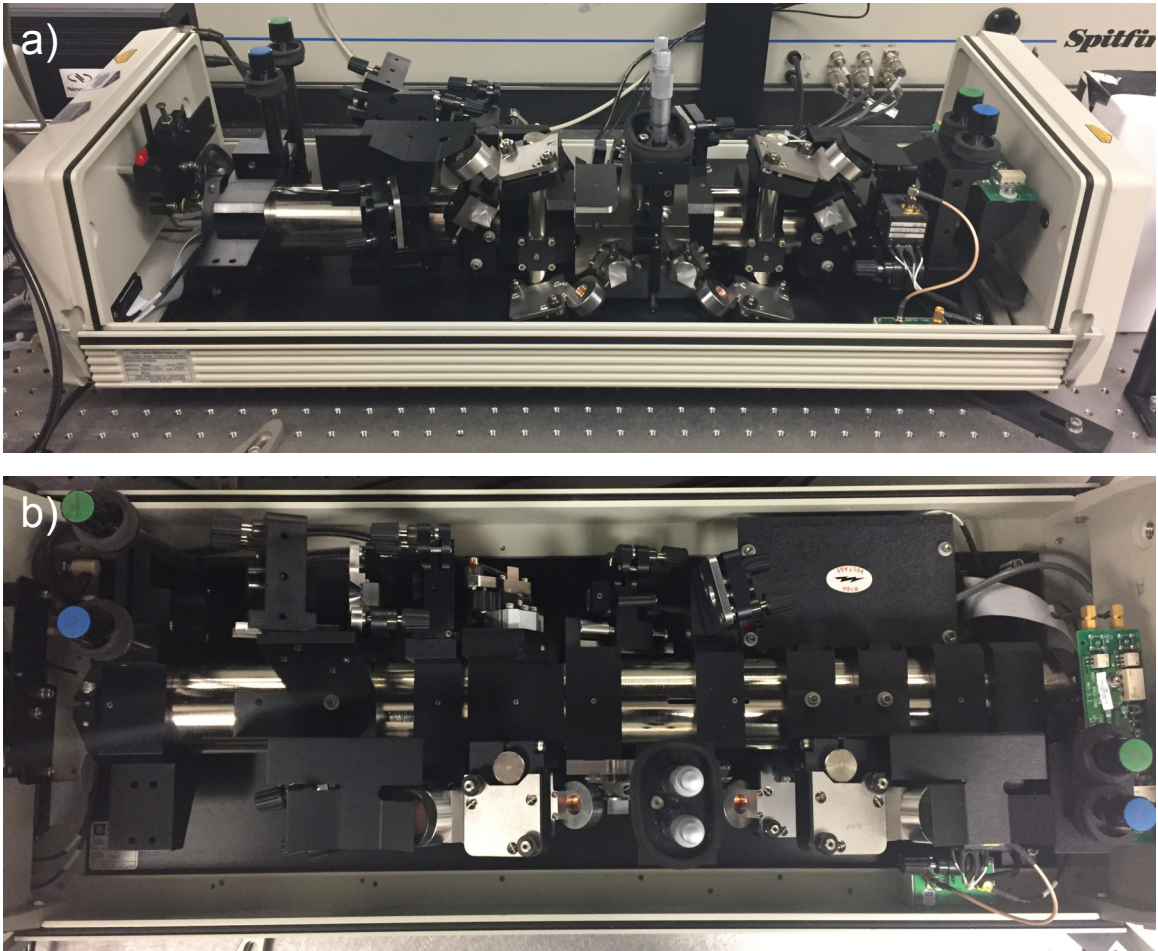
Figure 2.3: The Ti:Sapphire oscillator, viewed with the cover removed. The view from the front is shown in (a), and a view from the top is shown in (b).

The laser system used for the experiments described here was provided and maintained by the laboratory of Kees Uiterwaal, with regular maintenance and repairs performed diligently by his graduate student, Joshua Beck. The intensity of the output from a Ti:Sapphire oscillator, shown in Fig. 2.3 (Spectra Physics Tsunami, 80 MHz repetition rate, 800 nm central wavelength, 100 fs pulse width) is controlled by a variable attenuator (VA), which consists of a $\lambda/2$ plate and a Brewster window. The attenuated beam is split into a pump and a probe beam by a balanced Mach-Zehnder interferometer (IFM), which is shown in Fig. 2.4.
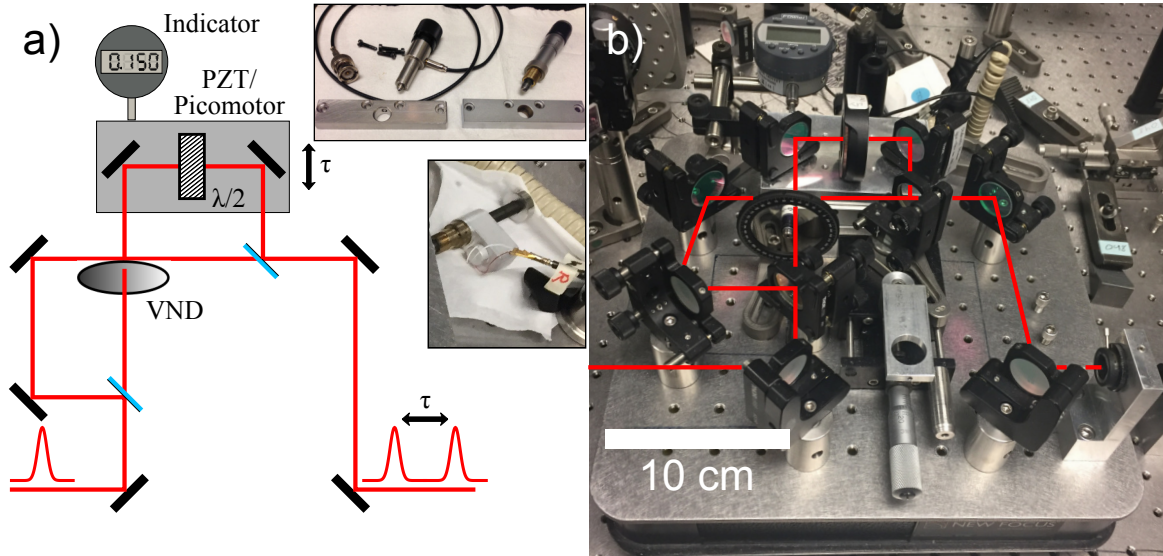
Figure 2.4: (a) Schematic of the Mach-Zehnder interferometer, showing beam path and optical components. The probe beam passes through both a variable neutral density (VND) filter and a $\lambda/2$ plate to control the power and polarization, respectively. Insets show the translation stage adapter plate, which can be used with the Thorlabs model PE4 PZT micrometer (top), and the Newport model 8302-V picomotor (bottom). A Fowler electronic indicator, mounted to the interferometer slab, is used to measure the displacement of the translation stage relative to the slab. (b) Picture showing the beam path through the Mach-Zehnder interferometer. The schematic, insets, and interferometer picture are to scale.

Photoelectron emission is observed in pump/probe and single beam experiments. The time delay between pump and probe pulses, τ, can be varied from $-4\,\mathrm{ps}$ to $4\,\mathrm{ps}$ manually by a micrometer that varies one arm length of the interferometer. The additive ratio, $\mathcal{R}(\tau)$, measured as a function of the delay τ, is defined as

$$\mathcal{R}(\tau) \equiv \frac{R_{both}(\tau)}{R_{pump}(\tau) + R_{probe}(\tau)}, \tag{2.1}$$

where $R_{pump}(\tau)$ and $R_{probe}(\tau)$ are the emission rates from the pump and probe beams separately at each delay, and R_{both} is the rate measured when both beams are incident on the sample. Electron emission from the pump and probe beams is considered to be completely independent when the emission is additive, or when $\mathcal{R}(\tau) \approx 1$. Note that a

similar pump/probe measurement performed on GaAs shard samples will be described later in Ch. 5, and defined by Eq. 5.23 in a slightly different fashion than here in Eq. 2.1. This was historically due to different preferences regarding ratios. The only notable difference is that for Eq. 5.23, the condition for additive emission will be given by $\mathcal{R}(\tau) \approx 0$ instead of $\mathcal{R}(\tau) \approx 1$. A second $\lambda/2$ plate (HWP) rotates the polarization of both beams prior to delivery to the experimental chamber. A rotational stepper motor is used to scan the beam power and the polarization. The beam path, from the variable attenuator to the experimental chamber, is shown in Fig. 2.5.
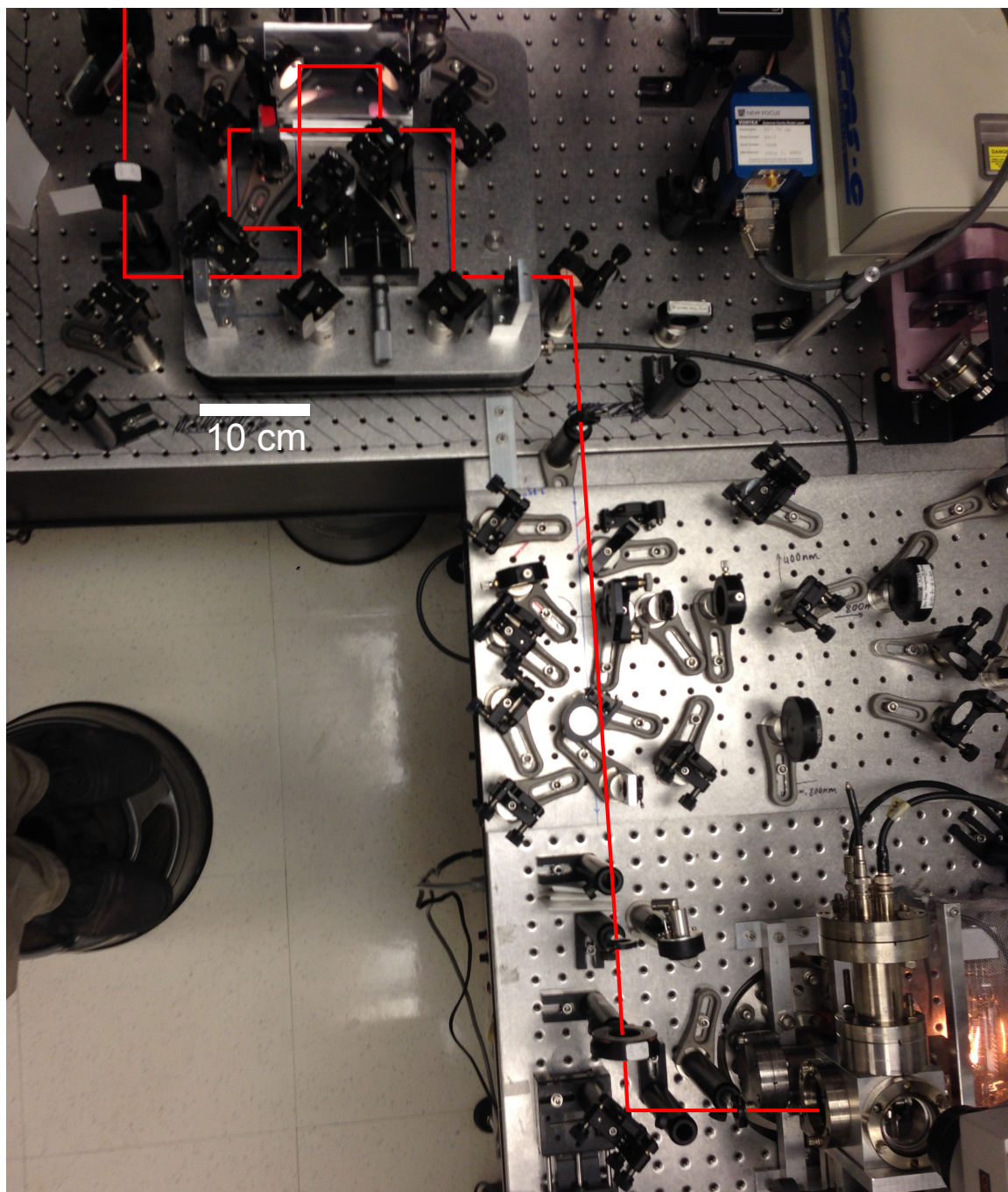
Figure 2.5: Picture showing the beam path, starting from the variable attenuator, and ending at experimental chamber.

The experimental chamber, which is also detailed in Ref. [5], is maintained at 2×10^{-7} Torr. The beams are focused within the chamber by an off-axis parabolic

mirror to a full-width half maximum of 4.5 µm. A 3-axis stage, coupled to the chamber by flexible bellows, positions tip samples into the focus. Mounted tip samples were biased at -100 V, as this was lower than the threshold for Fowler-Nordheim dc field emission. A brief discussion on Fowler-Nordheim emission now follows.

Fowler-Nordheim emission describes the tunneling of electrons bound in a metal from the Fermi level through a triangular potential barrier into vacuum at low temperature. The expression describing the Fowler-Nordheim emission current, in Hartree units, can be found in Eq. 56 of Ref. [74]. The physical elements in the expression include the electric field at the emitter tip, the material work function, and the emitter temperature. The dc electric field, F_{dc}, at the surface of a conducting sphere with radius of curvature r, and held at an applied voltage V, is given by $F_{dc} = V/r$. For a field emission tip, which can be approximately described as the union of a hemisphere with a conical taper, the dc electric field is described similarly. The electric field at the surface of a field emission tip with a radius of curvature r_{tip} held at an applied voltage V can be expressed as $F_{dc} = V/(kr_{tip})$, where $k \approx 5$ is a geometric correction factor that accounts for the shank of the tip.[134] The conversion to Hartree units follows from dividing the electric field strength, F_{dc}, in units of V/m, by the constant $m^2 e^5 \hbar^{-4} = 5.15 \times 10^{11}$ V m^{-1}. The emitter material has a work function, ϕ_{wf}, and a thermal energy $k_B T$, where k_B is the Boltzmann constant. The conversion of these quantities, expressed in eV, to Hartree units, is accomplished by division by the constant $me^4 \hbar^{-2} = 27.2$ eV. The emission current j can then be written, with electric field F, work function ϕ, and thermal energy E_T in Hartree units,

$$j = \frac{F^2}{16\pi^2 \phi \left[t(y)\right]^2} \left(\frac{\pi c E_T}{\sin \pi c E_T}\right) \exp\left[-\frac{4\sqrt{2}\phi^{3/2}v(y)}{3F}\right], \qquad (2.2)$$

where $y = \sqrt{F}/\phi$ is a dimensionless parameter, $t(y)$ and $v(y)$ are functions of elliptic

integrals that arise in the derivation of Eq. 2.2, and c is a constant depending on F, ϕ, y, and $t(y)$ as $c = 2\sqrt{2}F^{-1}\phi^{1/2}t(y)y$. The expression is valid when $cE_T < 1$, which at a temperature of $300\,\mathrm{K}$ is assured for voltages greater than $6\,\mathrm{V}$. The functions $t(y)$ and $v(y)$ are related by a third function, $s(y)$, as $3t(y) = 4s(y) - v(y)$. The functions $v(y)$ and $s(y)$, historically referred to as Fowler-Nordheim field emission functions, are determined numerically. Selected values were tabulated by Burgess, Kroemer, and Houston as a correction to the original analysis of the tunneling process by Nordheim.[135,136] The tabulated values of $v(y)$ and $s(y)$ can be interpolated to find the values of $t(y)$ in the range $0 \le y \le 1$. A plot of these functions, and their interpolated values, is shown in Fig. 2.6.
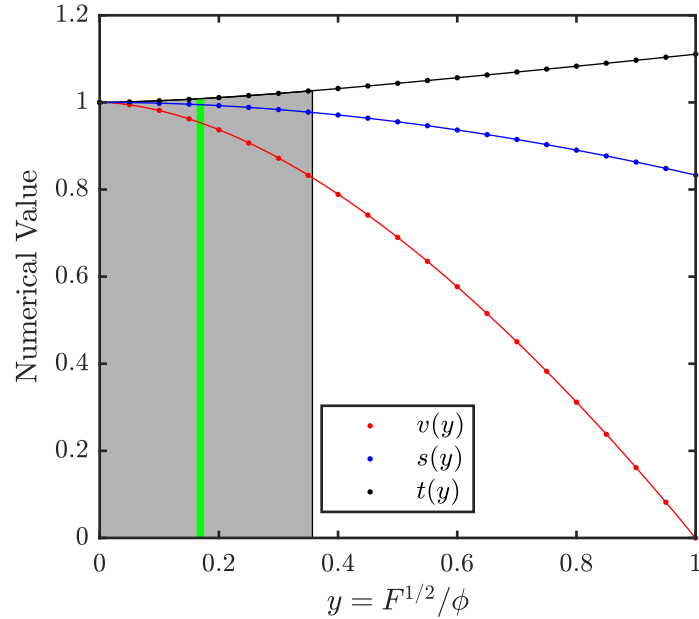
Figure 2.6: Plot of the corrected values of the Fowler-Nordheim functions $v(y)$ (red) and $s(y)$ (blue) tabulated in Ref. [136]. Also shown is the related function, $t(y)$ (black markers), that appears in Eq. 2.2. Lines connecting data points are the result of a 4th-order polynomial fit. The gray area under the curve represents the range of voltages from 0 to $-450\,\mathrm{V}$ applied to a tungsten tip having a work function $\phi_{WF} = 4.5\,\mathrm{eV}$ and radius of curvature $r_{tip} = 50\,\mathrm{nm}$. The green line indicates the values of the Fowler-Nordheim functions for a typical applied voltage of $-100\,\mathrm{V}$.

In Fig. 2.6, the markers indicate the tabulated values provided in Ref. [136]. The lines connecting the markers arise from a 4th-order polynomial fit. The range of y-values that describe the range of voltages applied to our typical sources, which are tungsten tips having a radius of curvature of $50\,\mathrm{nm}$ and a work function of $4.5\,\mathrm{eV}$, is indicated by the gray area under the curves, and represents voltages between 0 and $-450\,\mathrm{V}$. The green line indicates the typical operating voltage of $-100\,\mathrm{V}$. For this voltage, the values of the relevant functions $v(y)$ (red) and $t(y)$ (black) do not vary significantly from 1.

The count rate can be predicted from the theoretical expression for the emission current given in Eq. 2.2. Multiplying the current j by the Hartree unit conversion constant $m^3 e^9 \hbar^{-7} = 2.37 \times 10^{14}\,\mathrm{A\,cm^{-2}}$ gives the current density in SI units. The current in Amperes can be estimated by assuming the entire current passes through an area of $1\,\mathrm{cm^2}$. Division by the electron charge then gives the rate of electron detection. Theoretical predictions for the emission rate are plotted in Fig. 2.7.
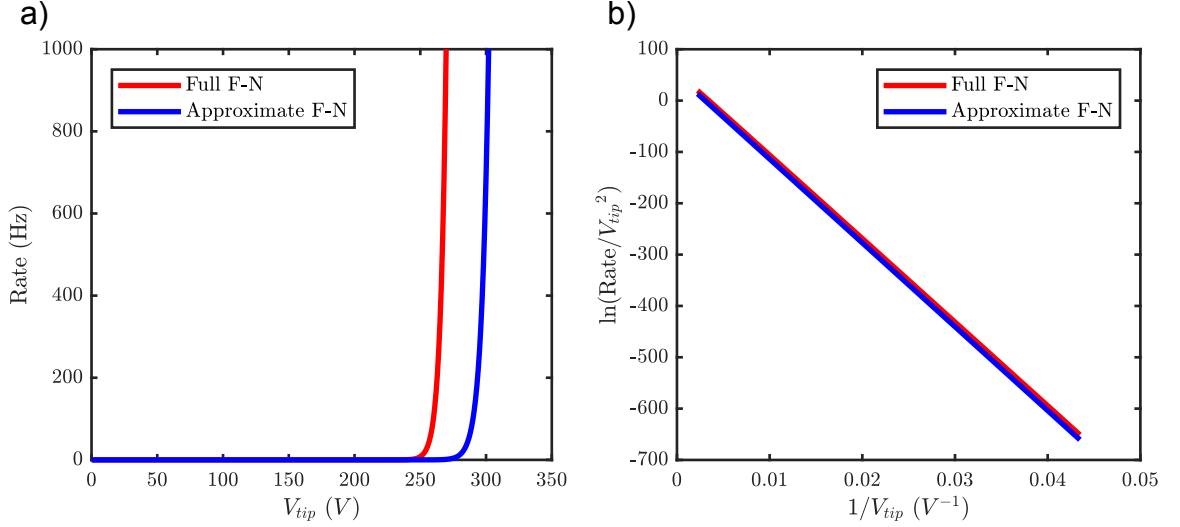
Figure 2.7: Theoretical Fowler-Nordheim emission plots. In (a), the count rate predicted from Eq. 2.2 is plotted as a function of the negative voltage applied to the tip. The red curve shows the rate predicted for the full expression in Eq. 2.2, while the blue curve gives the rate for the approximated form taking the limit $\pi c E_T / \sin \pi c E_T \rightarrow 1$ and the approximation $t(y) = v(y) \approx 1$. In (b), the red and blue curves shown in (a) are presented in the typical form of a Fowler-Nordheim plot, where the quantity $\ln(\text{Rate}/V_{tip}^2)$ is plotted against $1/V_{tip}$. In this form, the slope of these plots can provide the emitter radius assuming the work function is known.

In Fig. 2.7(a), the predicted emission rate is plotted against the applied tip voltage. The red curve shows the emission rate for the full expression in Eq. 2.2, while the blue curve shows the emission rate for the approximate form of the expression. The approximate form is found in the limit $\pi c E_T / \sin \pi c E_T \rightarrow 1$ and by taking $t(y) = v(y) \approx 1$, which is the form of the original Fowler-Nordheim formula.[74] When plotted on these axes, the distinction between the full expression and the approximate form can be readily seen. In Fig. 2.7(b), the full expression (red) and approximate (blue) curves are shown in what is referred to as a Fowler-Nordheim plot. The vertical scale is obtained by dividing the emission rate by $V_{tip}{}^2$ and then taking the natural logarithm. The horizontal scale is obtained by taking the inverse of the tip voltage, V_{tip}. Ideally, this

will result in a line to be fitted with a slope given by

$$FN_{slope} = -\frac{4\sqrt{2}\phi^{3/2}}{3}(kr_{tip})\left(5.15 \times 10^{11}\,\text{V/m}\right),\qquad(2.3)$$

where again ϕ is the work function in dimensionless Hartree units, k is the geometric correction factor for the shank, and r_{tip} is the tip radius. If the work function is a known value, the tip radius can then be determined in this fashion. Practically, as this method is harsh to both field emission tip samples and our detectors (extended measurement of high count rates can decrease the lifetime of our detectors), it is not often used to determine emitter properties. What is more commonly done in our apparatus is to check metallic sources for the onset of Fowler-Nordheim dc emission, which for sharp tips occurs around $-300\,\text{V}$ as shown in Fig. 2.7(a). It is later shown in Sec. 2.3 that electron time-of-flight measurements performed with a nanoribbon sample held at a moderate dc voltage (resulting in a low dc background) illuminated by femtosecond laser light allow for the fitting of the material work function, emitter radius, and temperature without concerns of damaging the sample or the detectors.

Electrons emitted from the source were collimated through two 4 mm apertures before detection by a microchannel plate (MCP). More detailed pictures of the experimental chamber are shown below in Fig. 2.8.
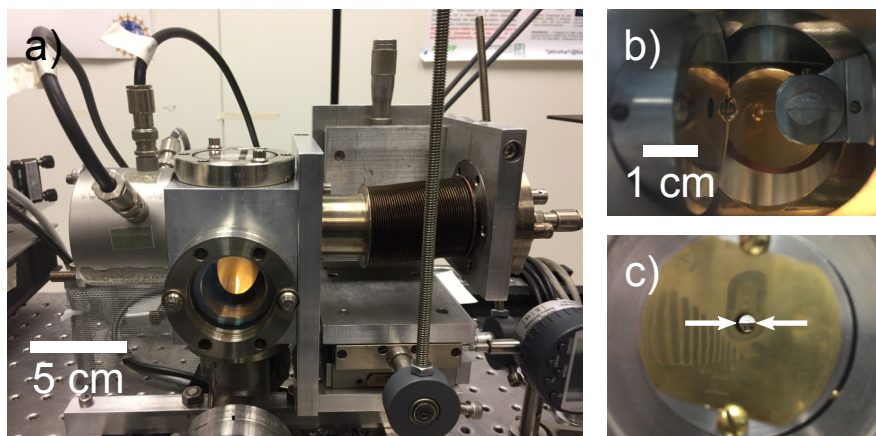
Figure 2.8: Detailed pictures are shown for the experimental chamber. (a) Overview of the chamber, showing the 3-axis stage and exterior of the MCP. (b) Top view of a mounted tip sample showing a mounted tungsten tip and its position relative to the first 4 mm aperture. (c) View from the detector side through the second 4 mm aperture of a mounted sample positioned in the laser focus. White arrows indicate the visible top edge of the sample mount. The image scale is the same as in (b).

Electron pulses from the MCP were amplified and discriminated. Discriminator pulses were counted by a multichannel scaler, and used as the start trigger for a time-to-amplitude converter (TAC). The output reference signal from the Ti:Sapphire oscillator was used as the TAC stop trigger to measure the arrival time of electrons. Timing spectra were obtained by sending the TAC output pulses to a multichannel analyzer (MCA).

Nanoribbon samples were prepared using the DENA methodology.[26,83] Nanoribbon samples are reported to have a rectangular cross section, with a thickness of 40 nm, and widths ranging from 130 nm–360 nm along the length of the sample. The tip apex can have a radius of curvature of 10 nm.[27] These dimensions can be tailored during the growth process to make nanoribbons that are well-suited for photoemission. The apparatus used for nanoribbon growth is shown below in Fig. 2.9.
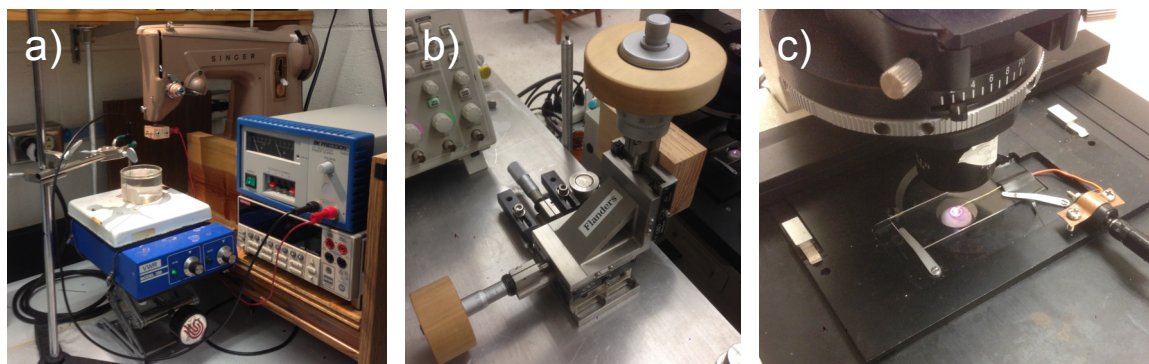
Figure 2.9: Apparatus used for nanoribbon growth in the Flanders group at Kansas State University. (a) Etching process of the working electrode. A gold wire is electrochemically etched to a long, thin taper via oscillation into a solution of KCl. The etching duration is controlled by an electronic timer (not shown). (b) Sharpened working electrodes are mounted to a 3-axis stage, which is used to position the working electrode in relation to the counter electrode. The nanoribbon is then formed by drawing the working electrode away from the counter electrode. (c) Microscope set-up used to image and facilitate nanoribbon growth. Growth parameters are described in detail in Ref. [27] and summarized below. The working electrode and counter electrode are submerged in a $20\,\mu\text{L}$ drop of 40.0 mM $KAuCl_4$. A $37\,\text{MHz}$ square wave applied between the electrodes drives the nanoribbon growth.

The process begins by etching a polycrystalline Au wire into a long, narrow taper. Fig. 2.9(a) shows the etching rig used in the Flanders group, which produced our nanoribbon samples. The etchant used was a solution of KCl, which was periodically stirred and heated. The counter electrode used in the etching process was a graphite rod obtained from mechanical pencil refills. Gold wire was mounted in the modified sewing machine, which was used to oscillate the sample in and out of the KCl solution. The etching process was repeated until the working electrode had the desired shape.

The next step in nanoribbon production was to immerse the sharpened working electrode and blunt counter electrode in a solution of aqueous $KAuCl_4$. This was performed while being monitored by an optical microscope, shown in Fig. 2.9(c). A $37\,\text{MHz}$ square wave applied between the electrodes causes the Au to crystallize on the working electrode. The growth of the crystal is controlled by slowly drawing the

working electrode away from the counter electrode. This is accomplished with a 3-axis stage mounted next to the microscope system, which is shown in Fig. 2.9(b). Fig. 2.10 shows a series of optical microscope images illustrating the growth and branching of a nanoribbon. In the images, the sharp working electrode moves from left to right, while the blunt counter electrode remains stationary.
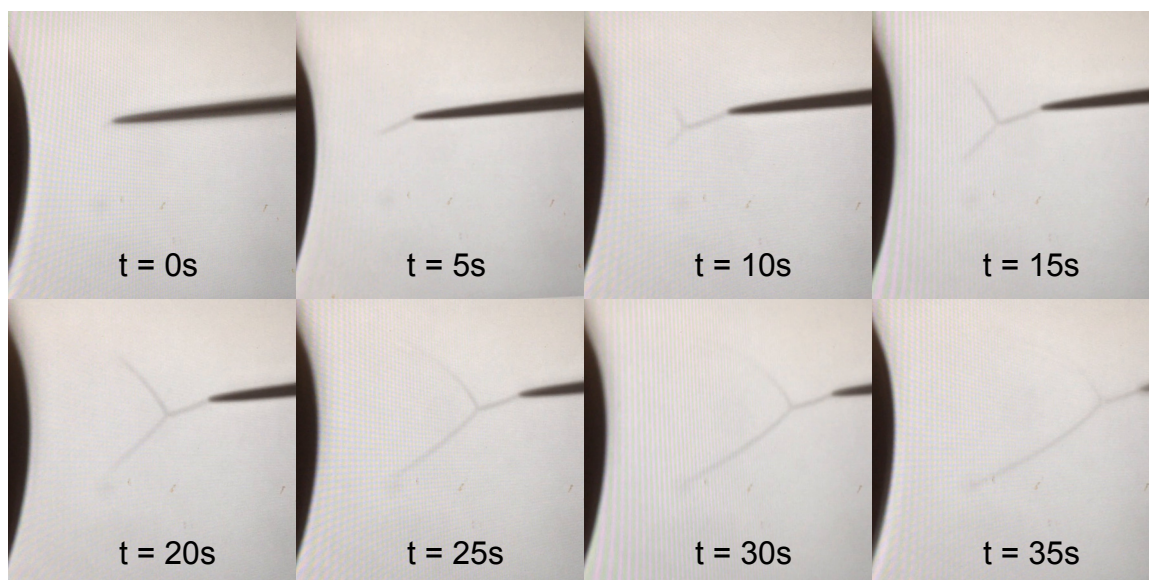
Figure 2.10: Shown is a series of images, taken 5 s apart, highlighting the growth and branching of a single nanoribbon. Visible in each frame is the blunt counter electrode (left side) and the sharp working electrode (right side).

In order to distinguish which photoemission properties arise due to the material or geometry of the nanoribbon samples, single-crystal tungsten (W) and gold (Au) field emission tips were prepared for comparison. Samples of W wire (200 μm diameter) were annealed under vacuum according to Ref. [137], and then etched via the lamella drop-off method.[138] A 13 cm length of polycrystalline W wire was clamped between two sections of copper tubing. The wire was then annealed under a vacuum of 1×10^{-6} Torr, with a current of 4.92 A and voltage of 20 V for one hour. The annealing mount, and an image of the chamber during the annealing process, is shown in Fig. 2.11. A

solution of 2.5 M KOH was prepared as the etchant, and an etching voltage of 15 V was supplied by a Variac across the electrodes. The W etching mount set-up is shown in Fig. 2.12.
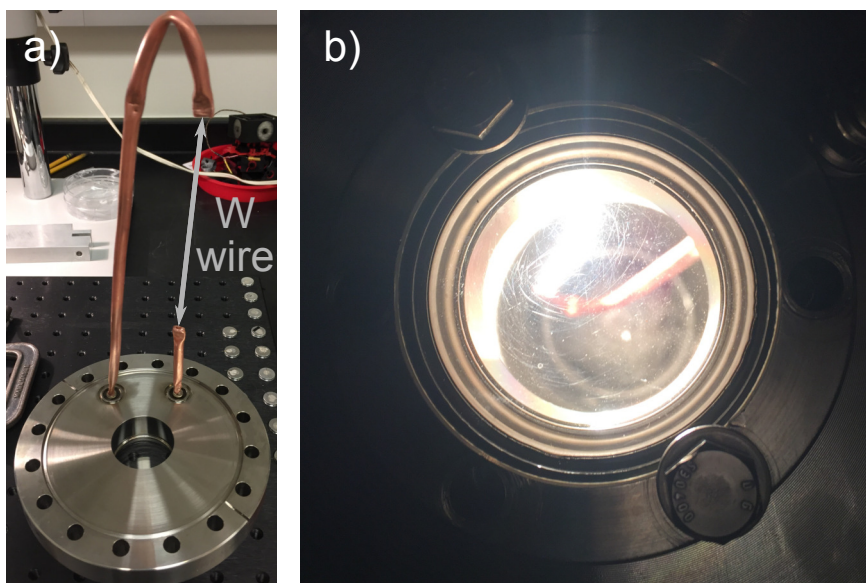
Figure 2.11: (a) Picture of the W wire annealing rig. A 13 cm length of W wire was clamped between the ends of the copper tubing. This corresponds to the length reported in Ref. [137], but with a commercially available mount. (b) Picture of the W wire during the annealing process. The voltage and current applied to the wire were chosen to obtain a dissipated power of 100 W, which corresponds to the value reported in Ref. [137].
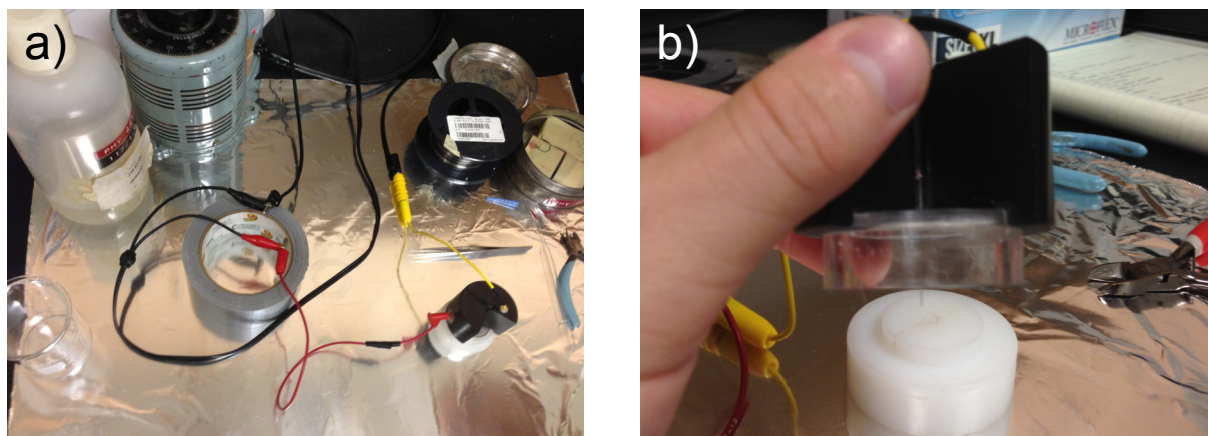
Figure 2.12: (a) Overview of the W wire etching rig used for the lamella drop-off method. (b) Picture showing the approximate amount of wire that should be visible from the bottom edge of the etching device. The lamella is formed by squeezing a small amount of KOH solution from a small glass dropper topped with a rubber bulb. The most consistent method to form a lamella is to use a volume of solution measured off approximately halfway to the first division on the glass dropper, orient the dropper at 45 deg to the electrode plate, touch the dropper to the plate, and expel the solution quickly into the hole in the electrode. The electrode plate should be dry before attempting to form a lamella.

Au wire samples (99.95% purity, Ted Pella, 200 μm diameter) were annealed according to Ref. [28], and etched as according to Refs. [29,30]. The Au wire samples were annealed in an oven at 800 °C for 8 hours in order to obtain larger crystal grains in the sample.[28] The Au wire electrode, and a graphite rod counterelectrode, were immersed in an etching solution of 3.0 M NaCl and 1 % $HClO_4$.[29,30] A sinusoidal etching voltage was supplied by an SRS 345 function generator, with a peak-to-peak voltage of 4.8 V and frequency of 60 Hz. The ac etching current was monitored by a Fluke 8840a multimeter to determine when to terminate etching. When the current read 0 A, the etching circuit was broken manually. An image of the Au etching rig is shown in Fig. 2.13.
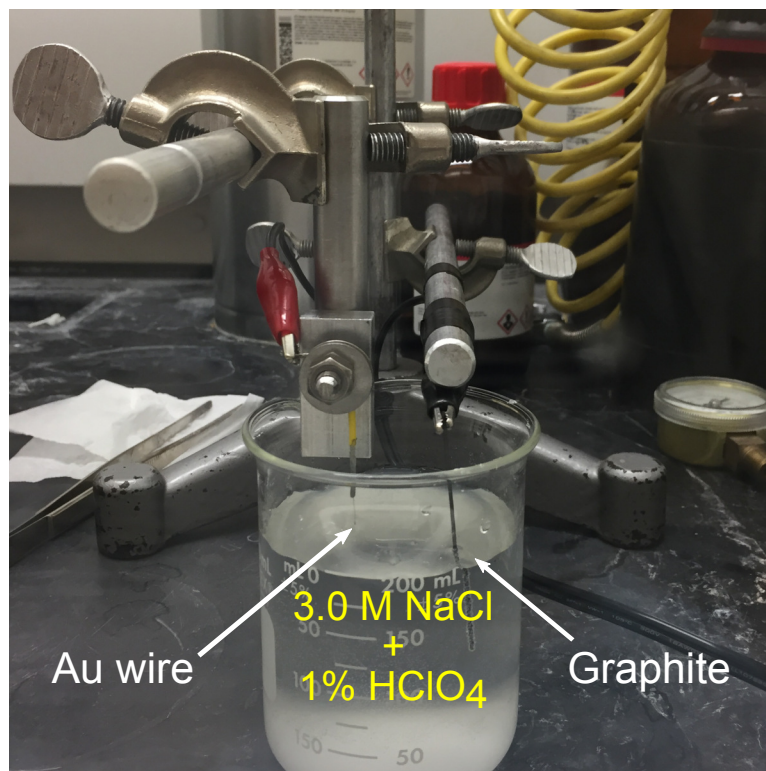
Figure 2.13: Picture of the gold wire etching rig. Etching is performed behind a fume hood as a precaution against the perchloric acid. An approximately 2 cm length of annealed Au wire is held by a recycled nanoribbon mounting electrode. The tip of the sample is lowered until it is approximately 2 mm below the fluid surface. An etching current is applied between the Au wire and the graphite counter electrode and is monitored by a multimeter. The etching circuit was broken once the current reached 0 A. The most consistent results were obtained for alternating current (ac), but etching with direct current (dc) is possible. The drawback with dc etching is that the time to produce samples can be several hours, whereas ac etching takes only several minutes.

The tip and nanoribbon samples were mounted to SEM pin stubs with silver paste. SEM images of the samples are given in Fig. 2.15(a) along with plots of the beam focus (red) and intensity profile (white) as measured by photoemission. From left to right is shown W (I), Au (II), an undamaged 23 μm Au nanoribbon (III), and an 11 μm Au nanoribbon (IV) obtained after the 23 μm nanoribbon was blunted during pump/probe experiments. Images were taken before and after experimental characterization to

determine the extent of damage due to laser illumination.

2.3   Results

The motivation to measure electron yields from pump/probe experiments on Au nanoribbons came from the notion that the unique geometry and structure of the nanoribbons could lead to interesting propagation effects within the structure. Electron photoemission rates could be effected by thermal exchange between free electrons and ions comprising the crystalline lattice,[84] by collective electron oscillations (plasmons) in the nanostructure,[78] or by ballistic currents. To see if this was the case, the relative position between the pump and probe beams was controlled to focus on specific locations on the available nanoribbon sample, namely at the tip of the nanoribbon and at the junction with the Au substrate. This was accomplished in practice by initially having both beams spatially overlap at the nanoribbon tip, using the photoemission signal as an indication of alignment. The nanoribbon was then positioned using the 3-axis stage so that both beams were focused at the nanoribbon/substrate junction. The polarization of both beams was chosen to be parallel to the plane of incidence. Then, the probe beam was aligned to obtain photoemission from the nanoribbon tip. The delay between the pump and probe beams was scanned using the picomotor mounted in the interferometer stage, as shown in Fig. 2.4(a). The photoemission rates measured in this arrangement, for both beams and the probe beam alone, are shown as a function of the MCS scanning time in Fig. 2.14.
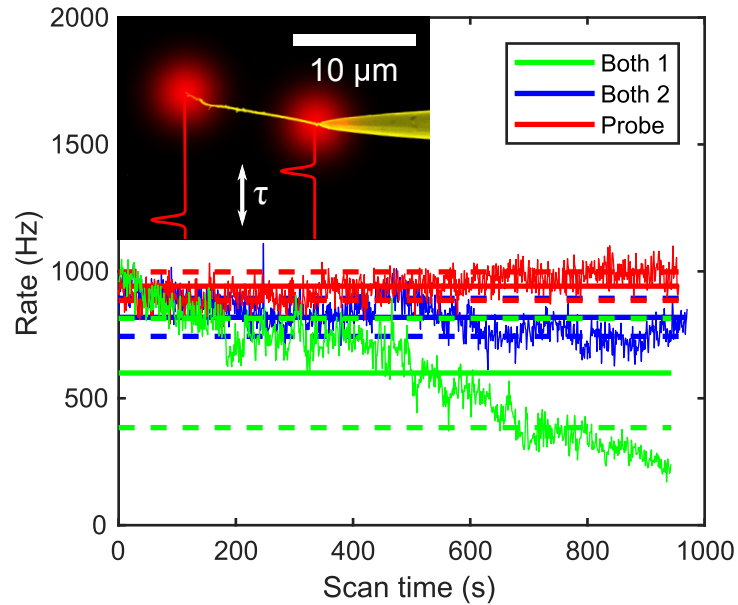
Figure 2.14: Graph of photoemission rates as a function of scan time as the delay is scanned. The green lines are the data (thin, jagged), average rate (bold), and standard deviation of the average (dashed) of a scan taken from $-8\,\text{ps}$ to $8\,\text{ps}$. The scan was repeated, and the resulting photoemission data, average, and standard deviation are plotted in blue. The scan was performed for a delay of $8\,\text{ps}$ to $-8\,\text{ps}$ for the probe beam alone, and is shown in red. This should not have affected the probe beam, as it was chosen to be the fixed reference beam. The graph inset shows the micrograph of the $11\,\mu\text{m}$ nanoribbon of Fig. 2.15(a) superimposed with plots of the laser focus to indicate the pump (right, junction) and probe (left, tip) positions on the nanoribbon. The distance between the focal spots, measured by the translation of a $25.4\,\text{cm}$ rod used as an extension to the z-position translation stage, was $11.6\,\mu\text{m}$

The data are inconclusive that any propagation effect was observed in this arrangement. Full picomotor scans required $1000\,\text{s}$ to acquire, so drifts can be significant. This arrangement could be modified in the future to measure thermal propagation if the polarization of the pump beam is chosen to optimize the thermal electron signal while the probe polarization is chosen to minimize it. Properties of the thermal emission signal is discussed below.

Photoemission data from single-beam experiments are shown in Fig. 2.15(b)–(d). In Fig. 2.15(b), the emission rate is shown as samples were translated through the

laser focus. The W (I) and Au (II) tip samples show emission localized at the tip apex only, while the nanoribbon samples (III and IV) can emit from multiple locations along their length. This feature confirmed that a nanoribbon remained attached to the Au substrate after imaging and transfer to the experimental chamber. Thin lines between data points serve as a guide to the eye. Fig. 2.15(c) shows the dependence of electron yield on the average power of the beam, plotted on a log-log scale. The value, n, of the power dependence ($\propto I^n$), is often used to identify the emission process of a tip. The W tip and 23 μm nanoribbon have slopes of $n = 3$, while the Au tip is found to have a slope of $n = 3$ for low power, and $n = 5$ for higher power. Such behavior, that is, the increase in power law slope with increasing laser power, has been observed in W tips and studies of above threshold photoemission.[5,82] The 11 μm nanoribbon has a slope of $n = 5$. With these values of n, the position dependence of the samples in Fig. 2.15 (b) can be fit with a Gaussian function to determine the size of the focal waist (bold lines). The focal waist has a fitted full width at half maximum of 4.5 μm from the W data. This is consistent with knife edge profiles taken of the beam prior to entering the experimental chamber. For an initial beam radius $w_0 = 1.2$ mm incident on the OAPM having a parent focal distance $f = 12.7$ mm, the focused beam radius will be $w_0' = \lambda f/(\pi w_0) = 2.7$ μm, corresponding to a full width at half maximum of 3.2 μm, which is still smaller than our measured focal size. Fig. 2.15(d) shows the variation of emission rate as the polarization of the beam is rotated by a $\lambda/2$ plate. The high contrast 90° spaced peaks in the tip samples and 23 μm nanoribbon support that the sample geometry is well-defined with respect to the laser polarization in the focus, and that the emission process is dominated by a preferred laser polarization. The broadened peaks and reduced contrast of the 11 μm nanoribbon electron yield (black squares, IV) indicate that the emission process depends on both transverse components of the exciting field. A feature consistent with multiphoton emission
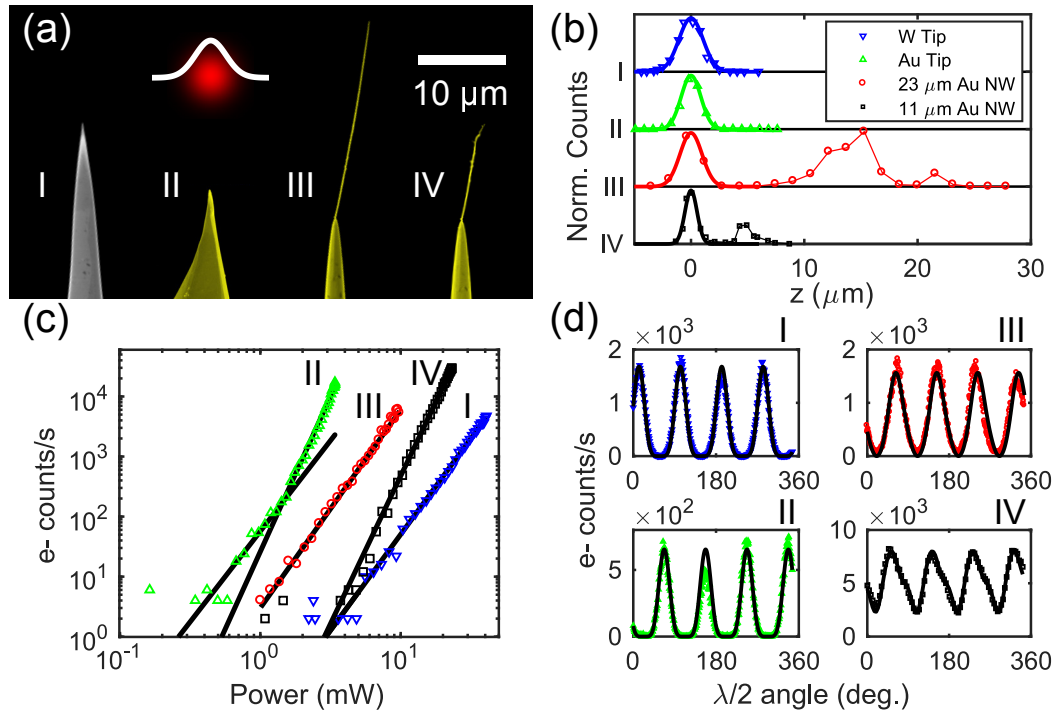
Figure 2.15: Tip sample characteristics. (a) Scanning electron microscope (SEM) micrographs of the tip samples: from left to right is shown annealed W (I), annealed Au (II), a 23 μm Au nanoribbon (III), and an 11 μm Au nanoribbon (IV). The laser spot size (red) and intensity profile (white) have a full width half maximum of 4.5 μm as fit from the W data in (b) and (c). (b) Scaled electron counts as function of tip position in focus. Gaussian fits to the data are shown in bold lines. Thin lines are guides to the eye. (c) Power dependence of electron emission. (d) Polarization dependence of electron emission.

is that the power law slope, n, will agree with the polarization dependence on the emission rate. The emission rate is $\propto cos^{2n}(\theta)$ in a multiphoton emission model, where θ is the polarization of the laser relative to the tip direction. The W and Au polarization data agree with a fit with $n = 3$, while both nanoribbon samples require a combination of $n = 1$ and $n = 3$. This peculiarity of both nanoribbon samples indicates a deviation from typical multiphoton emission.

Pump/probe and single beam experiments with the TAC/MCA configuration revealed the timing features of electron emission. The additive ratio of emission from

the samples is plotted in Fig. 2.16(a) as a function of τ. The polarization of the focus was chosen for the optimum electron yield from each sample. A ratio of 1 indicates that the emission yield from the probe pulses are independent from the pump pulses. A ratio significantly greater than 1 indicates emission processes that are slower than the time delay between pulses.[5] When the delay is shorter than the pulse duration, the additive ratio can vary due to interference between the pulses. The W tip (blue triangles), Au tip (green triangles), and 23 μm nanoribbon all have additive ratios that are close to 1 when the pulse delay is outside of the ±200 fs interference window, so the emission processes are as fast as the 100 fs laser pulse duration and thus prompt. The 11 μm nanoribbon (black squares) has an average additive ratio of 14.9 for delays longer than the pump/probe interference window, therefore the process is not prompt. Measurement of the ratio for delays with high constructive interference were avoided to prevent damage to the Au tip and 11 μm nanoribbon samples.

Normalized time spectra of electron emission from tip samples are plotted in Fig. 2.16(b). Shown, grouped from left to right, are the spectra from the W tip (blue line), Au tip (green line), 23 μm nanoribbon (red line), and the 11 μm nanoribbon (black line). The peak separation for each sample shows the 13 ns pulse separation of the oscillator. Sharp peaks indicate *pulsed* electron emission, while sustained signal after the laser pulse indicates *background* emission. The 11 μm nanoribbon has a significant background as compared to the other samples, indicating that electron emission is continuing after the exciting laser pulse is gone. The emission process of the 11 μm nanoribbon is therefore ruled out as purely multiphoton, and is likely due to both multiphoton and laser heating of the nanoribbon structure.

To further investigate this feature, the pulsed and background contributions to emission from the 11 μm nanoribbon are plotted as a function of $\lambda/2$ angle in Fig. 2.16(c). Time spectra were recorded for each $\lambda/2$ angle. The process for dividing
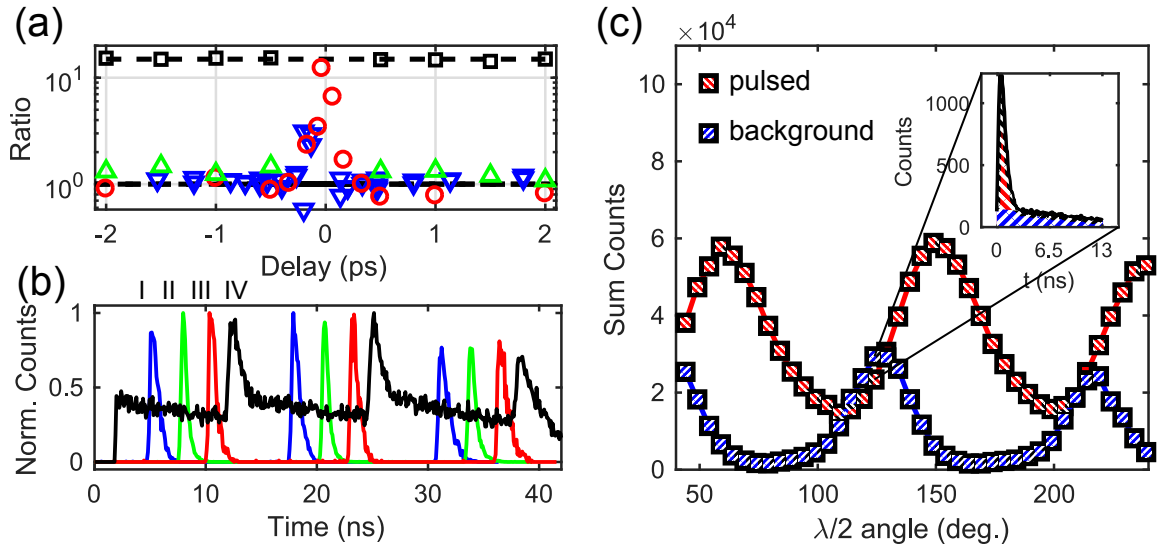
Figure 2.16: Pump/probe, timing, and polarization control of emission processes. (a) Additive ratio of electron emission vs. pulse delay. Color and marker conventions follow Fig. 2.15. Ratio values of 1 and 14.9 are highlighted by dashed black lines. (b) Normalized time spectra of electron emission from tip samples. Grouped from left to right are the W tip (blue), Au tip (green), 23 µm nanoribbon (red), and 11 µm nanoribbon (black). (c) Polarization dependence of summed counts of time spectra background (blue hatched) and pulsed (red hatching) emission vs. $\lambda/2$ angle for the 11 µm nanoribbon. Colored lines are guides to the eye. The inset shows the background and pulsed signal for a single timing peak taken at $\lambda/2$ angle = 124°.

each spectrum into pulsed and background contributions is illustrated in the inset of Fig. 2.16(c), which shows a portion of the time spectrum taken at $\lambda/2$ angle of 124°. The red hatched region of the inset indicates the pulsed contribution, and the blue hatched region indicates the background. The background regions are defined by taking linear fits to the tails of the timing spectra, and extending those fits to the rising edges of the timing peaks. This procedure is performed for two 13 ns oscillator periods. The counts in the background regions are summed, giving the data points marked by the blue hatched squares. The background contributions are then subtracted from the total counts in each spectrum. This results in the data points marked by the red hatched squares. The maximum emission for the background process occurs at a $\lambda/2$

angle that is shifted relative to the pulsed process. For example, for a $\lambda/2$ angle of 79°, the photoemission signal is dominated by the pulsed process, as the number of counts in the tails of the electron time of flight spectra is low. For a $\lambda/2$ angle of 124°, the photoemission signal is dominated by the background process, which is marked by a comparatively high number of counts in the delayed tail of the electron time of flight spectrum. The explanation for the variation in electron signal is likely due to the nanoribbon absorbing more of the incident laser pulse energy at 124°, and less at 79°. The higher degree of energy absorption in the 11 μm nanoribbon requires a higher degree of energy dissipation, which occurs by an additional process–thermal dissipation–that is much slower than multiphoton-driven processes. This interpretation is consistent with the results of Ref. [19], which demonstrated polarization control of thermally enhanced photoemission from nanotips. The polarization control of these multiphoton (pulsed) and thermal (background) processes indicates that they respond to different components of the laser field in the focus.

Thermal emission is the most likely process that could lead to the strongly superadditive behavior and slow timing features shown in Fig. 2.16. In order to demonstrate that the slow emission features observed in the 11 μm nanoribbon were indeed from a thermal process, time of flight spectra were obtained for a series of incident laser powers, varied from 6 mW to 15 mW, and tip voltages, varied from −100 V to −200 V. Care was taken to keep the count rates below 50 kHz, so as the incident power increased, the tip voltage was not applied over the full range. The 80 time of flight spectra thus obtained were then fit with a Richardson-Schottky model, which gives the emission current as a function of the emitter temperature and applied voltage.[72,73]

The emission current, $J(T, V_{\text{tip}})$, is given by the expression

$$J(T, V_{\text{tip}}) \propto T^2 \exp\left(-\frac{\phi - e\sqrt{\frac{eV_{\text{tip}}}{4\pi\epsilon_0 k r_{\text{tip}}}}}{k_B T}\right), \tag{2.4}$$

where T is the temperature in Kelvin, ϕ is the work function in eV, e is the fundamental electron charge in Coulombs, ϵ_0 is the vacuum permittivity in Coulombs per Volt-meter, k is a geometric constant, r_{tip} is the radius of the emission site, and k_B is the Boltzmann constant. The geometric constant k accounts for the reduction of the electric field from the field of a free sphere, V/r, which is caused by the presence of the emitter shank. The value of k near the emitter apex is $k \approx 5$, and increases as a function of angle from the tip. The value $k = 5$ then gives a reasonable approximation for the field in the forward direction.[134] This model of thermal emission is applicable when the electric field at the surface of the emitter is smaller than 5×10^7 V/cm, meaning it does not describe emission when a laser field is present.[74] The temperature of the emitter is assumed to increase from a steady-state value, $T_{S.S.}$, by an amount ΔT, the instant a laser pulse hits the tip. After the pulse hits the tip, the change in temperature is assumed to decay exponentially in time, with a form $T(t) = T_{S.S.} + \Delta T \exp(-\gamma t)$. In the fitting model, the maximum of a time of flight spectrum pulse is assumed to be the arrival time of the laser pulse at the nanoribbon apex, and thus the start time for the exponential decay of the temperature change. For each spectrum, the values for $T_{S.S}$, ΔT, γ, ϕ, and $e\sqrt{e/(4\pi\epsilon_0 k r_{\text{tip}})}$, as well as the Richardson constant, are taken as free parameters. The pulsed region of each spectrum is excluded, as that region does not meet the application criteria of the temperature-dependent model, and exclusion of the data simplifies the fitting procedure. A sample of three of these fits are shown in Fig. 2.17. Fig. 2.17(a) shows time of flight spectra taken at 12 mW and 15 mW to illustrate the differences in thermal background for different applied
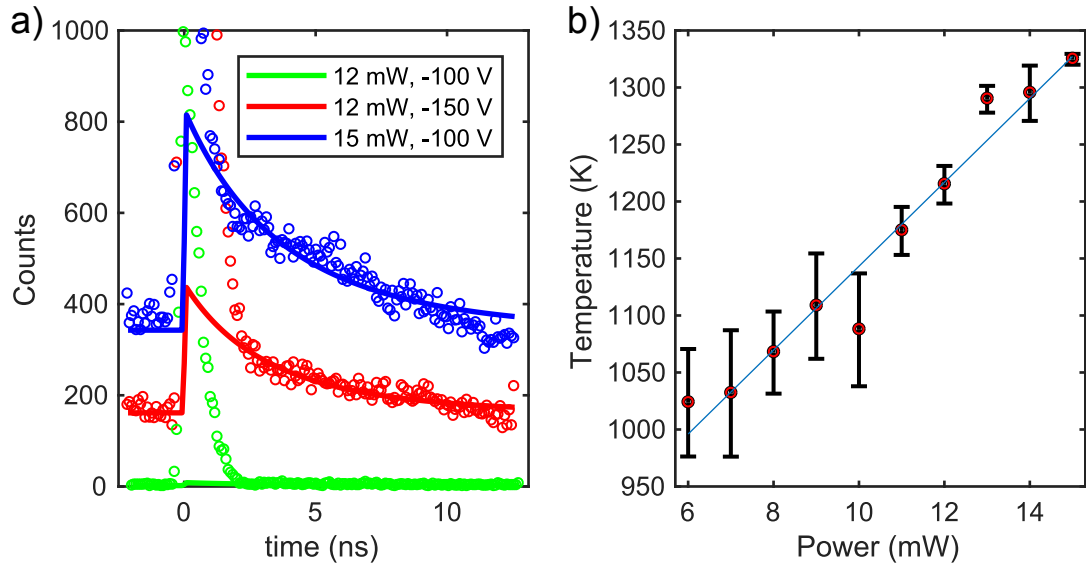
Figure 2.17: (a) Time of flight spectra taken for $12\,\mathrm{mW}$ and $-100\,\mathrm{V}$ (green), $12\,\mathrm{mW}$ and $-150\,\mathrm{V}$ (red), and $15\,\mathrm{mW}$ and $-100\,\mathrm{V}$ (blue). The fits result in values of T_0 of $1183\,\mathrm{K}$, $1225\,\mathrm{K}$, and $1330\,\mathrm{K}$, respectively. (b) Fit steady-state temperature vs. incident laser power. Vertical error bars are taken as the standard deviation of temperature values obtained from the fitting procedure for all applied voltages. Fitting line (blue) is shown to highlight the increase of fit temperature with increasing laser power.

voltages. The thermal background is significantly increased at $12\,\mathrm{mW}$ comparing the emission yield for $-100\,\mathrm{V}$ (green) to $-150\,\mathrm{V}$ (red), yet the fit gives consistent values for the steady-state temperature. At $12\,\mathrm{mW}$, the average fit temperature value is $(1215 \pm 17)\,\mathrm{K}$. At $15\,\mathrm{mW}$, the average fit temperature value is $(1325 \pm 5)\,\mathrm{K}$. The considerably small uncertainty at $15\,\mathrm{mW}$ is the result of performing the measurement with only two voltages. Deviations of the temperature from linear behavior could be attributed to small changes in alignment that occurred as time of flight spectra were obtained. From the fit parameters, the cooling time, $1/\gamma$, for nanoribbon apex emission is $(4.94 \pm 0.81)\,\mathrm{ns}$. The workfuntion ϕ is found to be $(5.29 \pm 0.09)\,\mathrm{eV}$, and the nanoribbon apex radius, r_{tip}, is $(19.6 \pm 2.2)\,\mathrm{nm}$. The fit value of the work function is consistent with the reported values of $5.31\,\mathrm{eV}$ and $5.37\,\mathrm{eV}$, which are obtained from measurement of the photoelectric effect for the [111] and [110] crystal planes,

respectively.[139,140] This value of tip radius, with $k = 5$, gives a maximum field at the apex of 2×10^9 V/m for an applied tip voltage of -200 V, which is less than the value considered for thermal emission and thus justifies the application of the model.

2.4   Conclusions

Ultralong Au nanoribbons are unique nanostructures for the study of electron, thermal, and plasmonic transport by laser-induced electron emission. Previous work indicated that nanoribbons are resilient to damage by laser intensities on the order of TW/cm^2,[84] but we found that damage can occur with lower intensities. This observation resulted in the 11 µm nanoribbon, which differed from the original 23 µm nanoribbon by having a less defined apex. An immediate consequence of the laser damage to the 23 µm nanoribbon was that the shorter 11 µm nanoribbon required higher incident laser power to emit, which is evident in Fig. 2.15(c). The change in the nanoribbon's apex geometry also coincided with emission from the 11 µm nanoribbon being superadditive for emission rates similar to the other samples. The superadditive emission in pump/probe experiments was accompanied by delayed tails in the photo-electron time of flight spectra in the 11 µm nanoribbon. Superadditive and delayed emission are not consistent with plasmon-induced field emission, as plasmonic emission is reported to have a standard pump/probe cross-correlation and thus is as fast as the exciting laser pulses.[79,132] Such tails were not observed at the 23 µm nanoribbon apex before it was damaged. These features, the superadditive emission and the delayed arrival times, are consistent with the 11 µm nanoribbon being more susceptible to laser heating than the 23 µm nanoribbon. The higher susceptibility to heating made the 11 µm nanoribbon sensitive to both transverse components of the focused laser field, as shown in Fig. 2.16(c). The sensitivity to both transverse components of the
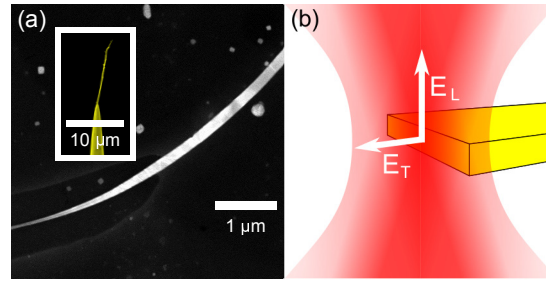
Figure 2.18: (a) Micrographs of a long nanoribbon and sample (IV) (inset). The nanoribbon is twisted to highlight that it is ribbon shaped. (b) Schematic of nanoribbon as a detector of longitudinal (E_L) and transverse (E_T) electric fields.

focused field is a unique feature of the thermal emission of the nanoribbon that was not observed in W or Au tips. The cone structure of the nanotip samples leads to much faster cooling times than the nanoribbon samples. This suggests that a tailored nanoribbon could be oriented to probe other polarization components in a focus as well. A schematic for an oriented nanoribbon as a probe of the longitudinal component of a focused non-paraxial beam is given in Fig. 2.18. Shown in Fig. 2.18(a) is a high-resolution SEM image of a nanoribbon and our 11 µm nanoribbon as the inset. The nanoribbon is twisted in the high-resolution image to highlight its shape. With the nanoribbon oriented as shown in Fig. 2.18(b), the broad side of the nanoribbon would heat depending on the strength of the longitudinal component of the exciting field, E_L, and the delayed electron yield would therefore depend on E_L, while the peaked electron yield could depend on a combination of the transverse component, E_T, and also E_L. The capability to distinguish the slow thermal electron yield at the nanoribbon apex makes electron emission from a nanoribbon a subwavelength probe of orthogonal polarizations.

Chapter 3

Path integrals and the double slit

Basic explanations of the double slit diffraction phenomenon include a description of waves that emanate from two slits and interfere. The locations of the interference minima and maxima are determined by the phase difference of the waves. An optical wave, which has a wavelength λ and propagates a distance L, accumulates a phase of $2\pi L/\lambda$. A matter wave, also having wavelength λ, that propagates the same distance L, accumulates a phase of $\pi L/\lambda$, which is a factor of two different from the optical case. Nevertheless, in most situations, the phase difference, $\Delta\varphi$, for interfering matter waves that propagate distances that differ by ΔL, is approximately $2\pi\Delta L/\lambda$, which is the same value computed in the optical case.

The difference between the matter and optical case hinders conceptual explanations of diffraction from two slits based on the matter-optics analogy. We provide a path integral description for matter waves with a focus on conceptual explanation. A thought experiment is provided to illustrate the validity range of the approximation $\Delta\varphi \approx 2\pi\Delta L/\lambda$.

3.1   Introduction

The presentation of the double slit typically begins with a discussion of Young's original experiments on the diffraction and interference of light.[141] Demonstrations such as a ripple tank, one of Young's own inventions, are used to reinforce the concept of wave interference and Huygens' Principle of the superposition of waves.[49,95] Fig. 3.1. shows circular waves that impinge on a pair of narrow slits having separation d. The slits become themselves new sources of circular waves. The phase associated with a wave is the number of wave-fronts counted along a line with length L, that is, L/λ, multiplied by 2π. Waves interfere constructively when the phase difference is an integer multiple of 2π. These ideas lead to the familiar condition for constructive interference,

$$\Delta L = d\sin(\theta) = n\lambda, \tag{3.1}$$

where n indicates the diffraction order that occurs at the diffraction angle θ. This analysis represented by Eq. 3.1 and Fig. 3.1 describes what we will hereby refer to as the optical analogy. Even though this approach is correct for light, it is not for matter. The first problem is that it uses an incorrect phase, $2\pi L/\lambda_{dB}$, for a matter wave (where λ_{dB} is the de Broglie wavelength). The second problem is that the use of the optical analogy will nevertheless give the correct phase difference for most situations.

In this article, the optical analogy and its limits of validity are discussed for matter waves. The analogy is also compared to a stationary phase method motivated by the path integral formalism. The path integral formalism is shown in Sec. 3.2 to give a single path phase of $\pi L/\lambda_{dB}$, and a phase difference between two interfering paths that is approximately $2\pi\Delta L/\lambda_{dB}$. This phase difference agrees with the optical analogy. The path integral formalism assigns different velocities (and thus wavelengths) to different paths. This appears to be inconsistent with the idea that a double slit is
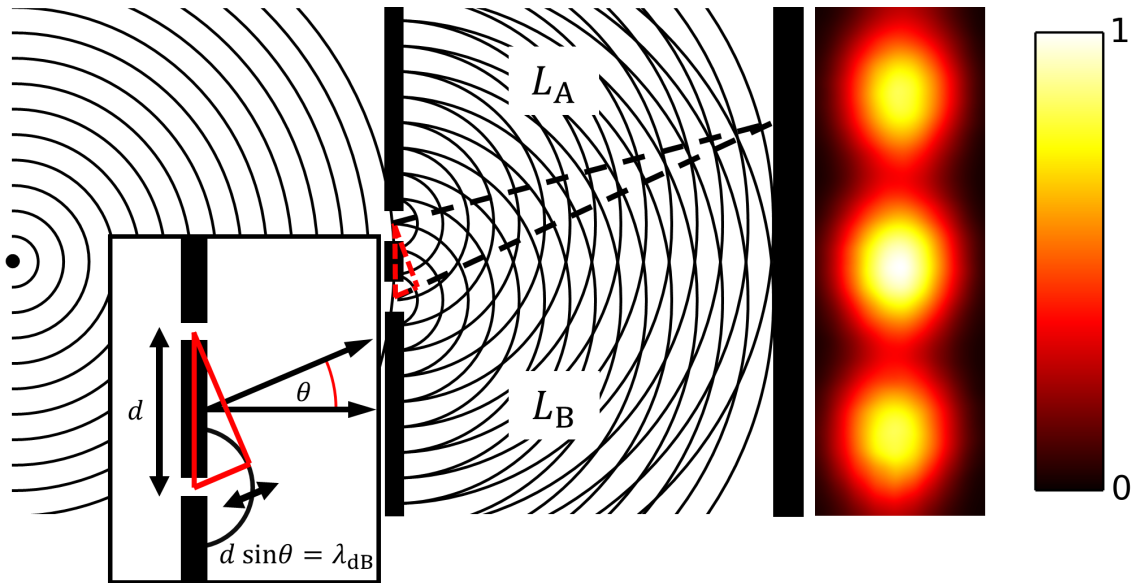
Figure 3.1: Typical schematic of Youngs two-slit arrangement. The condition for first-order constructive interference, $d\sin(\theta) = \lambda$, is illustrated. Shown right is recently published data for an electron double slit interference experiment.[37]

illuminated with a wave described by one velocity or wavelength. This apparent inconsistency will be clarified in the next sections. In sections Sec. 3.3, Sec. 3.4, and Sec. 3.5, the relation to the optical case, wave mechanics, and time-dependence is discussed, respectively. In Secs. 3.6 through 3.10, a stationary phase argument completes the justification for the path selections made in 3.2. At this point, it may appear that apart from some conceptual details, the optical analogys validity can be justified by the path integral method. In 3.11, a thought experiment is discussed for which the optical analogy predicts phase differences that disagree with the path integral method, with the purpose to illustrate that the optical analogy agrees only approximatively.

3.2   Determining the phase from the path integral

Feynman developed a method[42] to construct solutions to Schrödinger's equation[142] based on Dirac's observations on the relationship between the evolution of quantum states between points in space-time and the classical notion of particle trajectories.[85] In Feynman's path integral formalism, a probability amplitude is determined from a phase, φ_{path}, computed along a particular path connecting two space-time events. The total probability amplitude $K(\beta; \alpha)$ for finding a particle at location x_β at time t_β, having started at location x_α at the earlier time t_α, is given by the sum

$$K(\beta; \alpha) = \sum_{\text{all paths } \alpha \to \beta} c \exp\left(i\varphi_{path}\right), \tag{3.2}$$

where all paths connect events α and β.[86] The phase φ_{path} accumulated along any path is given by

$$\varphi_{path} = \frac{1}{\hbar} \int_{\text{path}} L(x, \dot{x}, t) \, \mathrm{d}t, \tag{3.3}$$

where L is the Lagrangian function, which depends on the position, x, velocity, $dotx$, and time, t, along the path. This path integral method is used to efficiently describe experimental results for matter interferometry[36], for example the double slit experiment for electrons (see the Supplementary Material of Ref. [37], available online).

For the case of a particle moving in free space in 1-D, the Lagrangian is simply

$$L(x, \dot{x}, t) = \frac{m}{2}\dot{x}^2. \tag{3.4}$$

In free space, the velocity, $\dot{x}$, is constant along the path of integration, and the

accumulated phase,

$$\varphi_{path} = \frac{m}{2\hbar} \left(\frac{x_\beta - x_\alpha}{t_\beta - t_\alpha} \right)^2 (t_\beta - t_\alpha) = \frac{\pi}{\lambda_{dB}} (x_\beta - x_\alpha), \tag{3.5}$$

is a function of the endpoints only. The phase of a single path is thus $\pi L / \lambda_{dB}$.

Now consider a double slit illuminated with a matter wave that is characterized by one velocity. This system can be qualitatively described by the interference of two paths, represented by the dashed lines of Fig. 3.1. A reasonable assumption would be that the velocity, and thus the de Broglie wavelength, is the same for both paths. The phase difference between the two indicated paths of lengths L_A and L_B would then be computed from Eq. 3.5 to be

$$\Delta\varphi = \varphi_B - \varphi_A = \frac{\pi}{\lambda_{dB}} (L_B - L_A). \tag{3.6}$$

This result is incompatible with the phase difference obtained from the optical analogy because it differs by a factor of 2. This result is also incompatible with experiment, which agrees with the optical analogy. This is fine because it is indeed incorrect; the false assumption made is that the velocities along both paths are the same. This is not a feature of the path integral formalism. The correct result can be recovered by noting that interfering paths have equal durations Δt in time; they both must begin at α and end at β, as expressed in Eq. 3.2. Because L_A and L_B are not equal, the consequence is that paths A and B have different velocities. The corresponding de Broglie wavelengths for paths A and B are then

$$\lambda_{A,B} = \frac{h\Delta t}{mL_{A,B}}. \tag{3.7}$$

The path length difference δL between the two paths is taken to be small in comparison

to the path lengths $L_{A,B}$. For $L_A < L_B$, the de Broglie wavelength can be expanded as

$$\lambda_B \approx \frac{h\Delta t}{mL_A}\left\{1 - \frac{\delta L}{L_A} + O\left[\left(\frac{\delta L}{L_A}\right)^2\right]\right\} \approx \lambda_A\left(1 - \frac{\delta L}{L_A}\right). \tag{3.8}$$

Terms of order $O[(\delta L/L_A)^2]$ are neglected. The phase difference between the two paths is

$$\Delta\varphi = \varphi_B - \varphi_A \approx \frac{\pi L_B}{\lambda_A\left(1 - \frac{\delta L}{L_A}\right)} - \frac{\pi L_A}{\lambda_A} \approx \frac{2\pi\left(L_B - L_A\right)}{\lambda_A}. \tag{3.9}$$

Thus, the correct result is recovered and justified by the path integral formalism of quantum mechanics.

3.3   Comparison to the optical case

The question may arise why the analogous situation of two slit diffraction for light presents no conceptual difficulty. The use of straight paths in figure 1 for light could be justified by the application of Fermat's principle of least time.[143] These paths are called rays in the geometrical optics formulation of light propagation.[144–146] Rays are constructed from the normals of a succession of electromagnetic wave-fronts. Each ray is associated with a phase called the eikonal ϕ that is calculated in a homogeneous medium as

$$\phi = \int_{\text{ray}} \mathbf{k} \cdot d\boldsymbol{l} = \int_{\text{ray}} \omega \, dt. \tag{3.10}$$

For light, this phase has the value $\int_{\text{ray}} \mathbf{k} \cdot d\boldsymbol{l} = kL = 2\pi/\lambda$ along a ray. This justifies the optical analogy of counting wave-fronts along the propagation paths as in the still pictures of Fig. 3.1. The equality of the two integrals in Eq. 3.10 implies (note $dl/dt = c$) that the dispersion relation for light is linear:

$$\omega = |\mathbf{k}|\, c. \tag{3.11}$$

The dispersion relation determines the group and phase velocities. For light propagating in free space, these velocities are the same. Matter wave propagation is different from light because it has a quadratic dispersion relation[35] and the group and phase velocities are not the same. The connection between velocity and phase for matter waves is discussed in the following section.

3.4 Determining the phase from the wave description: the motion picture

Consider the motion of a one dimensional electron wave packet, illustrated in Fig. 3.2. This superposition of waves $\psi(x,t)$ is given by the Fourier transform of the momentum distribution $f(k - k_0)$ of the constituent waves in the group:

$$\psi(x,t) = \int_{-\infty}^{\infty} f(k - k_0) \exp\left\{i\left[kx - \omega(k)t\right]\right\} \mathrm{d}k. \tag{3.12}$$
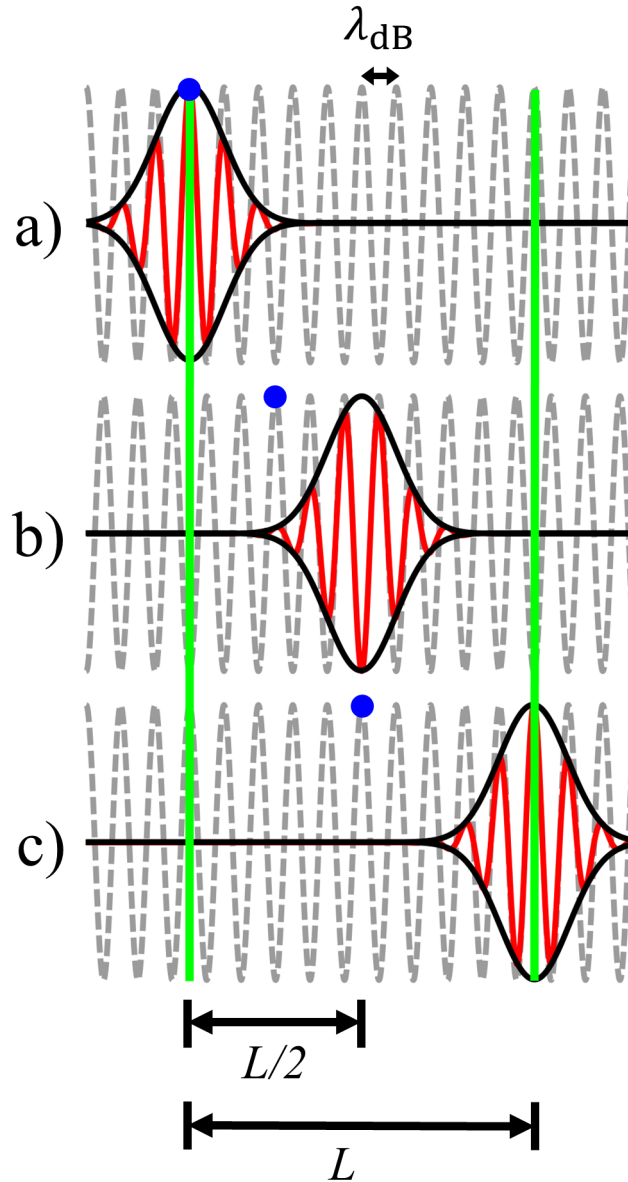
Figure 3.2: Matter wave propagation. Three snapshots of the evolution of a Gaussian wave packet are shown. The carrier wave moves at the phase velocity v_{p} to the right, indicated with the blue dot. The envelope moves at the group velocity $v_G = 2v_{\mathrm{p}}$. A pulse that propagates a length L accumulates a phase $\varphi = kL - \omega t$. The angular frequency is given by $\omega = kv_{\mathrm{p}}$, while the propagation time is given by $t = L/v_G$. Substitution gives that $\varphi = \pi L/\lambda_{dB}$, which differs from the optical analogy of counting waves along the distance multiplied by 2π.

For a Gaussian momentum distribution $f(k - k_0) = \exp[-(k - k_0)^2/(2(\Delta k)^2)]$ with

width δk and a dispersion relation $\omega(k) = (\hbar k^2)/2m$, the wave packet $\psi(x,t)$ is then approximately given by

$$\psi\left(x,t\right) \propto \exp\left\{i\left[kx - \omega(k)t\right]\right\} \exp\left[-\frac{(\Delta k)^2}{2}\left(x - \frac{\hbar k_0}{m}t\right)^2\right]$$

$$\propto \exp\left[ik_0\left(x - \frac{\hbar k_0}{2m}t\right)\right] \exp\left[-\frac{(\Delta k)^2}{2}\left(x - \frac{\hbar k_0}{m}t\right)^2\right] \tag{3.13}$$

A typical matter wave packet's width spreads and its frequency components disperse as time evolves; however, for sufficiently short times this spreading and dispersion can be neglected. The real part of Eq. 3.13 is illustrated in Fig. 3.2 for three times.[147,148] The first exponential factor, represented by a dashed gray line in Fig. 3.2, is a sinusoidal carrier wave traveling with the phase velocity

$$v_{\mathrm{p}} \equiv \left.\frac{\omega(k)}{k}\right|_{k=k_0} = \frac{\hbar k_0}{2m}. \tag{3.14}$$

The second factor is the Gaussian envelope, represented by a solid black line, whose center travels twice as fast as the sinusoidal wave at the group velocity

$$v_G \equiv \left.\frac{\partial\omega(k)}{\partial k}\right|_{k=k_0} = \frac{\hbar k_0}{m} = 2v_{\mathrm{p}}. \tag{3.15}$$

The group velocity is identified with the particle velocity and determines the de Broglie wavelength. Suppose that the wave packet in Fig. 3.2 travels a distance L in a time Δt. The connection between L and Δt is determined by the motion of the center of the Gaussian envelope as

$$L = \frac{\hbar k_0}{m}\Delta t. \tag{3.16}$$

Substituting this relationship into the phase argument of the carrier wave in Eq. refeq:pieq13

gives an accumulated phase φ of

$$\varphi = \frac{k_0 L}{2} = \frac{\pi L}{\lambda_0}.$$ (3.17)

Thus the phase accumulated by a matter wave packet moving from one position to another follows from inspecting a time-dependent solution, and not from the time-independent part alone.

3.5 The time-independent and time-dependent Schrödinger equations

The fact that none of the experimental parts of a double slit experiment changes over time suggests inspecting a steady state solution. Consider the time-dependent Schrödinger equation,

$$\frac{-\hbar^2}{2m}\nabla^2\psi - V\psi = i\hbar\frac{\partial\psi}{\partial t}.$$ (3.18)

When the potential V in the Schrödinger equation does not depend on time, then the time-independent equation is derived from the time-dependent equation by separation of variables and division by the common factor $\exp(-i\omega t)$. This results in the time-independent Schrödinger equation,

$$\nabla^2\varphi + \frac{2(E-V)}{m\hbar^2}\varphi = 0.$$ (3.19)

The factor $2(E-V)/m\hbar^2$ can be defined as k^2 to give the Helmholtz equation,

$$\nabla^2\varphi + k^2\varphi = 0,$$ (3.20)

the solutions of which also describe the steady state solutions for optics. This well-known analogy is a defining property of the field of matter-optics (see Sec. 2.1 of Ref. [35]).

Solutions to the Helmholtz equation with the same energy values (and thus k-values for free space solutions) can be summed to construct a new solution, and thus the superposition principle holds. The solutions in the case illustrated in Fig. 3.1 have the simple form $\varphi(r) = (C \exp{(ikr)}/r)$. The circles in Fig. 3.1 can then be thought of as depicting the wave fronts of the real part of the circular waves $\varphi_A(r_A)$ and $\varphi_B(r_B)$ that are the solutions to the Helmholtz equation. The probability to find a particle at a position x on the detection screen is then given by the Born rule, $|\psi(x,t)|^2 = |\varphi_A[r_A(x)] + \varphi_B[r_B(x)]|^2$. The result is time-independent because the time-dependent factor $\exp{(-i\omega t)}$ was factored out of the wave function. Using the lengths $r_{(A,B)} = L_{(A,B)} = n_{(A,B)}\lambda_{dB}$ for each dashed straight line in Fig. 3.1 leads immediately to the condition $\Delta L = n\lambda_{dB}$ at maxima in the probability distribution.

It is then reasonable to question why the optical analogy is not sufficient to return to a time-dependent description of the double slit experiment for matter. After all, it appears that we could recover the time-dependent description by multiplying the stationary solutions φ_A and φ_B with the factor $\exp{(-i\omega t)}$. Lets associate with the waves, for a fixed energy E, the kinematic velocity as given by $v = \sqrt{2E/m}$. The propagation time t along any direction is then $t = r/v$. This leads to the phase $kr - \omega t = kr/2$ evolving from either slit to the detection screen, as in Eq. 3.16, when the factor $\exp{(-i\omega t)}$ is added back to the wavefunction. The phase difference at a detection point would then be $(kr_B - kr_A)/2 = \pi(r_B - r_A)/\lambda_{dB}$, as in Eq. 3.6, which is incorrect. The correct use of time-dependent formalisms avoids this discrepancy, as shown in Sec. 3.2.

3.6 Revisiting the path integral propagator in free space

In Sec. 3.2, we restricted the discussion of path integral phase differences in a qualitative description of the double slit to a particular selection of two paths. However, the full path integral description for the double slit calls for a summation of probability amplitudes over all possible paths in space and time between fixed events, not just the particular selection. In the following, Sec. 3.6, we briefly review the free-space 1-D propagator in the path integral formalism. In Sec. 3.7, the free-space propagator is applied to the two-step event of crossing a slit at one particular time. In Sec. 3.8, the sum over all slit crossing times is shown to converge to the choice of a particular time for each path in space. In Sec. 3.9, the particular choice of time for each slit-crossing path is motivated by a stationary phase argument. In Sec. 3.10, the stationary phase argument is illustrated in the two-path description of the double slit, as in Fig. 3.1. In Sec. 3.11, the results from the stationary phase argument and a path integral sum over times are compared to the optical analogy in a near-field arrangement where paths are summed over the entire extent of the slits.

The probability amplitude for a particle to travel in free space from space-time event α, denoted (x_0, t_0), to event β, denoted (x_N, t_N), in a number N evenly-spaced time intervals ϵ, is given in Eq. 3.2 of Ref. [86] as

$$K\left(\beta; \alpha\right) = \lim_{\epsilon \to 0} \left(\frac{m}{2\pi i \epsilon \hbar}\right)^{N/2} \int \cdots \int \exp\left\{\frac{im}{2\hbar\epsilon}\left[\sum_{j=1}^{N}\left(x_j - x_{j-1}\right)^2\right]\right\} \mathrm{d}x_1 \cdots \mathrm{d}x_{N-1} \tag{3.21}$$

Feynman points out that the resulting nested Gaussian integrals can be performed iteratively, leading to the result

$$K\left(\beta; \alpha\right) = \left(\frac{m}{2\pi i \hbar N \epsilon}\right)^{1/2} \exp\left[\frac{im}{2\hbar N \epsilon}\left(x_N - x_0\right)^2\right]. \tag{3.22}$$

When the subscripts 0 and N are associated with their space-time events α and β, and the total time $N\epsilon$ is replaced with the time difference, $t_\beta - t_\alpha$, then Eq. 3.22 becomes

$$K\left(\beta;\alpha\right) = \left[\frac{m}{2\pi i\hbar\left(t_\beta - t_\alpha\right)}\right]^{1/2} \exp\left[\frac{im}{2\hbar\left(t_\beta - t_\alpha\right)}\left(x_\beta - x_\alpha\right)^2\right]. \qquad (3.23)$$

This result, which is readily generalized to higher dimensions, shows that the amplitude associated with the summation over all possible paths connecting two events in free space is equal to the amplitude associated with the classical path alone, as sketched in Fig. 3.3.
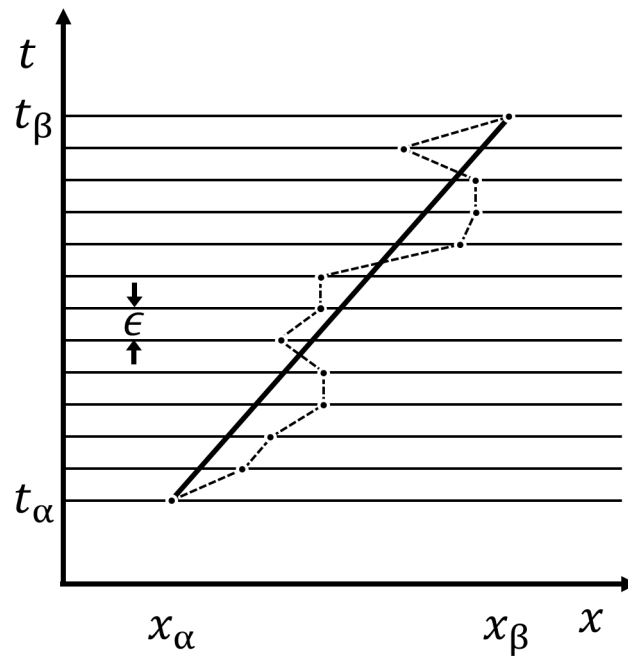
Figure 3.3: A general path (dotted line) is shown for a point particle that travels from space-time point (x_α, t_α) to (x_β, t_β). The locations x that the path crosses (indicated for times separated by ϵ) can by varied along the x-axis. The classical path is indicated with the bold dark line. Feynman showed that the total amplitude for motion from α to β summed over all paths (by integrating over the x-locations) is identical to the amplitude computed along the classical path alone, which is a central result from the path integral formalism.[42,86]

3.7 Two-step propagator for a slit

As the next step towards describing the double slit, consider the amplitude for an electron path intersecting a single slit. This path is described by three space-time events, labeled as follows: the source, defined as the event α; the slit crossing, denoted by slit; and the measurement at the screen, β.

The amplitude for such a path can be constructed as the product of the amplitude for two steps. The first step is to reach the slit from α, and the second step is to travel from the slit to β.[149,150] Applying the result of Eq. 3.23 to this case, one obtains

$$
\begin{aligned}
K\left(\beta;\alpha\right) &= K\left(\beta;\text{slit}\right) \cdot K\left(\text{slit};\alpha\right) \\
&= \left[\frac{m}{2\pi i\hbar\left(t_\beta - t_{\text{slit}}\right)}\right]^{1/2} \exp\left[\frac{im}{2\hbar\left(t_\beta - t_{\text{slit}}\right)}\left(x_\beta - x_{\text{slit}}\right)^2\right] \\
&\quad \cdot \left[\frac{m}{2\pi i\hbar\left(t_{\text{slit}} - t_\alpha\right)}\right]^{1/2} \exp\left[\frac{im}{2\hbar\left(t_{\text{slit}} - t_\alpha\right)}\left(x_{\text{slit}} - x_\alpha\right)^2\right] \\
&= \frac{m}{2\pi i\hbar}\left[\frac{1}{\left(t_\beta - t_{\text{slit}}\right)\left(t_{\text{slit}} - t_\alpha\right)}\right]^{1/2} \cdot \exp\left[\frac{imL^2\left(t_\beta - t_\alpha\right)}{2\hbar\left(t_\beta - t_{\text{slit}}\right)\left(t_{\text{slit}} - t_\alpha\right)}\right],
\end{aligned}
\tag{3.24}
$$

where the substitution $(x_\beta - x_\alpha)/2 = L$ was made. We note that this is an approximation: an exact construction for the propagator would take into account the boundary conditions set by the walls. The integrations from $-\infty$ to ∞ in Eq. 3.21 include paths that pass through the walls; therefore, the propagator in Eq. 3.24 adds extraneous paths to the sum. The times t_α and t_β defining the boundaries of this path are fixed, but the slit-crossing time, t_{slit}, is not. It is not a measured event in the same sense as α or β and thus cannot be specified. The total amplitude to cross the slit, $K(\beta;\alpha)$, is then a sum over all of the amplitudes having every possible value of t_{slit}.[1]

---

[1] The issue of slit crossing time is closely connected to the problem of diffraction in time. For context and a discussion, see Ref. [151].

3.8   Time summed amplitude for two-step propagator

To obtain the total amplitude to cross the slit, $K(\beta; \alpha)$, consider the sum of the products $K(\beta; \text{slit}) \cdot K(\text{slit}; \alpha)$ of Eq. 3.24 for every value of t_{slit} occurring between t_α and t_β. The result is written as

$$K(\beta; \alpha) = \sum_{t_{\text{slit}}=t_\alpha}^{t_\beta} K\left(x_\beta, t_\beta; x_{\text{slit}}, t_{\text{slit}}\right) \cdot K\left(x_{\text{slit}}, t_{\text{slit}}; x_\alpha, t_\alpha\right). \tag{3.25}$$

For more detail, see the derivation of Eq. 3.25 in Sec. 3.14. This formally establishes the sum over intermediate times that is required from the sum over all paths given in Eq. 3.21. The sum in Eq. 3.25 over the continuous value t_{slit} is proportional to the integral $I(\beta; \alpha)$, given by

$$I(\beta; \alpha) = \int_{\frac{t_\beta}{2}}^{\frac{t_\beta}{2}} dt \frac{m}{2\pi i \hbar} \left[\frac{1}{\left(\frac{t_\beta}{2} - t\right)\left(\frac{t_\beta}{2} + t\right)} \right]^2 \exp\left[\frac{i m L^2 t_\beta}{2\hbar \left(\frac{t_\beta}{2} - t\right)\left(\frac{t_\beta}{2} + t\right)} \right]. \tag{3.26}$$

Here, $t_\alpha = 0$, $(x_\beta - x_\alpha)/2 = L$ as before, and the variable time t at the slit has been defined to give a symmetric integrand. This integral is derived and evaluated in greater detail in Sec. 3.15. The result, given in terms of the complementary error function, $\text{erfc}(z)$ [152], is

$$I(\beta; \alpha) = \frac{m}{2\pi i \hbar} \pi \text{erfc}\left(-i\sqrt{i\varphi_0}\right), \tag{3.27}$$

with $\varphi_0 \equiv 2mL^2/(\hbar t_\beta)$. An asymptotic expansion given by (7.1.23) of Ref. [152] gives, for Eq. 3.27,

$$I(\beta; \alpha) \approx \frac{m}{2\pi i \hbar} \sqrt{\frac{\pi}{\varphi_0}} \exp\left(i\varphi_0\right) \exp\left(i\frac{\pi}{4}\right) \left[1 - \frac{i}{2\varphi_0} - \frac{3}{4\varphi_0^2} + \frac{15i}{8\varphi_0^3} + \cdots \right]. \tag{3.28}$$

The form of Eq. 3.28 illustrates that the total integrated amplitude experiences a phase shift of $\pi/4$ from the phase φ_0. This phase difference is independent of the choice of path and thus the global phase $\pi/4$ can be factored out. Fig. 3.4a shows the convergence of the real part of the numerical evaluation of Eq. 3.26 (blue curve) to the real part of the analytic result of Eq. 3.27 (black dashed), for $L = 3.37 \times 10^{-6}\,\mathrm{m}$ and $t_\beta/2 = 3.36 \times 10^{-13}\,\mathrm{s}$. The numeric results are computed for variable limits of integration and plotted as a function of the total time interval being integrated. Fig. 3.4b gives the phase argument of the numeric results (red curve) to show the convergence of the rotation from the initial phase argument given by φ_0, which is defined by choice of the parameters to be π (black dotted), to an angle of $-3\pi/4$ (black dashed). This establishes the appropriate choice of amplitude for a path crossing one slit. The physical meaning of φ_0 will now be discussed.
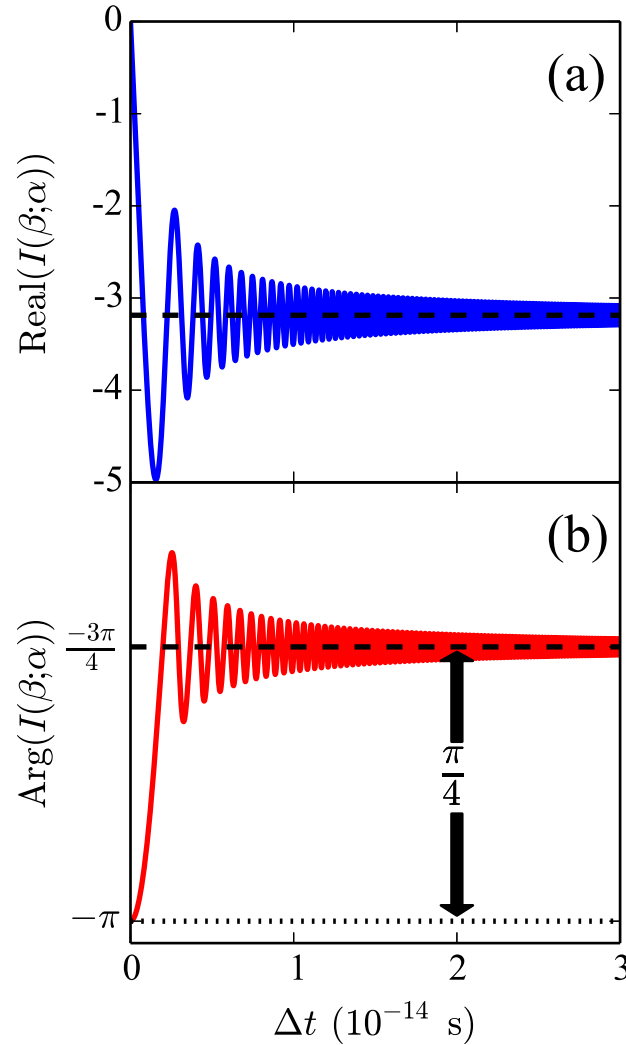
Figure 3.4: Numerical time integration for a single electron path. (a) Real part of Eq. 3.26 (solid blue), integrated from $-\Delta t/2$ to $\Delta t/2$ relative to $t_\beta/2$, showing convergence to the analytic value given in Eq. 3.27 (dashed line). (b) Complex argument of the integrated amplitude (solid red), showing convergence to $\pi/4$ phase shift (dashed line) from the argument of $\exp(i\varphi_0)$ (dotted black). The amplitude proportional to $\exp(i\varphi_0)$ is therefore the appropriate choice of a single amplitude to characterize the entire sum over time.

3.9   Stationary phase for the two-step propagator

The phase φ accumulated along a path crossing a slit is determined from Eq. 3.5 to be

$$\varphi = \frac{m}{2\hbar}\left(\frac{{L_1}^2}{t_{\text{slit}}} + \frac{{L_2}^2}{\tau - t_{\text{slit}}}\right), \tag{3.29}$$

where $\tau = t_\beta - t_\alpha$, L_1 is the path length from source to slit, and L_2 is the length from slit to screen. When t_{slit} is varied by δt_{slit}, the phase can be expanded as a power series in δt_{slit} as

$$\varphi = \varphi_0 + \frac{\partial \varphi}{\partial t_{\text{slit}}}\delta t_{\text{slit}} + \frac{1}{2}\frac{\partial^2 \varphi}{\partial t_{\text{slit}}^2}\left(\delta t_{\text{slit}}\right)^2 + \cdots, \tag{3.30}$$

where φ_0 is associated with a particular choice of t_{slit}. The first-order term of Eq. 3.30 is written out

$$\frac{\partial \varphi}{\partial t_{\text{slit}}} = \frac{m}{2\hbar}\left(\frac{{L_2}^2}{(\tau - t_{\text{slit}})^2} - \frac{{L_1}^2}{t_{\text{slit}}^2}\right). \tag{3.31}$$

The factor $\partial\varphi/\partial t_{\text{slit}} = 0$ when $L_2/(\tau - t_{\text{slit}}) = L_1/t_{\text{slit}}$: that is, when the velocities along the path are equal before and after the slit. The phase φ will then experience no first-order variation from φ_0 when t_{slit} is chosen by this condition. We then say that the phase is stationary for this choice of path, and the value of the stationary phase is φ_0. As shown in Sec. 3.8, this phase characterizes the amplitude arising from the sum of choosing all values of t_{slit}; therefore, it is the appropriate choice for a single path. The phase in terms of the de Broglie wavelengths along this single path is now established $\pi L_1/\lambda_{dB} + \pi L_2/\lambda_{dB} = \pi L_{\text{path}}/\lambda_{dB}$.

3.10   Stationary phase in the double slit

Fig. 3.5a shows two interfering paths (green and red) in a space-time diagram for the double slit. The times t_{slit1} and t_{slit2}, when paths 1 and 2 intersect the slits,

respectively, take any value between the initial time t_{initial} and final time t_{final}. The probability distribution at the screen is shown to the right of the screen as an intensity plot. In Fig. 3.5b, a phasor diagram of the complex amplitudes for the varying times t_{slit1} and t_{slit2} is shown. The highlighted paths in Figs. 3.5a and 3.5b are the paths of stationary phase. In Fig. 3.5c, the phases corresponding to the amplitudes in (b) are given as a function of time to illustrate the stationary phase behavior.

Notice that the stationary phase time for path 1, indicated by the largest red dot in Fig. 3.5a, occurs after the stationary phase time for path 2. The reason is that the length of path 1 (that is, the length of the dashed line in the $x - y$ plane) is shorter than the length of path 2. As the initial time and final times are the same for both paths, the velocities of the paths are different. The equal length of the part of both paths between the source and slits explains the difference in the stationary phase times for this example. For some other path integral calculations, the slit crossing times are chosen to be identical for all paths[37,149,150], while for the optical analogy, the times are the same for paths of the same length from source to slit.
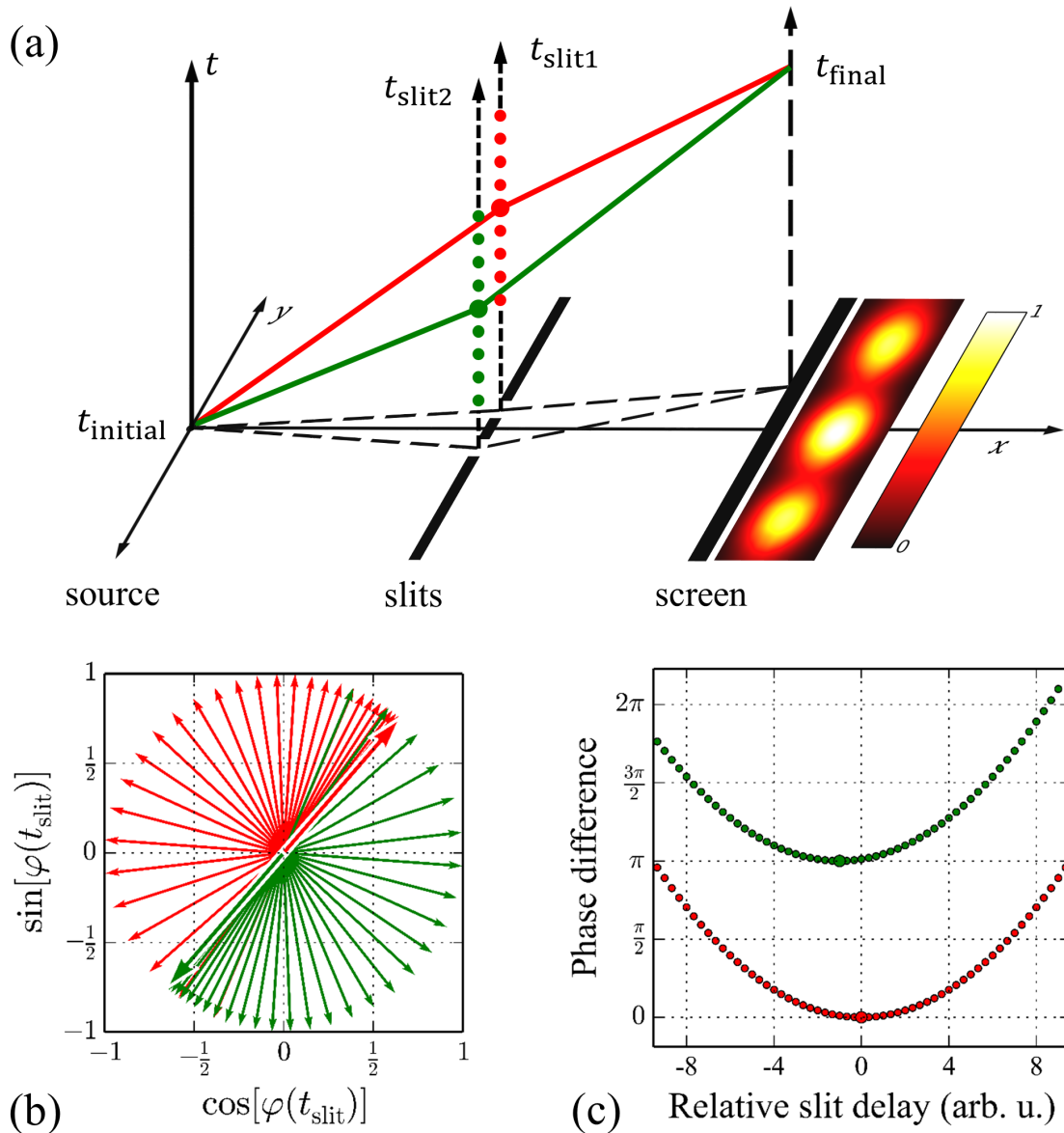
Figure 3.5: Path integral illustration for destructive interference in a double slit. (a) The times t_{slit1} and t_{slit2} at which the paths intersect the slits take any value between the initial time t_{initial} and final time t_{final}. The resulting probability distribution at the screen is the square of the sum of the amplitudes for all of the times t_{slit1} and t_{slit2}. (b) Shown is a phasor diagram for complex amplitudes associated with the intermediate times for slit 1 (red) and slit 2 (green). The highlighted paths in (b) are the paths of stationary phase shown in (a). (c) The phases corresponding to the amplitudes in (b) are shown as a function of intermediate time to illustrate the stationary phase behavior.

3.11 Phase matters

Does the optical analogy and the path integral method make the same predictions? In other words: "Does the phase of a single path matter?" After all, real experiments are only sensitive to phase differences, which were shown to agree for the optical analogy and the path integral formalism in Eq. 3.9. This agreement is not always the case. Consider now the double slit arrangement in Fig. 3.6, where the electron source and observation point are in-line with one of the slits. Computing the phases of the drawn paths by Eq. 3.5 (dashed lines) leads to a phase difference

$$\Delta\varphi_{\text{pathintegral}} = \frac{2md^2}{\hbar\Delta t}. \tag{3.32}$$

This result does not depend on the length L in this configuration. If instead we use the optical analogy, we compute the phase difference

$$\Delta\varphi_{\text{optical}} = 2\frac{2\pi}{\lambda_{dB}(v)}\left(\sqrt{L^2 + d^2} - L\right) \approx \frac{2md^2}{\hbar\Delta t} - \frac{md^4}{2\hbar\Delta t L^2}, \tag{3.33}$$

where the time and velocity between the two methods are connected by $v = 2L/\Delta t$. The phase difference in Eq. 3.33 now depends on L. The phase difference thus depends on the choice of method used for single path phases. When $d^2/(4L^2) \propto \pi\hbar\Delta t/(2md^2)$, Eq. 3.33 conflicts with Eq. 3.32, and thus the choice of method matters.
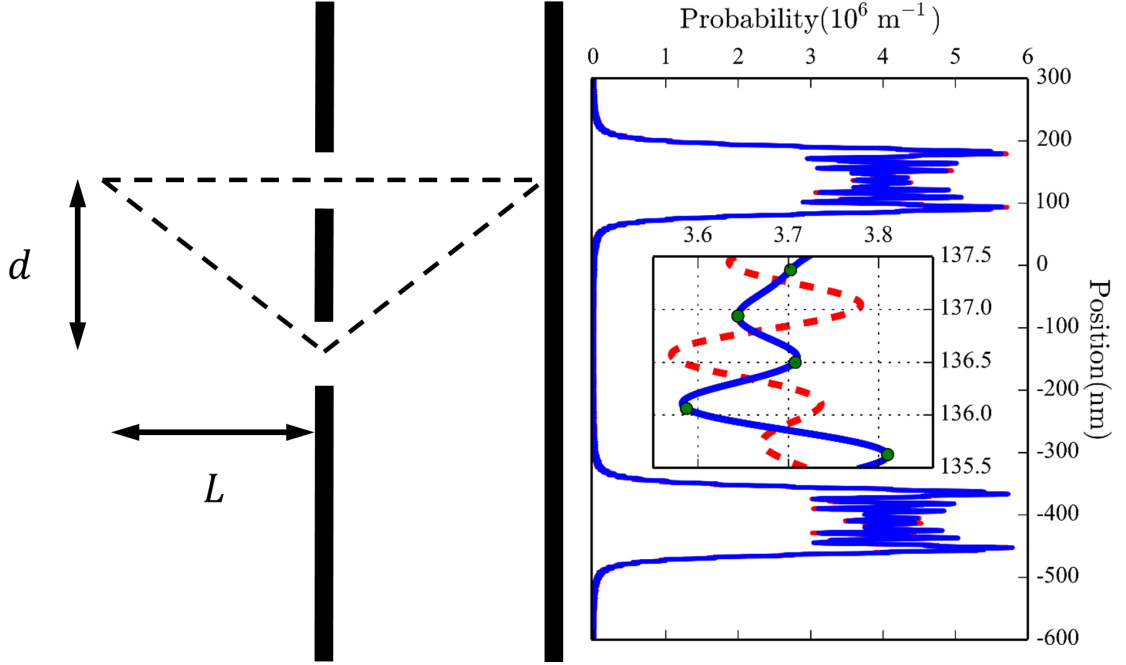
Figure 3.6: Feynman paths and probability distribution from all paths in a near-field two slit arrangement. The source is positioned in line with one of the slits and the detection point. The slit separation d, propagation length L, and velocity are chosen to highlight the discrepancy between the predictions of the two methods. The normalized probability distribution functions at the screen are computed with the path integral stationary phases (blue), the time-summed amplitudes (green points), and the optical analogy (dashed red).

To best exemplify this conflict, lets now choose the experimental conditions so that the common term of Eqs. 3.32 and 3.33 is set to an integer multiple of 2π, and the second term of Eq. 3.33 set to π. Now, Eq. 3.32 predicts constructive interference in line with the slit, while Eq. 3.33 predicts destructive interference.

For electron diffraction in the symmetric double slit arrangement of Fig. 3.6, a slit separation of $273\,\mathrm{nm}$ with widths of $63\,\mathrm{nm}$ can be chosen. Note that such a double slit has been demonstrated recently for electron diffraction in Ref. [37]. In contrast to Ref. [37], now the source and screen are placed at the much closer distances of $3.37\,\mathrm{\mu m}$ from the slits. When Δt is fixed for the path integral method by choosing the electron velocity to be $1 \times 10^7\,\mathrm{m/s}$ over the straight path, the difference of π is set

between the predictions of the two methods. The diffraction patterns are computed with both methods and shown on the right of Fig. 3.6. At a location on the detection screen that is in line with the source (at $y = 136.5\,\text{nm}$), the path integral method (solid blue) predicts a constructive maximum, while the optical analogy (dashed red) predicts a minimum. A time sum of the form of Eq. 3.25 performed for 6000 points per slit and five points on the observation screen over intervals of $6.88 \times 10^{-14}\,\text{s}$ centered on the stationary phase time of each path from the source to the screen points (green points) agrees with the blue curve computed with the stationary phase times alone. This configuration is experimentally challenging to realize. Nevertheless, near field interferometry for matter waves does exist and may be pushed towards this regime.[45,153] In conclusion, phase difference predictions from the optical analogy and the path integral formalism will not agree in some near-field conditions. While the global phase of a single path does not matter, to obtain correct phase differences, the single path phases must be handled appropriately.

3.12   Summary and conclusions

The optical analogy can give excellent approximate phase differences in most situations and thus leads to the correct prediction of the positions of interference extrema. This method is justified by considering stationary solutions to the Schrödinger equation. The conceptual trap is that a student may infer from the correct phase difference, $2\pi\Delta L/\lambda$, that the phase of a single path is given by $2\pi L/\lambda$ (as would be correct for optical waves). The path integral description of quantum mechanics gives the correct phase difference $2\pi\Delta L/\lambda$ between paths, the correct phase $\pi L/\lambda$ accumulated over time along a single path, and justifies drawing paths in space to compute phases. The path integral method (and the time-dependent Schrödinger equation) gives the exact

phase difference in all situations. It is therefore an appropriate method to use in conceptual discussions of matter wave diffraction.

In some physics textbooks, both paths and waves are omitted from the description of matter wave diffraction. Instead, the discussion refers back to water waves or Young's experiment for light waves and quotes the condition for interference or phase differences by analogy.[87–91] This presentation is correct to obtain phase differences, but it ignores the differences in propagation, that is, the time dependent behavior, between light and matter waves.

Some physics textbooks[89–91], as well as some advanced undergraduate and graduate texts, will draw attention to group and phase velocities in sections unrelated to the double slit description.[147,154,155] It is interesting to contemplate at what level and in what manner the conceptual difficulty discussed in this paper could be addressed. For example, it could follow a discussion of the group and phase velocities of a matter wave packet. The results from the path integral formalism could thus be presented at the undergraduate level[156–158] to elucidate the idea of a "path."

3.13   Acknowledgments

3.14   Time sum derivation

In the following, the propagator is derived for a single slit crossing as described in Sec. 3.8. In Eq. 3.21, each of the positions x_k represent the range of positions a point could have along a path at the kth time step of the sum. Requiring that a path intersects the slit at x_{slit} in the kth time step is defined as a multiplication of a term $\delta(x_{\text{slit}} - x_k)$ to the integrand. This intersection happens at any time step from the first up to the last, so a factor

$$\chi_{\text{slit}} = \sum_{k=1}^{N-1} \delta \left(x_{\text{slit}} - x_k \right) \tag{3.34}$$

must be included in (21) to describe all of the alternative times a path can intersect the slit. Substituting Eq. 3.34 into Eq. 3.21 gives the total amplitude to travel from α to β as

$$K\left(\beta;\alpha\right) = \lim_{\epsilon \to 0} \left(\frac{m}{2\pi i \epsilon \hbar}\right)^{N/2} \int \cdots \int \chi_{\text{slit}} \exp\left\{ \frac{im}{2\hbar\epsilon} \left[\sum_{j=1}^{N} (x_j - x_{j-1})^2 \right] \right\} \mathrm{d}x_1 \cdots \mathrm{d}x_{N-1}$$

$$= \lim_{\epsilon \to 0} \sum_{k=1}^{N-1} \left(\frac{m}{2\pi i \epsilon \hbar}\right)^{N/2} \int \cdots \int \exp\left\{ \frac{im}{2\hbar\epsilon} \left[\sum_{j=1}^{N} (x_j - x_{j-1})^2 \right] \right\} \delta\left(x_{\text{slit}} - x_k \right) \mathrm{d}x_1 \cdots \mathrm{d}x_{N-1}$$

$$\tag{3.35}$$

Performing the $N-1$ integrations in Eq. 3.35 leads to the total sum

$$K\left(\beta;\alpha\right) = \lim_{\epsilon \to 0} \sum_{k=1}^{N-1} K\left(x_\beta, t_\beta; x_{\text{slit}}, t_\alpha + k\epsilon \right) \cdot K\left(x_{\text{slit}}, t_\alpha + k\epsilon; x_\alpha, t_\alpha \right) \tag{3.36}$$

The substitution $t_{\text{slit}} \equiv t_\alpha + k\epsilon$ is made into Eq. 3.36 to obtain the final result

$$K\left(\beta;\alpha\right) = \lim_{\epsilon\to0} \sum_{t_{\text{slit}}=t_\alpha+\epsilon}^{t_\beta-\epsilon} K\left(x_\beta, t_\beta; x_{\text{slit}}, t_{\text{slit}}\right) \cdot K\left(x_{\text{slit}}, t_{\text{slit}}; x_\alpha, t_\alpha\right)$$

$$= \sum_{t_{\text{slit}}=t_\alpha}^{t_\beta} K\left(x_\beta, t_\beta; x_{\text{slit}}, t_{\text{slit}}\right) \cdot K\left(x_{\text{slit}}, t_{\text{slit}}; x_\alpha, t_\alpha\right). \tag{3.37}$$

3.15 Evaluating the integral of the full time sum

The time sum derived in Sec. 3.37 over the continuous value t_{slit} must be handled carefully near the singular points occurring at $t_{\text{slit}} = t_\beta$ and $t_{\text{slit}} = t_\alpha = 0$, so we convert the sum to an integral prior to performing the limit $\epsilon \to 0$ to obtain

$$I\left(\beta;\alpha\right) = \lim_{\epsilon\to0} \int_\epsilon^{t_\beta-\epsilon} \mathrm{d}t_{\text{slit}} \frac{m}{2\pi i\hbar} \left[\frac{1}{t_{\text{slit}}\left(t_\beta - t_{\text{slit}}\right)}\right]^{1/2} \exp\left[\frac{imL^2 \cdot t_\beta}{2\hbar t_{\text{slit}}\left(t_\beta - t_{\text{slit}}\right)}\right], \tag{3.38}$$

where $(x_\beta - x_\alpha)/2 = L$ as before. Next, $x = 2(t_{\text{slit}}/t_\beta - 1/2)$ is substituted to obtain

$$I\left(\beta;\alpha\right) = \lim_{\epsilon\to0} \int_{-1+\frac{2\epsilon}{t_\beta}}^{1-\frac{2\epsilon}{t_\beta}} \mathrm{d}x \frac{m}{2\pi i\hbar} \left[\frac{1}{\left(1+x\right)\left(1-x\right)}\right]^{1/2} \exp\left[\frac{i2mL^2}{\hbar t_\beta} \frac{1}{\left(1+x\right)\left(1-x\right)}\right].$$

$$\tag{3.39}$$

Eq. 3.39 is simplified by the definition of the stationary phase as $\varphi_0 \equiv 2mL^2/(\hbar t_\beta)$ as in Sec. 3.8. The next substitution to be performed is $x = \sin\left(\theta\right)$. This trigonometric

substitution eliminates the square root, as $\mathrm{d}x/\sqrt{1-x^2} = \mathrm{d}\theta$, and we obtain

$$
\begin{aligned}
I(\beta;\alpha) &= \lim_{\epsilon\to 0} \frac{m}{2\pi i\hbar} \int_{\sin^{-1}\left(-1+\frac{2\epsilon}{t_\beta}\right)}^{\sin^{-1}\left(1-\frac{2\epsilon}{t_\beta}\right)} \mathrm{d}\theta \exp\left[\frac{i\varphi_0}{\cos^2(\theta)}\right] \\
&= \lim_{\epsilon\to 0} \frac{m}{2\pi i\hbar} \int_{\sin^{-1}\left(-1+\frac{2\epsilon}{t_\beta}\right)}^{\sin^{-1}\left(1-\frac{2\epsilon}{t_\beta}\right)} \mathrm{d}\theta \exp(i\varphi_0)\cdot\exp\left[i\varphi_0\tan^2(\theta)\right],
\end{aligned}
\tag{3.40}
$$

where the identity $\sec^2(\theta) = 1+\tan^2(\theta)$ is used in order to factor out a term $\exp(i\varphi_0)$. Next, we substitute $u = \tan(\theta)$ and obtain

$$
I(\beta;\alpha) = \lim_{\epsilon\to 0} \frac{m}{2\pi i\hbar}\exp(i\varphi_0) \int_{\tan\left[\sin^{-1}\left(-1+\frac{2\epsilon}{t_\beta}\right)\right]}^{\tan\left[\sin^{-1}\left(1-\frac{2\epsilon}{t_\beta}\right)\right]} \mathrm{d}u\frac{\exp(i\varphi_0 u^2)}{1+u^2}.
\tag{3.41}
$$

The limits of integration are symmetric and now tend to $\pm\infty$ as $\epsilon\to 0$, so they are redefined as $\tan\left[\sin^{-1}(1-2\epsilon/t_\beta)\right] = R$ and $\tan\left[\sin^{-1}(-1+2\epsilon/t_\beta)\right] = -R$, with the limit $R\to\infty$. Finally, we extend the integrand into the complex plane by performing the substitution $t = -i\sqrt{i\varphi_0}u$ to obtain

$$
I(\beta;\alpha) = \lim_{R\to\infty} \frac{m}{2\pi i\hbar}\exp(i\varphi_0)i\sqrt{i\varphi_0} \int_{-i\sqrt{i\varphi_0}(-R)}^{-i\sqrt{i\varphi_0}R} \mathrm{d}t\frac{\exp(-t^2)}{\left(\sqrt{i\varphi_0}\right)^2-t^2}.
\tag{3.42}
$$

The integrand is analytic everywhere in the complex plane except for first-order poles at $\pm\sqrt{i\varphi_0}$, therefore the path of integration, which lies on the line $t = R\exp(i3\pi/4)$, can be rotated to lie entirely on the real axis. The integrand's even symmetry then

permits

$$I\left(\beta;\alpha\right) = \frac{m}{2i\hbar} \exp\left(i\varphi_0\right) \left[\frac{2i}{\pi} \sqrt{i\varphi_0} \int\limits_0^\infty dt \, \frac{\exp\left(-t^2\right)}{\left(\sqrt{i\varphi_0}\right)^2 - t^2} \right].$$ (3.43)

The term in square brackets of Eq. 3.43 has the form of the complex-valued function $w(z)$, given in (7.1.4) of Ref. [152], as

$$w\left(z\right) = \frac{2iz}{\pi} \int\limits_0^\infty dt \, \frac{\exp\left(-t^2\right)}{z^2 - t^2}$$ (3.44)

This function can be readily evaluated from the definitions given in (7.1.2) and (7.1.3) of Ref. [152], as

$$w\left(z\right) = \exp\left(-z^2\right) \mathrm{erfc}(-iz),$$ (3.45)

where $\mathrm{erfc}(z)$ is the complementary error function. Substituting Eq. 3.44 and Eq. 3.45 into Eq. 3.43, we obtain the result,

$$I\left(\beta;\alpha\right) = \frac{m}{2\pi i\hbar} \pi \cdot \mathrm{erfc}\left(-i\sqrt{i\varphi_0}\right),$$ (3.46)

which is Eq. 3.27.

Chapter 4

Bouncing droplets as quantum analogs

Analogous systems are useful in demonstrating phenomena that can be experimentally difficult to accomplish, or are otherwise conceptually challenging. In that regard, analogs can make such systems more accessible for basic research, or simpler to grasp for pedagogical purposes. Young's ripple tank, which was discussed in Chapter 3, is a classic example, where a fluid wave analog was applied to the diffraction of electromagnetic waves from slits[49], and later, potentially erroneously, to demonstrations of matter wave diffraction. A number of acoustic analogs to quantum phenomena have been explored, including a demonstration of level splitting[159], the formation of band structure[160], and an acoustic avoided crossing.[161] An acoustic quantum analog system is even commercially available for undergraduate laboratory courses, which can be used to study analogs of atomic hydrogen and semiconductor bandgaps.[162] These systems share in common a similar theoretical structure while being experimentally accessible to undergraduates studying physics.

A visually stunning quantum mechanical analog was developed recently in Paris, France, in the research group of Yves Couder. A system of bouncing oil droplets, coupled to dynamically evolving surface waves which guide the motion of the droplets, was found to exhibit properties that are typically considered beyond the capability of classical systems.[51,52] Oil droplet analogs have since been demonstrated for quantum

mechanical tunneling[98,163], Landau orbit quantization[53,101], orbital level splitting[100,164], and for the quantum corral.[99] One of the most significant of these analogs was the realization of a macroscopic single and double slit diffraction experiment.[57] Couder et al. reported the ability to obtain wave-like diffraction patterns from the macroscopic oil drop system, taken one trajectory at a time. The results were so fantastic that the system was featured in an episode of the science popularization series, *Through the Wormhole*.[165]

The original experimental results, which show wave-like diffraction patterns built up by the trajectories of single walking droplets, have been tested for repeatability by the Bohr group at the Technical University of Denmark[103], by our group at the University of Nebraska-Lincoln,[102] and the Bush group at MIT.[104] The work has inspired new experiments with the double slit,[166] as well as theoretical models,[167] while discussion over how single particles can diffract remains current and ongoing.[168]

In the following chapter, I will describe the oil drop system we developed, along with the data we obtained replicating Couder's single and double slit analog experiments. A second experiment is then described, of walkers confined to nearly 1-D motion in a linear channel,[54] which was developed to be performed by undergraduate or even high school-level researchers. The data presented for those experiments were obtained by visiting high school students, Summer 2017.

4.1 Experimental Apparatus

In all experiments, an electromagnetic mechanical shaker is used to oscillate a dish filled with silicone oil. The silicon oils used in experiments were pure polydimethylsiloxane (Clearco Products Comany, Inc.), with viscosities 20 cSt (centiStokes), which is identical to the oil viscosity reported in Couder et al. of $20 \times 10^{-3} \, \text{Pa} \, \text{s}$,[57] and 50

cSt ($50 \times 10^{-3}\,\mathrm{Pa \cdot s}$). The oils have a surface tension σ =0.0209 N/m and density ρ =$0.965 \times 10^3\,\mathrm{kg/m^3}$. We used a home-built mechanical shaker based around a Pioneer TS-W3002D2 subwoofer. The speaker was given an amplified sinusoidal signal supplied by a Stanford Research Systems DS345 function generator. The function generator signal was amplified by a home-built amplifier with a gain of 2. The amplifier was based around an LM12CLK OP amp, and was supplied $\pm$ 20 V by a Topward 6306A power supply, running in independent mode. It was necessary to use a power supply with adequate current, as the speaker places a considerable load on the circuit when it is driving a filled dish.

The dishes, which are shown in Fig. 4.1(a), are coupled to the speaker by a magnetic coupler, which is shown in Fig. 4.1(b).
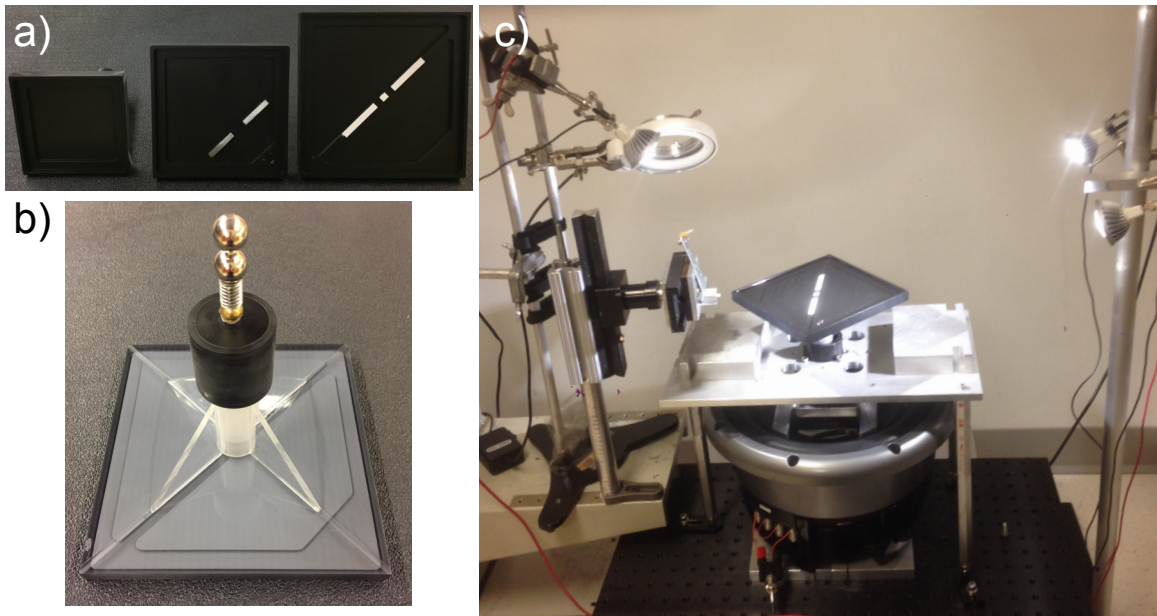
Figure 4.1: Images of oil drop experimental apparatus. Shown in a) are the dishes used in various experiments. The center and right-most dishes are used for reproducing the single and double slit oil drop experiments, respectively. Shown in b)is the underside of the double slit dish to highlight the magnetic coupler and Delrin bearing components. In c), the complete apparatus is shown, with lighting, and droplet guide. This setup forms the basis for all experiments shown. The imaging camera was not in the frame.

A Delrin cylindrical bearing constrains the motion of the dish to be vertical. This bearing assembly is lubricated before experiments with either valve oil (a petroleum distillate more regularly found with brass musicians) or WD-40. The bearing assembly can be positioned and oriented by a 3-legged leveling table, which in turn levels the dish. Complete drawings of all dish components, with relevant dimensions, can be found in Appendix B. A dish is leveled by filling it to with oil a depth of $\approx 4\,\text{mm}$, and then observing the onset of the Faraday instability.[50,169] The wave patterns of the Faraday instability are shown in Fig. 4.2. The Faraday instability is a parametrically forced wave pattern that spontaneously forms on the surface of the fluid when the oscillation acceleration reaches a threshold value. The Faraday waves on the surface of the fluid have a wavelength given by the shallow water dispersion relation,

$$\omega^2 = gk + \left(\frac{\sigma}{\rho}\right) k^3, \tag{4.1}$$

where ω is the driving frequency, g is acceleration due to gravity, $k = 2\pi/\lambda_F$ is the wavenumber, σ is the fluid surface tension, and ρ is the fluid density. The Faraday wavelengths for the 20 cSt and 50 cSt oils are then determined by the applied driving frequencies, which are $80\,\text{Hz}$ and $50\,\text{Hz}$, respectively. The value of the Faraday wavelengths, λ_F , are then $4.75\,\text{mm}$ and $6.95\,\text{mm}$, respectively.[57] When the waves at threshold start to form first in the center of the deepest portion of the dish, then the dish is appropriately level. Once the dish is level, the leveling table legs can be locked by thumb screws located at the base of the legs. The entire system is shown in Fig. 4.1(c). A refined version of this system, featuring an air bearing in place of the Delrin bearing assembly and a thin "stinger" rod to couple loads to the mechanical shaker, is detailed in Ref. [106]
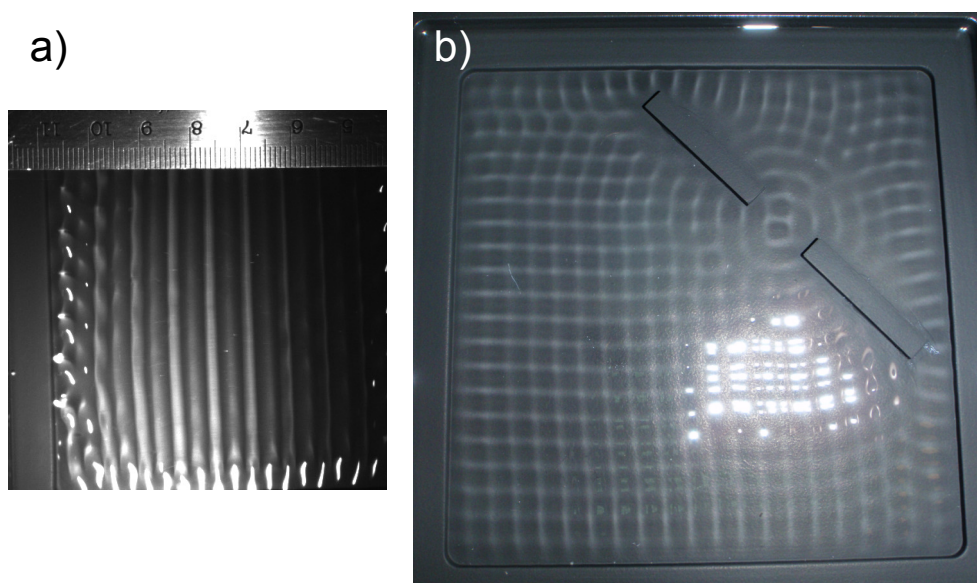
Figure 4.2: Images of Faraday wave excitations on the oil surface. Shown in a) is a Faraday wave in an open square dish filled with 50 cSt dimethicone. In b), the single slit dish was filled with 20 cSt dimethicone. The measured wavelengths are approximately 7 mm and 4.8 mm, respectively.

When a dish of oil is shaken below the Faraday threshold, a droplet can be suspended on the surface of the fluid nearly indefinitely.[51,52] The reason for this is the presence of a small air channel that is compressed between the drop and the fluid bath–the droplet is never in direct contact with the oil bath, so it does not coalesce. As the shaking acceleration is increased to near the Faraday instability threshold, the bouncing droplet will excite a ripple in the fluid surface. That ripple will be sustained by the parametric forcing of the surface, but will dissipate over time. As the dissipation time increases, the drop can fall on the slope of the wave created by the back action of the previous bounce. For a sufficient shaking amplitude, the drop bouncing period becomes twice the shaking period, and the location of where the drop strikes the Faraday wave packet becomes consistent between bounces. Such a wave/droplet pair is referred to as a walker.[51] A succession of frames of the motion of a walker is shown in Fig. 4.3. The shape of the surface wave is highlighted by a

method developed by the Bush group.[170] A translucent cell of alternating blue and red stripes is used as a filter to illuminate a walker. The cell diffuses the light, and the stripes provide patterns that add depth to the image.
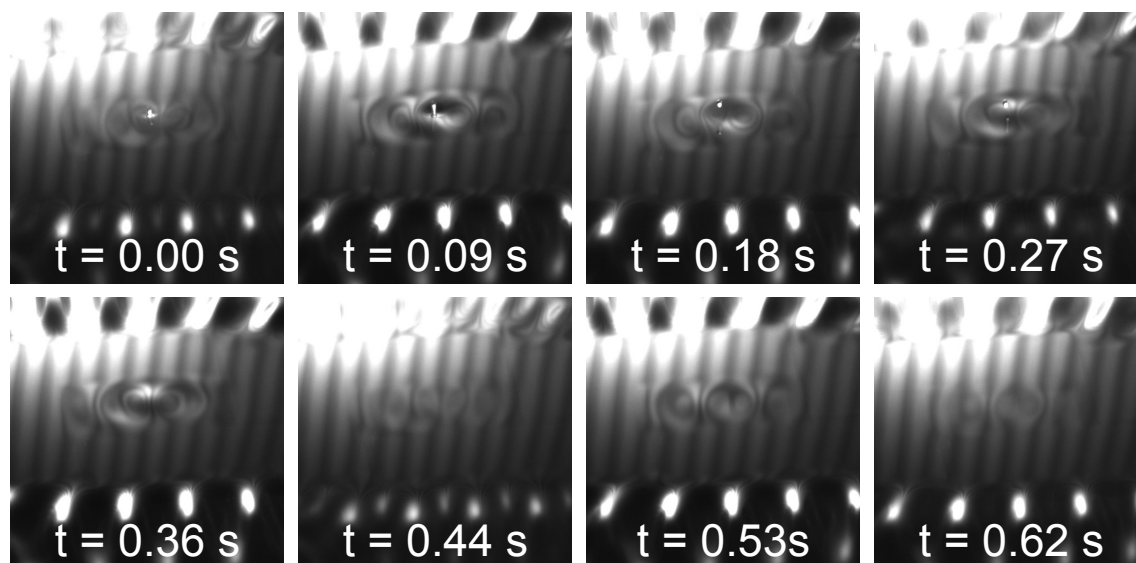
Figure 4.3: Visualization of the droplet/wave pair in a cavity. The surface wave features are highlighted via illumination of the dish through a colored filter consisting of alternating red and blue bars, as demonstrated in Ref. [BUSH REFERENCE]. Even though the drop spontaneously coalesced into the fluid at $t = 0.36$ s, the companion wave persisted in the fluid at least 1.8 s later.

Drop trajectories are recorded by a digital camera (JAI CM-030GE) mounted above the dish. The camera has a maximum acquisition rate of 90 frames per second (fps), but was typically run at 22.5 fps to save on memory and disk space. The frames were acquired by a LabVIEW code adapted by former graduate student Roger Bach. After a set of images were taken, the drop position was located by a blob-finding code. The first iteration of code was written by an undergraduate researcher, Adam Lif. The code was written to not only find the drop position in the thousands of acquired images, but organize the trajectory data in a reasonable fashion. Adam's source code, which can be compiled in Microsoft Visual Studios, is given in Appendix C.

A walker in an open cell, that is, a cell having no changes in topography of the cell floor, will undergo rectilinear motion. As a walker approaches the sides of the cavity, however, the surface wave begins to interact with the boundary and the motion of the walker will be deflected. Such behavior is referred to as "billiard motion," and is shown below in Fig. 4.4.
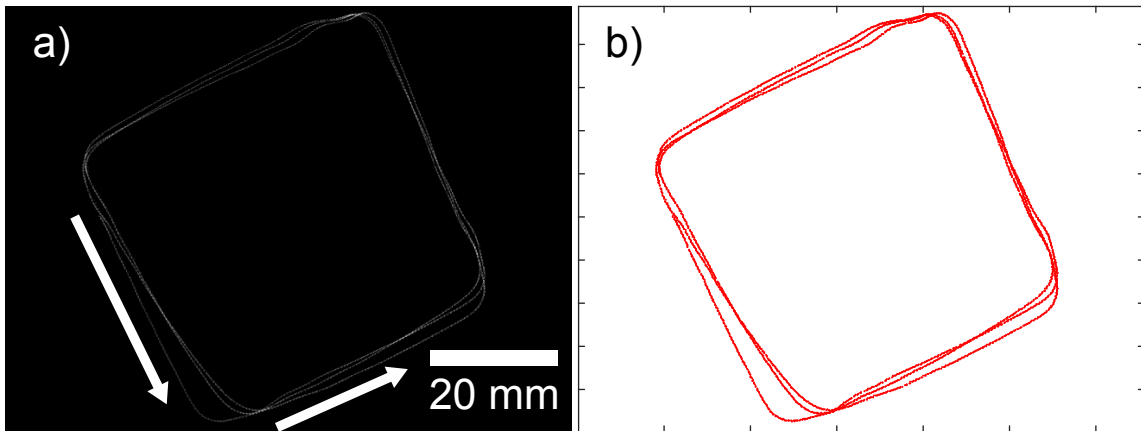
Figure 4.4: Shown is the recorded and analyzed motion of a free walker in a 76 mm × 76 mm square dish. (a) Compiled image of 3787 656 × 494 pixel frames recorded by the data acquisition camera. The image addition code is written to highlight the brightest pixels in each frame without increasing the background intensity. (b) Analyzed positions of the walker plotted as a trajectory. The horizontal ticks are spaced at 100 pixels, and the vertical ticks at 50 pixels.

In Fig. 4.4(a), a series of 3787 acquired images of a walker in motion were compiled into a single image by adding the pixel values in all of the frames. The Python script used to perform this compilation can be found in Appendix E.1, and is called "Compile.py." Fig. 4.4(b) gives the plotted trajectory of the walker The term "billiard motion" was first described in Ref. [51], but was not further investigated experimentally or theoretically until Ref. [97]. Pucci et al. shows that a walker does not undergo specular reflection at a submerged boundary. The consequences of this nonspecular reflection are the precessing orbits shown in Fig. 4.4. What is significant here is that a system that exhibits rectilinear motion, and therefore billiard motion, must be

sufficiently protected from air currents and is provided with uniform vibration.[104] In short, billiard motion indicates that our shaker system is actually quite decent.

4.2   Replicating Couder's Single and Double Slit Experiments

In an attempt to reproduce Couder's macroscopic interference results, a single slit dish was designed utilizing all the available dimensions and description at the time. The cell was made to have dimensions of $100\,\text{mm}\times100\,\text{mm}$, as this was close to the reported $70\,\text{mm}$ and $130\,\text{mm}$ square dishes reported in Ref. [57]. An allowance for a 0.35"-wide shallow region around the open area of the dish was made, as per the suggestion of Couder during a laboratory visit. This shallow region is necessary to dampen the Faraday guiding waves before hitting the meniscus of the dish. The materials used included polycarbonate, acrylic, and Delrin. Polycarbonate was used for the cell, and acrylic was used for a stem and supporting fins. These plastics were utilized for their strength and light weight, as there was concern that our speaker-based shaker would not be strong enough to drive a heavy dish. The acrylic parts were fused to the polycarbonate dish with methylene chloride (dichloromethane, Sigma Aldrich). Delrin was used for the stem guide because it performs well as a bearing surface. Detailed drawings of the components can be found in Appendix B.

To obtain a slit opening, two metal strips ($5.2\,\text{mm}\times30\,\text{mm}$) were glued to the bottom of the dish. The strips were $3\,\text{mm}$ thick, so that a fluid depth of $\approx4\,\text{mm}$ would leave $1\,\text{mm}$ of fluid covering the slit barriers. The single slit opening, L, was set at the reported $14.7\,\text{mm}$ length. For our experiment, we used the 20 cSt ($20\times10^{-3}\,\text{Pa\,s}$) viscosity oil, which has a Faraday wavelength given by the dispersion relation Eq. 4.1, λ_F, of $4.75\,\text{mm}$, when the dish is shaken at $80\,\text{Hz}$. Once a suitable walker was obtained,

usually by plucking at the surface until a number of walkers could be observed and then discarded, the walker was manually guided to the walker guiding system. The walker guiding system was a trap made of two wires that could be dropped into the launching side of the dish from above. The wires made slight deformations of the fluid that could temporarily trap a walker until it was nudged from behind, which resulted in repeatable starting positions for the walkers as they moved to the slits. The guide could be adjusted parallel to the slit structure, with the effect of having a series of starting positions that filled the slit opening with our best approximation of a "uniform distribution".[57] Walker trajectories were recorded by the camera, which was controlled by LabVIEW. Walkers of different sizes and velocities were launched at the slit 1519 times, resulting in 1092 trajectories that could be analyzed. The images were analyzed by undergraduate student Adam Lif's blob finding code. The trajectory files were analyzed by a series of Python scripts in order to make each analysis step more transparent. These Python scripts can be found in Appendix D.

The plotted trajectories, incidence angle distribution, and deflected angular distribution measured a distance $2L$ from the slit opening , are shown below in Fig. 4.5.
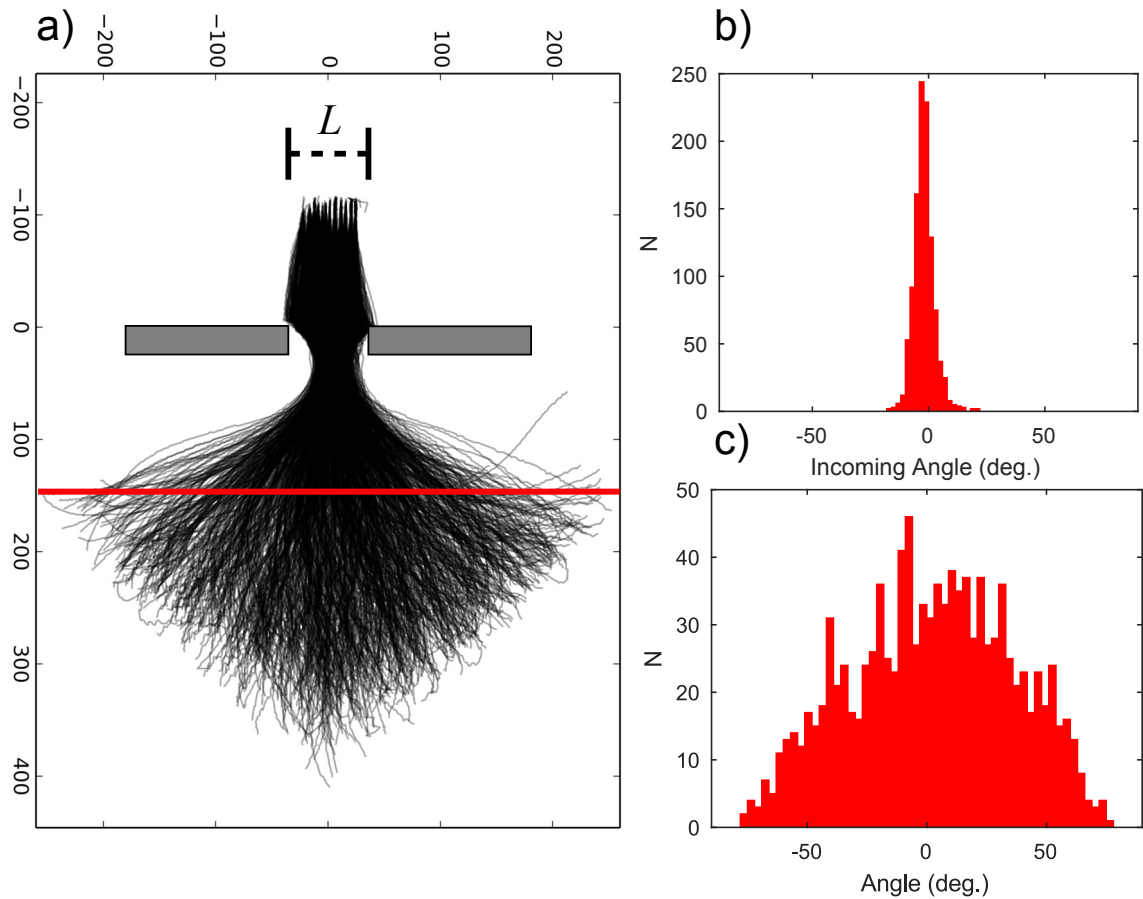
Figure 4.5: Shown are the results from the reproduction of the oil drop single slit analog. (a) Complete set of all walker trajectories that pass the detection plane. The detection plane, indicated by the solid red line, is spaced exactly 2 slit widths from the opening of the slit. The slit width, L, is 14.7 mm, as reported in Ref. [57]. Of the 1519 trajectories recorded, 1092 are plotted. (b) Histogram of the incidence angles of the 1092 walker trajectories approaching the submerged slit structure. An incidence angle of 0 is defined as a trajectory moving perpendicular to the slit plane. Incidence angles are measured as the average angle between the first 10 positions of each trajectory. (c) Histogram of the deflection angles of walker trajectories. The deflection angle is computed as the average angle between consecutive points for 5 points lying above the deflection plane and 5 points below.

In Ref. [57], the authors describe that trajectories used to build the diffraction pattern are selected so that their angles of incidence are nearly perpendicular with the slits. This indicates that post-selection could be necessary in order to obtain

the distributions they reported. So, in order to try and reproduce that experimental consideration, the 1092 trajectories were post-selected to have an incidence angle smaller than $\pm\,2\,\mathrm{deg}$. The resulting 358 trajectories, with their respective angular distributions, are shown as Fig. 4.6. The script used to define the selection of the incidence angle distribution and organize the data is given in Appendix D.4. The deflected angle distribution is plotted with the single slit amplitude function that was given as Eq. (1) of In Ref. [57]. The single slit amplitude, as a function of deflection angle, is

$$f(\alpha) = A \left| \frac{\sin\left(\pi L \sin\alpha / \lambda_F\right)}{\pi L \sin\alpha / \lambda_F} \right|. \tag{4.2}$$
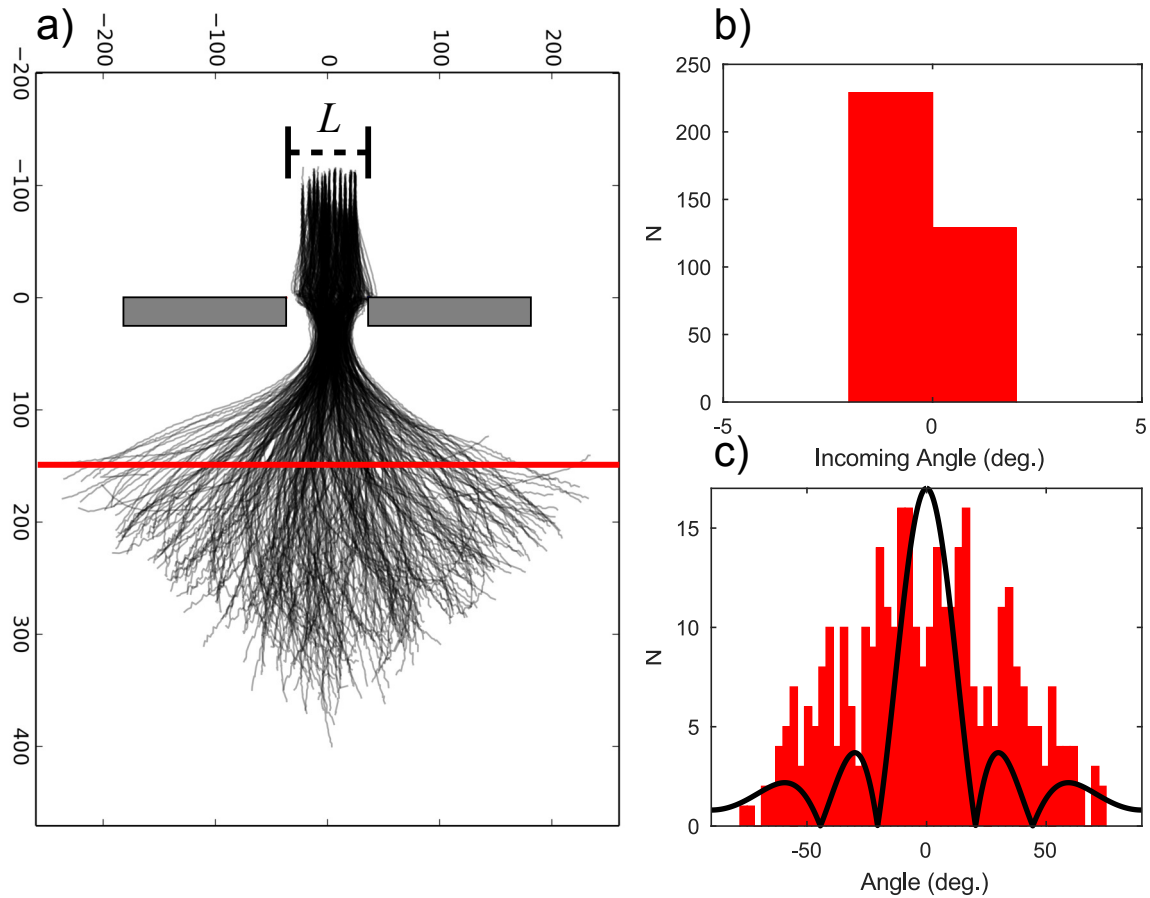
Figure 4.6: Shown above are the post-selected trajectories and angular distributions obtained for selecting only trajectories having an incidence angle smaller than $\pm\,2\,\mathrm{deg}$. (a) Plots of the 358 trajectories having an incidence angle within the $4\,\mathrm{deg}$ selection criteria. (b) Zoomed-in plot of the histogram of the selected angular distribution, binned with the same resolution as in Fig. 4.5, to confirm the incidence angle selection. (c) Histogram of the post-selected deflection angle distribution, measured 2 slit widths from the slit opening. Plotted in black is the single slit diffraction envelope reported in Ref. [57], with $L/\lambda_F = 2.86$.

Couder's double slit experiment was also performed. This dish was designed to be the largest size quoted ($130\,\mathrm{mm}\times130\,\mathrm{mm}$), and had the slit barrier machined along the diagonal of the dish. The width of the slit barrier was extrapolated from colloquium slides delivered at the Perimeter Institute[54], and taken to be $6.0\,\mathrm{mm}$. The single slit width, L, and slit separation, d, were taken to be the values quoted in Ref. [57],

which are 7.6 mm and 14.3 mm, respectively. The dish was given the same 0.35"-wide shallow barrier, with the addition of a flattened corner that was marked with the positions of the slits. These served as references for positioning the walker guides for consistent launches. The details of the double slit placing and reference markings are shown in Appendix B, Fig. B.1. The recorded trajectories and angular distributions are plotted below in Fig. 4.7.
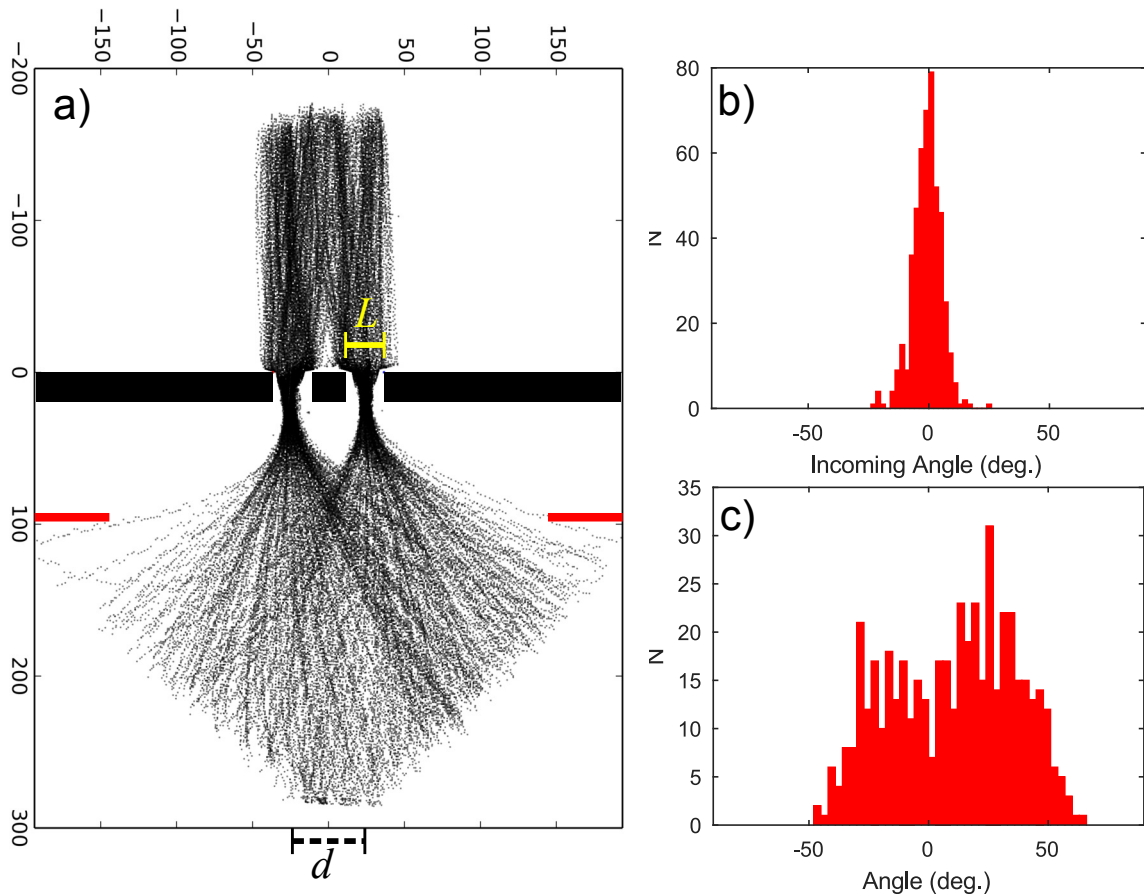
Figure 4.7: Shown above are the results from the reproduction of the oil drop double slit analog. (a) All 483 of 958 attempted walker trajectories that passed the detection plane for the oil drop double slit. The slit width, L , shown in black, is 7.6 mm, as reported in Ref. [57]. The slit separation, d, shown in yellow, is 14.3 mm. The detection plane is located a distance $2d$ from the slit openings, and is indicated by the red lines. The axes are scaled in pixels. (b) Histogram of the incidence angles of the 483 walker trajectories approaching the submerged slit structures. (c) Histogram of the deflection angle distribution, measured a length $2d$ from the slit opening.

Similar to the single slit analysis, the double slit trajectories are post-selected for an incidence angular spread of $\pm\,2\,\mathrm{deg}$. The 149 trajectories that could be analyzed that fit this criteria are plotted below in Fig. 4.8. In Fig. 4.8(c), the deflected angle distribution is plotted with the double slit amplitude (black line), and single slit envelope function (cyan line), that were used to fit the data in Ref. [57]. The double slit amplitude, $f(\alpha)$, is given as a function of deflection angle, $alpha$, as

$$f(\alpha) = A \left| \frac{\sin\left(\pi L \sin\alpha/\lambda_F\right)}{\pi L \sin\alpha/\lambda_F} \cos \pi d \sin\alpha/\lambda_F \right| \tag{4.3}$$
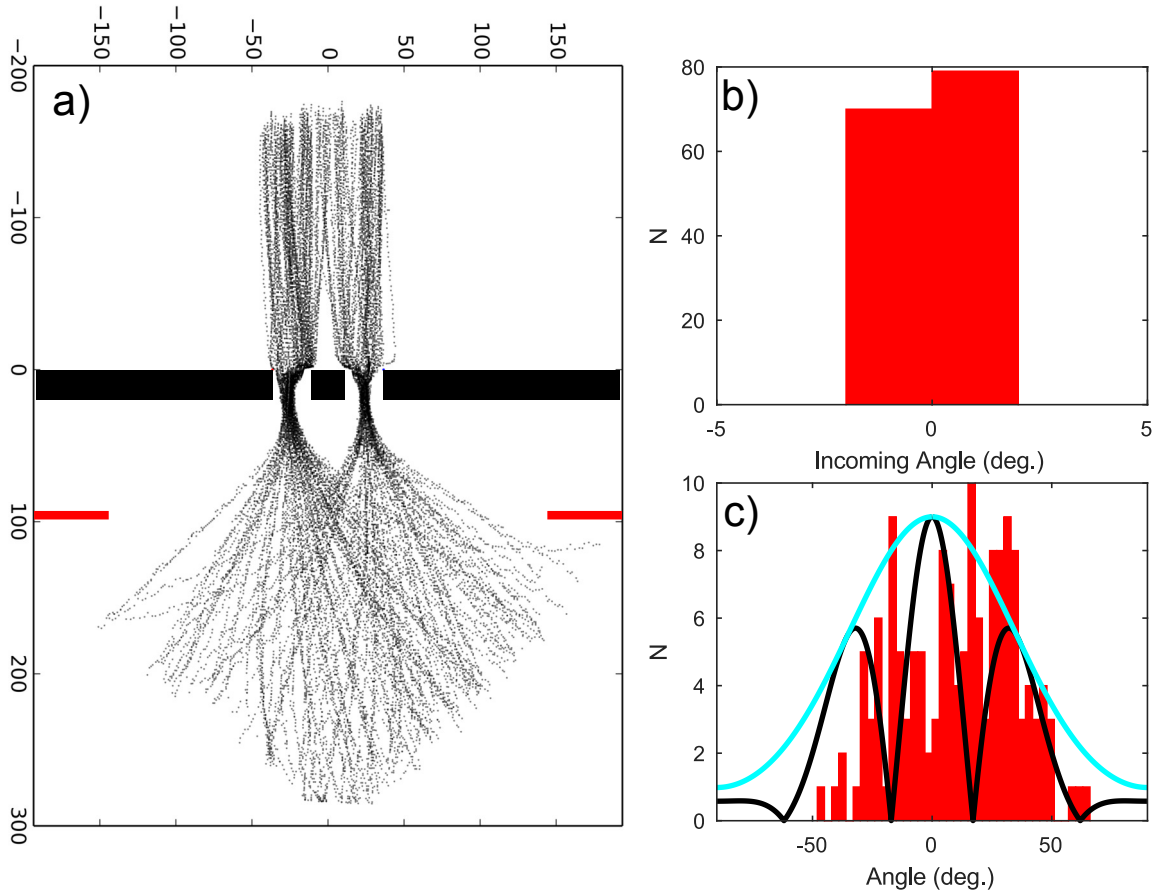
Figure 4.8: Shown above are the post-selected trajectories and angular distributions obtained for selecting only trajectories having an incidence angle smaller than $\pm\,2\,\deg$. (a) Plots of the 149 trajectories having an incidence angle within the $4\,\deg$ selection criteria. (b) Zoomed-in plot of the histogram of the selected angular distribution, binned with the same resolution as in Fig. 4.5(b) and Fig. 4.7(b), to confirm the incidence angle selection. (c) Histogram of the post-selected deflection angle distribution, measured a length $2d$ from the slit openings. Plotted in black is the double slit diffraction amplitude reported in Ref. [57], with $L/\lambda_F = 0.9$ and $d/\lambda_F = 1.7$. Plotted in cyan is the single slit envelope, again with $L/\lambda_F = 0.9$.

The results obtained in our reproduction clearly do not match those originally reported by Couder et al. in Ref. [57]. No clear diffraction peaks or cusps are visible in our data, with or without a trajectory post-selection. This result agrees with the data reported by Andersen et al. in Ref. [103]. Their conclusions following their reproduction of the single and double slit are that the data selected by Couder

et al. were not statistically significant to be distinguished from a fitted Gaussian. The analysis offered by Pucci et al. in Ref. [104] suggests another possibility, that the shaking amplitude has a significant effect on the kinds of trajectories that can appear in the distribution. For shaking that is less than the Faraday threshold, trajectories launched from the same initial positions are repeatable, an observation that is completely contrary to Couder et al.'s claims that the trajectories are chaotic. For shaking amplitudes that are closer to the Faraday threshold, walkers launched from the same initial position become less repeatable, and peaks form in the deflected angular distribution. However, those peaks are found to be consistent with the droplet interacting with the edges of the submerged slit structures, and make an angle consistent with the non-specular reflection observed at submerged barriers.[97,104]

An omission in the otherwise thorough analysis of Pucci et al. is that the incident angles of the analyzed trajectories are not reported. The incident walker position was controlled by a v-shaped guide submerged in the fluid; however, our data show that the use of a guide does not necessarily fix the incident trajectory angles. For a complete reproduction or modification of the original experiment, all of the experimental variables Pucci et al. considered, which include drop size, isolation from external air currents, fine tuning of the shaking amplitude, and initial position, must be considered with the distribution of incoming angles. As the mechanism that lead to the data reported in Ref. [57] is likely to be an edge interaction, it has been suggested during a conference meeting of oil droplet researchers that an alternative experiment should employ an external slit potential. Such an experiment performed by Perrard et al. used an external magnetic field to apply a force to ferrofluid-filled walkers to demonstrate orbital quantization in an external potential.[101] Ref. [104] concludes that an analog to Kapitza-Dirac diffraction will be investigated in the future.

4.3 Walkers Confined to a Waveguide

A less restrictive oil droplet analog was studied by guided high school researchers. Three high school seniors, Karissa Goosic, Greg Hubbard, and Taylor Morgan, were shown how to operate the oil droplet system, and performed experiments with walkers confined to linear channels, similar to experiments reported in Ref. [171]. What we observed early in the stages of developing the oil drop reproduction system was that a walker confined to such a channel would experience nearly 1-D motion, and the velocity would vary with walker position, leading to peaks and valleys in position distributions taken along the channel length. This observation was first reported by Couder during a colloquium at the Perimeter Institute,[54] and further studied by Filoux et al.[171]

The students made linear channels by magnetically attaching 3.1 mm thick iron strips to the bottom of the open 74 mm×74 mm dish. The iron strips formed the boundaries of the channel. The width of the channels varied between 10 mm and 12 mm, while the length of the channels was fixed by a set of calipers. The dish was filled with 50 cSt oil, which has a Faraday wavelength, λ_F, of 6.95 mm when driven at 50 Hz.[57]

One of the practical experimental tasks first accomplished by the students was the design and construction of an improved camera mount. Their camera mount, and experimental set-up, is shown in Fig. 4.9.
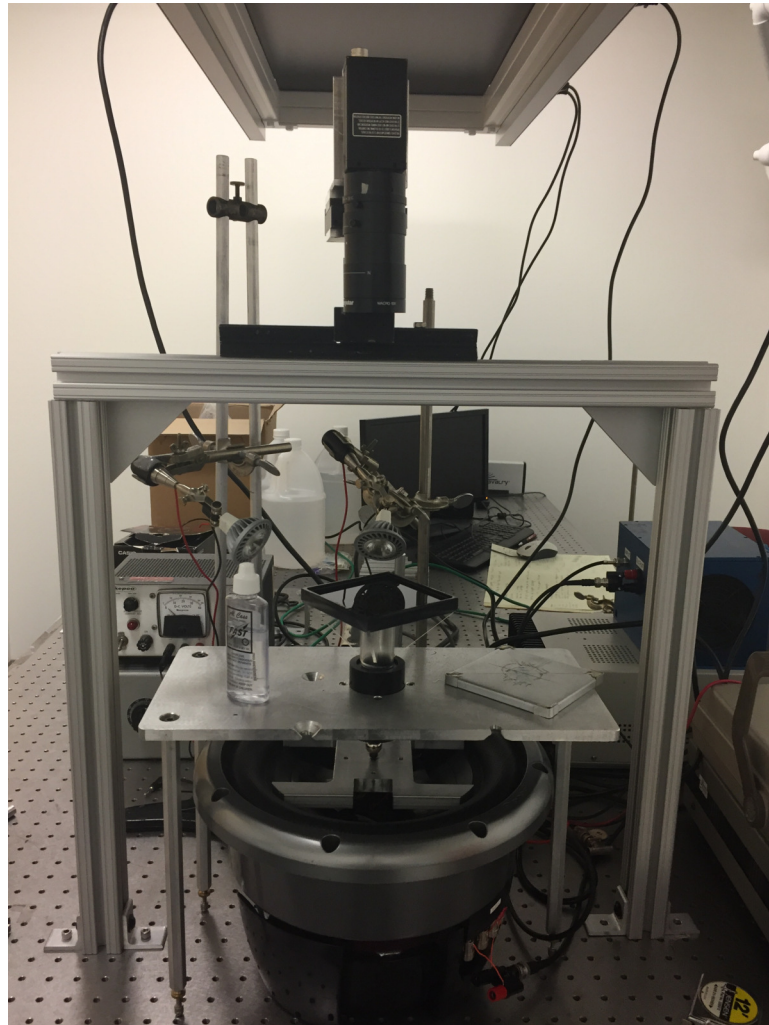
Figure 4.9: Shown above is a picture of the experimental apparatus adapted and used by visiting high school Summer researchers. The mechanical apparatus (shaker and controlling electronics, leveling table, and dish) were set up for them, while they improved on the camera mounting.

One of the next tasks the students were requested to perform was to see the effect of the shaking amplitude on the distribution of walker positions. In order to accomplish this, the students acquired trajectories of bound walkers that contained nearly $10\times$ as many images as needed for an oil drop slit trajectory. This increase in image volume caused the old droplet finding code to crash frequently, so a new script was written in Python to analyze the droplet positions. The new drop finding script

is given in Appendix E.2. Shown in Fig. 4.10 are the resulting position histograms for the x-coordinate for walkers confined in a $27.5\,\mathrm{mm}\times10\,\mathrm{mm}$ channel, as the driving voltage (and thus shaking amplitude) is increased.
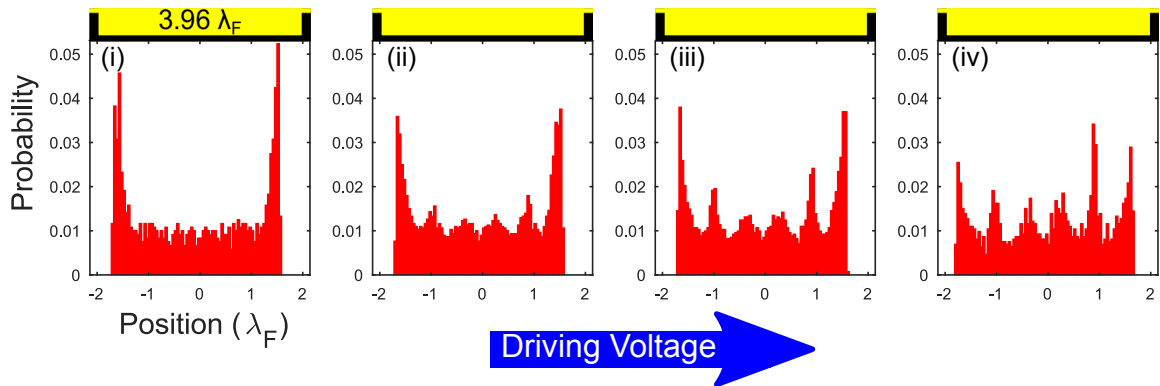
Figure 4.10: Shown above are a series of position histograms, normalized to probability, obtained for a walker confined to nearly 1-D motion in a $27.5\,\mathrm{mm}\times10\,\mathrm{mm}$ cavity. The fluid used has a viscosity of 50 cSt, so the Faraday wavelength λ_F is $6.95\,\mathrm{mm}$ as before. The data are plotted in units of λ_F. Yellow rectangles located above the histograms indicate the cavity length, fluid depth, and location of the cavity walls (to scale). From left to right, the peak-to-peak driving voltage provided by the function generator was increased from $5.8\,\mathrm{V}$ to $6.2\,\mathrm{V}$ in steps of $0.1\,\mathrm{V}$.

Another task was to determine the relationship between the length of the channel and the number of peaks that could be obtained in droplet position distributions taken along the channel length. Shown below in Fig. 4.11 are the position histograms obtained by the students as channel length was varied from $16.5\,\mathrm{mm}$ $(2.37\lambda_F)$ to $29.0\,\mathrm{mm}$ $(4.17\lambda_F)$. The shaking amplitude was adjusted throughout so that peaks would be visible in the position histograms.
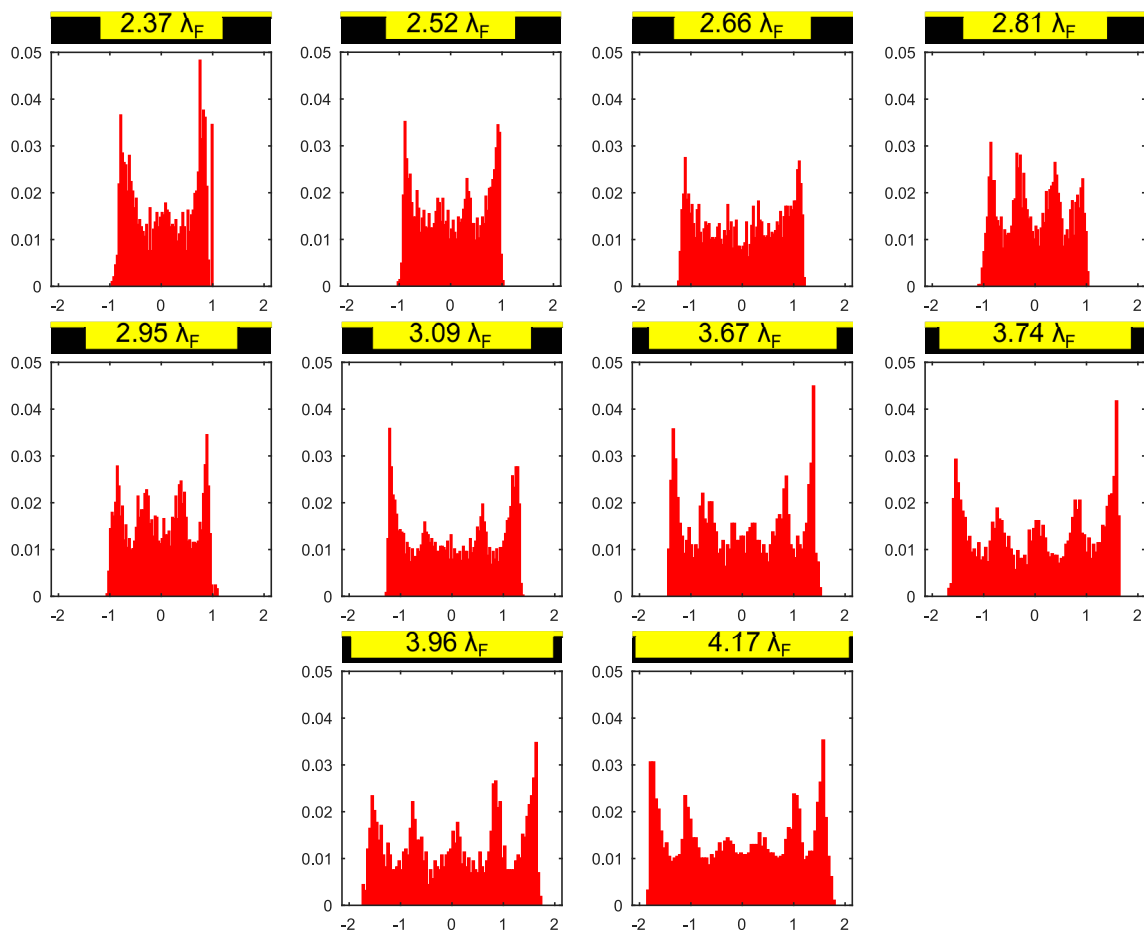
Figure 4.11: Shown above are a series of position histograms, normalized to probability, obtained for a walker confined to nearly 1-D motion in a cavity. The cavity lengths, depths, and boundaries, which are as in Fig. 4.10 represented to scale by the yellow rectangles above each histogram, are varied from $2.37\lambda_F$ (16.5 mm) to $4.17\lambda_F$ (29.0 mm), where λ_F is the fluid's Faraday wavelength of 6.95 mm. The horizontal axes are again plotted in units of λ_F.

As the students took data, they observed that the motion of walkers in the cavity changed depending on the position and direction of motion. It appeared that a walker trajectory was effected more as it moved away from a channel boundary than when it moved toward a boundary. They then asked, is this an actual effect, or a trick of the eyes? In order to answer their question, a Python script was provided for them to determine if the walker was moving to the left or the right of the channel. The script is

included in Appendix E.3 Fig. 4.12 shows the resulting histograms for channel lengths of 26.0 mm ($3.74\lambda_F$) (a) and 29.0 mm ($4.17\lambda_F$) (b) separated into distributions for motion toward the right (i), motion toward the left (ii), and the distribution sum (iii).
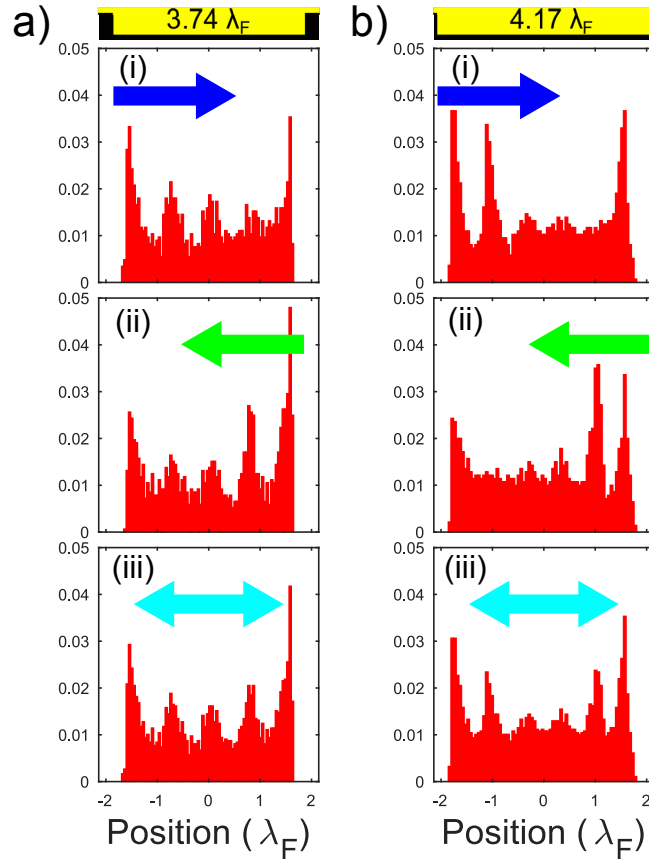
Figure 4.12: Shown above are the position histograms for walkers confined to cavities with widths of (a) $3.74\lambda_F$ (26.0 mm) and (b) $4.17\lambda_F$ (29.0 mm), separated into distributions for motion toward the right boundary of the cavity (i), motion toward the left boundary (ii), and the combined left-right distributions (iii). The distribution asymmetry indicates a stronger interaction while the walker is moving away from a cavity boundary than when it approaches a boundary. This test was instigated by observations made by the high school students obtaining the data.

One of the last experimental tasks that the students were able to perform was to image the Faraday waves in a cavity so they could be compared to the position probability distribution. First, they were able to obtain the walker images that were produced earlier in Fig. 4.3, utilizing the method described in Ref. [170]. Then, they

chose a series of channel lengths, and acquired ≈ 30 frames of Faraday wave images for each length. Those images were processed in a summing script called CompileBright.py that highlighted the features that changed the most (that is, the antinodes of the Faraday waves) while diminishing the contribution from static features. This image analysis script is given in Appendix E.4. The resulting compiled images are plotted with the channel position histograms in Fig. 4.13
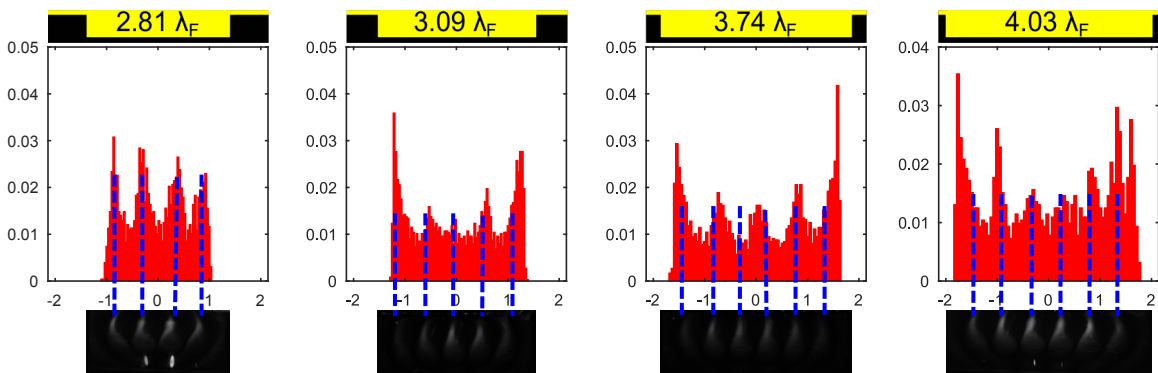
Figure 4.13: Shown above are position histograms for walkers confined to cavities of widths $2.81\lambda_F$ (19.5 mm), $3.09\lambda_F$ (21.5 mm), $3.74\lambda_F$ (26.0 mm), and $4.03\lambda_F$ (28.0 mm), which are compared to images of walker-free Faraday waves. The images highlighting the amplitude of the Faraday waves were made by compiling $\approx 1.3\,\text{s}$ (≈ 30 frames) of acquired images of the cavities excited to the Faraday instability. The positions of the histogram peaks, that is, where the walker velocities are the slowest, mostly align with the position of the Faraday wave extrema, where the surface gradient of the fluid surface changes at the slowest rate.

The data taken by the students leads to a number of observations. The first is that indeed, the shaking amplitude has an effect on the 1-D probability distribution of a confined walker. As the shaking amplitude approaches the Faraday threshold, the walker trajectories are more affected by the channel boundaries, which is evidenced by the increase in peak contrast. The resulting probability distribution does not bear a strong resemblance to the quantum mechanical "particle in a box." A surprising omission in the study performed by Filoux et al. is that the 1-D walker probability distributions are not plotted.[171] The channels they used are also long, so the walkers

do not appear to have wall interactions. As the channel length is increased, the number of Faraday waves supported by the cavity increases, and so the number of peaks in a subsequent probability distribution will also increase. Even and odd numbers of peaks are possible, and the location of distribution peaks tend to line up with the Faraday excitation of the cavity, with exception to the data observed for the channel of length $3.74\lambda_F$ (26.0 mm). Lastly, the motion of walkers depends on where the walker is in relation to the boundary walls. This is complementary to the study of Pucci et al. that measured non-specular reflection from submerged barriers.[97]

Oil drop walker experiments are rich areas to study particle and wave dynamics. They can be developed as analog systems that can be used both for fundamental research and in pedagogical settings. Although the results of the single and double slit analogs do not hold up under scrutiny, it appears that other successful analogs can be developed. Such analogs provide research opportunities accessible to high school students and undergraduate researchers, and thus they are useful for teaching.

Chapter 5

Degenerate electron sources and diffraction in time

The field of the quantum optics of light essentially began with the radio telescopic measurements of Hanbury Brown and Twiss.[64,65] Robert Hanbury Brown, an expert in radio telescopes, developed a telescope based on the intensity interferometer, which was inherently less sensitive to atmospheric fluctuations than the optical Michelson interferometers of the day. Essentially, the intensities of light, incoherently emitted from opposite sides of a star, will give spatial correlations when measured with a pair of radio detectors. In order to measure the angular widths of distant stars emitting in optical frequencies, the intensity interferometer would have to be modified to use photomultiplier tubes as detectors. While the function of the radio wave intensity interferometer was accepted and understood at the time, there was considerable doubt when photons were to be considered.[172] Hanbury Brown and Twiss showed, in a table-top experiment using a filtered mercury lamp, that the detection of photons in two coherent beams of light was correlated in time.[59,66] That is, photons, which are formally treated by Bose-Einstein spin statistics, can bunch, or occupy similar quantum states. Experiments showing such correlations are typically referred to as Hanbury Brown-Twiss (HBT) measurements. This experiment was the first formal demonstration that the intensity interferometer would indeed work in the photon counting regime, and motivated the expansion of quantum optics.

The analogous experiments for particles obeying Fermi-Dirac statistics typically demonstrate the opposite effect. The detection of coherent beams of fermions is generally expected to be anticorrelated in time, or in other words, fermions demonstrate antibunching. This is due to the Pauli exclusion principle (PEP). Formally, the PEP is expressed as the condition that the overall wave function describing two identical spin-1/2 particles must be antisymmetric under particle exchange. The first experiments demonstrating antibunching effects for electrons were performed in solid-state systems,[61,62] and then finally for free electrons in the Hasselbach group.[70] Realizing the experiment for free electrons was difficult, due to the low degeneracy of electrons in the source, which was reported to be on the order of 10^{-4} electrons in the coherence volume. Here, the source degeneracy is defined as the number of electrons produced from the source within the coherence time, or as will later be shown as the fraction of electrons produced within a phase space volume that are also within the coherence volume. One of the problems was that this low degeneracy resulted in a correspondingly small experimental signature, namely, a change of $\sim 10^{-4}$ was reported in the detected coincidence signal when comparing coherent to incoherent electron detection. There is further controversy as the experimental apparatus could not in principle distinguish between the effects of degeneracy pressure and Coulomb pressure in the coincidence measurements.[70,71,109] As degeneracy pressure is polarization-dependent, while Coulomb pressure is not, a femtosecond, nm-scale, spin-polarized source could resolve the controversy of the measurements reported by Hasselbach. One possibility for falsifying or verifying Hasselbach's result is to implement a free electron source that incorporates a higher quantum degeneracy, that is, a source that produces electrons with consistent quantum numbers in the smallest phase space volume. A femtosecond, nanometer-scale, spin-polarized electron source would accomplish such a goal by increasing the quantum degeneracy to be on the order

of 1; however, such sources combining all three attributes are not currently available. Such a source is desirable for tests of quantum degeneracy and for implementation in ultrafast electron microscopy.[12,24,25,173]

The current state-of-the-art spin-polarized electron sources are planar photo-cathodes. The best combined spatial and temporal resolution in ultrafast electron microscopes has been provided by nanotip sources triggered by femtosecond lasers, as the spatial resolution of photocathodes with planar geometry is limited by the laser focus size.[174,175] Direct measurements of the electron pulse duration in ultrafast electron microscopy have shown that the electron and the illuminating laser pulse durations are of the same order.[17] Implementing a spin-polarized source in an ultrafast electron microscope to study magnetic nanostructures on the fs-scale is currently underway in a globally collaborative research effort[176], while a CW source that can also operate at ps-scale resolution has been developed in Japan with the goal of producing quantum degenerate electron beams.[177–179] In particular, their planar photocathode installed in a $200\,\mathrm{keV}$ transmission electron microscope demonstrated a spin polarization of $82\,\%$, transverse coherence length of $170\,\mathrm{nm}$, and a degeneracy of 4×10^{-6} The authors claim such an arrangement can enhance electron antibunching.[178] In the Batelaan, Gay, and Uiterwaal labs at the University of Nebraska-Lincoln, we are currently installing such a fast spin-polarized source in an electron HBT experiment.

In this chapter, the degeneracy of a pulsed electron source is defined and quantified. The system is described by a single two-particle wavefunction that is obtained by first using the path integral formalism to propagate two single-particle probability amplitudes from the source toward two identical detection points. The general apparatus for measuring fermion anticorrelations in a HBT experiment is described. Finally, a candidate for a fast, localized, spin-polarized source of electrons is obtained from a sharp p-GaAs bulk [110] crystal shard illuminated with femtosecond laser

light. The size of the emission site is approximately $1\,\mu m$ in scale, and the electron polarization achieved so far is $13\,\%$. The electron emission was studied using methods similar to those developed to characterize pulsed emission from metallic nanotips, whose spatial resolution has been shown to be determined by the size of the emitter and not by the laser focus used. It is shown that through chemical etching, GaAs shards can be sharpened into sub-micron structures, with the potential to be further shaped by improved etching techniques or other nanofabrication schemes. Whether the sharpened tips retain the spin polarization obtained from the shard samples remains to be seen, but with these refinements, it appears that a femtosecond, nanometer scale, spin-polarized electron source is now available.

5.1   Description of a degenerate electron source

Obtaining a degenerate beam is a necessary step to realize HBT-type correlations for free electrons in the beam. The derivation of estimating the degeneracy of a pulsed, tip electron source, was developed in detail in Refs. [180] and [25], but will be repeated here for clarification and consistency. The degeneracy, δ, is defined as the number of electrons within the coherence volume of the source.[181,182] The coherence volume, V_c, is approximated as cylindrical, with a radius defined by the beam's transverse coherence length, l_t, and cylindrical length as the longitudinal coherence length, l_c. The longitudinal coherence length is related to the coherence time of the electron source, t_c, which is determined from the Heisenberg uncertainty relation between energy and time as $t_c \approx \Delta t \geq \hbar/\Delta E$. Electrons traveling with a velocity v will then have a longitudinal coherence length $l_c = vt_c \approx v\hbar/\Delta E$. The transverse coherence length, l_t, is determined from a momentum selection of detected electrons. This is accomplished by confining the beam to an acceptance angle of α by means of an aperture of size

Δx. The Heisenberg uncertainty relation between position and momentum then gives $l_t \approx \Delta x \geq \hbar/\Delta p \approx \hbar/(\alpha p)$. Substituting the de Broglie wavelength $\lambda = h/p$ gives the transverse coherence length as $l_t \approx \lambda/(2\pi\alpha)$. The coherence volume of the source is then

$$V_c = \left(\pi l_t{}^2\right) l_c \ \approx \ \left[\pi \left(\frac{\lambda}{2\pi\alpha}\right)^2\right] \left[\frac{v\hbar}{\Delta E}\right] = \frac{\lambda^2 v\hbar}{4\pi\alpha^2 \Delta E} \ = \ \frac{h^3\sqrt{2E}}{16\pi^2\alpha^2 m^{3/2} E\Delta E}. \quad (5.1)$$

A pulsed electron source will produce a number of electrons in a cylindrical volume determined by the source size and the electron pulse duration. The degeneracy of the electron source is then the product of the coherence volume with the number of electrons produced per unit volume from the source. The source volume is defined by the cross-sectional area of the source surface, which has a radius $r_{\text{tip}} = d_{\text{tip}}/2$. The longitudinal length l of the source volume is determined from the electron packet's temporal width, Δt_p, as $l = v\Delta t_p$. The degeneracy is then approximated as

$$\delta \approx \frac{N}{\pi r_{\text{tip}}{}^2 v\Delta t_p} V_c \ = \ \frac{N}{\pi r_{\text{tip}}{}^2 \Delta t_p} A_c t_c, \quad (5.2)$$

where N is the number of electrons per pulse, and $l_c = vt_c$. The current density, j, of the pulsed electron source is defined as $j \equiv Nq/(\pi r_{\text{tip}}{}^2)$, where q is the charge of a single electron. The current density j can be substituted back into Eq. 5.2 to obtain

$$\delta \approx \left(\frac{j}{q}\right) A_c t_c. \quad (5.3)$$

The degeneracy in the form of Eq. 5.3 was derived in Ref. [182] and Ref. [181] considering the brightness of a DC electron source, but it is here interpreted to also describe a pulsed source. In terms of the experimental parameters that describe our

apparatus, the degeneracy is estimated as

$$\delta \approx \frac{N}{\pi r_{\text{tip}}{}^2 \Delta t_p} \frac{\lambda^2 v \hbar}{4\pi \alpha^2 \Delta E} = \frac{N h^3 L^2}{\pi^3 m d^2 d_{\text{tip}}{}^2 E \Delta E \Delta t_p}, \tag{5.4}$$

where the substitutions $E = mv^2/2$, $\lambda^2 = h^2/(2mE)$, and the divergence angle $\alpha \approx d/(2L)$ were made. An illustration of a coherent source obtained in this fashion is given in Fig. 5.1(a), and the coherence volume is shown in Fig. 5.1(b).
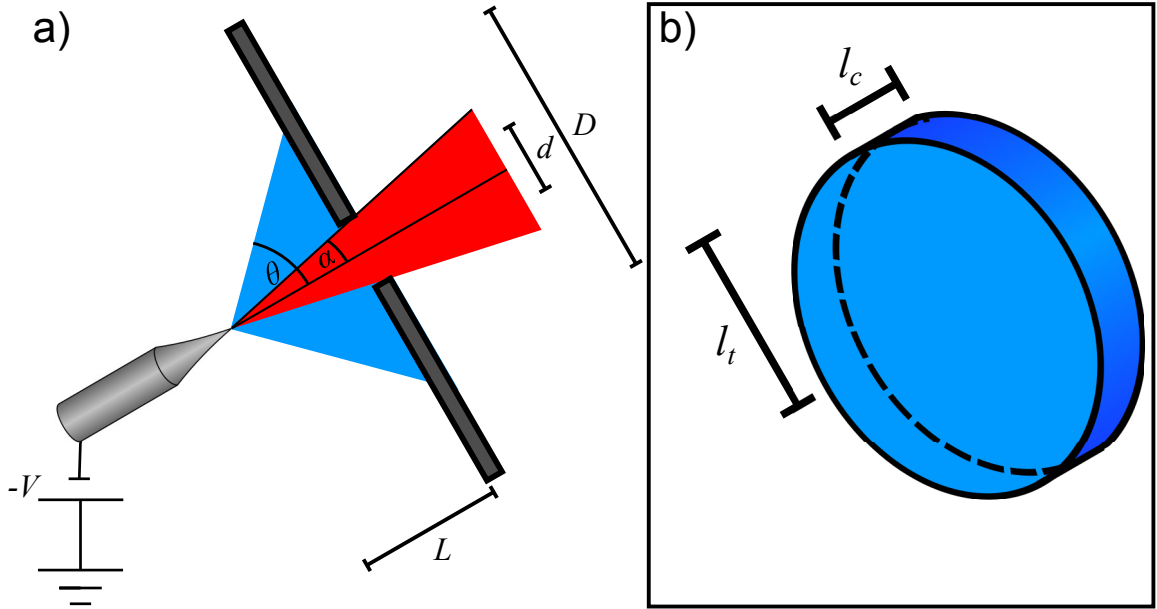
Figure 5.1: A schematic of a degenerate electron source. In (a), a field emission tip is biased at a voltage of $-V$, which determines the central value of the electron energy, E. The emission diverges from the source with an angle θ, but an aperture located a distance L from the source with width d constrains the divergence angle to an angle $alpha$. Electrons propagate toward a detector with effective width D. In (b), the transverse (l_t) and longitudinal (l_c) coherence lengths are illustrated. For an initial energy of $E =$30 eV and energy uncertainty of $\Delta E =$0.8 eV as shown in Table 5.1, the ratio $l_c/l_t \approx 2/100$.

The degeneracy is calculated using Eq. 5.4 and parameters typical for our apparatus. The laser pulse duration, Δt_p, of the Ti:Sapph oscillator, is 100 fs. Etched tips have a typical diameter of $d_{\text{tip}} = 50$ nm. The standard DC voltage applied to tip samples

Table 5.1: Summary of experimental values used to estimate the source degeneracy, and the resulting optimum detection rates.

Parameter	Description	Value
N	Electrons/pulse	10
L	Source to aperture distance	1 cm
d	Aperture diameter	5 μm
d_{tip}	Source diameter	50 nm
E	Electron energy	30 eV
ΔE	Electron energy width	0.8 eV
Δt_p	Pulse temporal width	100 fs
δ	Degeneracy	≈ 2.7
θ	Source divergence angle	45°
D	Beam diameter at aperture	2 cm
N_{det}	Detected electrons/pulse	10^{-6}

in our experiments ranges between $-100\,\mathrm{V}$ and $-200\,\mathrm{V}$, but a bias of $-30\,\mathrm{V}$ can be considered, giving electrons an energy distribution centered at $E = 30\,\mathrm{eV}$, with a measured root mean square (RMS) energy uncertainty of $\Delta E_{\mathrm{RMS}} = 0.8\,\mathrm{eV}$[1] for a source emitting less than one electron per pulse; however, tip sources are capable of producing an average of $N = 10$ electrons per pulse.[180,183,184] A pinhole having a diameter of $d = 5\,\mathrm{\mu m}$ can be positioned a distance $L = 1\,\mathrm{cm}$ from the source. This combination of experimental parameters results in a degeneracy of $\delta \approx 1$. A fully quantum mechanical description of the degeneracy, with similar parameters, resulted in a degeneracy of $\delta \approx 0.2$, where considerations were made concerning the effects of Coulomb repulsion between pairs of electrons.[24] An estimate of the signal passing through the selection aperture gives a count rate of $N_{aperture} \approx Nd^2/D^2 \approx 10^{-6}$ electrons per pulse, or with respect to the oscillator repetition rate, 100 electrons per second. The experimental values and resulting detection rates are summarized in Table 5.1.

---

[1] It is noted that there is some disagreement between the reported value of the width of our electron pulses.

The electron pulse duration and temporal coherence will now be discussed, because the degeneracy depends on the duration of the electron pulse, and modeling two-electron pulses will depend on the temporal coherence. A result published by Krüger et al. showed interference effects in the kinetic energy spectra of electrons produced by illuminating a tip with a carrier envelope phase (CEP) controlled laser.[22,23] The short laser pulse duration of ∼6 fs with CEP control could contain one or two oscillations of the laser field. When there were two field oscillations, the electron energy spectra showed a spacing consistent with the electron source being gated in time by two temporal slits. They argued that the measured energy peak spacing of $\Delta E =$1.56 eV corresponded to a temporal slit spacing Δt determined by $\Delta t \approx h/\Delta E =$2.67 fs, where h is Planck's constant. This value of Δt corresponded well to the oscillation period of the laser, indicating that the electron temporal coherence must exceed the laser field oscillation period. A similar electron energy spacing was also observed in above-threshold photoemission, but was attributed to an excess of energy imparted in the multiphoton emission process.[82] The temporal single slit width was determined to be ≈450 as. Considering our measured single-electron pulse energy spread of $\Delta E =$0.8 eV, it is intriguing that the estimated temporal coherence of our source then has a minimum value of $\Delta t \geq \hbar/(2\Delta E) = 412$ as. These time scales are all relevant in determining the behavior of two-electron systems as they evolve in time. In the following, a theoretical formalism will be given for diffraction in time, where the temporal coherence will play an important role. This formalism will then be applied to a degenerate electron source to illustrate a HBT-type experiment for free electrons produced by a completely polarized pulsed electron source.

5.2 Path integral propagation in time for a Gaussian energy distribution

In order to describe our quantum degenerate pulsed electron source, it is necessary to consider the evolution of the source's temporal distribution, as experiments to measure correlations between electrons at the source will depend on coincidence measurements at the detectors in time. Discussion of the time evolution of temporally gated matter waves is referred to as "diffraction in time," as first coined by Moshinsky.[185] The original problem considered gating a matter wave by a time-dependent shutter that could be instantaneously opened, resulting in a temporal analog to diffraction from a sharp edge. The effect of temporal diffraction from single and double slits was experimentally realized by Szriftgiser, by temporally gating cold Cs atoms bouncing on a mirrored surface with a pulsed laser.[186] The data were modeled using the path integral formalism, where the propagator for particles in a gravitational potential was integrated over the appropriate temporal slit time.[187] The reason for why matter waves will experience diffraction in time is that matter waves have a nonlinear dispersion relation, as is discussed in Ref. [187] and earlier. The effect of this nonlinear dispersion relation was shown in Chapter 3.11 in that even spatial diffraction experiments, which are typically incorrectly described by time-independent equations, can exhibit time-dependent effects. As our electron source is gated by a laser pulse, the approach to compute how the resulting electron pulses propagate in time is then considered in a similar fashion, where the temporal coherence of the electron pulses acts as the duration of the temporal slits. The effect of temporally gating a matter wave source results in an unavoidable energy spread that follows the Heisenberg uncertainty relation for energy and time.[188] Therefore, the duration of the temporal slits of our gated source will be deduced from the typical measured energy uncertainty. In the

following, both Gaussian and Heaviside slits will be considered.

One of the cornerstones of the discussion of the spatial diffraction of matter waves is the evolution of a Gaussian wavepacket propagating in space and time. A spatial wavepacket, having an initially Gaussian momentum distribution, will broaden in spatial width as time evolves. An analogy can be made for a temporal wavepacket, with an initially Gaussian energy distribution. That is, a temporal wavepacket, having an initially Gaussian energy distribution, will broaden in temporal width as time evolves. Consider a Gaussian probability amplitude, $\phi(E)$, centered at an energy E_0, and with an energy width corresponding to our measured RMS energy uncertainty of $\Delta E = 0.8\,\text{eV}$. The normalized probability amplitude for electrons at the source position is written

$$\phi(E) = \frac{1}{\sqrt{\sqrt{\pi}\sigma_E}} \exp\left[-\frac{(E - E_0)^2}{2\sigma_E{}^2}\right], \tag{5.5}$$

where σ_E is the Gaussian width that will result in the RMS energy uncertainty defined by $(\Delta E)^2 = \langle E^2 \rangle - \langle E \rangle^2$. Here, the brackets denote the operator average value defined by

$$\langle \hat{A} \rangle = \int_{-\infty}^{\infty} \phi^* \hat{A} \phi \, \text{d}a. \tag{5.6}$$

With the above definitions, $\sigma_E = \sqrt{2}\Delta E$.

The energy distribution of Eq. 5.5 can be cast into the time domain via a Fourier transform as

$$\psi(t) = \frac{1}{\sqrt{2\pi\hbar}} \int_{-\infty}^{\infty} \phi(E) \exp{-\frac{iEt}{\hbar}} \, \text{d}E \quad = \sqrt{\frac{\sigma_E}{\hbar\sqrt{\pi}}} \exp\left(-\frac{t^2\sigma_E{}^2}{2\hbar^2}\right) \exp\left(-\frac{iE_0 t}{\hbar}\right). \tag{5.7}$$

The result of Eq. 5.7 is a temporal wavepacket, initially traveling "forward" in time, with an initial temporal spread $\Delta t = \hbar/(2\Delta E)$ given by the Heisenberg uncertainty

relation for energy and time. This temporal wavepacket can be propagated from a source position point (taken at $x = 0$) to a detection position point located a distance $x' = L$ by the application of the Feynman path integral kernel. With fully coherent *spatial* propagation, integration is performed over all source *positions* to determine the spatial distribution at a detector for a single propagation time. In analogy, to describe fully coherent *temporal* propagation, integration is performed over all source *times* to determine the temporal distribution at a detector for a single propagation position. The resulting probability amplitude at the detector position, L', as a function of the detection time, t', is then

$$\psi(t') = \int_{-\infty}^{\infty} K(x' = L, t'; x = 0, t)\psi(t)\, \mathrm{d}t \quad = \int_{-\infty}^{\infty} \sqrt{\frac{m}{2\pi i\hbar\,(t'-t)}} \exp\left[\frac{imL^2}{2\hbar\,(t'-t)}\right]\psi(t)\, \mathrm{d}t. \tag{5.8}$$

The temporal probability distribution, $\propto \psi(t')^*\psi(t')$, has a width that can be estimated by direct analogy to a Gaussian *spatial* wave packet spreading in space. The probability distribution of a spatial wavepacket, having an initial width of $\sigma_{x,t=0}$, will spread as a function of time as

$$\sigma_{x',t'} = \sqrt{\frac{\sigma_{x,t=0}^4 + \left(\frac{\hbar t'}{m}\right)^2}{\sigma_{x,t=0}^2}}. \tag{5.9}$$

The evolution of the temporal width, which is initially $\sigma_{t,x=0}$, can then be found by the substitution of $\sigma_{t'} = \sigma_{x',t'}/v_0$ and $\sigma_t = \sigma_{x,t=0}/v_0$ into Eq. 5.9, where v_0 is the group velocity of the centroid of the temporal wavepacket. Agreement is shown for the case where $L = 20\,\mathrm{cm}$, $E_0 = 30\,\mathrm{eV}$, and $\Delta E = 0.8\,\mathrm{eV}$. The temporal wavepacket, which initially had a width $\sigma_t = 0.58\,\mathrm{fs}$, arrives at the classical time of flight predicted by $t_{flight} = \sqrt{2E_0/(mL^2)} = 61.6\,\mathrm{ns}$, with a width $\sigma_{t'} = 1.16\,\mathrm{ns}$. Plots of the single-particle source amplitude and probability distribution are shown with the screen amplitude and probability distribution in Fig. 5.2. In Fig. 5.2(d), the path integral result (black) is

plotted with the Gaussian estimate (green) to show agreement with the evolution of the distribution temporal width $\sigma_{t'}$. The Fortran code used to generate the single particle distributions, and later the two-particle distributions, can be found in Appendix F.1.
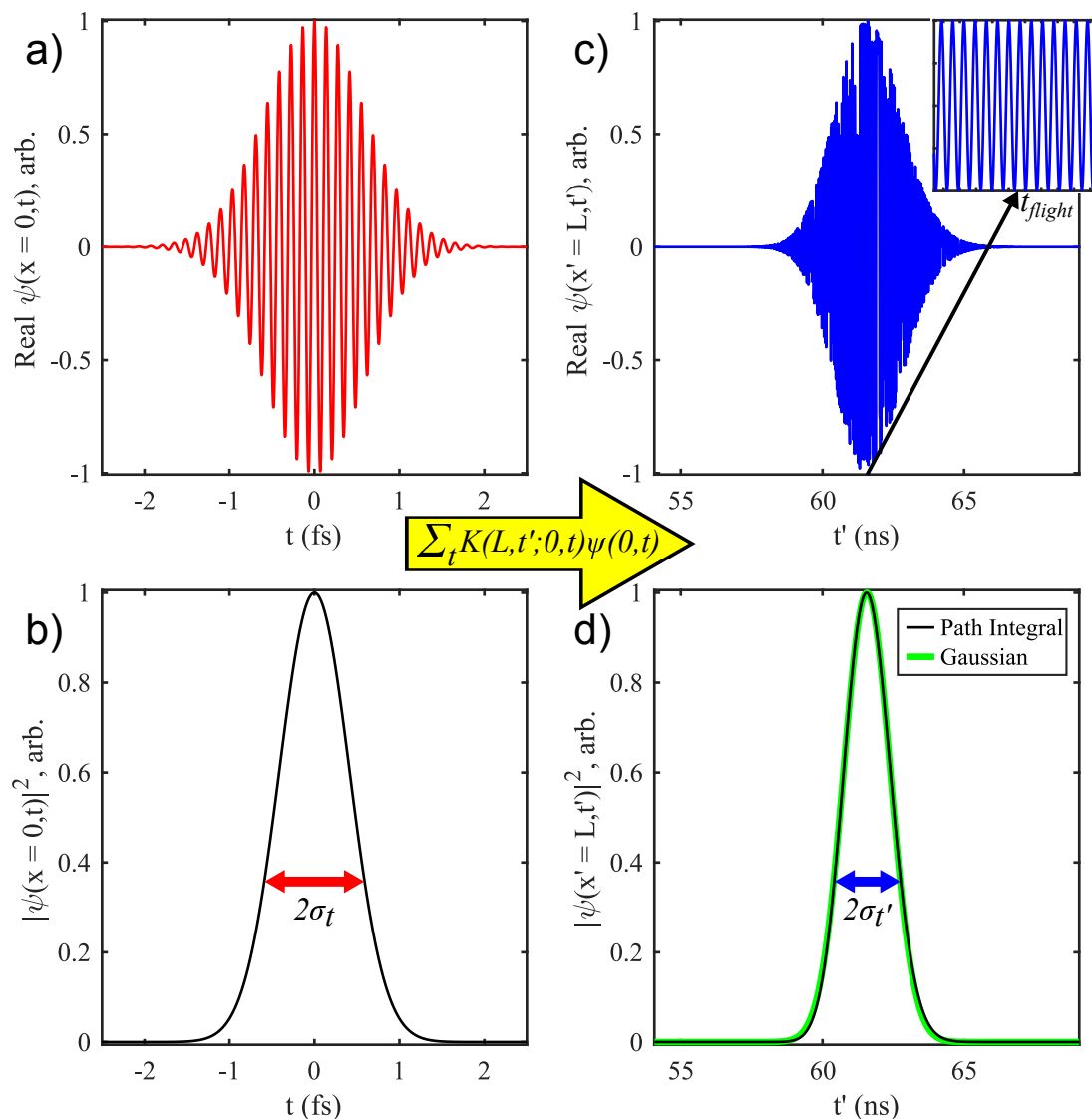
Figure 5.2: Evolution of a temporal wavepacket in free space, with all plots normalized to the maximum value. (a) Probability amplitude of the source distribution (real part), as a function of time. This result is obtained by taking the Fourier transform of a Gaussian energy distribution centered at $E_0 =30\,$eV. (b) Probability distribution of the source, with Gaussian width $\sigma_t = 0.58\,$fs. (c) Probability amplitude of the screen distribution (real part), with inset to show fast oscillations (inset scale is $2\,$fs). The propagation length is taken to be $L =20\,$cm. (d) Probability distribution at the screen, showing the path integral result (black line) and the Gaussian distribution estimate (green line) obtained taking $\sigma_{t'} =1.16\,$ns. The path integral result is slightly skewed when compared to the Gaussian, which is a feature of diffraction in time not seen in the typical case for spatial Gaussian wavepackets.

A second approach to obtain the single particle probability distribution is to consider the time-of-flights resulting from the different kinetic energies present in the initial energy distribution.[110] Taking the initial energy distribution as in Eq. 5.5, the substitution $E \rightarrow mL^2/(2t^2)$ will transform the energy distribution $\phi(E)$ into a time-of-flight distribution, $\phi(t)$, where L is the distance between the source point and the detector point, and t is the time elapsed between the production of an electron at $t = 0$ and the detection of that electron. Note that this semiclassical approach produces a probability distribution that is identical to that obtained from the path integral formalism, which is fully quantum mechanical. The screen probability distributions obtained from the path integral formalism (black) and the time-of-flight substitution (green) are plotted together in Fig. 5.3 to show they are indeed identical. The MATLAB script used to compute and plot the single particle time-of-flight distributions can be found in Appendix F.3.
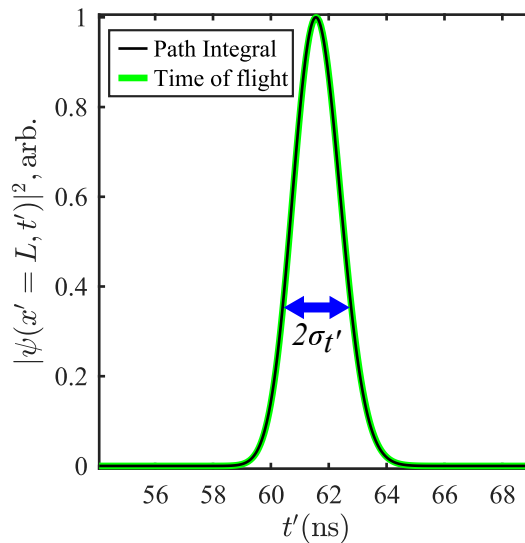
Figure 5.3: Probability distribution obtained from substituting the classical time of flight via $E \rightarrow mL^2/(2t^2)$ into the energy distribution given by Eq. 5.5 (green line) plotted with the path integral result shown in Fig. 5.2 (black line).

It is unusual to consider only the temporal evolution of a wave function, so some

discussion is provided here. A first concern might be toward regarding quantum states in an energy and time representation. An argument developed by Pauli asserts that while the Hamiltonian is an appropriately defined operator, a conjugate operator for time can not be defined.[189] Combining descriptions of quantum systems with classical environments can lead to a definable time operator, as reviewed in Ref. [190]. Nonetheless, energy and time can be treated as conjugate variables through the standard Fourier transform.[191] It might also be concerning that the time-dependent part of the wavefunction is here considered separately from the spatial part, especially when temporal effects were already shown to be present in near-field arrangements in Chapter 3.11. However, in the case when the diffracted matter wave satisfies far-field conditions, and the distribution time approaches the classical arrival time, the amplitudes contributing to the purely spatial and purely temporal effects can be factorized.[187] Therefore, considering the evolution of the temporal part of the wavefunction separately can be justified. As the time-dependent part of the wavefunction must also be a solution to the Schrödinger equation at all times and positions, it is then appropriate to propagate that part with the path integral kernel to compute how that solution evolves. Finally, while the concept of an arrival time is difficult if not contentious to formally define quantum mechanically,[192] the distributions arising from the path integral method have so far agreed well with experimental data.[186]

5.3 Path integral propagation in time for a temporal slit

A second physical system used to describe the evolution of matter waves, specifically, to demonstrate the Heisenberg uncertainty relationship between position and momentum, is the single slit. A plane monochromatic matter wave directed toward a spatial slit

becomes spatially confined by the slit, and as a result the momentum distribution immediately following the slit obtains a width and structure as predicted by the Fourier transform of the spatial distribution. It should be noted, that while this is the typical example used to demonstrate the effects of the uncertainty principle and the relationship between the widths of distributions related by Fourier transformation, the RMS width used in the Gaussian case cannot be used for single slit distributions.[147,193] This is because the signature $\operatorname{sinc} p^2$ momentum distribution does not have a meaningful RMS width Δp as defined in Sec. 5.2. The momentum distribution width that is frequently used in discussions is the half width of the central interference maximum. The following will show the analogous case of an initially plane monoenergetic matter wave confined by a temporal slit. The energy distribution immediately following the temporal slit obtains a width and structure predicted by the Fourier transform of the temporal distribution. As this energy distribution can not be measured directly, the half width of the central interference maximum is not as useful to the discussion as the measured RMS energy width of $0.8\,\mathrm{eV}$. This width will be used in the following to develop the temporal evolution of a temporal slit.

The normalized wavefunction for a slit in time at the source point is written,

$$\psi(t) = \frac{1}{\sqrt{\Delta t}} \Xi(t) \exp\left(\frac{-iE_0 t}{\hbar}\right), \tag{5.10}$$

where E_0 is the initial energy of the particle being described, and $\Xi(t)$ is a square aperture function with width Δt[188,194] which truncates the value of $\psi(t)$ to 0 for all times outside of the temporal slit width. The aperture function could be thought to describe the action of a shutter that can open and close instantaneously to define a square pulse from a continuous beam. While the Heisenberg limit sets the lower bound for the temporal widths of the Gaussian distribution shown before, here, the energy

distribution arising from the Fourier transform of Eq. 5.10 will set the minimum slit width. The normalized probability amplitude as a function of energy is obtained by an inverse Fourier transform as

$$
\begin{aligned}
\varphi(E) &= \frac{1}{\sqrt{2\pi\hbar}} \int_{-\infty}^{\infty} \psi(t) \exp\left(\frac{iEt}{\hbar}\right) dt \\
&= \frac{2\sin\frac{(E-E_0)\Delta t}{2\hbar}}{\sqrt{2\pi\hbar}\Delta t (E-E_0)/\hbar},
\end{aligned}
\tag{5.11}
$$

which gives the probability distribution, $|\varphi(E)|^2$, of

$$
\mid \varphi(E) \mid^2 = \frac{4\sin^2\frac{(E-E_0)\Delta t}{2\hbar}}{2\pi\hbar\Delta t\left((E-E_0)/\hbar\right)^2}.
\tag{5.12}
$$

Choosing a temporal slit width of $\Delta t = 1.95\,\text{fs}$ for the distribution defined by Eq. 5.12 results in a probability distribution in energy that has a width of $\Delta E = 0.8\,\text{eV}$. An observation of an energy distribution with this width would then be in principle indistinguishable from the Gaussian distribution. The normalized energy distribution resulting from a temporal slit of width $\Delta t_{slit} = 1.95\,\text{fs}$ (red), having initial energy $E_0 = 30\,\text{eV}$, is plotted along with a Gaussian energy distribution with a width $\Delta E_G = 0.8\,\text{eV}$ in Fig. 5.4(a), with the initial Gaussian (black) and slit (red) temporal distributions normalized to the Gaussian plotted in the inset. The Fortran code used to compute the single- and two-particle amplitudes and probability distributions can be found in Appendix F.2.
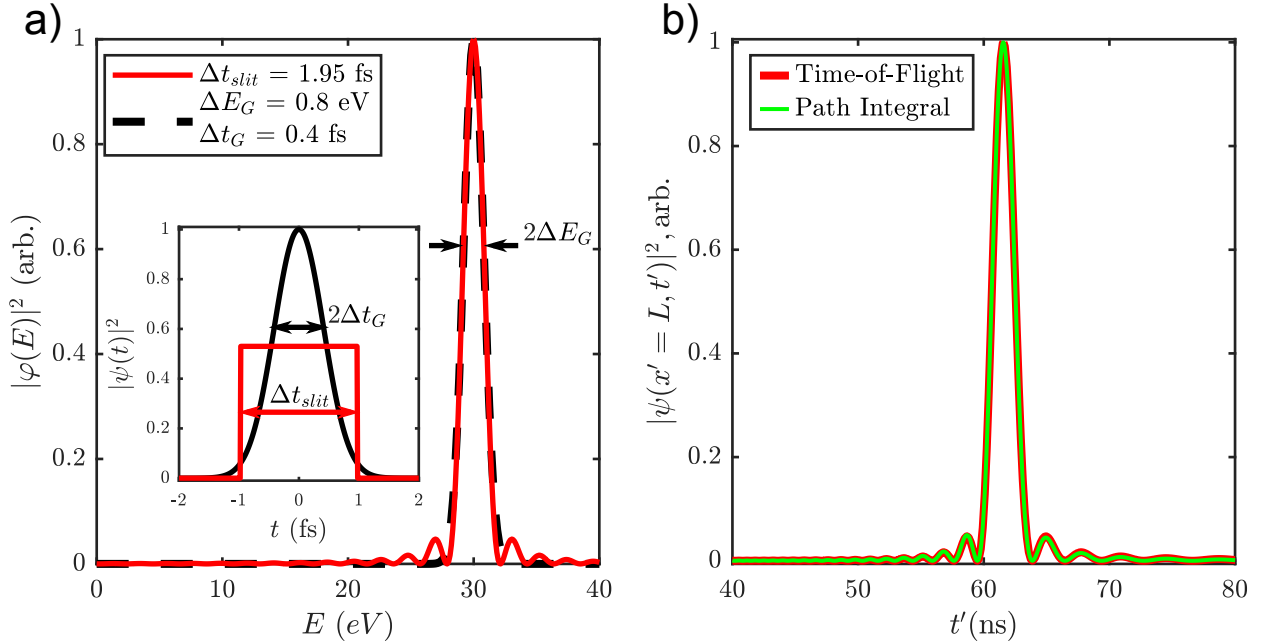
Figure 5.4: Probability distributions for diffraction in time from a single temporal slit. (a) Shown is the normalized energy distribution, $|\varphi(E)|^2$, for a temporal slit with width $\Delta t = 1.95\,\text{fs}$ (red curve), and a Gaussian having a RMS energy width $\Delta E = 0.8\,\text{eV}$. The width of the temporal slit, Δt_{slit}, plotted in the inset, is chosen so that the energy distribution, $|\varphi(E)|^2$, will have the same FWHM as the Gaussian distribution. (b) Arrival time distributions, normalized to the maximum amplitude, for a temporal slits of width $\Delta t = 1.95\,\text{fs}$ (red and green), for a propagation length of $L = 20\,\text{cm}$ and initial energy $E_0 = 30\,\text{eV}$. The red curve was obtained by the arrival time substitution, while the green curve was obtained from a path integral simulation. The first maximum can be seen approximately $3.4\,\text{ns}$ after the main arrival peak. These values are within the temporal resolution of our electron time of flight apparatus.

Following the path integral method as in the previous section, the single-particle probability amplitude $\psi(t')$ after propagation to the detector a distance L away is

$$
\begin{aligned}
\psi(t') &= \int_{-\infty}^{\infty} K(x' = L, t'; x = 0, t)\psi(t)\,\mathrm{d}t \\
&= \int_{-\Delta t/2}^{\Delta t/2} \sqrt{\frac{m}{2\pi i\hbar\,(t' - t)}} \exp\left[\frac{imL^2}{2\hbar\,(t' - t)}\right] \exp\left(\frac{-iE_0 t}{\hbar}\right)\,\mathrm{d}t.
\end{aligned}
\tag{5.13}
$$

The probability distribution in time, $\psi(t')^*\psi(t')$, is computed and plotted in Fig. 5.4(b) for the slit width of 1.95 fs (green) for a slit distance of $L =$ 20 cm. The result obtained from making the time-of-flight substitution $E \to mL^2/(2t^2)$ into Eq. 5.12 is plotted in red. Again, the time-of-flight substitution for the single particle distribution agrees well with the path integral calculation. A notable feature is that the central maximum at 61.57 ns is separated by 3.4 ns from the later-arriving first-order peak. This signature would be easily distinguishable in the current electron time-of-flight apparatus, and could be used to test pulsed sources for an emission mechanism that results from temporal gating by the exciting laser pulses.

One concern regarding the peaked structure of the distribution shown in Fig. 5.4(b) is that this structure could be the result of above-threshold photoemission.[82] In above-threshold photoemission, the total energy of emitted electrons for a material that requires n photons in a conventional multiphoton process, with the absorption of m additional photons, is

$$E_{total} = (n + m)\hbar\omega - \phi, \tag{5.14}$$

where n and m are integers, $\hbar\omega$ is the laser pulse energy, and ϕ is the source material work function.[195] For sufficiently high intensities, it has been observed that strong-field effects shift the dominant emission process to a higher order, so the energy spectrum of this situation will exhibit a prominent peak positioned in a train of equally spaced satellite peaks. A simplified plot of this kind of energy spectrum is plotted in Fig. 5.5(a) along with a single-slit energy distribution.
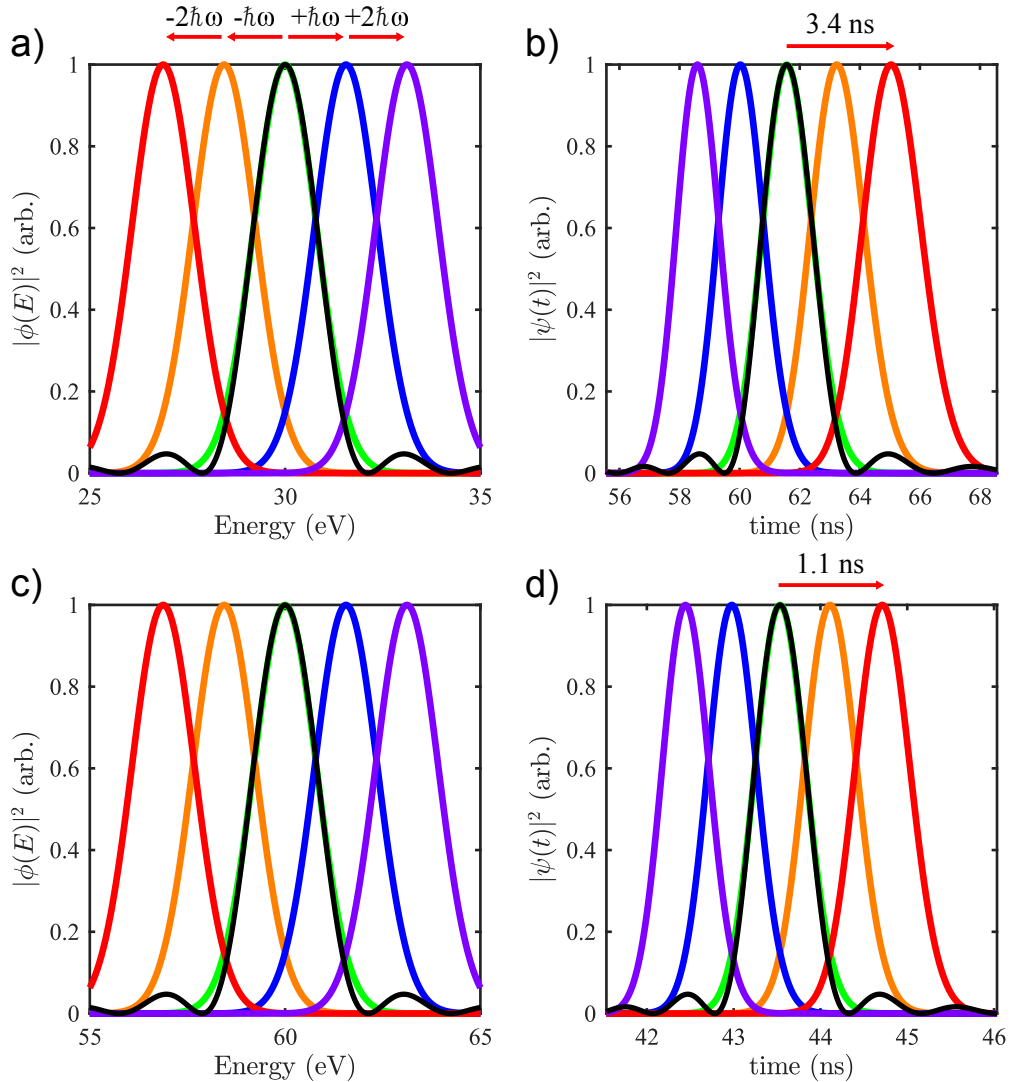
Figure 5.5: Temporal diffraction from a single slit is compared to a hypothetical distribution spacing generated by a multiphoton process. In (a), the initial energy distribution obtained from diffraction from a $\Delta t = 1.95$ fs temporal slit (black) is plotted with a series of Gaussian 0.8 eV-wide energy distributions shifted by multiples of 1.56 eV (red, orange, green, blue, and purple). Such a distribution could result from above-threshold photoemission at a source. In (b), $\psi(t)$ (black) is plotted with the time-of-flight distributions of the shifted Gaussian distributions. The separation from the zeroth-order maximum to the first-order is 3.4 ns, which overlaps with the $-2\hbar\omega$ Gaussian (red), but not with the $-\hbar\omega$ Gaussian (orange). In (c), the same distributions with 0.8 eV width are shown for a central energy of 60 eV. In (d), $\psi(t)$ is plotted with the Gaussian time-of-flight distributions. The spacing between the central zeroth-order maximum and the first-order maximum has decreased to 1.1 ns.

The black curve, centered at $30\,\text{eV}$, is the distribution obtained from a $\Delta t = 1.95\,\text{fs}$ duration temporal slit given by Eq. 5.12. Overlapping this distribution is a series of $0.8\,\text{eV}$-wide Gaussian distributions (red, orange, blue, and purple), spaced evenly about the central distribution (green curve) by multiples of $1.56\,\text{eV}$, which is the energy characteristic of our laser oscillator. What is immediately apparent is that the spacing of the Gaussian peaks does not match the spacing of the temporal slit energy distribution. A longer temporal slit duration (for example, $\Delta t = 3.78\,\text{fs}$) could decrease the energy peak spacing to match the $1.56\,\text{eV}$ separation, but that would also create a clear distinction of the energy width from the $0.8\,\text{eV}$ Gaussian distribution. Since the peak spacing of the single-slit energy distribution is distinguishable from the constant peak spacing of the multiphoton distribution, the temporal spacing of the resulting arrival time distribution will be distinguishable from the spacing predicted by the above-threshold photoemission model. One last feature to distinguish the two models is that the lowest photon order in above-threshold photoemission tends to be the dominant order, with a shift to the next highest order as intensity increases.[82] This shift is similar to a mechanism seen in above-threshold ionization of atoms. In above-threshold ionization, this spectral shift has been referred to as peak suppression, threshold shifting, or the onset of channel closing.[196,197] This would mean that for our electron source, the number of peaks in the energy spectrum of a multiphoton process preceding the dominant process should depend on the laser intensity. In terms of the temporal spectrum, the number of peaks arriving in time after the dominant process should increase and the arrival time of the dominant process will shift to an earlier peak position with increasing laser intensity. The temporal slit distribution should have no such intensity dependence. These two differences, observed in changing the source voltage and laser intensity, allow for distinguishable results between the two mechanisms.

5.4 Path integral propagation for two particles

With the methods of computing single-particle amplitudes and probability distributions established, it is now straightforward to extend the results for a pair of identical particles. Following the discussion Ref. [182], in particular pp. 75–79, a degenerate pulsed electron source is directed toward a pair of detectors, as illustrated in Fig. 5.6(a).
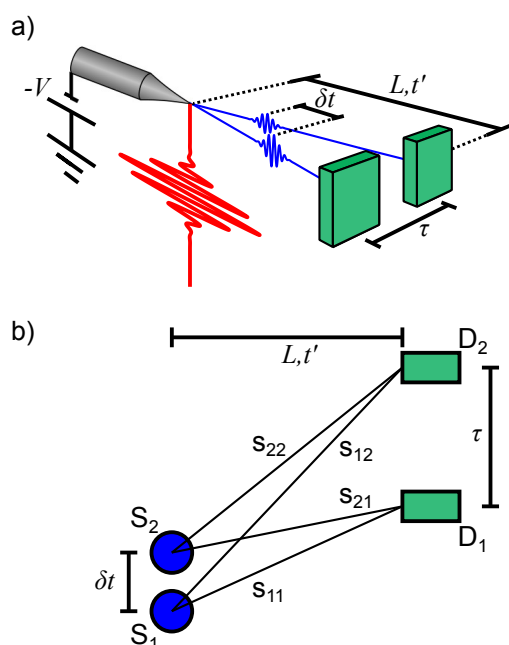
Figure 5.6: Simplified schematic describing two-particle interference. (a) Basic experimental set-up and components. A pulsed laser (red) focused onto a tip source produces electron pulses with an initial time separation of δt. As δt must be within the coherence time of the source, it is greatly exaggerated here in order to distinguish the two pulses schematically The electron pulses travel a distance L over the propagation time t' toward a split detector (green rectangles). The yield of electron pulses reaching the detectors separated by an arrival time delay τ is determined by the two-particle probability distribution. (b) Illustration of elements used to compute the two-particle probability distribution as a function of the detector delay. Two identical source distributions (S_1 and S_2) separated by an initial time delay of δt are propagated a distance L and time t' toward a pair of detectors (D_1 and $D2$) with correlated outputs. The paths from the source distributions to the detectors, for example, s_{11} and s_{12}, are labeled to indicate that those paths originated at source 1 and terminated at detector 1 and 2, respectively.

Here, instead of considering spatially separated amplitudes propagating toward spatially separated detectors, we will consider temporally separated amplitudes propagating in space and time toward temporally delayed detectors, as shown in Fig. 5.6(b). Identical particles originate at S_1 and S_2, where S_2 is delayed in time after S_1 by a time δt. In a fully coherent description, δt must be shorter than the coherence time of the source distributions. The source distributions are propagated a distance L toward a pair of detectors, D_1 and D_2, located equidistant from the source point, but delayed in time by τ. There are 4 propagation paths connecting the two source points to the two detection points. These paths are labeled s_{jk}, where j indicates the source distribution and k the detection point. Each of the 4 paths is associated with a single-particle probability amplitude. The 4 individual amplitudes are computed by the path integral formalism as

$$\psi_1(D_1) \quad = \int_{-\infty}^{\infty} K(x' = L, t'; x = 0, t)\psi(t)\,\mathrm{d}t, \tag{5.15}$$

$$\psi_2(D_2) \quad = \int_{-\infty}^{\infty} K(x' = L, t' - \tau; x = 0, t)\psi(t - \delta t)\,\mathrm{d}t, \tag{5.16}$$

$$\psi_1(D_2) \quad = \int_{-\infty}^{\infty} K(x' = L, t' - \tau; x = 0, t)\psi(t)\,\mathrm{d}t, \tag{5.17}$$

$$\mathrm{and}\,\psi_2(D_1) = \int_{-\infty}^{\infty} K(x' = L, t'; x = 0, t)\psi(t - \delta t)\,\mathrm{d}t, \tag{5.18}$$

where $\psi(t)$ is a source temporal probability amplitude, which in our specific examples is given by by Eqs. 5.7 or 5.10. The two-particle coincidence amplitude for identical electrons, $\Psi_{(1,2)}$, is

$$\Psi_{(1,2)} = \frac{1}{\sqrt{2}}\left[\psi_1(D_1)\,\psi_2(D_2) - \psi_1(D_2)\,\psi_2(D_1)\right]. \tag{5.19}$$

Eq. 5.19 presumes 100% spin polarization and total coherence. The effects of incomplete or no polarization have been shown previously, and forthcoming work will demonstrate the effects of partial coherence.

The two particle probability distribution, $P(1,2)$, is computed as a time-average of the probability density, $\Psi^*_{(1,2)}\Psi_{(1,2)}$, at the detector, written as

$$P_{(1,2)}(\tau) = \int_{-\infty}^{\infty} \Psi(1,2)(t',\tau)^* \Psi(1,2)(t',\tau)\, \mathrm{d}t'. \tag{5.20}$$

The case when the source distribution $\psi(t)$ is a Gaussian temporal wavepacket is shown in Fig. 5.7.
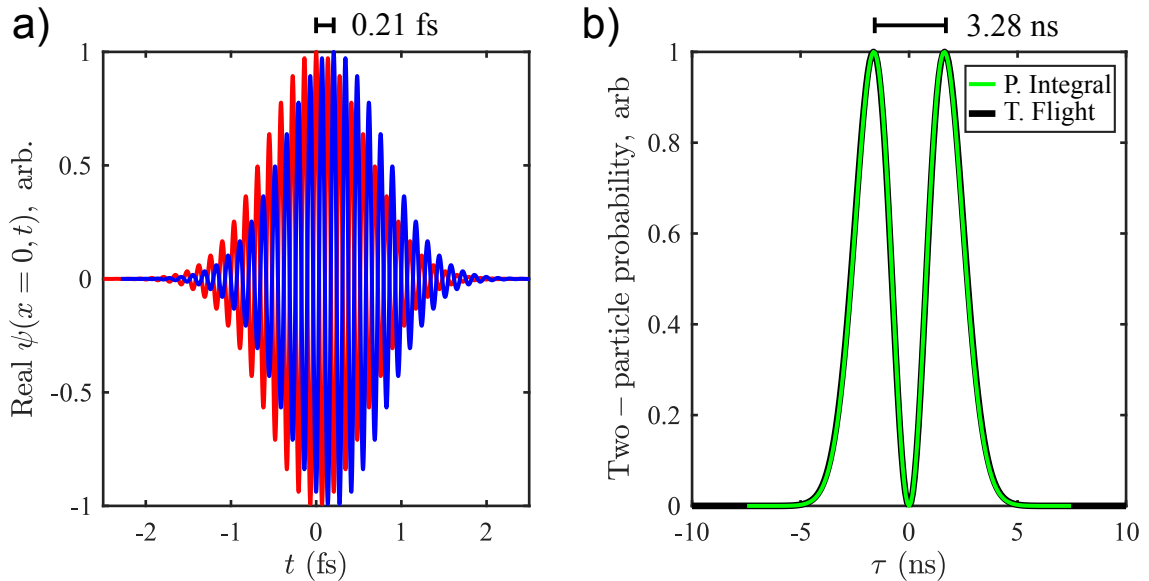
Figure 5.7: (a) Probability amplitudes of the source distributions (real part), as a function of the source time t. As before, these distributions are obtained from the Fourier transform of a Gaussian energy distribution centered at $E_0 =30\,\text{eV}$ with a width determined by $\Delta E =0.8\,\text{eV}$. The source distributions are delayed by a time $\delta t = \Delta t/2$, where $\Delta t = \hbar/(2\Delta E)$ is the coherence time given by the Heisenberg uncertainty relation. For the parameters chose, δt has a value of $0.21\,\text{fs}$. (b) Joint probability distribution at the detection point, located $L =20\,\text{cm}$ from the source point. The distribution determined from the semiclassical time of flight (black line) agrees with the path integral calculation (green line). The resulting peaks for this configuration have a delay separation of $3.28\,\text{ns}$, which can be achievable by both channel plates or channel electron multipliers.

In Fig. 5.7(a), the real part of the source probability amplitudes are plotted as a function of time, indicating the $0.21\,\text{fs}$ time delay between them. Fig. 5.7(b) shows the two-particle probability distribution, $P_{(1,2)}(\tau)$, resulting from both a path integral calculation (green) and the semiclassical time-of-flight substitution into the Gaussian energy distribution. For a propagation distance of $L = 20\,\text{cm}$, both calculations predict a peak separation of $3.28\,\text{ns}$.

The case when the source distributions are temporal single-slits is plotted in Fig. 5.8.
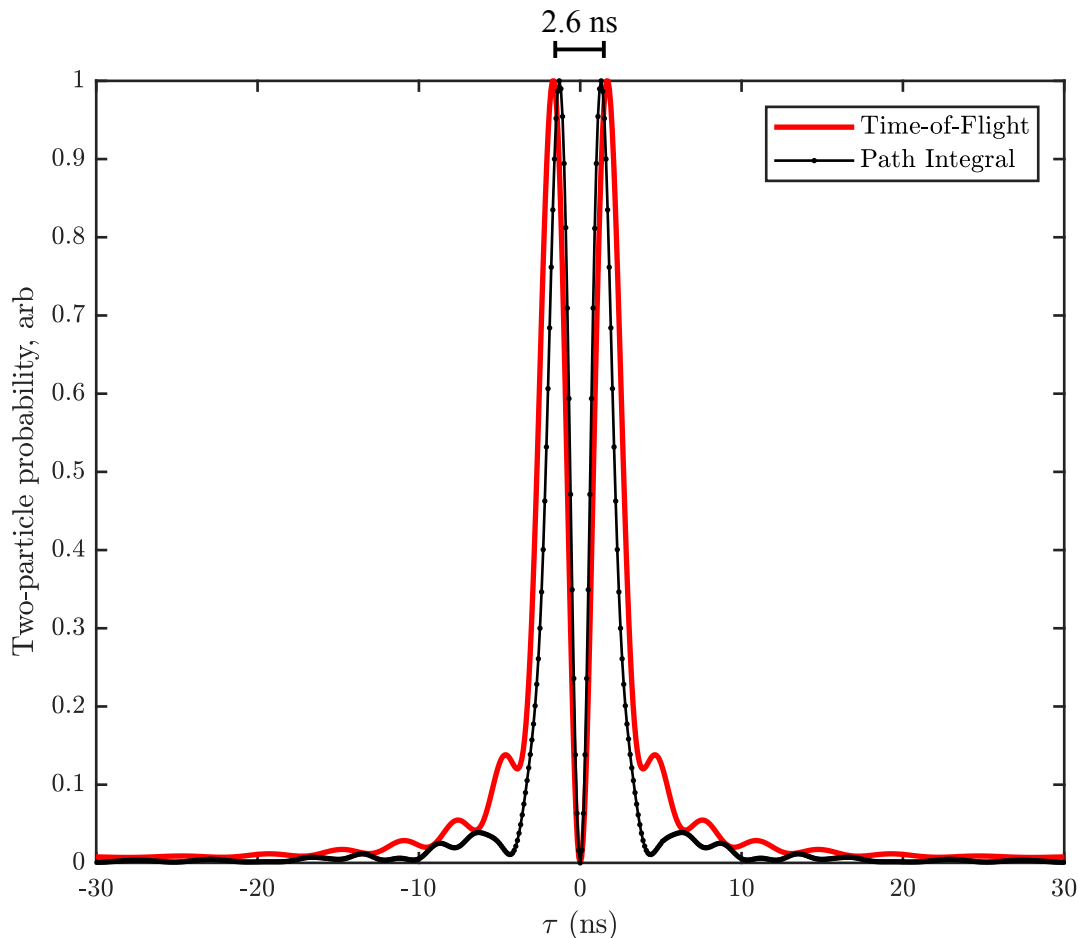
Figure 5.8: Joint probability distributions are shown for diffraction in time from two temporal slit distributions, using the path integral method (black) and semiclassical time-of-flight (red), as a function of detector delay (τ). The temporal slits considered have a width of $\Delta t = 1.95$ fs. Both methods are plotted for comparison as they do not agree as well as for Gaussian source distributions plotted in Fig. 5.7(b); however, they give roughly the same predictions for the distribution peak separation. For a slit width of 1.95 fs, the separation of the dominant peaks is 2.6 ns. The peak separation appears to scale with the ratio of the slit widths, meaning that a shorter temporal slit will give a broader peak separation. These values are within the temporal resolution of our electron time of flight apparatus.

Here, the slit separation is half of the slit width, or 0.975 fs. The path integral calculation (black connected dots) is compared to the semiclassical time-of-flight substitution into the energy distribution (red). The two methods give similar results, with some distinguishing features. In particular, the path integral method results in

interference minima where the semiclassical method results in maxima. This may be a consequence of how phase appears in both methods. In the path integral method, the amplitude is complex, and the phase evolves with the path integral propagator. For the time-of-flight substitution, the amplitude is exclusively real, with no clear phase evolution. Both methods demonstrate a peak separation that scales with the initial temporal slit width, and interference structure. In an experiment, the presence of such structure would indicate that the electron source behaved as if electrons were emitted from a temporal slit, and the main peak separation would give the temporal slit duration for that process, thus providing a direct measurement of the temporal coherence of the source. The code used to generate the graphs in Fig. 5.7 and Fig. 5.8 can be found in Appendix F.1, Appendix F.2, and Appendix F.3.

5.5   Experimental progress toward a degenerate source

Development of the elements necessary to realize a degenerate electron source, as discussed in Sec. 5.1 is described below. As shown in Fig. 5.1, an aperture needs to be positioned after the tip in order to define the transverse coherence length of the source. Hardware to mount an aperture, as well as the method to position and align it with respect to the tip apex, is shown in Fig. 5.9.
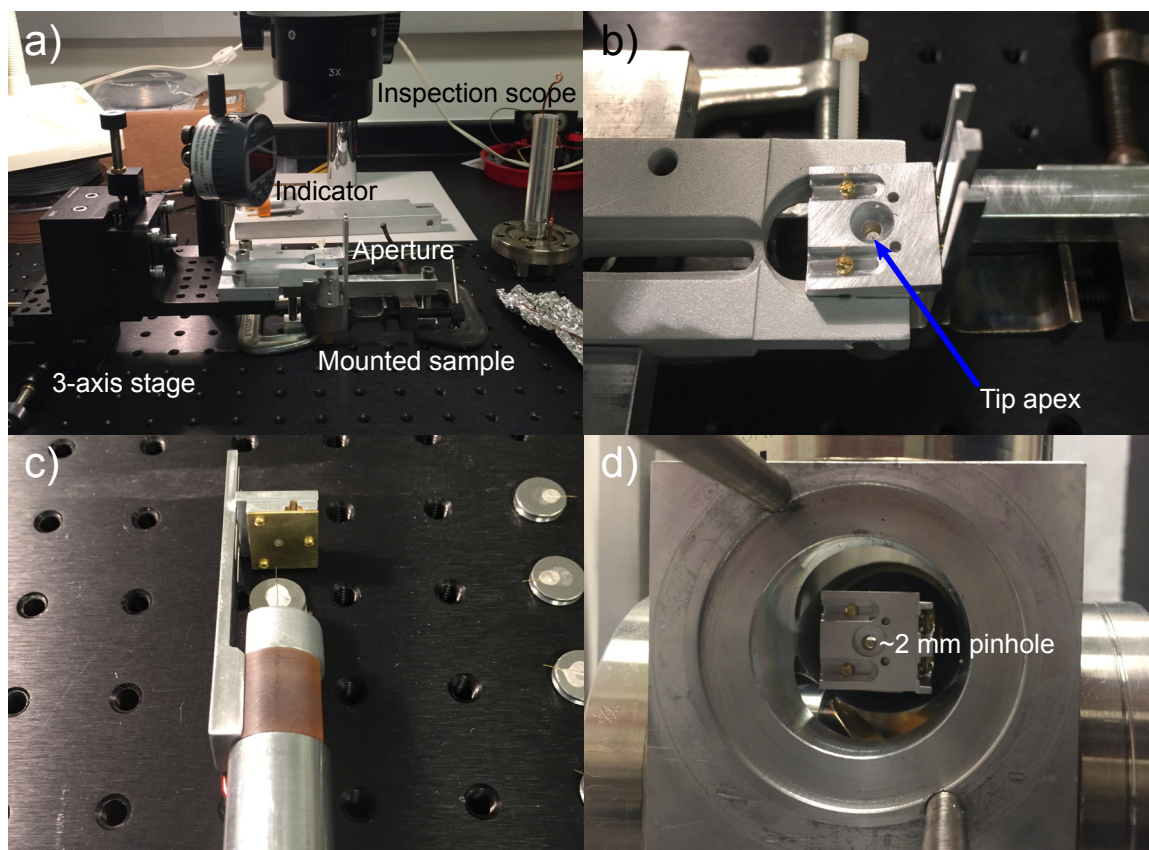
Figure 5.9: Apparatus for mounting an aperture behind a tip source. In (a), the full aperture alignment apparatus is shown. A tip sample is mounted, and held in place vertically by the mount base (Duratron, burnt orange) and the aperture side extension piece (aluminum). A 3-axis stage is used to position the aperture (2 mm, brass) mount above the tip. The vertical position of the aperture is monitored by an electronic indicator, and the position of the aperture is determined by observation in the inspection scope above. In (b), a top-view is shown of how the aperture is positioned. The tip apex is barely visible, but highlighted by the blue arrow. The tip-to-aperture separation is set by first focusing on the tip apex and then adjusting the 3-axis stage so the back side of the aperture is also focus, off to the side of the tip apex. The aperture is translated by the desired distance added to the aperture material thickness. Then, the aperture can be gradually brought back down over the tip apex by adjusting the $x-$ and $y-$axis micrometers until the apex is imaged in the center of the aperture hole. The vertical position is then readjusted to the desired distance. In (c), a successfully mounted sample is shown. In (d), the full mount is pictured from the detector side in the field emission tip experimental chamber with the tip positioned in the laser focus.

The mounting procedure requires an optical bread board and an inspection micro-

scope with a reasonably bright light source. A tip sample is mounted and held in place vertically by the feedthrough base (Duratron, burnt orange) and the aperture side extension piece (aluminum). A 3-axis stage is used to position the aperture ($2\,\mathrm{mm}$, brass) mount above the tip. The vertical position of the aperture is monitored by an electronic indicator, and the position of the aperture is determined by observation in the inspection scope above. In (b), a top-view is shown of how the aperture is positioned. The tip apex is barely visible, but highlighted by the blue arrow. The separation between the tip apex and the aperture back surface is set by first focusing on the tip apex, and then adjusting the 3-axis stage so the back side of the aperture is also in focus off to the side of the tip apex. The aperture is translated in the z-direction by the desired distance added to the aperture material thickness. Then, the aperture can be gradually brought back down over the tip apex, adjusting the $x-$ and $y-$axis micrometers until the apex is imaged in the center of the aperture. The vertical position is then readjusted to the desired distance. In (c), a successfully mounted sample is shown. In (d), the full mount is pictured from the detector side in the field emission tip experimental chamber, with the tip positioned in the laser focus. This method could be used to mount a smaller aperture, the only concern being that a higher magnifying power would be needed if the aperture chosen is $5\,\mathrm{\mu m}$. The aluminum rail can be modified to mount and align electron optic elements as well, such as a quadrupole lens.

The second element developed was a detector scheme to measure two-particle correlations. The assembled detector is shown in Fig. 5.10.
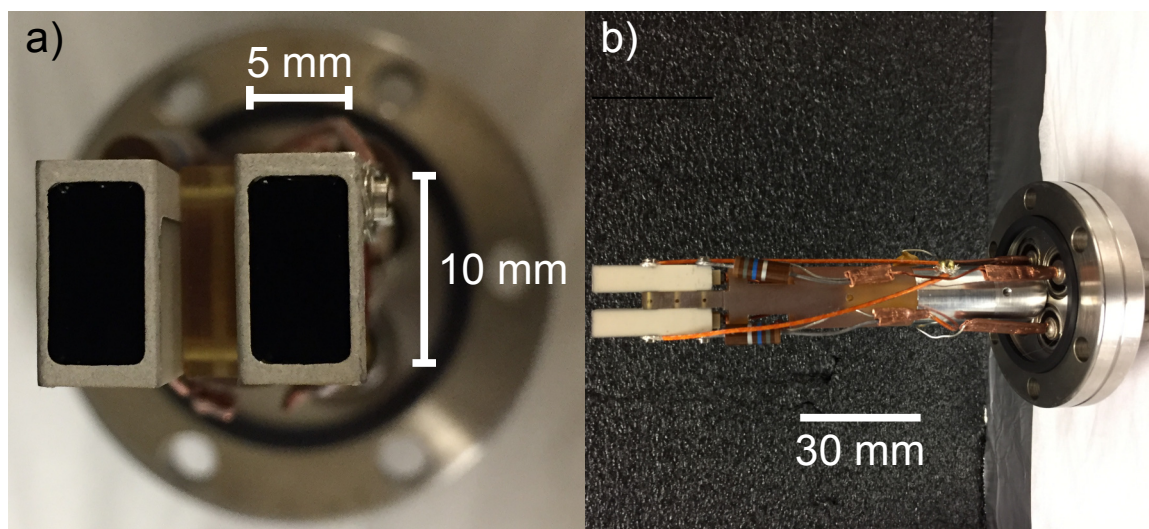
Figure 5.10: Shown is a first attempt at making a two-particle coincidence detector. In (a), the front facing view of the detector assembly is shown. The detector is comprised of two Dr. Sjuts KBL 510 channel electron multipliers (channeltrons), which have rectangular openings of 5 mm×10 mm. The channeltrons are fixed to a Duratron mount, which provides 4.4 mm of separation as a precaution against arcing, which could occur between the sharp edges of the collection plate assemblies, which are held near 2 kV, located at the rear of the detectors. In (b), a top view of the detector assembly is provided to show further detail of its construction.

Part of this work involved the design of the mounts and electronic components, as well as fabrication of the feedthroughs for mounting the dual Dr. Sjuts KBL 510 channel electron multipliers. The elements of the detector were assembled by graduate student Sam Keramati.

The third element developed for studying electron degeneracy was a fast, spin-polarized electron source in close collaboration with the Gay research group, with significant overlap with former graduate student Evan Brunkow. In the next section, the source will be described, and a potential outlook will be proposed.

5.6 Femtosecond-Laser-Induced Spin-Polarized Electron Emission from a GaAs Tip

In the following section, a fast, localized, spin-polarized source of electrons is described. The source was obtained from a sharp p-GaAs bulk [110] crystal shard illuminated with femtosecond laser light. The size of the emission site is approximately $1\,\mu m$ in scale, which give it characteristics similar to metallic nanotips.[4–6,198] The best polarization achieved so far from this source was $13\,\%$. The electron emission was studied using methods similar to those developed to characterize pulsed emission from metallic nanotips. This source is referred to as "fast," meaning that the temporal response of the emission process is comparable to that of the light pulse duration.

Standard CW polarized electron sources use a planar GaAs photocathode that must be layered with, e.g., Cs and O_2 to lower the vacuum potential below that of the conduction band. This creates a "negative electron affinity" (NEA) condition that allows electron emission by absorption of a single photon from a CW laser.
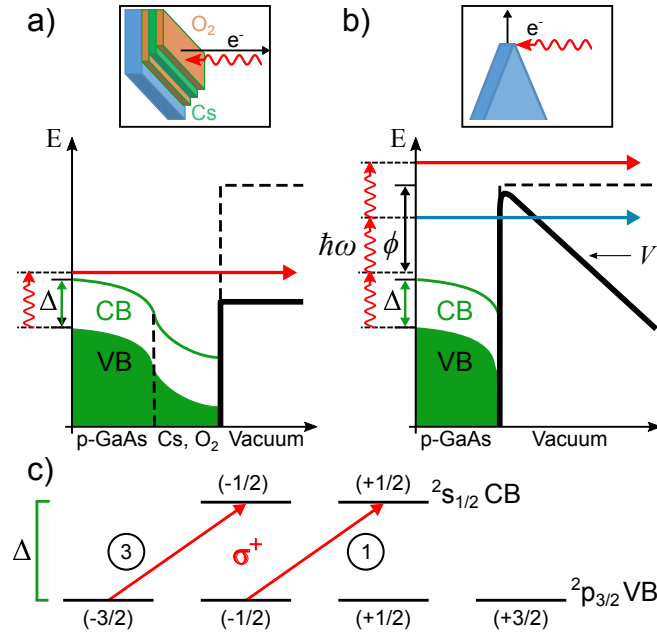
Figure 5.11: GaAs energy levels for (a) NEA bulk surfaces and (b) a non-NEA shard apex. The diagrams indicate bending of both the valence band (VB) and conduction band (CB) at the surface due to heavy p-doping. (a) The vacuum energy (dashed black line), is lowered (solid black line) due to the deposition of alternating layers of Cs and O_2 (top inset). Electron emission from the NEA surface proceeds by the absorption of a single photon with energy that exceeds the band gap Δ of the bulk. (b) Multiphoton emission from an uncoated (non-NEA) GaAs shard apex (see text). (c) Allowed transitions at the GaAs Γ-point for absorption of right-hand circularly-polarized light by Zeeman (m_j) sublevels. Selection rules ($\Delta m_j = +1$) and the relative line strengths (indicated in circles) yield a nascent conduction-band electron polarization of $(3 - 1)/(3 + 1) = 50\%$ for valence-conduction band resonant transitions. [75]

When circularly-polarized light with an energy near the bandgap Δ of GaAs is used to excite electrons, there is an imbalance in excitation probabilities of the two excited $^2s_{1/2}$ Zeeman substates (Fig. 5.11(c)), [75] causing the emitted electrons to be spin-polarized. Such sources are used in a variety of fields, including atomic and molecular, [77] high-energy, [199] and condensed matter physics. [200]

Alternative planar photocathodes with and without NEA have been developed to optimize the spin-polarization of the emitted electrons, to provide short pulse operation, and to enhance source brightness. NEA strained and unstrained thin

photocathodes have produced 2.5 ps electron pulses.[201] There, the electron pulse duration is limited by the slow emission process of diffusion through the material. A strained, back-illuminated GaAs-GaAsP superlattice with NEA activation resulted in a 16 ps pulse duration with high brightness[177–179], and was used in a spin-polarized transmission electron microscope. The source was determined to have a degeneracy 2 orders of magnitude lower than the cathode tip used to first study free electron degeneracy,[70] with a source size that was limited by the diffraction limit of the laser focus. A planar GaAs photocathode with a Ag overlayer a few nm thick has functioned as a polarized electron source without NEA activation by utilizing a multiphoton electron emission process.[81] Electron yields were increased by employing local field enhancement through plasmonic coupling on the surface of a p-doped GaAs wafer, while the spin-polarization of emitted electrons was largely maintained. Pulsed $\sim$100 fs laser light produced a spin-polarization as high as 21 %, with a value of $\sim$15 % for illumination at a central wavelength of 800 nm.

Tips of magnetized iron and cobalt-coated tungsten have been used to produce spin-polarized electrons, although these sources have used only CW lasers to date.[202,203] Such magnetized sources have a further limitation in that their spin polarization is not optically reversible, unlike that of of GaAs photocathodes. An array of etched GaAs tips, illuminated with CW laser light for both positive electron affinity (PEA) and NEA surface conditions resulted in a maximum polarization of 37 %, but the electrons were not pulsed.[32] Implementation of a tip geometry results in field enhancement at the tip apex, which increases the yield of emitted electrons. While a more robust activation surface of layered Cs and Te has been demonstrated,[204] a tip geometry, particularly in combination with a multiphoton emission process, eliminates the need for NEA activation that is generally extremely sensitive to vacuum conditions.[205]

The work reported here focuses on obtaining fast, spin-polarized electrons from a

sharp p-GaAs bulk [110] crystal shard, which naturally incorporates optical reversibility. To do this, Ti:Sapph pulsed lasers with wavelengths centered around 800 nm, the appropriate wavelength for single-photon excitation across the band gap, were used to induce multiphoton emission without requiring that the samples have NEA. Fig. 5.11(b) illustrates this. The vacuum potential (dashed black line) is modified at the surface by the application of a negative DC bias voltage V and the local laser field (solid black line). A single photon with energy just exceeding the bandgap Δ can promote an electron from the valence band to the conduction band. Absorption of a second photon can in principle result in emission via tunneling through the vacuum potential (blue arrow). Absorption of one or more additional photons provides sufficient energy for the electron to exceed the additional ionization energy ϕ and escape into the vacuum (red arrow). The 800 nm central wavelength of our lasers accesses the relative excitation probabilities for circularly-polarized light that make standard NEA GaAs sources produce polarized electrons (Fig. 5.11(c)).

5.6.1   Experiment

The vacuum system, with a nominal base pressure of 10^{-7} Torr, comprised two sections. A sample chamber contained an off-axis front-surface Au parabolic mirror to change the direction and focusing of the laser to a 20 μm-FWHM spot size. The GaAs shard was mounted on a 3-axis stage to position it in the laser focus. A channel electron multiplier (CEM) near the sample monitored the electron emission current. We also measured the total emission current from the electrically-isolated sample. Emitted electrons were directed to a compact, cylindrical Mott polarimeter,[206]
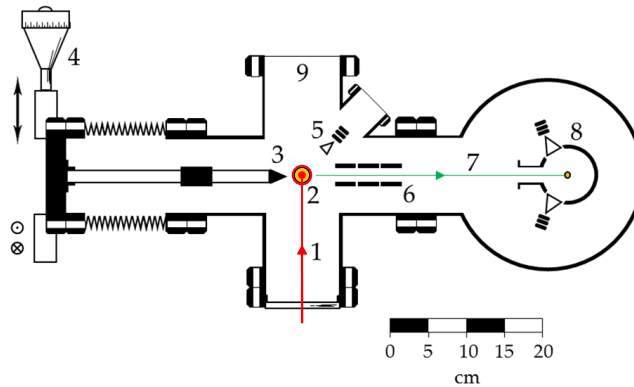
Figure 5.12: The experimental setup for polarimetry and dichroism measurements. The pulsed laser beam (1) enters the chamber and hits the off-axis parabolic mirror (2) which focuses the laser onto the sample (3). Note that the beam is propagating out of the plane at (2), indicated by the red circle. The sample is mounted on an XYZ translator (4) that allows the sample tip to be positioned in the laser focus. A CEM (5) can be used to monitor electron emission. Transport optics (6) guide emitted electrons (7) toward the Mott polarimeter (8) in the adjoining chamber with top (T) and bottom (B) CEM detectors.

comprising two concentric cylindrical electrodes and two CEMs placed symmetrically about the entrance that defined the electron scattering plane. The central gold-plated electrode was biased at $+20\,\mathrm{kV}$, whereas the outer electrode and the mouths of the CEMs were biased at $+500\,\mathrm{V}$.

To measure the electron polarization, P_e, the count rates measured by the top and bottom CEMs (C_T and C_B) were monitored for electrons produced by light pulses that were right-hand circularly-polarized, and then compared with the rates when the light helicity was flipped. The electron polarization, P_e, is given as $P_e = S_{\mathrm{eff}}/A$, where

$$A = \frac{\chi - 1}{\chi + 1} \text{ and } \chi = \sqrt{\frac{C_T C_B'}{C_T' C_B}}. \tag{5.21}$$

Here, S_{eff}, the "effective Sherman function," is the polarimeter's analyzing power, and the primes indicate the CEM rates for left-handed incident laser light. The advantage of measuring P_e this way is that it eliminates first-order instrumental

asymmetries.[77] Measurements of the electron polarization were performed entirely in the Gay laboratory.

Measurements of the linear and circular emission dichroism were also made in the Gay laboratory to better understand the emission process . The dichroism, calculated using total emission as measured by the CEM proximate to the sample, is

$$D \equiv \frac{R_1 - R_2}{R_1 + R_2};$$ \hfill (5.22)

$R_{1,2}$ is the rate of emission for orthogonal polarizations.

Electron emission from the samples was optimized at the edge of the crystal shard. Sharp tip-like shards were made by shattering crystalline wafers and using an optical microscope to determine the "sharpest" pieces.[207] When using these, total emission currents between $50\,\mathrm{pA}$ and $3\,\mathrm{nA}$ were obtained with an average laser power of $\sim 100\,\mathrm{mW}$, an $80\,\mathrm{MHz}$ pulse repetition rate, and a DC sample bias of $-100\,\mathrm{V}$.

A second, similar apparatus was used to study emission rates as a function of the shard apex morphology, to measure the dependence of emission rate on laser intensity, and to assess the temporal width of the emission process.[33] The entire apparatus is described in Ch. 2, Sec. 2.2, in Figs. 2.2 through 2.5, and Fig. 2.8. Pulses from a Ti:Sapph oscillator (Spectra Physics Tsunami) were focused to a FWHM of $4.5\,\mu\mathrm{m}$. The laser pulse intensity FWHM, τ_{laser}, was measured to be $100\,\mathrm{fs}$. The laser power delivered to the shard apex was controlled by a Brewster window variable attenuator. Pulsed electron emission was detected by a microchannel plate (MCP) placed close to the shard apex, or by an electrometer connected directly to the sample. Prior to entering the chamber, the primary beam was split into pump and probe components in a balanced Mach-Zehnder interferometer. The delay τ between pump and probe pulses could be adjusted for values between $\pm 4\,\mathrm{ps}$.

When two temporally-separated light pulses hit the sample, the integrated electron emission can be categorized as either "additive" or "super-additive." Additive emission means that the integrated signal is the same as the sum of the emission from each pulse individually. Super-additivity occurs when the emission is greater than the sum of that due to the individual beams. Additive emission for $\tau > \tau_0$ shows that the emission process does not exceed τ_0; if $\tau_0 \approx \tau_{laser}$, the emission process is "fast" as defined in the Introduction. Superadditivity for $\tau \gg \tau_{laser}$ implies the process is slow, e.g., due to thermally assisted processes. [4,5,19,33]
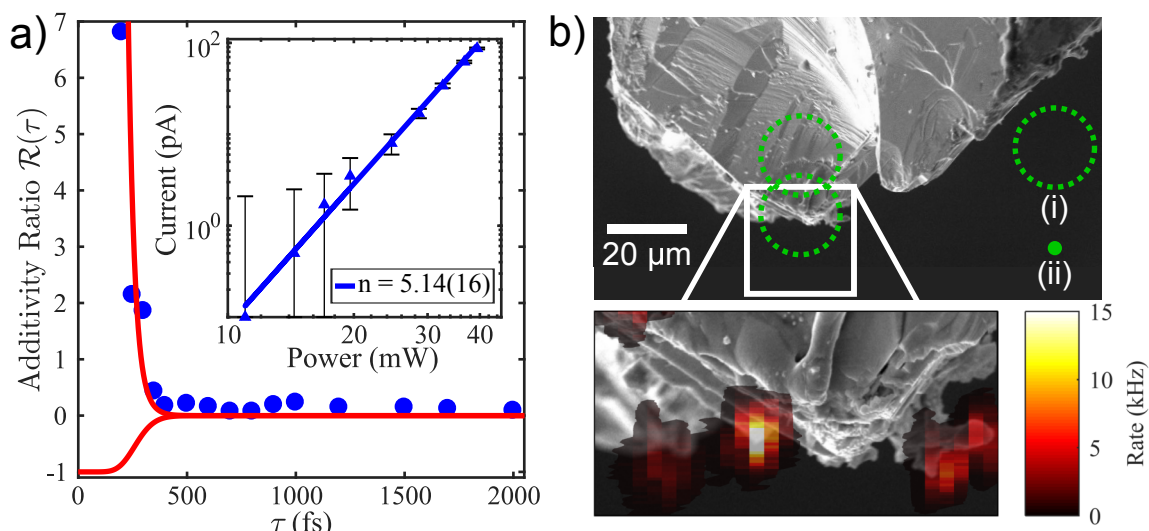
Figure 5.13: Emission data from a GaAs shard "tip." In (a), $\mathcal{R}$ is plotted vs. τ (blue circles). The red line is the theoretical curve obtained with an electric field width of 160 fs and an I^5 intensity dependence. The bifurcation of the $\mathcal{R}(\tau)$ curve for $\tau < 400$ fs is due to the flipping of the sign in Eq. 5.24 of E_{probe}, and corresponds to the envelope function for the rapidly oscillating autocorrelation interference pattern in this region. The power dependence of emission is plotted in the inset. (b) A scanning electron microscope (SEM) micrograph of the apex area with an expanded square section 20 µm on a side. The laser focal spot size from the P_e measurements (dashed green circle, (i)) is shown to the scale of the top micrograph and compared to the focal spot size (solid green circle, (ii)) used for the measurements shown in (a). The tip and shank positions used for measurements of P_e and D are indicated by the 20 µm dashed green circles (bottom and top, respectively). Localized emission from the shard's sharpest features (inset) indicates that multiple sites may have been emitting in the P_e and D measurements.

5.6.2   Results

We first consider the electron pulse emission process. Electron emission from nanotips, if measured to be both nonlinear and additive for $\tau > \tau_{laser}$, has been shown to be fast.[4,5,198] Our electron emission current shows non-linearity as a function of intensity. It fits with a power law of $n = 5.14(16)$ (Fig. 5.13(a) inset; blue line). The Keldysh parameter for a solid, γ, characterizes the emission. For $\gamma \gg 1$, field emission is dominated by multiphoton processes.[23,208] Given our focal spot sizes of $20\,\mu$m and $4.5\,\mu$m, and an average power that never exceeded $150\,$mW, our Keldysh parameter readily satisfied this condition in all our experiments and supports our simple multiphoton model. The fifth order non-linearity indicates a five-photon process. (This result is in excess of the three-photon process illustrated in Fig. 5.11(b)). Generally speaking, the order of the multiphoton process in a given sample can vary with the details of the emitting surface, its local surface electric field, and the nature of surface states near the emission point. For a full discussion, see, e.g., Section 3.1 of Ref. [209].

Pump-probe measurements as described above were used to determine if the emission was additive.[5,33] In Ch. 2, the additive ratio was defined in Eq. 2.1 such that an additive ratio of $\mathcal{R}(\tau) \approx 1$ indicated fully independent electron emission from the pump and probe pulses. Instead, the additive ratio is defined here such that $\mathcal{R}(\tau) \approx 0$ indicates fully independent electron emission from the pump and probe pulses. This choice was made for consistency on collaborative work between the Batelaan and Gay research groups. The additive ratio is then defined here as

$$\mathcal{R}(\tau) \equiv \frac{R_{both}(\tau) - (R_{pump}(\tau) + R_{probe}(\tau))}{R_{pump}(\tau) + R_{probe}(\tau)}, \tag{5.23}$$

where $R_{pump}(\tau)$ and $R_{probe}(\tau)$ are the emission rates from the pump and probe beams

separately at each delay, and the rate $R_{both}(\tau)$ was modeled as

$$R_{both}(\tau) = \int\limits_{-\infty}^{\infty} [E_{pump}(t) \pm E_{probe}(t + \tau)]^{2n} \, \mathrm{d}t. \qquad (5.24)$$

The individual pump and probe field amplitudes were modeled as Gaussians with $E(t) = E_0 \exp[-(t/\tau_{pulse})^2]$. The best fit to the data (red line in Fig. 5.13(a)) is obtained for $\tau_{pulse} = 160\,\mathrm{fs}$ ($n = 5$). The electron emission process is additive ($\mathcal{R}(\tau) = 0$ for $\tau > 400\,\mathrm{fs}$) and is thus shown to be faster than this value. Note that this is not a direct measurement of the electron pulse duration. Nevertheless, fast emission processes have so far indicated short electron pulses.[23] For emission rates with an average of less than one electron per pulse, this is not surprising, given that space charge effects are essentially absent.

We now turn our attention to electron polarization. Measurements of P_e were taken with a $20\,\mu\mathrm{m}$-diameter focal spot for two focal positions on the three samples we studied. In the first "tip" position, the focal spot was centered on the shard apex. In the second "shank" position, the focus center was moved about $15\,\mu\mathrm{m}$ away from the tip towards the bulk. The results of all measurements of P_e and emission dichroism, taken with the $20\,\mu\mathrm{m}$ focus, are given in Table 5.2.

In the "tip" position, with circularly-polarized laser illumination, P_e was $13\,\%$ for samples 1 and 2, and $10\,\%$ for sample 3. Note that these results are comparable to those of Ref. [81]. Variations in the local structure or p-doping could be responsible for the differences in P_e.[209] Each P_e value is the result of between 4 and 87 runs, typically taken over several hours. Individual runs yielded uncertainties that we based on counting statistics alone. Occasionally, these error bars were increased to account for small temporal drifts. The values quoted in Table 5.2 are the uncertainty-weighted averages of these individual run values. As expected, when the laser was linearly-

Table 5.2: Polarization and dichroism results for circularly- and linearly-polarized light incident on either the apex ("tip") or the bulk ("shank") of three different shard samples.

Target	Light Polarization	P_e(%)	D(%)
#1 Tip	Circular	13.1(9)	
#2 Tip	Circular	13.3(7)	4.7(6)
	Linear	0.1(5)	41.3(1.0)
#3 Tip	Circular	10.4(2)	1.8(2)
	Linear	2.6(2.5)	18.5(6)
#1 Shank	Circular	1.7(8.0)	6.4(1.4)
	Linear	1.0(2.1)	23.7(5)
#2 Shank	Circular	3.4(1.6)	
	Linear	5.2(1.0)	

polarized, the values of P_e were consistent with zero. One exception, which we have yet to understand, was observed with sample 2 in the shank position. We note only that this value of P_e is less than half that of the polarization measured at the tip with circularly-polarized light.

Finally, we consider the sample morphology. The electron emission rate was found to depend sensitively on the position of the laser focus at the sample. Fig. 5.13(b) shows a plot of the emission rate measured in a 20 μm square area of a shard apex. The two laser focal spot sizes used in this work are shown relative to the size of the 20 μm scale bar in the top micrograph. The brightest emission feature was used for the measurements plotted in Fig. 5.13(a).

Non-zero linear emission dichroism (Eq. 5.22) was observed for the GaAs shards similar to a field emission tip (FET). That is, emission is higher when the light's linear polarization is parallel to the axis of the tip.[4,5] In contrast, emission dichroism is absent for standard planar GaAs sources.[75,77] Dichroism measurements were taken at both focal positions as well. At the tip of the GaAs, the circular dichroism is small (<5%) and the linear dichroism for tips 1 and 2 are 41% and 19%, respectively.

Linear dichroism measured for tip 1 drops to 24 % at the shank, possibly because there is less of a tip-like structure with which the light interacts. The full polarization dependence of an older sample is shown in Fig. 5.14.
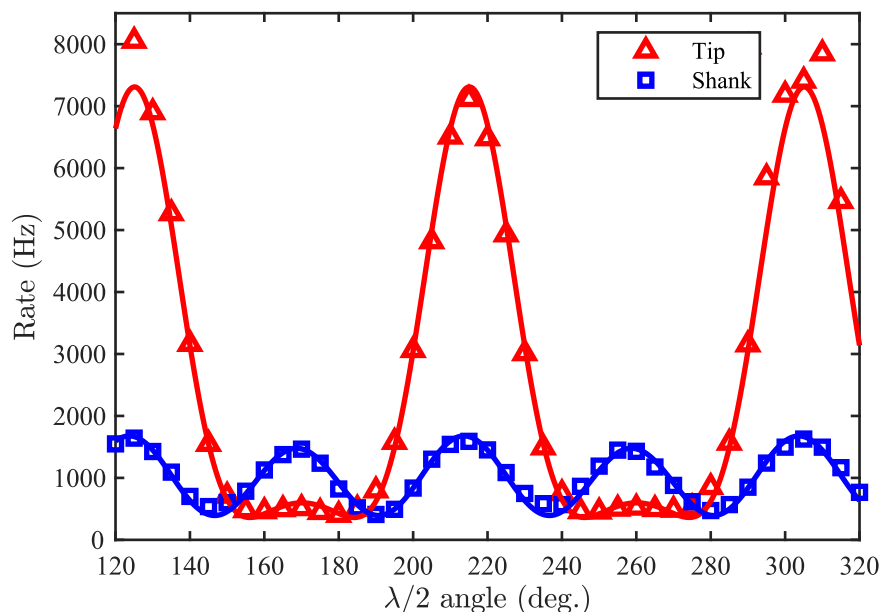
Figure 5.14: Shown is the polarization dependence of electron emission from a p-GaAs shard sample, taken for two positions in the laser focus at 60 mW. The emission rate from the apex of the shard (Tip, red triangles) was fit by a sum of two I^3 processes in the form Rate $= A\cos^6(2\theta) + B\cos^6(2\theta + 90°)$, where θ is the recorded half wave plate angle with an offset determined by the fit. Emission from the apex is dominated by the process due to laser polarization in-line with the shard, similar to a sharp tip. The linear dichroism, determined from the fit parameters, was approximately 85 %. The emission rate several microns behind the apex (Shank, blue squares) was fit by a similar function, except that the contributions from orthogonal polarizations were nearly equal. The linear dichroism at this sample position was approximately 6.3 %.

Electron emission was measured at both the tip and shank locations, and the data were then fit with with a $\cos\theta^{2n}$-model, where θ is the recorded angle of the HWP as in Chapter 2.3. The data are best fit by two separate processes that differ in phase by 90°. Such behavior is indicative of emission from separate surfaces, or possibly crystal facets, present near the GaAs tip. The linear dichroism at the tip position was determined to be 85 %, while at the shank it was 6.3 %. Thus our shard

"tips" therefore have emission characteristics similar to those of FETs[4–6,198] in terms of nonlinearity, additivity, polarization and local morphology although it is apparent from Fig. 5.13(b) that the overall shard morphology is complex.

In summary, we have demonstrated a source that is able to produce fast pulses of polarized electrons from a micrometer-size area. This can, in principle, enable the imaging of a small electron spot on a target to measure spin-dependent effects with fs-scale resolution. The reduced vacuum requirements of this source when compared with NEA GaAs sources make it easier and less costly to operate. Although the observed electron polarization is modest, our results demonstrate that this source follows the selection rules illustrated in Fig. 5.11(c). Polarization might be increased by having a sharper, more well-defined GaAs tip, or varying the laser wavelength. The parameter space is large and open to future study. Through the use of chemical etching and ion milling, it is possible to shape the tip. An optical parametric amplifier can be used to explore the wavelength-dependence of polarization. Investigation of the effects these parameters have on the total yield and polarization of the emitted electrons is needed.

5.6.3   Subadditive electron emission from a GaAs shard

An unexpected feature was observed for electron emission induced from samples in the $20\,\mu m$ focus and from shank emission with the $5\,\mu m$ focus. Instead of the emission being strictly superadditive for when the pump and probe pulses overlapped in time, and then additive when the pulses were temporally separated, the emission yield was found to be subadditive for long delays. That is, the total electron emission yield for both pump and probe beams incident on the sample was less than the summed yields from the pump and probe pulses alone. This feature was first described in Evan Brunkow's dissertation work, Ref. [210], using the methods and the initial model

developed here. This work builds on what was first reported in Ref. [210] by improving

the subadditive model to take the laser pulse shape into account and by testing the

spatial dependence of subadditive emission.

The first attempt at modeling the emission is reproduced in Fig. 5.15. Fig. 5.15(a)

shows the measured additive ratio, $\mathcal{R}(\tau)$, plotted for $100\,\text{fs}< \tau <1\,\text{ns}$, with an I^3

model (cyan).
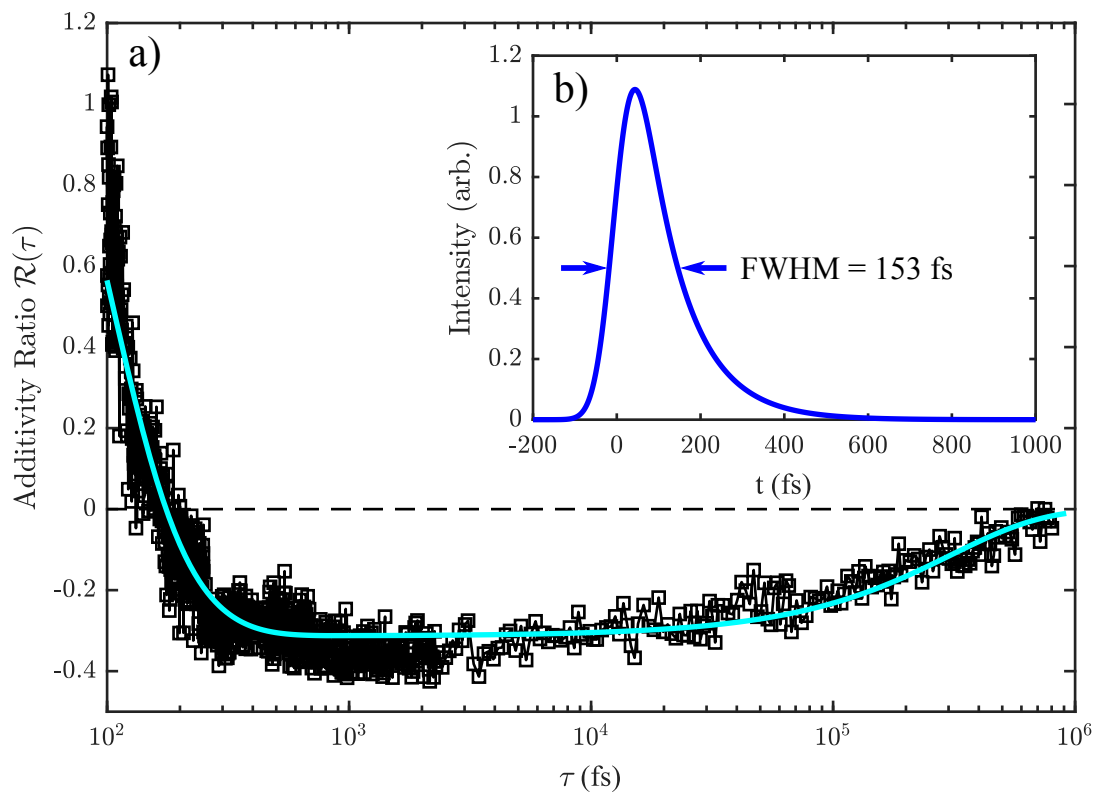
Figure 5.15: A plot (a) of the measured additivity ratio $\mathcal{R}(\tau)$ (black connected squares) for delays ranging from $100\,\text{fs}$ to $1\,\text{ns}$ is shown with an I^3 model (cyan) is shown. The figure inset (b) shows a plot of the intensity profile constructed in the model to obtain the best fit. The intensity distribution has a full width at half maximum (FWHM) of $153\,\text{fs}$, which does not agree with the measured temporal width of the oscillator of $75\,\text{fs}$. The question is open, is this due to a physical emission process or a consequence of the model chosen?

The pulses used in the best-fit are plotted in Fig. 5.15(b). The difference between this

model and the model shown for Fig. 5.13(a), given by Eq. 5.24, is that these pulses are

not Gaussian, and the emission dependence is on the intensity, not the electric field. The intensity profiles chosen for this first attempt were composed of a complementary error function joined smoothly to a decaying exponential function. Those pulses were then used to model the emission rate with two pulses incident on a shard as

$$R_{both}(\tau) = \int\limits_{-\infty}^{\infty} \left[I_{pump}(t) + \chi(\tau) I_{probe}(t + \tau) \right]^n \, dt, \qquad (5.25)$$

where $\chi(\tau)$ is a delay-dependent suppression function given by

$$\chi(\tau) = 1 - \alpha \exp\left(-\tau/\tau_{sub}\right), \qquad (5.26)$$

with α being the strength of the emission suppression and τ_{sub} the characteristic time for the subadditive process to decay. The additivity ratio $\mathcal{R}(\tau)$ is then computed as in Eq. 5.23. The model was computed with the Fortran code given in Appendix G.1.

One of the drawbacks of the subadditive model presented so far is that it is purely heuristic, as it does not derive from any particular emission or transport mechanism. Improving the heuristic model to better fit the available data is then one approach to discerning what processes could be responsible for the observed subadditive emission. For example, the emission response pulses used so far do not describe the emission data when there is temporal overlap of the pulses. The measured pulse duration used in the pump/probe experiments, that is, the intensity FWHM, was reported as 75 fs. The pulse duration of the model pulses is 153 fs. This does not at first seem like a significant difficulty, but the result of this error is that the drop of the data from positive to negative near $\tau =$170 fs is due to the pulse shape chosen and not a physical process. This issue is enhanced when the short delay ($|\tau| <$100 fs) data is modeled, which could not possibly be due to pulses much longer than 100 fs. This

claim will be further explained as the improvements to the subadditive emission model are presented. Further, as this model assumes subadditivity for all $\tau > 0$, there is no room for dynamics, which hinders the elucidation of what mechanisms could be responsible for the effect.

The subadditive model is refined by first considering a linearly chirped Gaussian electric field pulse. Such a pulse has the form

$$E_{chirp} = E_0 \exp \frac{-t^2}{2\sigma_t^2} \cos\left(\omega t + bt^2\right), \tag{5.27}$$

where E_0 is the field amplitude, σ_t is the Gaussian temporal pulse width, ω is the central frequency of the pulse, and b is the chirp parameter. Fig. 5.16(a) gives a plot of a chirped Gaussian electric field pulse (red) and the resulting intensity profile (green) used in a refinement of the subadditive model.
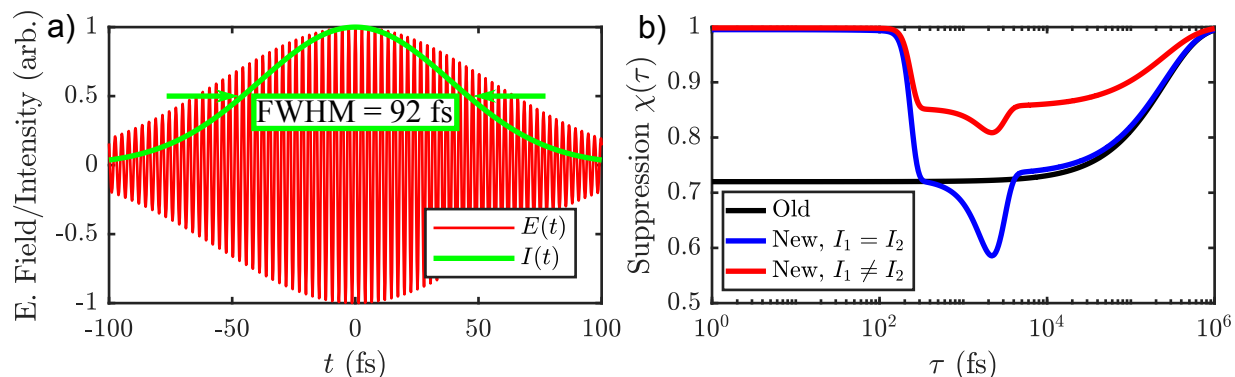
Figure 5.16: In (a), the real part of the electric field amplitude (red) is plotted with the resulting intensity distribution (green) as a function of time. The values used for the new model give a FWHM of 92 fs with a linear chirp. The suppression function, $\chi(\tau)$, is shown in (b). The original model (black) only considered an exponentially increasing function. The new model (blue and red) accounts for the onset of subadditive emission as well as unequal emission rates from the pump and probe pulses. The Gaussian dip in $\chi(\tau)$ near 2.2 ps may be the result of such a case. Unequal emission could be due to both the imbalance of the interferometer (accounting for 75 to 80 percent) as well as slight misalignments of the pump and probe beams at the emission apex.

The suppression function, $\chi(\tau)$, is then modified to include a term that allows for the subadditive effect to gradually turn on. A form of the function that achieves this effect is found as

$$\chi(\tau) = 1 - \alpha \left\{ \exp\left(-\frac{\tau}{\tau_{sub}}\right) \text{erfc}\left[\frac{\tau_w - (\tau - \tau_0)}{\sqrt{2}\tau_w}\right] + k(\tau) \right\}, \tag{5.28}$$

where α is again the strength of the emission suppression, τ_{sub} is the characteristic time for the subadditive process to decay, τ_w is the delay width of the onset of subadditivity, τ_0 is the effective starting time for the subadditive process, and $k(\tau)$ is a function chosen to try to improve agreement with the data, which appear to cluster below the old model fit in Fig. 5.15(a) around 1 ps. The addition of the Gaussian function was made to highlight this region of data, and if there could be another mechanism to which the subadditive measurement is sensitive. Fig. 5.16(b) gives gives a plot of the suppression functions, $\chi(\tau)$, used in the old model (black), the refined model with $I_1 = I_2$ (blue), and a further refinement that allows for $I_1 \neq I_2$ (red). Specifically, a best-fit is obtained for the short-delay data when $I_2 = 0.57 I_1$. The blue and red curves result in the same best-fit to the long-delay data shown in Fig. 5.17. The Gaussian feature shown around 2.2 ps in Fig. 5.16(b) and Fig. 5.18 is accomplished by taking a value of $k(\tau)$ given by

$$k = \alpha' \exp - \left(\frac{\tau - \tau_0'}{\tau_w'}\right)^2, \tag{5.29}$$

where α' is the strength of the feature, τ_0' is the central time of the dip, and τ_w' is the width of the dip. The feature can then be eliminated by setting $k = 0$.
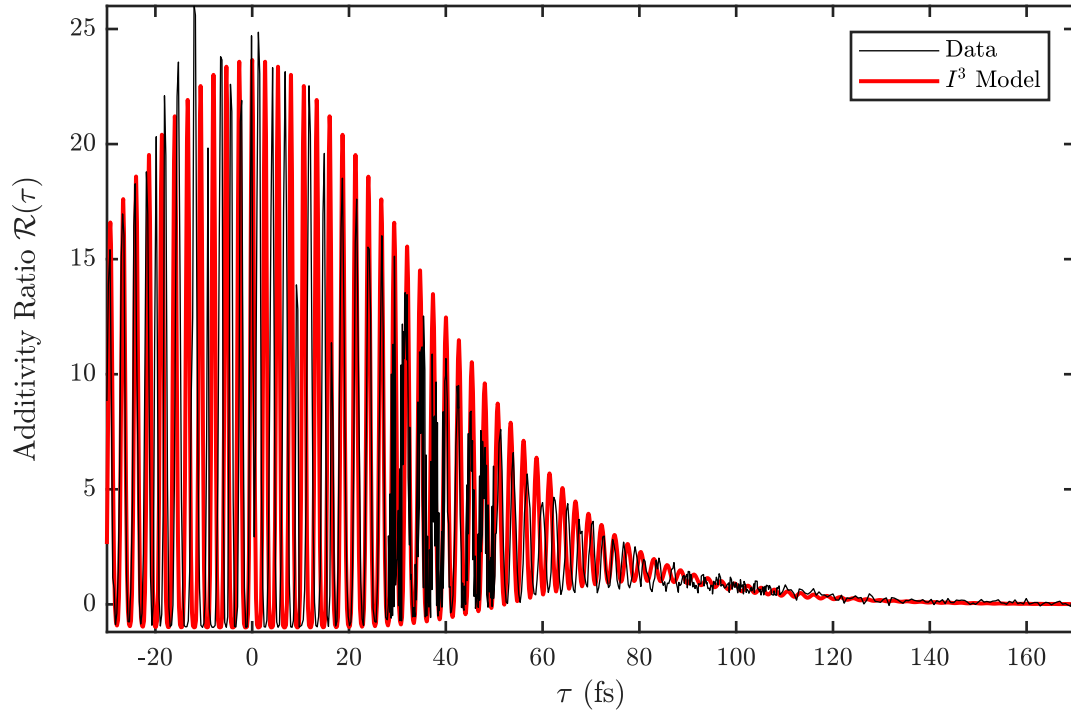
Figure 5.17: Shown is the additive ratio $\mathcal{R}(\tau)$ for short delays using the electric field and suppression function $\chi(\tau)$ shown in Fig. 5.16. For $\tau < 170\,\text{fs}$, the crosscorrelation ratio shows no subadditive behavior when the model (red) accounts for a linear temporal chirp.

In Fig. 5.17, the short delay (less than $170\,\text{fs}$) crosscorrelation ratio shows no subadditive behavior when the model (red) accounts for a linear temporal chirp. The subadditive behavior truly starts near $\tau_0 = 190\,\text{fs}$. The distinction between the two regimes is shown in Fig. 5.18- the tail at $\tau = 100\,\text{fs}$ (assuming $\chi(\tau) = 0$) is extended to later delays to show how typically additive emission behavior would drop to a ratio of 0. The extension of the subadditive model earlier from $190\,\text{fs}$ to $100\,\text{fs}$ shows how the two processes meet. This data shows that the GaAs emission process, that is, the intensity response, is shorter than $100\,\text{fs}$, with a long-delay subadditive feature. The subadditive feature effectively starts at a delay of $190\,\text{fs}$, and has a sharp turn-on time of $40\,\text{fs}$. The effect that results in subadditive emission is thus likely to be a fast process. The MATLAB script used to compute the new subadditive model is provided

in Appendix G.2.
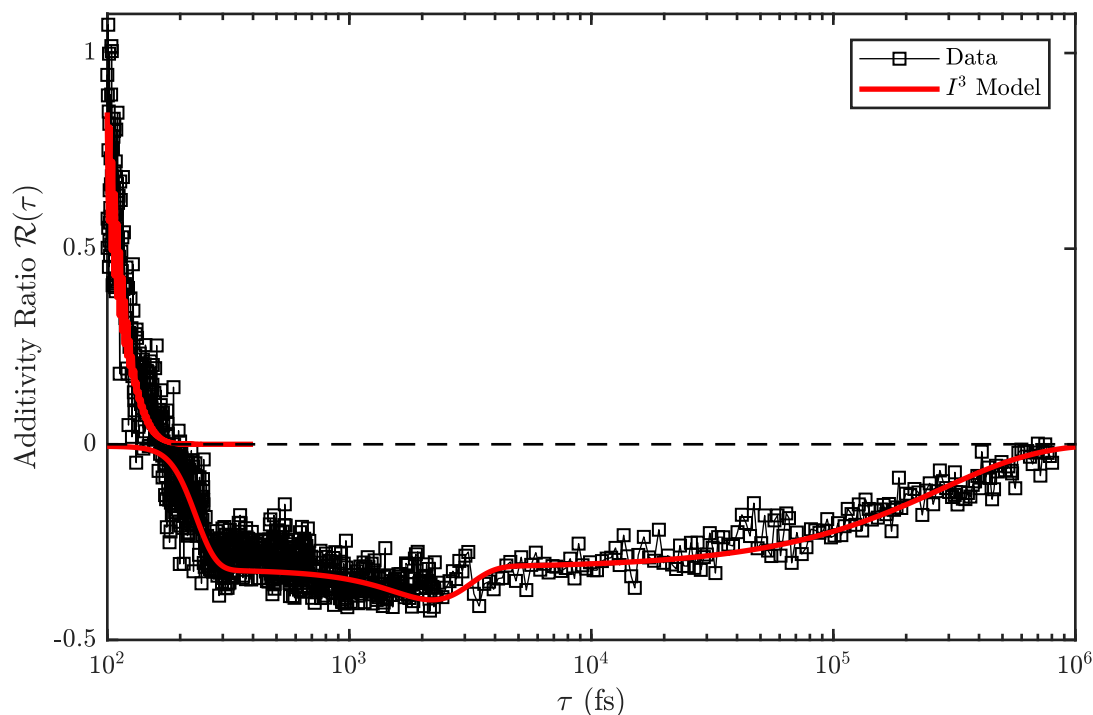
Figure 5.18: Shown is the additive ratio $\mathcal{R}(\tau)$ for long delays plotted in a logarithmic scale, using the electric field and suppression function $\chi(\tau)$ shown in Fig. 5.16. The subadditive behavior appears to start near 190 fs. The tail from the coming down from 100 fs, which was plotted without the inclusion of the suppression function, is extended to later delays to show how typical additive behavior would drop to a ratio of 0. The extension of the subadditive model earlier to 100 fs shows how the two processes meet. The model suggests that the mechanism responsible for subadditive emission has a width of $\tau_w = 40$ fs.

The complicated morphology of the shards begs the question, which of the local features is responsible for subadditive emission? To answer this question, pump/probe data were obtained from the sample shown in Fig. 5.13(b) as it was translated through the 5 μm laser focus. The count rates for the pump (blue), probe (green), and both (black) beams incident on the shard for $\tau = 2$ ps are plotted in Fig. 5.19(a) vs. the tip position.
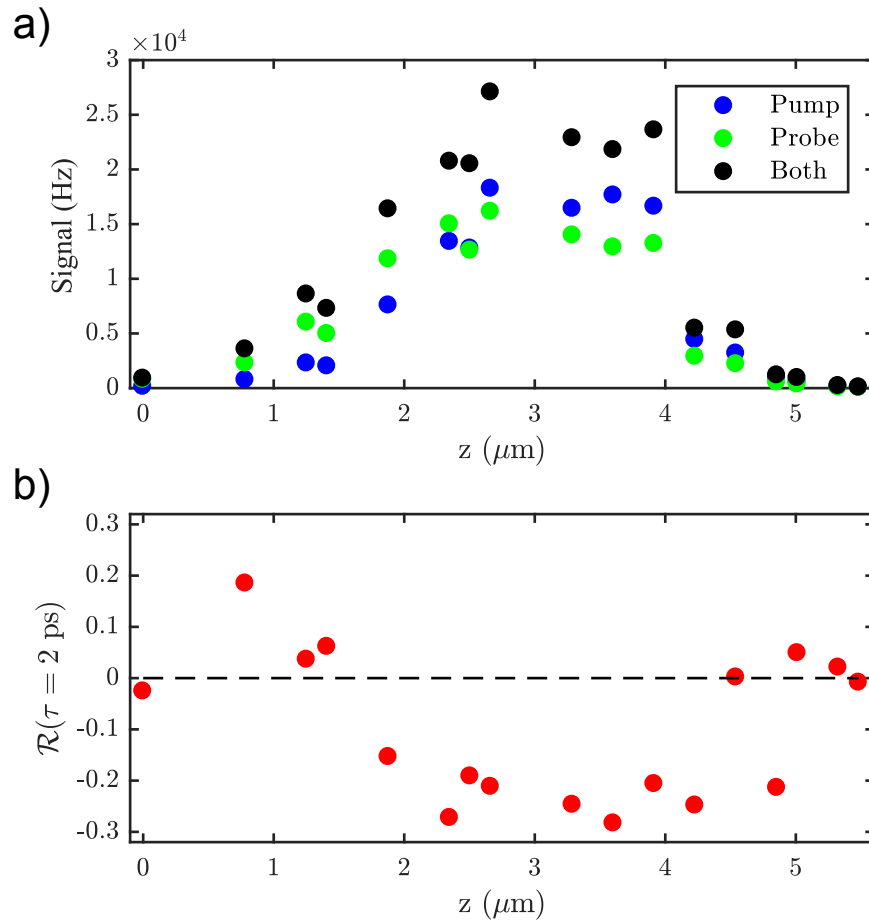
Figure 5.19: Shown is the position-dependence of electron emission of a GaAs shard translated into a laser focus. The emission rates from the pump (blue), probe (green) and both beams (black) incident on the shard apex at a delay of $\tau = 2\,\mathrm{ps}$ is plotted in (a). A Gaussian fit to the pump and probe count data, accounting for the I^5 emission process, gives a focal intensity FWHM of $5\,\mu\mathrm{m}$, which is slightly wider compared to the $4.5\,\mu\mathrm{m}$ width determined in Chapter 2.3. The resulting additive ratio $\mathcal{R}(\tau)$ is plotted in (b). The emission begins as additive, but becomes increasingly subadditive as the shard is translated past the focus.

Assuming an I^5 intensity dependence (as shown in Fig. 5.13(a)) to the single-beam data gives a focal intensity FWHM of $5\,\mu\mathrm{m}$. The resulting additive ratio, $\mathcal{R}(\tau)$, is plotted in Fig. 5.19(b). The emission remains additive until there is substantial overlap of the laser focus and the shard shank. The subadditivity then saturates as the shard apex is translated past the focus, until emission ceases.

In order to mitigate the complications arising from the unpredictable apex morphology arising from mechanically breaking samples into shards, an etching method was explored. The possibility of thinning GaAs shards via an etching solution was first demonstrated by Gobind Basnet in the research group of Bret N. Flanders, where our nanoribbon samples were prepared. Here, at the University of Nebraska-Lincoln, an undergraduate researcher, Zachary Rohde, prepared GaAs etchant solutions to reproduce regular arrays of GaAs pyramid structures.[31,32] The etching solution typically contained $52.1\,\text{mL}$ of $85\,\%$ H_3PO_4, $2.35\,\text{mL}$ of $30\,\%$ H_2O_2, and $1.8015\,\text{mL}$ of H_2O. The resulting ratio, in moles, of $H_3PO_4 : H_2O_2 : H_2O$, was then $10 : 0.30 : 8.23$. A GaAs shard sample was electrochemically etched in this solution in a method similar to that used to produce the gold nanotips shown in Fig. 2.13. The etching apparatus is shown in Fig. 5.20(a), with a simplified schematic in Fig. 5.20(b).
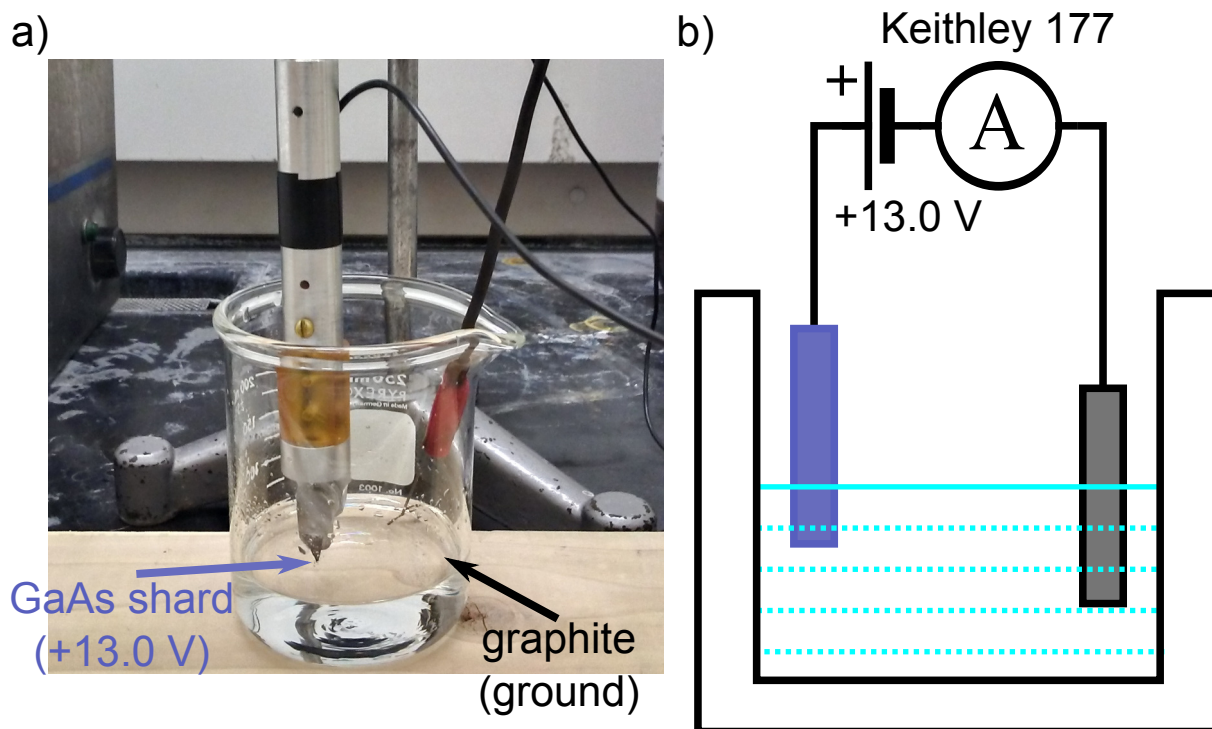
Figure 5.20: Schematic of GaAs wet etching, which is always performed under a fume hood. (a) A shard of GaAs is shown mounted to an SEM stub and lowered into a beaker of etching solution. The tip is biased with a DC voltage of 13.0 V relative to a graphite counterelectrode, similar to the method used to etch gold tips illustrated in Fig. 2.13. To etch the GaAs, a solution comprised of a $10 : 0.30 : 8.23$ molar ratio of $H_3PO_4 : H_2O_2 : H_2O$ is used, prepared by undergraduate researcher Zach Rohde. A Keithley 177 digital multimeter, connected in series with the graphite counterelectrode, was used to monitor the etching current during the process. As with the gold etching, the circuit was disconnected as soon as the etching current dropped to 0 A. A simplified schematic of the arrangement is shown in (b).

The shard sample was biased at 13.0 V relative to the graphite counterelectrode. This produced an etching current that drifted around 300 µA until dropping abruptly to 0 µA after several hours of etching. Once the current ceased, the etching circuit was disconnected and the sample was removed from the solution. As soon as it was possible, the shard was washed with methanol to rinse the excess solution.

The results of this round of etching on a single shard are shown in Fig. 5.21.
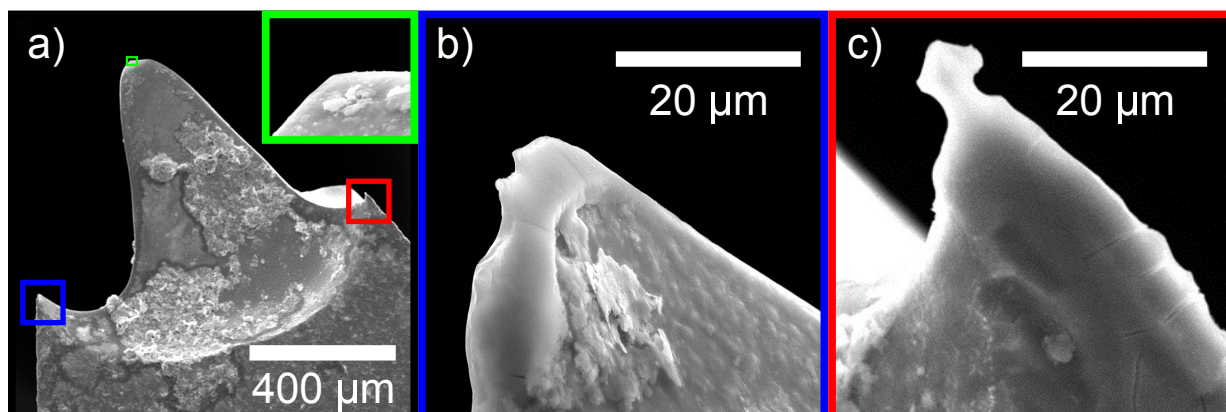
Figure 5.21: Shown are SEM micrographs of the shard etched by the process given in Fig. 5.20. (a) Full detail of the etched apex with a 400 µm scale indicated. The colored boxes highlight areas that are interesting to try as sources. The area at the very apex (green) is given as the inset. (b) A micrograph of the sharp feature to the left of the apex is shown. (c) A micrograph of the feature to the right of the apex is shown. What is intriguing about these features is that they are considerably more localized than the shard features indicated in Fig. 5.13. This suggests that an improved wet etching technique could be used to produce a suitable GaAs tip, or that wet etching could provide a good start for further processing, such as focused ion beam milling.

The entire sample is shown in (a) with a 400 µm scale bar indicated. The inset (green border) shows the central sharp feature, while (b) and (c) show the left (blue border) and right (red border) sharp tip-like features. The inset, (b), and (c) are all shown with the same scale. Compared to the sample imaged in Fig. 5.13(b), the sharp features shown here are clearly distinguishable from the bulk. While the features shown are not quite nanoscale, it is feasible that this electrochemical wet etching procedure could produce a more well-defined substrate for further tip shaping. What remains to be determined is if the etched shards will emit under femtosecond laser illumination, and if that emission maintains or improves upon the 13 % P_e measured from the shard samples.

5.7   Conclusions

Improving the quantum degeneracy of an electron source will make falsifiable free electron HBT measurements a possibility. It is proposed that the quantum degeneracy can be increased orders of magnitude from what is currently available by employing nanostructures illuminated by a femtosecond laser. As HBT measurements for photons heralded the beginning of quantum optics, so too could degenerate electron sources lead to free electron quantum optics. The results of an electron HBT measurement have been shown here to have implications on describing the emission mechanism from a sharp tip illuminated by a femtosecond laser and in the free propagation of electron wave packets through the diffraction in time phenomenon. Distinguishing the anticorrelations due to Pauli pressure from Coulomb pressure in the electron HBT signal can be accomplished with a femtosecond, nanometer, spin-polarized source, which is now achievable due to our efforts with obtaining pulsed electron emission from GaAs shards.

Chapter 6

Reactions and outlook

6.1   Reception of "Path integrals, matter waves, and the double slit"

The work presented in Chapter 3 was published in the *European Journal of Physics.*[48] The original arXiv posting of a draft of the manuscript gained immediate attention from Dr. Mathieu Beau, a Postdoctoral Research Fellow at the University of Massachusetts Boston.[211] In his correspondence, he pointed out that the path integral methods we used to compute double slit interference, that is, summing over the intermediate slit time or choosing the appropriate paths of stationary phase, gave similar results to those he had obtained with the Green's function method.[151] He indicated that he was not able to solve his particular problem with the path integral formalism. This interaction is what eventually lead to my considering to use the path integral method to obtain the results of Chapter 5, where after some months of developing simulations, I discovered that the research group of Jean Dalibard had earlier used the summing over time method with path integrals to describe their first experimental realizations of diffraction in time.[186] After publication, our manuscript was selected by the editors of EJP for inclusion in the "Highlights of 2015" collection. The certificate signifying this distinction is reproduced on the following page.
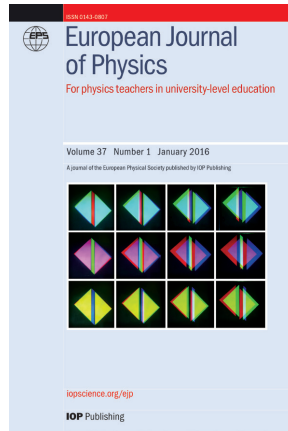
European Journal of Physics

This is to certify that the article

Path integrals, matter waves, and the double slit
by Eric R Jones, Roger A Bach and Herman Batelaan

has been selected by the editors of *European Journal of Physics* for inclusion in the exclusive 'Highlights of 2015' collection. This paper has been chosen for its quality and contribution to the community.

Michael Vollmer
Editor-in-chief
European Journal of Physics
iopscience.org/ejp

6.2   Reactions to "Momentum exchange in the electron double-slit experiment"

A portion of the work presented in Chapter 4 toward replicating Couder's single- and double-slit oil drop diffraction experiments[57] was published in a Journal of Physics: Conference Series article titled, "Momentum exchange in the electron double-slit experiment."[102] Our conclusion from the data we obtained is that we were unable to reproduce Couder's results.

The publication of our article followed the publication of an article to Physical Review E from the fluid mechanics group of Thomas Bohr at the Technical University of Denmark, titled "Double-slit experiment with single wave-driven particles and its relation to quantum mechanics."[103] They reported no deflection in their walker trajectories, remarking that their distribution was indistinguishable from a Gaussian. They conceived of a Gedankenexperiment that considered a double-slit scenario where the slits were separated by a long and thin barrier, claiming that such a barrier would prevent the real wave field of walkers from interacting with the second slit, while for a quantum mechanical scenario the wall would have no effect on the interference pattern. The argument was that the oil drop analogue would here deviate from what was expected from quantum mechanics, and therefore defeated the correspondence. They concluded that "the long and variable slit passage times of the droplets, together with the weakness of the wave field through the other slit, cast strong doubt on the feasibility of the interference reported by Couder and Fort." Nonetheless, they concurred with Couder and Fort's observation that oil droplet trajectories were not repeatable, meaning that a distribution of walkers launched from the same initial position would not follow identical trajectories.

Contradictory results to both experimental reports were obtained from the fluid

mechanics group of John W. M. Bush at MIT, where through careful control of the apparatus parameters and walker initial conditions, it was shown that walker trajectories could not only be repeated, but that they could in principle show peaked diffraction-like behavior.[104] While this particular effect was attributed to interactions between the walkers and the submerged slit boundaries, the experiment demonstrated rather conclusively that the results of any oil drop experiment depend on how the experiment is carried out and the environmental conditions in which the experiment is performed. It is important to note that Couder's original results were not verified here. As these results differed from both Couder's and Bohr's, it would seem that there is now a controversy to be settled and an open question if oil droplet analogues can demonstrate diffraction from slits.

The controversy was picked up and reported recently in an article published online October 11, 2018 in *Quanta Magazine*, which is a nationally syndicated science journalism publication funded by the Simons Foundation. The article, titled "Famous Experiment Dooms Alternative to Quantum Weirdness," written by senior writer Natalie Wolchover, focused almost singularly on Bohr's argument that the oil drop analogue had been defeated.[105] From the subheading, Wolchover asserts that the failure of Bohr to replicate Couder's original results meant that "[o]il droplets guided by 'pilot waves' have failed to reproduce the results of the quantum double-slit experiment, crushing a century-old dream that there exists a single, concrete reality."

Wolchover's article in *Quanta* picked up immediate attention from Emmanuel Fort, who was a member of Couder's research group and the second author on the original 2006 Physical Review Letters paper demonstrating oil droplet diffraction. Fort engaged Wolchover in the public comments to criticize the tone and biased presentation of the article.[212] He pointed out that none of the original researchers from Couder's group were interviewed prior to the publication of the article. He also pointed out that the

conclusion of the article could not be supported by the contradictory results obtained from Bohr and Bush. Fort wrote, "This is why my colleague Yves, who is a true scientist, naturally said that the reason for which there was such a disparity in the results obtained by the different groups was still to be discovered and understood. By the way, John Bushs quote in your paper states exactly that in contradiction with the tone of your article!" Fort continued, "What you could say is this: given the fact that ALL the experiments give different results, there is probably a parameter still hidden and yet to be found. As you will note, I am not saying that our results are devoid of some experimental biases. We just, for now, dont know. This is the definition of research." He wrote, that while the system of walkers is not quantum mechanical, "Walkers give an intuition about what a dual wave-particle object can be, in our macroscopic world where waves and particles are usually separated. [...] Walkers are bouncing droplets not quantum objects and you cannot pretend to answer the debate on reality (which is mainly related to entanglement and Bells inequality) with this experiment." In short, while the system of walking droplets can inform what ways particle-wave duality could emerge in classical systems, the failure of a walker experiment to reproduce a quantum mechanical result does not exclude the system from further investigation, nor does it have any bearing on quantum foundations.

John W. M. Bush had prepared a statement to add to the comments in defense of the field, but declined to post it publicly.[213] As it clearly summarizes the failures of the article and defends the study of the quantum hydrodynamic analogy, it is in part reproduced here. Bush concurred with Fort's claims, in that the results from Pucci's 2018 paper on the droplet single- and double-slit were more in line with Couder's and Fort's original observations and contradictory to Bohr's. He wrote,

> First, our single-slit results were largely in line with the experiments of Couder & Fort; specifically, there were three peaks, a central peak and a pair of side-

peaks centered at roughly 60 degrees. Second, in the double-slit geometry, the trajectory of a drop passing through either slit is affected by both slits, a feature erroneously contested by Andersen et al. (2016). Third, the fact that Andersen et al. (2016) saw no multimodal structure in their histograms simply reflects the shortcomings of their experiments, specifically, the dominant influence of the bounding geometry and air currents. With all due respect to the authors, their experiments were by no means definitive, and their gedanken experiment debatable. It is thus that their study has failed to discourage any of those capable of making serious contributions to the problem.

In regards to the claim of the *Quanta* article's subheading, Bush said:

Furthermore, as noted by Emmanuel Fort, it is important to bear in mind that there are three pilot-wave systems being discussed in this forum, each different. The first two, Bohmian mechanics and de Broglies double-solution theory, are quantum pilot-wave theories. The third is the hydrodynamic pilot-wave system discovered by Couder & Fort. The failure of the hydrodynamic pilot-wave system to capture a particular feature of quantum mechanics simply reflects its shortcomings as a quantum analog. Such has no bearing whatsoever on the viability of quantum pilot-wave theories to provide a dynamical underpinning for quantum statistics.

Bush goes on to argue that the hydrodynamic system is worthy of study in its own right.

The hydrodynamic pilot-wave system is an example of a particle moving in synchrony with its own wave field. As such, it is a rich dynamical system worthy of study in its own right. It extends the range of classical systems to include certain features of quantum systems; moreover, it bears a striking resemblance to de Broglies original pilot-wave framework, which provided a number of cornerstones of quantum theory. Given the philosophical extravagance of the prevailing view somehow promulgated from Copenhagen, that there is no quantum reality beyond the wave function, it would seem irresponsible not to explore the dynamical range of this hydrodynamic system. Its ability to capture certain features of quantum systems is remarkable; its inability to capture others is to be expected. By declaring one such shortcoming, debatable as it is, to be fatal for the entire field of pilot-wave hydrodynamics and, by unjustified extrapolation, for quantum pilot-wave theory, the article unfortunately encourages a return to the defeatist stance that 'No one understands quantum mechanics, so dont even bother trying,' a position that best assures that no progress be made. I believe that a more thoughtful, constructive article would have detailed the many successes of both hydrodynamic and quantum pilot-wave theories.

Bush then expressed his feelings regarding the quality of argument provided by the reporting in *Quanta*, stating:

> Were the bar for mechanistic understanding in quantum mechanics not set so pitifully low, perhaps we would be less encouraged by the conceptual headway being made by our field, more easily put off by impossibility proofs of dubious relevance, and more concerned by the errant news of our doom.
>
> To summarize, the best research asks good questions. I would put Couder & Forts paper in that category. The worst type of research answers these questions incorrectly. And the worst type of scientific journalism cant tell the difference.

To summarize both Fort's and Bush's sentiments, the reporting presented in *Quanta* was made in poor taste. At worst, it was as Fort suggested, an exercise in calumny. The response, though, is worth a discussion, and is included as Appendix H. In my opinion, the field of hydrodynamic analogues to quantum systems remains open to further investigation, and serious researchers in the field are continuing to determine if systems of walkers can indeed reproduce single- and double-slit diffraction.

6.3 Outlook for "Femtosecond-laser-induced spin-polarized electron emission from a GaAs tip"

A portion of the work discussed in Chapter 5, Section 5.6 was recently published in Applied Physics Letters as "Femtosecond-laser-induced spin-polarized electron emission from a GaAs tip."[34] Using a semiconductor shard illuminated with femtosecond laser light to produce a fast, spin-polarized electron source has been written into a provisional patent, tentatively titled "Fast spin-polarized electron source."[214] The first claims of the provisional patent thus far cover:

1. A source of fast spin-polarized electrons as substantially described herein.

2. A method of producing fast spin-polarized electrons as substantially described herein.

3. A source of fast spin-polarized electrons, comprising: a target material comprising a sharp tip or a sharp edge or a cusp, the sharp tip comprising at least two intersecting edges; and a pulsed light source that emits light pulses focused on the sharp tip or the sharp edge or the cusp to thereby

induce emission of spin-polarized electrons from the sharp tip or the sharp edge or the cusp of the target material.

4. The source of fast spin-polarized electrons according to claim 3, wherein the target material comprises GaAs.

5. The source of fast spin-polarized electrons according to claim 3, wherein the target material comprises ZnSe, or GaAsP, or GaAs doped with Zn or Cd.

6. The source of fast spin-polarized electrons according to claim 3, wherein the pulsed light source comprises a pulsed laser.

7. The source of fast spin-polarized electrons according to claim 3, wherein the pulsed light source comprises a pulsed laser that emits laser pulses each having a duration of between about 10 fs and 0.1 ps.

The wording of Claim 5 was introduced to accommodate an idea I proposed for an alternative spin-polarized source that utilized zinc selenide (ZnSe), which is a II-VI semiconductor having a 2.72 eV band gap and a long spin coherence time.[215,216] My proposal followed from the experimental observation of spin currents in GaAs utilizing pulses of 1600 nm and frequency-doubled 800 nm laser light,[217] and then later in ZnSe utilizing collinear pulses of 800 nm and frequency-doubled 400 nm laser light.[218] It was found that the spin currents optically injected into the ZnSe samples could be coherently controlled, meaning that the process did not require high intensities. Combining cocircularly polarized ω and 2ω pulses, delayed by a time τ, resulted in pure spin currents parallel to the propagation direction of the exciting laser pulses, with a spin-polarized electrical current transverse to the propagation of the exciting laser pulses (see Fig. 1(a) of Ref. [218]). The direction of the current depends on the delay τ between the two pulses, and the spin orientation depends on the helicity of the light chosen. As it has been shown that spin currents can be transferred between materials sharing an interface,[219] I reasoned that the spin-polarized electric current might be extracted from an appropriate ZnSe nanostructure into the vacuum, by either a dc voltage or multiphoton emission process. As the resulting electric current is completely polarized, such a source might result in significantly higher spin

polarizations than have been realized yet with our GaAs tip. A schematic of the source is given in Fig. 6.1.
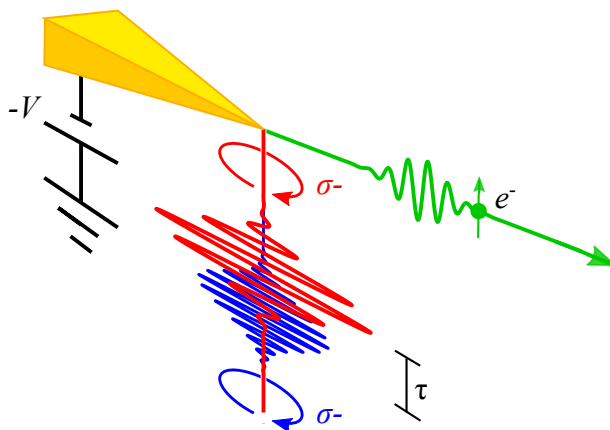
Figure 6.1: Shown is a schematic of a proposed fast, spin-polarized source utilizing a ZnSe nanostructure. Pulses of left-handed circularly polarized ($\sigma-$) $\omega - 2\omega$ light are delayed by a time τ, and then focused onto the ZnSe nanostructure tip (gold structure, upper left), which is biased at a voltage $-V$. The resulting electron pulses (green) should have a spin polarization determined by the light helicity chosen. As ZnSe reacts with acids, it is in principle feasible to etch a crystalline sample into a sharp tip.

Pulses of cocircularly polarized light are produced by first frequency-doubling $800\,\mathrm{nm}$ laser light into its second harmonic at $400\,\mathrm{nm}$. The pulses are divided by means of a dichroic beam splitter, delayed by a time τ such that the two pulses remain temporally overlapped, and then delivered to the tip of a ZnSe nanostructure biased at a voltage $-V$. For our purposes, the bias voltage is typically $-100\,\mathrm{V}$. As we have previously developed and demonstrated an $\omega - 2\omega$ interferometer in our research group,[130] what remains to be developed is the appropriate source target. ZnSe can be etched by acids, but one of the by-products of the etching process is H_2Se gas, which is toxic. Crystalline samples of ZnSe are also costly (for example, one price quote from Semiconductor Wafer Inc. gave a price of \$400 for a single [110] or [111] $10 \times 10 \times 0.5$ mm wafer, with a minimum order of 3). In Ref. [218], the ZnSe was grown epitaxially

on a GaAs substrate to a thickness of 290 nm. As we understand how to etch GaAs samples, it may be possible to combine the processes to obtain ZnSe nanostructures.

Appendix A

Path Integral Source Code

A.1   Path integral Fortran Code, with time summing

```fortran
PROGRAM Fig6

!————————————————————————————————
! 2015−03−23
!
! Generate PDF of all paths summed over time
! and slit position for stationary phase,
! intuitive, and full sum amplitudes to be
! incorporated into Figure 6 of
! "Path integrals and the double slit"
!————————————————————————————————

IMPLICIT NONE
!Define generic subroutine that takes any of the arrays the program encounters
!(real1D, complex, complex2D) and sets all the values to 0d0

INTERFACE init_array
    SUBROUTINE init_array1d(A, alpha)
    INTEGER*8 :: i
    REAL*8   :: A(:), alpha
    END SUBROUTINE init_array1d

    SUBROUTINE init_array2d(R, alpha)
    REAL*8   :: R(:,:), alpha
    INTEGER*8 :: s, t
    END SUBROUTINE init_array2d

    SUBROUTINE init_arrayC(B, alpha)
    INTEGER*8 :: r
    COMPLEX*16 :: B(:), alpha
    END SUBROUTINE init_arrayC

    SUBROUTINE init_array2dC(D, alpha)
    COMPLEX*16   :: D(:,:), alpha
    INTEGER*8 :: j, k
    END SUBROUTINE init_array2dC
END INTERFACE init_array

INTERFACE
    SUBROUTINE init_random_seed()
    IMPLICIT NONE
    INTEGER, ALLOCATABLE :: seed(:)
```

```fortran
        INTEGER                     :: i,n,un,istat,dat(8),pid,tim(2),s
        INTEGER(8)                  :: cownt, tms
        END SUBROUTINE init_random_seed
END INTERFACE

INTERFACE randfill
    SUBROUTINE randfill1d(A,arbinterval)
    IMPLICIT NONE
    INTEGER*8           :: i
    REAL*8, INTENT(IN) :: arbinterval
    REAL*8              :: A(:),B(size(A))
    END SUBROUTINE randfill1d

    SUBROUTINE randfill2d(B,arbinterval)
    IMPLICIT NONE
    INTEGER*8           :: i,j
    REAL*8, INTENT(IN) :: arbinterval
    REAL*8              :: B(:,:)
    REAL*8 :: C(size(B,1),size(B,2))
    END SUBROUTINE randfill2d
END INTERFACE randfill

! Define sqrt(-1) to double-precision
COMPLEX*16, PARAMETER :: I = (0d0, 1d0)
COMPLEX*16, PARAMETER :: Psi0 = (0d0,0d0),K0 = (0d0,0d0)

! Take Nscreen = 2 when time summing (for inset)
INTEGER*8, PARAMETER :: Nmid = 3000, Nscreen = 1000, &
                        Ntimediv = 0, & ! 2 paths from slits converge for 500000 500000
                        intorder = 305

!Define real constants defining experimental set-up
!and grid sizes
REAL*8, PARAMETER :: Pi = 3.1415926535898d0, &
        Hbar = 1.05457173d-34, m = 9.10938291d-31, &
        wslit = 63d-9, dslit = 273d-9, &
        yoffset1 = dslit / 2d0, yoffset2 = dslit / 2d0- 2.73d-7, & !
        ymidgrid = wslit, yscreengrid = 1d-6, &
        !1d-6 for fig6, 2d-9 for inset, 1.75d-9 for tsum comparison
        tinterval = 1d-13, & !2d0*1.10142833717d-15, 5.0462446d-29 gives no change
        deltatint = 1d-13, &
        ! 7.200007502769d-15 for +/-5%, 3.443408599950290802669d-14 for +/-1% in Phi
        deltat = deltatint !/ DFLOAT(Ntimediv)

!Step sizes for ymid and yscreen. Skip these if Nmid and Nscreen = 0
REAL*8, PARAMETER :: deltaymid = ymidgrid / (2d0 * Nmid), &
                     deltayscreen = yscreengrid / (2d0 * Nscreen)

!Use these values when Nmid and Nscreen = 0
! REAL*8, PARAMETER :: deltaymid = ymidgrid, &
        ! deltayscreen = yscreengrid

!Arrays for time and distance
REAL*8 :: xsource, ysource, tsource

REAL*8 :: xmid(-Nmid:Nmid),ymid(-Nmid:Nmid), &
        yslit1(-Nmid:Nmid),yslit2(-Nmid:Nmid)

REAL*8 :: tmin1, tmin2, tslit1, tslit2, alpha!, deltat

REAL*8 :: xscreen(-Nscreen:Nscreen), &
        yscreen(-Nscreen:Nscreen), &
        tscreen(-Nscreen:Nscreen)

REAL*8 :: phaseslitmin1( -Nmid:Nmid ), &
        phaseslitmin2( -Nmid:Nmid )

REAL*8 :: phasescreenmin1( -Nmid:Nmid,-Nscreen:Nscreen ), &
```

```fortran
                  phasescreenmin2( -Nmid:Nmid,-Nscreen:Nscreen )

COMPLEX*16  ::  Ksourcemin1T( -Nmid:Nmid ), &
                Ksourcemin2T( -Nmid:Nmid )

COMPLEX*16  ::  Kslitmin1T( -Nmid:Nmid, -Nscreen:Nscreen ), &
                Kslitmin2T( -Nmid:Nmid, -Nscreen:Nscreen )

! Intuitive method definitions
REAL*8  ::  phaseslit1( -Nmid:Nmid ), &
            phaseslit2( -Nmid:Nmid )

REAL*8  ::  phasescreen1( -Nmid:Nmid,-Nscreen:Nscreen ), &
            phasescreen2( -Nmid:Nmid,-Nscreen:Nscreen )

COMPLEX*16  ::  Ksource1T( -Nmid:Nmid ), &
                Ksource2T( -Nmid:Nmid )

COMPLEX*16  ::  Kslit1T( -Nmid:Nmid, -Nscreen:Nscreen ), &
                Kslit2T( -Nmid:Nmid, -Nscreen:Nscreen )

!Arrays for the amplitudes
COMPLEX*16  ::  Psisource
COMPLEX*16  ::  Psislitmin1(-Nmid:Nmid), &
                Psislitmin2(-Nmid:Nmid)
COMPLEX*16  ::  Psitimetempmin(-Nscreen:Nscreen)
COMPLEX*16  ::  Psiscreenmin(-Nscreen:Nscreen)

REAL*8  ::  PDFmin(-Nscreen:Nscreen)

COMPLEX*16  ::  Psislit1(-Nmid:Nmid), &
                Psislit2(-Nmid:Nmid)
COMPLEX*16  ::  Psiscreen(-Nscreen:Nscreen)

REAL*8  ::  PDF(-Nscreen:Nscreen)

INTEGER*8      ::  p,q,n,j
REAL*8         ::  sumintmin, sumint

! COMPLEX*16 :: Psitemp1,Psitemp2
COMPLEX*16  ::  Psitempmin1,Psitempmin2
COMPLEX*16  ::  Psitemp1,Psitemp2

!Set variables that were previously parameters
REAL*8  ::  lambda, v , &
            sourcet, screent, &
            Lscale, lambscale, sourcedist, screendist

Lscale = DSQRT(DFLOAT(intorder)/2d0)
lambscale = DSQRT(2d0/(DFLOAT(intorder))**3d0)

sourcedist = Lscale * dslit
screendist = Lscale * dslit

lambda = lambscale * dslit
v = 2d0 * Pi * Hbar / (lambda * m)

!v = 1d7
sourcet = sourcedist/v
screent = screendist/v

alpha = (2d0 * m * sourcedist**2d0) / &
        (hbar * (sourcet + screent))

PRINT*, 'Value of alpha:', alpha
PRINT*, 'Source distance:',sourcedist
PRINT*, 'sourcet:',sourcet
PRINT*, 'Lambda:', lambda
```

```
PRINT*, 'd^4 / L^3:', dslit**4d0 / (2d0*sourcedist**3d0)

PRINT*, 'Velocity (10^7 m/s):', v/1d7

!Initialize all 1-d arrays to zero
PRINT*, 'Initializing 1-D arrays'
xsource = 0d0
ysource = 0d0 + yoffset1
tsource = 0d0

PRINT*, 'sourcet', sourcet
PRINT*, 'screent', screent

CALL init_array(xmid,sourcedist)
CALL init_array(ymid,0d0)
CALL init_array(yslit1,0d0)
CALL init_array(yslit2,0d0)

tmin1 = 0d0
tmin2 = 0d0
tslit1 = 0d0
tslit2 = 0d0

CALL init_array(xscreen,sourcedist+screendist)
CALL init_array(yscreen,0d0)
CALL init_array(tscreen,sourcet+screent)

!Initialize the complex arrays to zero
PRINT*, 'Initializing complex arrays'
Psisource = COMPLEX(1d0,0d0)

CALL init_array(Psislitmin1,Psi0)
CALL init_array(Psislitmin2,Psi0)
CALL init_array(Psitimetempmin,Psi0)
CALL init_array(Psiscreenmin,Psi0)

CALL init_array(Psislit1,Psi0)
CALL init_array(Psislit2,Psi0)
CALL init_array(Psiscreen,Psi0)

!Initialize the phase arrays to zero
PRINT*, 'Initializing phase arrays'

CALL init_array(phaseslitmin1,0d0)
CALL init_array(phaseslitmin2,0d0)
CALL init_array(phasescreenmin1,0d0)
CALL init_array(phasescreenmin2,0d0)

CALL init_array(phaseslit1,0d0)
CALL init_array(phaseslit2,0d0)
CALL init_array(phasescreen1,0d0)
CALL init_array(phasescreen2,0d0)

!Initialize the propagators
PRINT*, 'Initializing propagators'

CALL init_array(Ksourcemin1T,K0)
CALL init_array(Ksourcemin2T,K0)
CALL init_array(Kslitmin1T,K0)
CALL init_array(Kslitmin2T,K0)

CALL init_array(Ksource1T,K0)
CALL init_array(Ksource2T,K0)
CALL init_array(Kslit1T,K0)
CALL init_array(Kslit2T,K0)

!Initialize the PDF
```

```
PRINT*, 'Initializing PDF'

CALL init_array(PDFmin,0d0)
CALL init_array(PDF,0d0)


! Initialize the random number generator once per execution
! This was not used in final figure prep
CALL init_random_seed()

!Set up y grids (slit1 is top slit, slit2 is bottom)
DO p = -Nmid, Nmid
     ymid(p) = DFLOAT(p) * deltaymid
     yslit1(p) = ymid(p) + dslit / 2d0
     yslit2(p) = ymid(p) - dslit / 2d0
END DO

DO q = -Nscreen, Nscreen
     yscreen(q) = DFLOAT(q) * deltayscreen + yoffset2
END DO

PRINT*, 'Timesumming!'
! Used for testing turning off a slit (* Psi0), time sum, or inset
! OPEN(UNIT=29, FILE="stphase_full_slit2off.txt")
! OPEN(UNIT=30, FILE="stphase_inset_slit2off.txt")
! OPEN(UNIT=31, FILE="intuitive_inset_slit2off.txt")
! OPEN(UNIT=32, FILE="tsum_inset_points.txt")
! OPEN(UNIT=33, FILE="intuitive_full_slit2off.txt")

DO q = -Nscreen, Nscreen
! q = 0
     ! j = Ntimediv * 0
     ! deltat = deltatint / DFLOAT(j)

     j = Ntimediv

     Psitemp1 = COMPLEX(0d0,0d0)
     Psitemp2 = COMPLEX(0d0,0d0)

     Psitempmin1 = COMPLEX(0d0,0d0)
     Psitempmin2 = COMPLEX(0d0,0d0)

          DO p = -Nmid,Nmid
          ! p = 0

          tmin1 = (DSQRT((xmid(p)-xsource)**2d0 + &
                         (yslit1(p)-ysource)**2d0)) / &
                       ( (DSQRT((xscreen(q)-xmid(p))**2d0 + &
                         (yscreen(q)-yslit1(p))**2d0)) + &
                         (DSQRT((xmid(p)-xsource)**2d0 + &
                         (yslit1(p)-ysource)**2d0)) ) * &
                         (sourcet + screent)

          tmin2 = (DSQRT((xmid(p)-xsource)**2d0 + &
                         (yslit2(p)-ysource)**2d0)) / &
                       ( (DSQRT((xscreen(q)-xmid(p))**2d0 + &
                         (yscreen(q)-yslit2(p))**2d0)) + &
                         (DSQRT((xmid(p)-xsource)**2d0 + &
                         (yslit2(p)-ysource)**2d0)) ) * &
                         (sourcet + screent)

               ! Internal time-summing loop.
               ! Uncomment shift in tslit1 and tslit2, as sum is performed symmetrically
               ! about tmin1 and tmin2, respectively.
               ! DO n = -j,j

               tslit1 = tmin1  !+ DFLOAT(n)* deltat
```

```fortran
tslit2 = tmin2 !+ DFLOAT(n)* deltat

phaseslitmin1(p) = (0.5d0 * m / Hbar) * &
    (((xmid(p) - xsource)**2d0 + &
        (yslit1(p)-ysource)**2d0)) / &
            (tslit1 - tsource)

phaseslitmin2(p) = (0.5d0 * m / Hbar) * &
    (((xmid(p) - xsource)**2d0 + &
        (yslit2(p)-ysource)**2d0)) / &
            (tslit2 - tsource)

phasescreenmin1(p,q) = (0.5d0 * m / Hbar) * &
        (((xscreen(q) - xmid(p))**2d0 + &
            (yscreen(q)-yslit1(p))**2d0)) / &
                (tscreen(q) - tslit1)

phasescreenmin2(p,q) = (0.5d0 * m / Hbar) * &
        (((xscreen(q) - xmid(p))**2d0 + &
            (yscreen(q)-yslit2(p))**2d0)) / &
                (tscreen(q) - tslit2)

Ksourcemin1T(p) = CDEXP(I*phaseslitmin1(p)) * &
                    DSQRT(m / (2d0*Pi*Hbar * &
                    (tslit1 - tsource)))* &
                    CDEXP(-I*Pi/4d0)

Ksourcemin2T(p) = CDEXP(I*phaseslitmin2(p)) * &
                    DSQRT(m / (2d0*Pi*Hbar * &
                    (tslit2 - tsource)))* &
                    CDEXP(-I*Pi/4d0)

Kslitmin1T(p,q) = CDEXP(I*phasescreenmin1(p,q)) * &
                    DSQRT(m / (2d0*Pi*Hbar * &
                    (tscreen(q) - tslit1)))* &
                    CDEXP(-I*Pi/4d0)

Kslitmin2T(p,q) = CDEXP(I*phasescreenmin2(p,q)) * &
                    DSQRT(m / (2d0*Pi*Hbar * &
                    (tscreen(q) - tslit2)))* &
                    CDEXP(-I*Pi/4d0)

phaseslit1(p) = ( m / Hbar) * v * &
            DSQRT( (xmid(p) - xsource)**2d0 + &
                    (yslit1(p) - ysource)**2d0 )

phaseslit2(p) = ( m / Hbar) * v * &
                DSQRT( (xmid(p) - xsource)**2d0 + &
                        (yslit2(p) - ysource)**2d0 )

phasescreen1(p,q) = ( m / Hbar) * v * &
                DSQRT((xscreen(q) - xmid(p))**2d0 + &
                        (yscreen(q)-yslit1(p))**2d0)

phasescreen2(p,q) = ( m / Hbar) * v * &
                DSQRT((xscreen(q) - xmid(p))**2d0 + &
                        (yscreen(q)-yslit2(p))**2d0)

!Use path length to set time interval when using 2piL/lambda phase
Ksource1T(p) = CDEXP(I*phaseslit1(p)) * &
                DSQRT(m / (2d0*Pi*Hbar * &
                (DSQRT( (xmid(p) - xsource)**2d0 + &
                        (yslit1(p) - ysource)**2d0 ))/v)) * &
                CDEXP(-I*Pi/4d0)
```

```
Ksource2T(p) = CDEXP(I*phaseslit2(p)) * &
                DSQRT(m / (2d0*Pi*Hbar * &
                (DSQRT(  (xmid(p) - xsource)**2d0 + &
                         (yslit2(p) - ysource)**2d0 ))/v)) * &
                CDEXP(-I*Pi/4d0)

Kslit1T(p,q) = CDEXP(I*phasescreen1(p,q)) * &
                DSQRT(m / (2d0*Pi*Hbar * &
                (DSQRT((xscreen(q) - xmid(p))**2d0 + &
                       (yscreen(q)-yslit1(p))**2d0))/v)) * &
                CDEXP(-I*Pi/4d0)

Kslit2T(p,q) = CDEXP(I*phasescreen2(p,q)) * &
                DSQRT(m / (2d0*Pi*Hbar * &
                (DSQRT((xscreen(q) - xmid(p))**2d0 + &
                       (yscreen(q)-yslit2(p))**2d0))/v)) * &
                CDEXP(-I*Pi/4d0)

!Propagate the wavefunction from source to slit (min phase)
Psislitmin1(p) = Ksourcemin1T(p) * Psisource
Psislitmin2(p) = Ksourcemin2T(p) * Psisource !* Psi0

Psitempmin1 = Psitempmin1 + Kslitmin1T(p,q) * &
                Psislitmin1(p) / (2d0 * Nmid)

Psitempmin2 = Psitempmin2 * Psi0 + Kslitmin2T(p,q) * &
                Psislitmin2(p) / (2d0 * Nmid)

!lambda phase
Psislit1(p) = Ksource1T(p) * Psisource
Psislit2(p) = Ksource2T(p) * Psisource !* Psi0

Psitemp1 = Psitemp1 + Kslit1T(p,q) * Psislit1(p) / &
             (2d0 * Nmid)

Psitemp2 = Psitemp2 * Psi0 + Kslit2T(p,q) * Psislit2(p) / &
             (2d0 * Nmid)

! END DO ! uncomment to run time loop


        END DO !slit loop

Psitimetempmin(q) = Psitempmin1 + Psitempmin2 + &
                     Psitimetempmin(q)

Psiscreenmin(q) = (Psitimetempmin(q)) !* &
              ! 2d0*deltatint / (DFLOAT(2*Ntimediv+1))
              ! Factor to compare time sum to integral- use when time summing.
PDFmin(q) = REALPART(DCONJG(Psiscreenmin(q)) * &
              Psiscreenmin(q)) !* &
              ! alpha / (Pi * (sourcet)**2d0)
              ! Factor to compare time sum to stationary phase PDF
              ! Use when performing time sum, turn off for stationary phase

Psiscreen(q) = Psitemp1 + Psitemp2
PDF(q) = REALPART(DCONJG(Psiscreen(q)) * &
              Psiscreen(q))

! WRITE(29,100) yscreen(q),PDFmin(q)/1.3021245418689126E+023,q
! WRITE(33,100) yscreen(q),PDF(q)/1.2999689400111953E+023,q

END DO !screen loop

100 FORMAT(E24.17,4x,E24.17,4x,I8)
! 101 FORMAT(E24.17,4x,E24.17,4x,E24.17,4x,E24.17,4x,I8)
```

```fortran
! 102 FORMAT(E24.17,4x,I8)

CLOSE(29)
! CLOSE(30)
! CLOSE(31)
! CLOSE(32)
! CLOSE(33)

PRINT*
PRINT*, 'Numerically integrate stationary distribution'
sumintmin = 0d0
DO q = -Nscreen, Nscreen
     sumintmin = PDFmin(q) * deltayscreen + sumintmin
END DO
PRINT*, sumintmin ! should be 1.30212454186689126E+023

OPEN(UNIT=34, FILE="stphase_normed.txt")
PRINT*, 'Normed distribution:'
DO q = -Nscreen, Nscreen
    WRITE(34,100) yscreen(q),PDFmin(q)/sumintmin,q
END DO
CLOSE(34)

PRINT*, 'Numerically integrate intuitive distribution:'
sumint = 0d0
DO q = -Nscreen, Nscreen
    sumint = PDF(q) * deltayscreen + sumint
END DO
PRINT*, sumint ! =  1.2999689400111953E+023 for Nscreen=1000

OPEN(UNIT=35, FILE="intuitive_normed.txt")
PRINT*, 'Normed distribution:'
DO q = -Nscreen, Nscreen
    WRITE(35,100) yscreen(q),PDF(q)/sumint,q
END DO
CLOSE(35)

ENDPROGRAM Fig6

!sets all values of any 1-D real*8 array to alpha
SUBROUTINE init_array1d(A,alpha)
IMPLICIT NONE
INTEGER*8 :: i
REAL*8      :: A(:),alpha
    DO i=1,size(A)
        A(i) = alpha
        !PRINT*, A(i),i
    END DO
END SUBROUTINE init_array1d

!sets all values of a 2-D real*8 array to alpha
SUBROUTINE init_array2d(R,alpha)
IMPLICIT NONE
REAL*8   :: R(:,:),alpha
INTEGER*8 :: s,t
    DO t=1, size(R,2)
        DO s=1,size(R,1)
            R(s,t) = alpha
            !PRINT*, R(s,t), s,t
        END DO
    END DO
END SUBROUTINE init_array2d

!sets all values of a complex*16 array to alpha
SUBROUTINE init_arrayC(B,alpha)
IMPLICIT NONE
INTEGER*8  :: r
COMPLEX*16 :: B(:),alpha
```

```fortran
      DO r=1,size(B)
          B(r) = alpha
          !PRINT*, B(r), r
      END DO
END SUBROUTINE init_arrayC

 !sets all values of a 2-D complex*16 array to alpha
SUBROUTINE init_array2dC(D,alpha)
 IMPLICIT NONE
COMPLEX*16  :: D(:,:),alpha
INTEGER*8 :: j,k
DO k=1, size(D,2)
      DO j=1,size(D,1)
      D(j,k) = alpha
       !PRINT*, D(j,k), j,k
      END DO
END DO
END SUBROUTINE init_array2dC

FUNCTION delta(stepnum,interval) RESULT(rout)
      IMPLICIT NONE
      INTEGER*8, INTENT(IN)  :: stepnum
      REAL*8,    INTENT(IN)  :: interval
      REAL*8                 :: rout

      rout = DFLOAT(stepnum) * interval
END FUNCTION

SUBROUTINE randfill1d(A,arbinterval)
      IMPLICIT NONE
      INTEGER*8              :: i
      REAL*8,   INTENT(IN) :: arbinterval
      REAL*8                :: A(:),B(size(A))

      CALL RANDOM_NUMBER(B)
      !CALL RANDOM_NUMBER(A)
      DO i=1,size(A)
          !CALL RANDOM_NUMBER(A(i))
          A(i) = A(i) + arbinterval * (B(i) - 0.5d0)
          !A(i) = arbinterval * (A(i) - 0.5d0)
      END DO
END SUBROUTINE randfill1d

SUBROUTINE randfill2d(B,arbinterval)
      IMPLICIT NONE
      INTEGER*8 :: i,j
      REAL*8, INTENT(IN) :: arbinterval
      REAL*8 :: B(:,:)
      REAL*8 :: C(size(B,1),size(B,2))

      CALL RANDOM_NUMBER(C)
      DO j=1, size(B,2)
          DO i=1, size(B,1)
          !CALL RANDOM_NUMBER(B(i,j))
          B(i,j) = B(i,j) + arbinterval * (C(i,j) - 0.5d0)
          END DO
      END DO
END SUBROUTINE randfill2d


SUBROUTINE init_random_seed()
      IMPLICIT NONE
      INTEGER, ALLOCATABLE :: seed(:)
      INTEGER               :: i,n,un,istat,dat(8),pid,tim(2),s
      INTEGER(8)            :: cownt, tms

      CALL random_seed(size = n)
```

```fortran
ALLOCATE(seed(n))

!The first bit tries to check if the OS has its own
!native random number generator. Otherwise, the PID
!is XOR:ed with the current time and numbers are
!adjusted with primes.

OPEN(NEWUNIT = un, file="/dev/urandom", access="stream", &
    form="unformatted", action="read", status="old", &
    iostat=istat)

!IF (istat == 0) THEN
!    READ(un) seed
!    CLOSE(un)
!    PRINT*, 'Used urandom'
!ELSE
    !PRINT*, 'Not using urandom'
    CALL system_clock(cownt)
    IF (cownt /= 0) THEN
        tim = transfer(cownt, tim)
    ELSE
        CALL date_and_time(values = dat)
        tms = (dat(1) - 1970) * 365_8 * 24 * 60 * 60 * 1000 &
            + dat(2) * 31_8 * 24 * 60 * 60 * 1000 &
            + dat(3) * 24 * 60 * 60 * 60 *1000 &
            + dat(5) * 60 * 60 * 1000 &
            + dat(6) * 60 * 1000 + dat(7) * 1000 &
            + dat(8)
        tim = transfer(tms, tim)
    END IF

    s = ieor(tim(1), tim(2))
    pid = getpid() + 1099279 ! Adding a prime number
    s = ieor(s, pid)

    IF (n >= 3) THEN
        seed(1) = tim(1) + 36269
        seed(2) = tim(2) + 72551
        seed(3) = pid
        if(n > 3) then
            seed(4:) = s + 37 * (/ (i, i = 0, n - 4) /)
        END IF
    ELSE
        seed = s + 37 * (/ (i, i = 0, n-1) /)
    END IF
!END IF

CALL random_seed(put=seed)
END SUBROUTINE init_random_seed
```

A.2   Path integral Fortran Code, time sum normalization

```fortran
PROGRAM F6pointshift
!---------------------------------------------------------------------
! Code used to renormalize 5 time sum data points from path integral sum code
! to values of the normalized stationary phase distribution.
!---------------------------------------------------------------------

IMPLICIT NONE
REAL*8 :: dataf(1:5,1:2), newdata(1:5,1:2)
INTEGER :: i

OPEN(UNIT=30, FILE="tsum_inset_points.txt", STATUS="old")


DO i=1,5
READ(30,100) dataf(i,1), dataf(i,2)
END DO

OPEN(UNIT=31, FILE="points_scaled.txt")
! manipulations- set center value equal to stationary value from tsum_inset_points.txt
DO i=1,5
newdata(i,1) = dataf(i,1)
newdata(i,2) = (dataf(i,2)/dataf(3,2))*3.7074643704598104E+06
PRINT*, newdata(i,2)
WRITE(31,100) newdata(i,1),newdata(i,2),i
END DO


CLOSE(30)
CLOSE(31)

100 FORMAT(E24.17,4x,E24.17,4x,I8)

END PROGRAM F6pointshift
```

Appendix B

Oil Drop Dish Components

The following schematics show the details and dimensions of components machined at the University of Nebraska-Lincoln Instrument Shop by Pat Pribil and Keith Placek. Fig. B.1 shows the double slit dish measurements and details, which include a highlighted region indicating marked rulings that served as a launching guide. Fig. B.2 highlights channels that were used to provide an accurate centering location of the dish as well as placement of supporting fins. Fig. B.3 shows the Delrin bearing component that was fastened to the apparatus leveling table. Fig. B.4 shows the various components that comprise the dish stem, Delrin bearing, and supporting fins. Fig. B.5 gives an exploded view of the entire assembly.
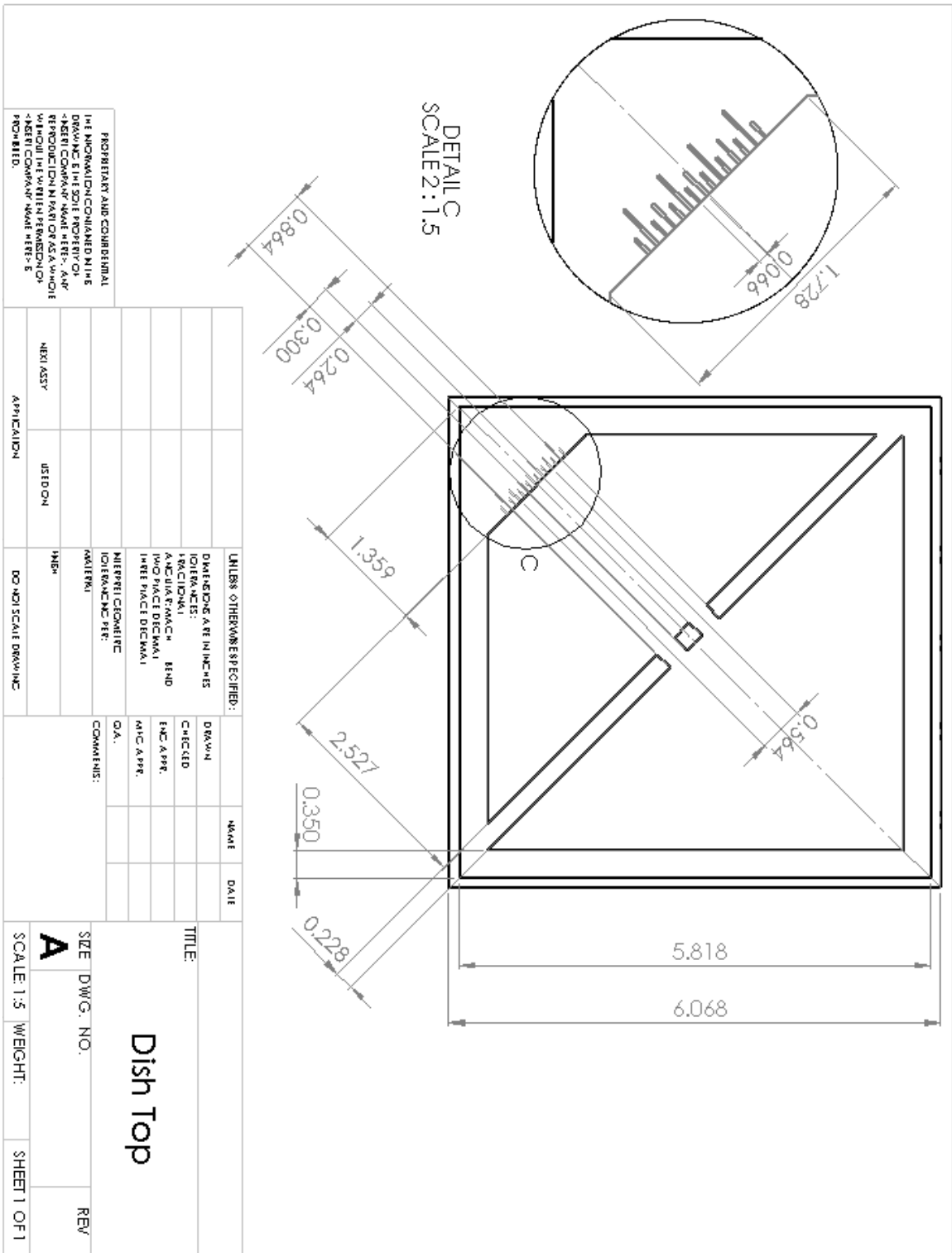
Figure B.1: Double slit dish, with relevant dimensions. Units are given in inches.

Figure B.2: Double slit dish, bottom view. Units are given in inches.
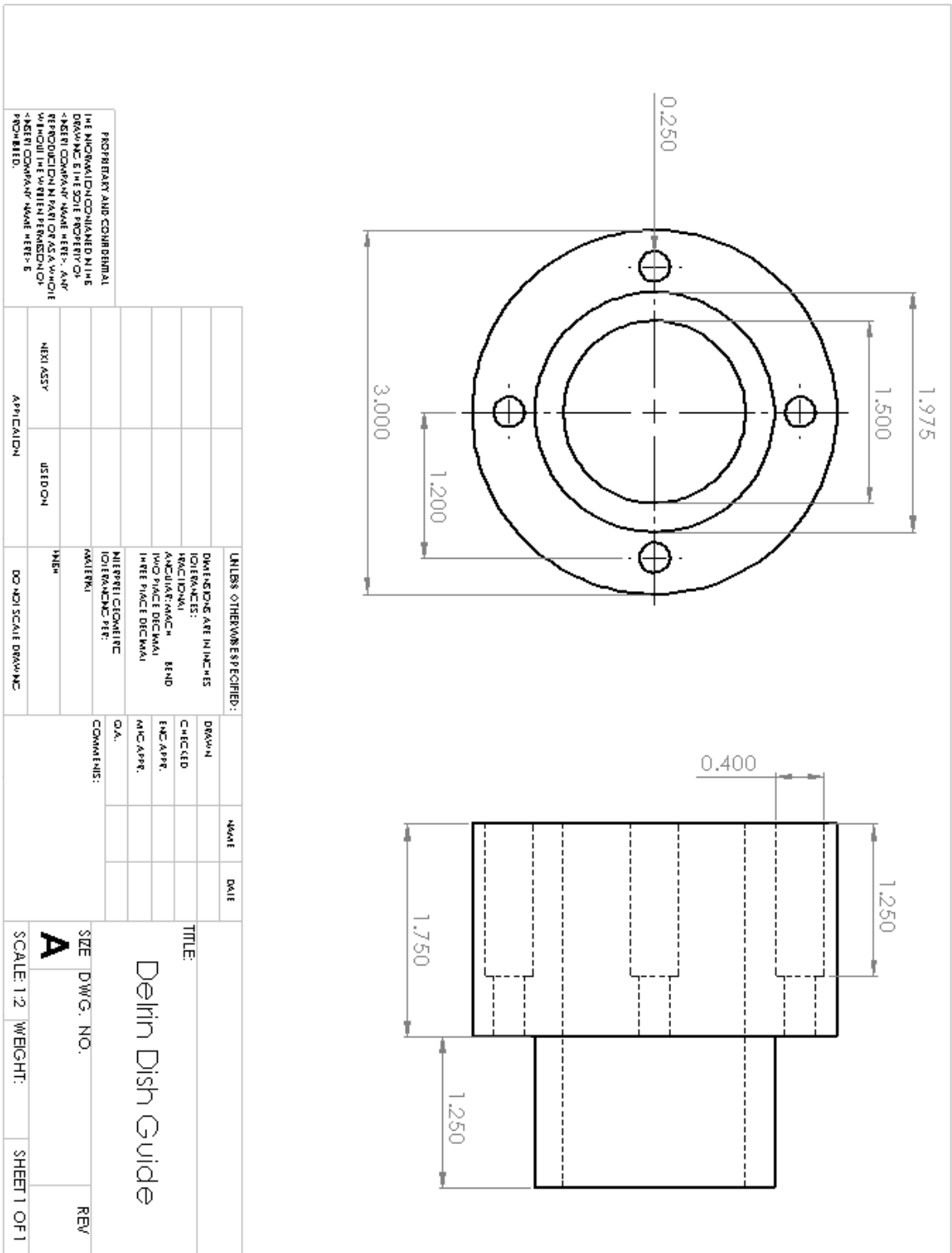
Figure B.3: Delrin bearing component used for the leveling table. Units are in inches.

Figure B.4: Dish stem components. Units are in inches.
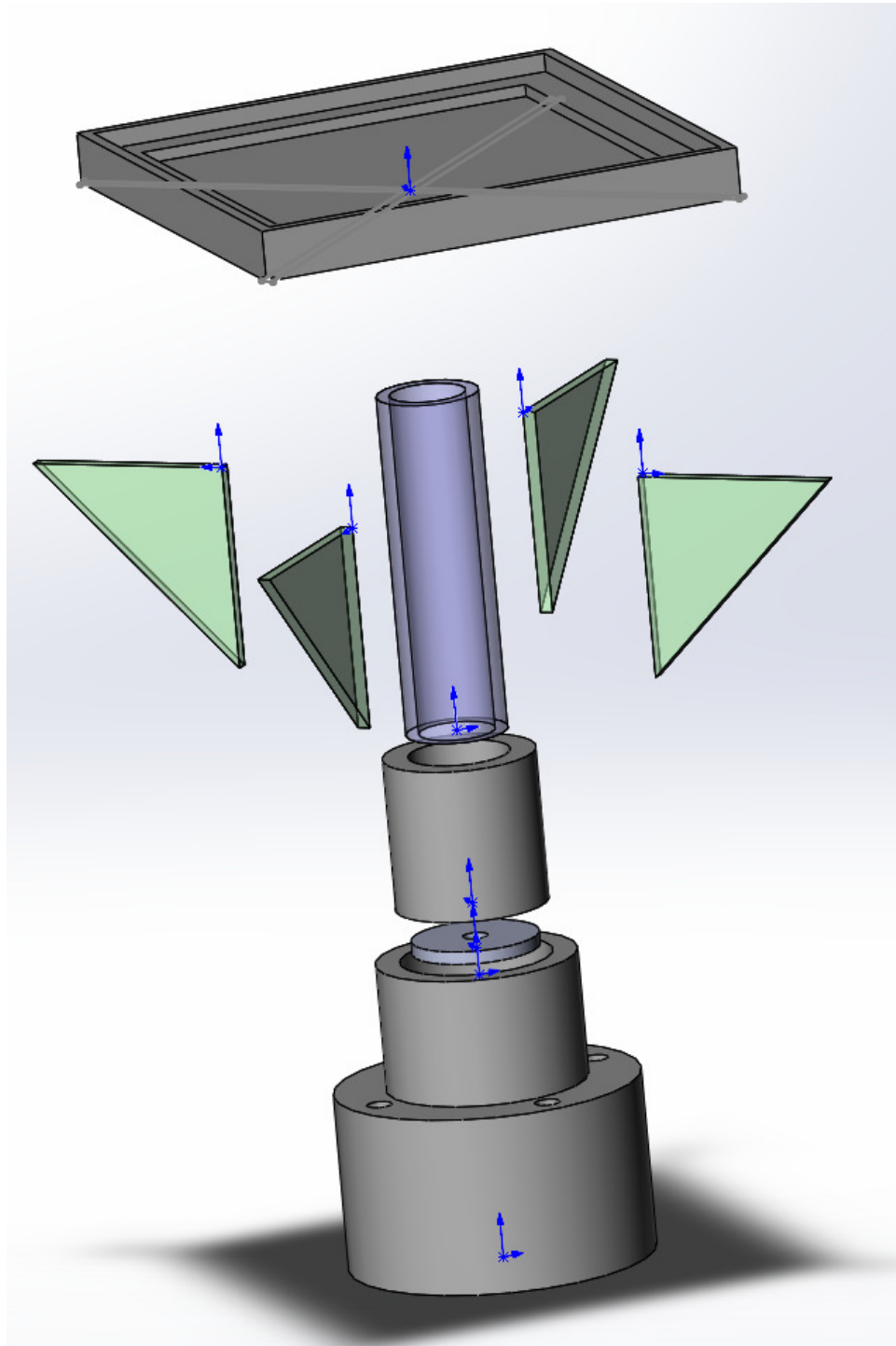
Figure B.5: Exploded view of all assembled dish components.

Appendix C

Oil Drop C++ Code

C.1   BitmapDriver.cpp

```cpp
/*
        BitmapDriver.cpp
        Created by Adam Lif

        Contains a series of functions used for analysing bitmap (.bmp) pictures
*/

//Avoid Microsoft unsafe function warnings
#define _CRT_SECURE_NO_WARNINGS

#include <iostream>
#include <fstream>

#include "BitmapDriver.h"
#include "TextFileDriver.h"

using namespace std;

BitmapDriver::BitmapDriver() {}


void BitmapDriver::GetInfo(FILE *pInputImage, unsigned int *fileHeaderInfo,
                           unsigned int *fileColorTable) {
        //Copies bitmap file header and color table to fileHeaderInfo and fileColorTable

        fileHeaderInfo = 0;
        fileColorTable = 0;

        unsigned char nullChar = '0';
        unsigned char *pReadFileInfo = &nullChar;

        fseek(pInputImage, 0L, SEEK_SET);

        //Read bitmap file header
        for(int i = 0; i < 54; i++) {
                fread(pReadFileInfo, sizeof(char), 1, pInputImage);
                fileHeaderInfo[i] = *pReadFileInfo;
        }

        //Read bitmap file color table
        for(int i = 0; i < 1024; i++) {
                fread(pReadFileInfo, sizeof(char), 1, pInputImage);
```

```cpp
                        fileColorTable[i] = *pReadFileInfo;
                }
}


void BitmapDriver::GetPixelData(FILE *pInputImage, unsigned int pictureWidth,
                        unsigned int pictureHeight, unsigned int **filePixelData) {
        //Reads bitmap file pixel data into 2D array

        unsigned char   nullChar = '0';
    //information being read in from the picture
        unsigned char *pReadFileInfo = &nullChar;
        //brightest color value in the picture
    unsigned int maxPixel = 0;

        fseek(pInputImage, 1078L, SEEK_SET);

        //Read data, find whitest pixel & its location
        for (unsigned int row = 0; row < pictureHeight; row++) {
                for (unsigned int column = 0; column < pictureWidth; column++) {
                        fread(pReadFileInfo, sizeof(char), 1, pInputImage);

                        filePixelData[row][column] = (int) *pReadFileInfo;
                }
        }
}


void BitmapDriver::FindDropMax(unsigned int **filePixelData, int pictureWidth,
                                int pictureHeight, unsigned int &xMax,
                                unsigned int &yMax, unsigned int &lastX,
                                unsigned int &lastY, int searchAreaSize) {
        //Finds the brightest spot in the picture. Based of previous points if not first
    //point
        xMax = 0;
        yMax = 0;

        unsigned int maxPixel = 0;
        int xStart = 0;
        int yStart = 0;
        int xEnd = pictureWidth - 1;
        int yEnd = pictureHeight - 1;

        //Narrows down search area in x direction if not first picture
        if(lastX != 0) {
                xStart = lastX - searchAreaSize;
                if(xStart < 0) xStart = 0;

                xEnd = lastX + searchAreaSize;
                if(xEnd > pictureWidth - 1) xEnd = pictureWidth - 1;
        }
        //TODO: Temp fix, delete
        else {
                xStart = 100;
                xEnd = 400;
        }

        //Narrows down search area in y direction if not first picture
        if(lastY != 0) {
                yStart = lastY - searchAreaSize;
                if(yStart < 0) yStart = 0;

                yEnd = lastY + searchAreaSize;
                if(yEnd > pictureHeight - 1) yEnd = pictureHeight - 1;
        }
        //TODO: Temp fix delete
        else {
```

```cpp
                        yStart = 493−350;
                        yEnd = 493−150;
                }

                //Searches for brightest point in given search area
                for(int row = yStart; row <= yEnd; row++) {
                        for(int column = xStart; column <= xEnd; column++) {
                                unsigned int pixelColor = filePixelData[row][column];

                                if (pixelColor > maxPixel) {
                                        maxPixel = pixelColor;
                                        xMax = column;
                                        yMax = row;

                                        lastX = xMax;
                                        lastY = yMax;
                                }
                        }
                }
}


void BitmapDriver::CreateCopy(unsigned int *header, unsigned int *colorTable,
                              unsigned int **pixelData, std::string fileName,
                              double virtualMassX, double virtualMassY,
                              unsigned int pictureWidth, unsigned int pictureHeight,
                              unsigned int dotMarkerSize) {
        //Copies analysed bitmap with white dot placed on tracked location of drop

        unsigned char  nullChar = '0'; //Data to write to new bitmap file
        unsigned char *pWriteFileInfo = &nullChar;
        FILE*          pOutputBmpFile = NULL; //New bitmap file


        pOutputBmpFile = fopen(fileName.c_str(), "wb");

        fseek(pOutputBmpFile, 0L, SEEK_SET);

        //Write new bitmap file header
        for(int i = 0; i < 54; i++) {
                *pWriteFileInfo = header[i];
                fwrite(pWriteFileInfo, sizeof(char), 1, pOutputBmpFile);
        }

        fseek(pOutputBmpFile, 54L, SEEK_SET);

        //Write new bitmap color table
        for(int i = 0; i < 1024; i++) {
                *pWriteFileInfo = colorTable[i];
                fwrite(pWriteFileInfo, sizeof(char), 1, pOutputBmpFile);
        }

        fseek(pOutputBmpFile, 1078, SEEK_SET);

        //Write new bitmap pixel data
        for(unsigned int row = 0; row < pictureHeight; row++) {
                for(unsigned int column = 0; column < pictureWidth; column++) {

                        if (column >= (virtualMassX − dotMarkerSize) &&
                    column <= (virtualMassX + dotMarkerSize) &&
                                row >= (virtualMassY − dotMarkerSize) &&
                    row <= (virtualMassY + dotMarkerSize)) {

                                        pixelData[row][column] = 255;
                        }

                        else if(pixelData[row][column] <= 8) pixelData[row][column] = 0;
```

```
                                *pWriteFileInfo = pixelData[row][column];
                                fwrite(pWriteFileInfo, sizeof(char), 1, pOutputBmpFile);
                    }
          }
          pWriteFileInfo = 0;

          fclose(pOutputBmpFile);
}


void BitmapDriver::FindDropCenter(unsigned int xMax, unsigned int yMax, int dropSize,
                                  double &virtualMassX, double &virtualMassY,
                                  unsigned int **pixelData, double pictureWidth,
                                  double pictureHeight) {
          //Calculates virtual center of mass where white = mass.
      //Location stored in virtualMassX, virtualMassY

          double intensitySum = 0.0;

          virtualMassX = 0.0;
          virtualMassY = 0.0;

          for (int y = -dropSize; y <= dropSize; y++) {
                    for (int x = -dropSize; x <= dropSize; x++) {

                              if (yMax - y > 0 &&
                    yMax + y < pictureHeight &&
                    xMax - x > 0 &&
                    xMax + x < pictureWidth) {
                                    //Formula:SUM(color-table-value*pix-coordinate-of-point)
                    // / SUM(color-table-value).

                                    //Numerator
                                    virtualMassX += pixelData[yMax + y][xMax + x] * (xMax + x);
                                    virtualMassY += pixelData[yMax + y][xMax + x] * (yMax + y);

                                    //Denominator
                                    intensitySum += pixelData[yMax + y][xMax + x];
                        }
              }
          }

          virtualMassX = virtualMassX / intensitySum;
          virtualMassY = virtualMassY / intensitySum;
}
```

C.2   BitmapDriver.h

```
/*
        BitmapDriver.h
        Created by Adam Lif

        See BitmapDriver.cpp for more information
*/

#ifndef BITMAPDRIVER_H
#define BITMAPDRIVER_H

class BitmapDriver {

  public:
        BitmapDriver();
        void GetInfo(FILE *pInputImage, unsigned int *fileHeaderInfo,
                unsigned int *fileColorTable);
        void GetPixelData(FILE *pInputImage, unsigned int pictureWidth,
                    unsigned int pictureHeight,
                    unsigned int **filePixelData);
        void FindDropMax(unsigned int **pixelData, int pictureWidth, int pictureHeight,
                    unsigned int &xMax, unsigned int &yMax, unsigned int &lastX,
                    unsigned int &lastY, int searchAreaSize);
        void CreateCopy(unsigned int *header, unsigned int *colorTable,
                    unsigned int **pixelData, std::string fileName,
                    double virtualMassX, double virtualMassY,
                    unsigned int pictureWidth, unsigned int pictureHeight,
                    unsigned int dotMarkerSize);
        void FindDropCenter(unsigned int xMax, unsigned int yMax, int dropSize,
                        double &virtualMassX, double &virtualMassY,
                        unsigned int **pixelData, double pictureWidth,
                        double pictureHeight);
};
#endif
```

C.3 Oil Droplet Analyzer 3.1.cpp

```
/*
    Oil Droplet Analyser
    Created by Adam Lif
    University of Nebraska-Lincoln
    Department of Physics and Astronomy

    Last Updated - August 15, 2012

    Analyses a series of 8-bit bitmap(.bmp) pictures following the trajectory of a
    brighly-lit drop
    Creates text(.txt) files of each drop's position

    Since this program was designed for internal use, the program catches many,
    but not all errors.
    Most errors not caught are user-input errors, such as entering a letter
    instead of a number.

    For errors that are clearly not do to user input, a quick examination of the
    text files created by the program will often show the issue.
    If the program stops before finishing analysis, looking through the text files
    will show which one was the issue, and the corresponding picture files can be
    examined, which will usually reveal the issue with little difficulty
*/

//Avoid Visual Studio unsafe function warnings
#define _CRT_SECURE_NO_WARNINGS

#include <iostream>
#include <fstream>
#include <vector>
#include <sstream>
#include <direct.h>
#include <Windows.h>

#include "TextFileDriver.h"
#include "BitmapDriver.h"

using namespace std;


int main() {
    /*
    The pictures to analyse should be kept in directories following this naming
    convention:

    The program should be in the directory containing a list of directories named
    PRIMARY_FILEX
    and each PRIMARY_FILE may contain multiple SECONDARY_FILEX directories full of
    pictures, replacing the names accordingly where X = an incremental number
    */

    //These should be left alone
    //Picture type, program currently works for .bmp only
    const char *EXTENSION = ".bmp";
    //Writes copy of all position text files to this directory
    const char *TXTFILE_DIR = "ALL TXT";

    TextFileDriver textDriver;
    textDriver.CreateSettingsFile();

    //Load program settings from SETTINGS.txt
    vector<string> settings;
    textDriver.ReadSettingsFile(settings);

    bool readSuccess = true;
```

```cpp
//Checks for empty settings
for(unsigned int set = 0; set < settings.size(); set++) {
    if(settings.at(set).length() < 1) readSuccess = false;
}

    if(!readSuccess) {
            cout << "Error: Unable to read SETTINGS.txt\nPress Enter to exit";
            getchar();
            return 0;
    }
//Outer directories
const char *OUTER_FILE = settings.at(15).c_str();
//Main directories
const char *PRIMARY_FILE = settings.at(12).c_str();
//Sub-directories
const char *SECONDARY_FILE = settings.at(13).c_str();

//Information about the slit, used for various tests and calculations
double slitSlope = (stod(settings.at(9)) - stod(settings.at(7))) /
                    (stod(settings.at(8)) - (stod(settings.at(6))));
double slitYIntercept = stoi(settings.at(7)) - slitSlope * stoi(settings.at(6));

double slitWidth = sqrt((pow((stod(settings.at(9)) - stod(settings.at(7))), 2)) +
                        (pow((stod(settings.at(8)) - stod(settings.at(6))), 2)));
double slitMidPtX = (stoi(settings.at(6)) + stoi(settings.at(8))) / 2.0;
double slitMidPtY = (stoi(settings.at(7)) + stoi(settings.at(9))) / 2.0;


cout << "Oil Droplet Analysis Program\n\nFirst file: \n" + settings.at(11);

//The first picture to start analysing from in each sub-directory
string startFileName;
getline(cin, startFileName);
unsigned int startFileNumber = stoi(startFileName);

startFileName = settings.at(11) + startFileName;
startFileName = textDriver.Trim(startFileName);

//If file extension not specified by user
if(startFileName.substr(startFileName.length() - 4, 4) != EXTENSION) {
    startFileName.append(EXTENSION);
}

cout << "\nLast file: \n" + settings.at(11);

//Last picture to analyse from in each sub-directory
string endFileName;
getline(cin, endFileName);

unsigned int endFileNumber = stoi(endFileName);

if(endFileNumber < startFileNumber) {
    cout << "\nIncorrect range\nPress Enter to exit";
    getchar();
    return 0;
}

//User-entered starting and ending main / sub-directories
string numberInput;

cout << "\nStart at " << OUTER_FILE << " ";
getline(cin, numberInput);
unsigned int startPositionNumber = stoi(numberInput);

cout << "\nEnd at " << OUTER_FILE << " ";
getline(cin, numberInput);
```

```cpp
unsigned int endPositionNumber = stoi(numberInput);

cout << "\nStart at " << PRIMARY_FILE << " ";
getline(cin, numberInput);
unsigned int startDropNumber = stoi(numberInput);

cout << "\nEnd at " << PRIMARY_FILE << " ";
getline(cin, numberInput);
unsigned int endDropNumber = stoi(numberInput);

cout << "\nStart at " << SECONDARY_FILE << " ";
getline(cin, numberInput);
unsigned int trajectoryStartNumber = stoi(numberInput);

cout << "\nEnd at " << SECONDARY_FILE << " ";
getline(cin, numberInput);
unsigned int trajectoryEndNumber = stoi(numberInput);

if(endDropNumber < startDropNumber ||
    trajectoryEndNumber < trajectoryStartNumber) {
    cout << "\nIncorrect range\nPress Enter to exit";
    getchar();
    return 0;
}

//Prompt creation of additional pictures with marker on drop location
//Note: Selection of this choice causes significant increase in runtime
cout << "\nCreate " << EXTENSION << " pictures (y/n) ";
getline(cin, numberInput);
char yesOrNo = numberInput.at(0);

boolean createBitmaps = false;
if(yesOrNo == 'y' || yesOrNo == 'Y') createBitmaps = true;


//*******************************************************************************
// Data Retrieval

cout << "\nAnalysing. Picture size " << settings.at(0) << " x "
    << settings.at(1) << endl;

textDriver.CheckDirectory(TXTFILE_DIR);

double percentCompleted = 0;
cout.precision(0);
cout << "Completed: " << fixed << percentCompleted << "%\r";
//Writes the located drop position for each picture to text files in the
//TEXTFILE_DIR directory
ofstream masterFileWriter;

for(unsigned int outer = startPositionNumber; outer <= endPositionNumber; outer++) {
    string currentOuter = textDriver.itos(outer);

    //Analyses each drop, will skip drops that do not exist
    for(unsigned int x = startDropNumber; x <= endDropNumber; x++){
        string cartesianFile;
        string currentDrop = textDriver.itos(x);
        //Both used to search for next drop based on position of previous one

        unsigned int lastX = 0;
        unsigned int lastY = 0;

        //Analyses each trajectory, will skip trajectories that do not exist
        for(unsigned int y = trajectoryStartNumber;
            y <= trajectoryEndNumber; y++) {
```

```
                    //Placeholders that shorten file locations
                    string currentTraj = textDriver.itos(y);
                    string dropTraj = currentOuter + "." +
                    currentDrop + "." + currentTraj;
                    string preDirect = OUTER_FILE + currentOuter + "\\" +
                    PRIMARY_FILE + currentDrop + "\\" + SECONDARY_FILE + currentTraj;
                    string directory = preDirect + "\\";

                    lastX = 0;
                    lastY = 0;

                    cartesianFile = (string) TXTFILE_DIR +
                    "\\" + dropTraj + ".txt";

                    //Checks if directory exists
                    WIN32_FIND_DATA dirInfo = {0};
                    HANDLE hFind = FindFirstFile(preDirect.c_str(), &dirInfo);

                    //If directory exists
                    if(hFind != INVALID_HANDLE_VALUE) {

                        //Holds the pixel values for each picture
                        unsigned int **pixelData =
                        new unsigned int *[stoi(settings.at(1))];
                        for (int i = 0; i < stoi(settings.at(1)); i++) {
                        pixelData[i] =
                        new unsigned int [stoi(settings.at(0))];
                        }

                        masterFileWriter.open(cartesianFile);
                        string fileName = startFileName;

                        //Analyses each picture, will skip pictures
                        //that do not exist
                        for(unsigned int z = startFileNumber;
                        z <= endFileNumber; z++) {
/*
For each picture, the program runs through it to find the brightest point
(xMax, yMax).
If the first picture of a trajectory, searches the entire picture,
otherwise searches a small area based on the last location.
virtualMassX and virtualMassY become the "true" location of the drop by
using an algorithm to effectively calculate a center of mass, where
color = mass, which is referred to as the "virtual center of mass"
*/
                            //The current image to analyse
                            FILE *pInputImage = 0;
                            //See BitmapDriver.cpp for information
                            //about bitmap files
                            BitmapDriver bitmap;

                            unsigned int *bitmapHeader = 0;
                            unsigned int *bitmapColorTable = 0;

                            //If the bitmap file exists
                            //and is sucessfully opened
                            if ((pInputImage =
                            fopen((directory + fileName).c_str(),
                            "rb")) != 0) {
                                bitmapHeader = 0;
                                bitmapColorTable = 0;

                                //The location of the brightest
                                //spot in the picture
                                unsigned int xMax = 0;
                                unsigned int yMax = 0;
```

```cpp
                                //Location of the virtual
                                //center of mass
                                double virtualMassX = 0;
                                double virtualMassY = 0;

                                //Gets all necessary information
                                //from the picture
                                if(createBitmaps) bitmap.GetInfo(
                                pInputImage, bitmapHeader,
                                bitmapColorTable);
                                bitmap.GetPixelData(pInputImage,
                                stoi(settings.at(0)), stoi(settings.at(1)),
                                pixelData);
                                fclose(pInputImage);

                                //Calculates drop location and
                                //writes to text file
                                bitmap.FindDropMax(pixelData,
                                stoi(settings.at(0)),
                                stoi(settings.at(1)),
                                xMax, yMax, lastX, lastY, 8);
                                bitmap.FindDropCenter(xMax, yMax,
                                stoi(settings.at(3)),
                                virtualMassX, virtualMassY, pixelData,
                                stoi(settings.at(0)), stoi(settings.at(1)));

                                textDriver.WriteDropPosition(
                                virtualMassX, virtualMassY,
                                masterFileWriter);

                                if(createBitmaps)
                                bitmap.CreateCopy(bitmapHeader,
                                bitmapColorTable, pixelData, fileName,
                                virtualMassX, virtualMassY,
                                stoi(settings.at(0)), stoi(settings.at(1)),
                                stoi(settings.at(2)));

                                //Sets up the name of the next
                                //picture to analyse
                                fileName =
                                textDriver.IncrementFile(
                                fileName,
                                settings.at(11).at(settings.at(11).length() - 1));
                            } //end fopen if
                        } //end z loop

                        for (int i = 0; i < stoi(settings.at(1)); i++) {
                        delete(pixelData[i]);
                        }
                        delete(pixelData);

                        masterFileWriter.close();
                    } //end hfind if

                    //Calculates and displays the progress of analysis
                    int trajectFileCount = (
                    trajectoryEndNumber - trajectoryStartNumber + 1) *
                    (endDropNumber - startDropNumber + 1) *
                    (endPositionNumber - startPositionNumber + 1);
                    percentCompleted += 100.0 / (double) (trajectFileCount);

                    cout << "Completed: "<<fixed << percentCompleted<<"%\r";
                    cout.flush();
                } //end y loop
            } //end x loop
        } //end outer loop
```

```
        cout << "\n\nAnalysis complete\nPress Enter to Quit\n";
        getchar();
}
```

C.4 TextFileDriver.cpp

```cpp
/*
        TextFileDriver.cpp
        Created by Adam Lif

        Contains a series of functions for file I/O and string manipulation related to
    analysing Oil Droplet pictures
*/

//Avoid Microsoft unsafe function warnings
#define _CRT_SECURE_NO_WARNINGS

#include <iostream>
#include <fstream>
#include <vector>
#include <sstream>
#include <Windows.h>
#include <direct.h>

#include "TextFileDriver.h"

using namespace std;

TextFileDriver::TextFileDriver() {}


void TextFileDriver::CreateSettingsFile() {
        //Creates file "SETTINGS.txt" with savable parameters if does not already exist

        /*
                Parameters:
                0 PICTURE_WIDTH - Bitmap width
                1 PICTURE_HEIGHT - Bitmap height
                2 DOT_MARKER_SIZE - Size of drop position marker (Pixels)
                3 DOT_SIZE - Distance in x/y direction from maximum point to calculate drop
                        position (Pixels)
                4 START_INITIAL - First picture to start line 1 calculations (depreciated)
                5 END_INITIAL - Last picture to end line 1 calculations (depreciated)
                6-9 SLIT_POINT1X - SLIT_POINT2Y - X/Y coordinates (from bottom left) of 2
                                        opposite points on slit
                10 SLIT_WIDTHS - Number of slit widths to calculate line 2 at
                11 FILE_BASE_NAME - Bitmap filename excluding incremental numbers
                12 PRIMARY_DIR - The name of the main picture directory
                13 SECONDARY_DIR - The name of the picture subdirectories
                14 START_SLIT_WIDTHS - The number of slit widths away to measure the first
                                angle from
                15 OUTER_FOLDER_NAME - The outer folder holding number 12 and 13

                NOTE: Missing parameters will cause crash, not fixed to allow easy
        additions of new parameters

                Adding additional parameters to file, use format:
        "<< \nPARAMETER_NAME = value"
                The reader looks for "=" and will consider only lines with it to have a
        value
*/
        fstream settingsFileWriter;
        settingsFileWriter.open("SETTINGS.txt", ios::in);

        //If settings file does not exist, creates and writes to it
        if (!settingsFileWriter.is_open()) {

                settingsFileWriter.close();
                settingsFileWriter.open("SETTINGS.txt", ios::out);

                settingsFileWriter
```

```
                                    << "Oil Droplet Analyser Settings\n
              \nNote: Do not edit anything in this document other than the
              numbers."
                                    << "To reset the numbers to default settings, delete this file.\n"
                                    << "\nPICTURE_WIDTH = 656"
                                    << "\nPICTURE_HEIGHT = 494"
                                    << "\nDOT_MARKER_SIZE = 3"
                                    << "\nDOT_SIZE = 10"
                                    << "\nSTART_INITIAL = 0"
                                    << "\nEND_INITIAL = 20"
                                    << "\nSLIT_POINT1X = 0"
                                    << "\nSLIT_POINT1Y = 0"
                                    << "\nSLIT_POINT2X = 0"
                                    << "\nSLIT_POINT2Y = 0"
                                    << "\nSLIT_WIDTHS = 2"
                                    << "\nFILE_BASE_NAME = Camera_black_"
                                    << "\nPRIMARY_DIR = drop"
                                    << "\nSECONDARY_DIR = traj"
                                    << "\nSTART_SLIT_WIDTHS = 2"
                                    << "\nOUTER_FOLDER_NAME = Position";

                    settingsFileWriter.flush();
                    settingsFileWriter.close();
          }
          else settingsFileWriter.close();
}


void TextFileDriver::ReadSettingsFile(vector<string> &fileInfo) {
          //Reads SETTINGS.txt to get information, stores in fileInfo
          ifstream fileReader;
          vector<string> file;

          fileReader.open("SETTINGS.txt");

          if(fileReader.is_open()) {
                    //Reads entire file into vector "file"
                    while(!fileReader.eof()) {
                              string info;
                              getline(fileReader, info);
                              file.push_back(info);
                    }

                    //Pulls necessary information from vector and stores in fileInfo
                    for(unsigned int x = 0; x < file.size(); x++) {
                              for(unsigned int y = 0; y < file[x].length(); y++) {

                                        if(file[x].at(y) == '=') {
                                                  //Adds everything to the vector that comes after
                              //'=', trims start/end whitespace
                                                  int length = file.at(x).length() -
                              file.at(x).find_first_of('=') + 1;
                                                  string fileInfoNumber =
                              file[x].substr(file[x].find_first_of('=') +
                              1, length);

                                                  if(fileInfoNumber.length() > 0) {
                                                            fileInfoNumber = Trim(fileInfoNumber);
                                                            fileInfo.push_back(fileInfoNumber);
                                                  }
                                        }
                              }
                    }
                    fileReader.close();
          }
```

```cpp
}


void TextFileDriver::WriteDropPosition(double virtualMassX, double virtualMassY,
ofstream &fileWriter) {
        //Writes x/y positions to a text file in format: xxx.xxx        yyy.yyy
        fileWriter.precision(3);

        //Calculates number of spaces between numbers to properly allign in colums
        unsigned int spaces = 6;
        unsigned int vmxLength = itos(floor(virtualMassX)).length();

        spaces += 3 - vmxLength;
        if(spaces < 1) spaces = 1;

        fileWriter << fixed << virtualMassX;

        for(unsigned int x = 0; x < spaces; x++) {
                fileWriter << " ";
        }

        fileWriter << virtualMassY << endl;
        fileWriter.flush();
}


string TextFileDriver::itos(int integerNum) {
        //Converts integer to a string
        stringstream ss;
        ss << integerNum;
        return ss.str();
}


string TextFileDriver::Trim(string inputString) {
        //Returns original string with leading and trailing whitespace removed
        size_t found = inputString.find_last_not_of(' ');

        if(found != string::npos) {
                int length = inputString.find_last_not_of(' ') -
inputString.find_first_not_of(' ') + 1;
                return inputString.substr(inputString.find_first_not_of(' '), length);
        }

        else return "";
}


string TextFileDriver::IncrementFile(string fileName, char escapeChar) {
        //Increments the incremental file numbers by 1

        string fileBaseName = fileName.substr(0, fileName.find_last_of(escapeChar,
                        string::npos) + 1);
        string fileNumberString = fileName.substr(fileName.find_last_of(escapeChar) + 1,
                        fileName.length() - 1);

        for(int a = fileNumberString.length() - 2; a >= 0; a--) {
                if(!isdigit(fileNumberString.at(a))) fileNumberString.erase(a);
        }

        string zeroString = "";
        while (fileNumberString.at(0) == '0' && fileNumberString.length() > 1) {
                zeroString.append("0");
                fileNumberString.erase(0, 1);
        }

        unsigned int fileNumber = stoi(fileNumberString);
```

```cpp
        fileNumber++;

        //If the file's number is a multiple of 10, causing an extra digit, this deletes
    //a 0
        for (double x = (double) fileNumber; x >= 10; x) {
                x = x / 10;

                if (x == 1) zeroString.erase(0,1);
        }

        fileNumberString = itos(fileNumber);

return fileBaseName + zeroString + fileNumberString + ".bmp";
}


void TextFileDriver::CheckDirectory(string directory) {
        //Creates directory if nonexistant
        WIN32_FIND_DATA dirInfo = {0};

        if(FindFirstFile(directory.c_str(), &dirInfo) == INVALID_HANDLE_VALUE){
                _mkdir(directory.c_str());
        }
}
```

C.5 TextFileDriver.h

```
/*
        TextFileDriver.h
        Created by Adam Lif

        See TextFileDriver.cpp for more information
*/

#include <vector>

#ifndef TEXTFILEDRIVER_H
#define TEXTFILEDRIVER_H

class TextFileDriver {

  public:
            TextFileDriver();
        void CreateSettingsFile();
            void ReadSettingsFile(std::vector<std::string> &);
            void WriteDropPosition(double, double, std::ofstream &);
            std::string itos(int);
            std::string Trim(std::string);
            std::string IncrementFile(std::string, char);
            void CheckDirectory(std::string file);
};

#endif
```

Appendix D

Python Analysis Scripts

D.1   Trajectory List Management

```python
import numpy as np
import matplotlib
import os.path
matplotlib.use('Agg')
from matplotlib.pyplot import *

fname = '0 Drop - Traj List.txt'
outfname = 'TrajectoryListAll.txt'
endname = '.txt'

# Some of the trajectories give gobbledegook, this is a measure to save on
# pulling them out later.
skiplines = ['1.1.4','3.1.3','3.3.19','3.3.22','4.3.1','4.3.11','5.1.23','5.1.30','6.4.2',
'7.1.16','7.1.18','8.2.7','8.2.26','9.2.11','10.3.11','10.3.20','11.1.18','13.3.4',
'13.3.7','14.1.2','14.1.3','14.1.4','14.1.5','14.1.6','14.1.8','14.1.10','14.1.15',
'14.1.16','14.3.1','14.3.5','14.4.1','18.1.2','18.5.4','18.5.16','19.1.11','20.2.12',
'20.4.2','21.1.11','22.1.11']
with open(fname,'r') as f, open(outfname,'w') as g:
    for cnt,line in enumerate(f,1):
        basename = line.rstrip('\n')
        if basename == '-':
            pass
        elif basename in skiplines:
            print ('Trajectory {} was skipped'.format(line.rstrip('\n')))
            pass
        else:
            linestr = basename+endname+'\n'
            g.write(linestr)
    print ('There were {} total lines'.format(cnt))

print "Done!"
```

D.2 Measuring Trajectory Deflection Angles

```python
import numpy as np
import matplotlib
import os.path
matplotlib.use('Agg')
from matplotlib.pyplot import *


fname = 'TrajectoryListAll.txt'
outfname = 'TrajListOutAnalyzed.txt'
out2fname = 'TrajSkipped.txt'
out3fname = 'Out_angles.txt'
out4fname = 'Out_angles_regression.txt'
out5fname = 'Out_angles_comparison.txt'

# values of pixels for slits for the data set
slitrightx1 = 261.0
slitrighty1 = 287.0
slitleftx1 = 334.0
slitlefty1  = 291.0
numslitwidths = 1.306

num_lines = 0
with open(fname) as f:
    for cnt, line in enumerate(f,1):
        pass
    num_lines = cnt
    print "New num_lines: ", num_lines

# outanglearray   = np.zeros([1,num_lines])
# regressionangle = np.zeros([1,num_lines])
# comparison      = np.zeros([1,num_lines])

# Note to self: 'r' is for read only, 'a' is for append new data to the end of the file
print "Opening the files!"
with open(fname,'r') as f, open(outfname,'w') as g, open(out2fname,'w') as h,
open(out3fname,'w') as q, open(out4fname,'w') as r, open(out5fname,'w') as s:
    for cnt, line in enumerate(f,1):
        basename = line.rstrip('\n')
        if not os.path.isfile(basename):
                        pass
        else:
            # here, can actually make condition with the line iterable.
            # if line < '1.1.2.txt\n': is equivalent to (and works just as well as)
            # if cnt < 2:
            if cnt < num_lines+1:
                slitrightx = slitrightx1
                slitrighty = slitrighty1
                slitleftx =  slitleftx1
                slitlefty  = slitlefty1

            elif cnt == num_lines+1:
                slitrightx = slitrightx1
                slitrighty = slitrighty1
                slitleftx  = slitleftx1
                slitlefty  = slitlefty1
                print("This is where we stop: {} {}".format(cnt, line))
                pass
            else:
                pass

            slitmidx = (slitrightx + slitleftx)/2.0
            slitmidy = (slitrighty + slitlefty)/2.0
            slit_slope = (slitlefty - slitrighty) / (slitleftx - slitrightx)
            slitangle = np.arctan(slit_slope)
            rot_angle = -slitangle + np.pi / 2.0
```

```python
slitrightxprime = slitrightx*np.cos(rot_angle) - slitrighty*np.sin(rot_angle)
slitrightyprime = slitrightx*np.sin(rot_angle) + slitrighty*np.cos(rot_angle)

slitleftxprime = slitleftx*np.cos(rot_angle) - slitlefty*np.sin(rot_angle)
slitleftyprime = slitleftx*np.sin(rot_angle) + slitlefty*np.cos(rot_angle)
slitwidth = slitleftyprime - slitrightyprime

slitmidxprime = slitmidx*np.cos(rot_angle) - slitmidy*np.sin(rot_angle)
slitmidyprime = slitmidx*np.sin(rot_angle) + slitmidy*np.cos(rot_angle)

data = np.loadtxt(basename, unpack=True)

N = np.arange(len(data[0]))
rot_data = np.zeros([2, len(data[0])])
ref_data = np.zeros([2, len(data[0])])

for j in N:
    rot_data[0,j] = np.cos(rot_angle)*data[0,j] - np.sin(rot_angle)*data[1,j]
                    - slitmidxprime
    rot_data[1,j] = np.sin(rot_angle)*data[0,j] + np.cos(rot_angle)*data[1,j]
                    - slitmidyprime


screenx = slitwidth*numslitwidths
# print ('slitwidth is {}'.format(slitwidth))
# print ('screenx is {}'.format(screenx))
max_points = 11 #choose an odd number for symmetry
max_counts = max_points - 1

for k in N:
    # print k
    if rot_data[0,k] < screenx:
        pass
    elif rot_data[0,k] >= screenx:
        break
    start_index = k
    # print start_index
    # print rot_data[0,k], rot_data[1,k], k
    # print line

if (start_index + max_counts/2) < len(data[0]) - 1:
# if start_index > 0:
    # g is 'TrajListOutAnalyzed.txt'
    g.write(line)
    numpoints = np.arange(start_index + max_counts / 2,
                          start_index - max_counts / 2 - 1, -1)
    # print numpoints
    avg_angle_out = 0.0
    for n in numpoints:
        deltax = rot_data[0,n] - rot_data[0,n-1]
        deltay = rot_data[1,n] - rot_data[1,n-1]
        angle_out = np.arctan(deltay / deltax) * 180.0 / np.pi
        avg_angle_out = avg_angle_out + angle_out


    avg_angle_out = avg_angle_out / max_counts
    q.write('{0:.3f}'.format(avg_angle_out)+'\n')

    #least-squares method- y has to be an N-dimensional array, not 1xN
    x_vector = np.zeros([1, max_points])
    y_vector = np.zeros(max_points)

    for j in numpoints:
        x_vector[0,j-start_index] = rot_data[0,j]
        y_vector[j-start_index] = rot_data[1,j]


    A = np.vstack([x_vector, np.ones(max_points)]).T
```

```
                m, c = np.linalg.lstsq(A, y_vector)[0]

                angle_diff = np.arctan(m) * 180.0 / np.pi
                r.write('{0:.3f}'.format(angle_diff)+'\n')

                angle_comp = avg_angle_out - angle_diff
                s.write('{0:.3f}'.format(angle_comp)+'\n')

        else:
            h.write(line)
            print ('Trajectory {} was skipped'.format(line.rstrip('\n')))
print 'Done.'
```

D.3   Measuring Trajectory Incidence Angles

```python
import numpy as np
import matplotlib
import os.path
matplotlib.use('Agg')
from matplotlib.pyplot import *

# The purpose of this script is to measure the incoming angles relative to the
# slit points, which in a data set may rotate.
# The statements that follow allow for a rotation so that a complete data set
# will be plotted on consistent axes.
fname = 'TrajListOutAnalyzed.txt'
out1fname = 'Incoming_angles.txt'
out2fname = 'Incoming_angles_comparison.txt'
out3fname = 'Incoming_angles_regression.txt'

# values of pixels for slits for the data set
slitrightx1 = 261.0
slitrighty1 = 287.0
slitleftx1 = 334.0
slitlefty1  = 291.0

num_lines = 0
with open(fname) as f:
    for cnt, line in enumerate(f,1):
        pass
    num_lines = cnt
    print "New num_lines: ", num_lines


with open(fname,'r') as f, open(out1fname,'w') as q, open(out2fname,'w') as r,
open(out3fname,'w') as s:
    for cnt, line in enumerate(f,1):
        basename = line.rstrip('\n')
        if not os.path.isfile(basename):
                        pass
        else:
            if cnt < num_lines+1:
                slitrightx = slitrightx1
                slitrighty = slitrighty1
                slitleftx =   slitleftx1
                slitlefty  = slitlefty1

            elif cnt == num_lines+1:
                slitrightx = slitrightx1
                slitrighty = slitrighty1
                slitleftx  = slitleftx1
                slitlefty  = slitlefty1
                print("This is where we stop: {} {}".format(cnt, line))
                pass
            else:
                pass

            slitmidx = (slitrightx + slitleftx)/2.0
            slitmidy = (slitrighty + slitlefty)/2.0
            slit_slope = (slitlefty - slitrighty) / (slitleftx - slitrightx)
            slitangle = np.arctan(slit_slope)
            rot_angle = -slitangle - np.pi / 2.0

            slitrightxprime = slitrightx*np.cos(rot_angle) - slitrighty*np.sin(rot_angle)
            slitrightyprime = slitrightx * np.sin(rot_angle) + slitrighty * np.cos(rot_angle)

            slitleftxprime = slitleftx*np.cos(rot_angle) - slitlefty*np.sin(rot_angle)
            slitleftyprime = slitleftx*np.sin(rot_angle) + slitlefty*np.cos(rot_angle)


            slitmidxprime = slitmidx*np.cos(rot_angle) - slitmidy*np.sin(rot_angle)
```

```python
        slitmidyprime = slitmidx*np.sin(rot_angle) + slitmidy*np.cos(rot_angle)

        data = np.loadtxt(basename,unpack=True)

        N = np.arange(len(data[0]))
        rot_data = np.zeros([2,len(data[0])])
        ref_data = np.zeros([2,len(data[0])])

        for j in N:
            rot_data[0,j] = np.cos(rot_angle)*data[0,j] - np.sin(rot_angle)*data[1,j]
                            - slitmidxprime
            rot_data[1,j] = np.sin(rot_angle)*data[0,j] + np.cos(rot_angle)*data[1,j]
                            - slitmidyprime

        max_points = 10
        max_counts = max_points - 1
        #will include max_counts, excludes zero
        numpoints = np.arange(max_counts,0,-1)
        #will include zero, excludes max_points value
        indexcount = np.arange(0,max_points)

        avg_angle_in = 0.0
        for j in numpoints:
            deltax = rot_data[0,j] - rot_data[0,j-1]
            deltay = rot_data[1,j] - rot_data[1,j-1]
            angle_in = np.arctan(deltay / deltax ) *180.0 / np.pi
            avg_angle_in = avg_angle_in + angle_in


        avg_angle_in = avg_angle_in / max_counts
        q.write('{0:.3f}'.format(avg_angle_in)+'\n')
        # if np.abs(avg_angle_in) > 20:
            # g.write(line)
            # h.write('{0:.3f}'.format(avg_angle_in)+'\n')
        # else:
            # pass

        #### regression method
        x_vector = np.zeros([1,max_points])
        y_vector = np.zeros(max_points)

        for j in indexcount:
            x_vector[0,j] = rot_data[0,j]
            y_vector[j] = rot_data[1,j]


        A = np.vstack([x_vector, np.ones(max_points)]).T
        m, c = np.linalg.lstsq(A,y_vector)[0]
        angle_diff = np.arctan(m) * 180.0 / np.pi
        angle_comp = angle_diff - avg_angle_in

        r.write('{0:.3f}'.format(angle_diff)+'\n')
        s.write('{0:.3f}'.format(angle_comp)+'\n')

print 'Done.'
```

D.4   Making Post-selection Cuts

```python
from numpy import *
import matplotlib
import linecache
import os.path
matplotlib.use('Agg')
from matplotlib.pyplot import *

# Rearranges files and names based on a cut in input angle.
# Hopefully, this cleans up all the other nonsense.
fname1 = 'Incoming_angles.txt'
fname2 = 'TrajListOutanalyzed.txt'
fname3 = 'Out_angles.txt'

out1fname = 'Incoming_cuts.txt'
out2fname = 'Traj_cuts.txt'
out3fname = 'Out_cuts.txt'

with open(fname1,'r') as f1,open(fname2,'r') as f2, open(fname3,'r') as f3,
open(out1fname,'w') as of1, open(out2fname,'w') as of2, open(out3fname,'w') as of3:
    for cnt,line in enumerate(f1,1):
        inangle = float(line.rstrip('\n'))
        if np.abs(inangle) <= 2.00:
            of1.write(linecache.getline(fname1,cnt))
            of2.write(linecache.getline(fname2,cnt))
            of3.write(linecache.getline(fname3,cnt))
        else:
            pass
```

D.5 Plotting Trajectories

```python
from numpy import *
import matplotlib
import linecache
import os.path
matplotlib.use('Agg')
from matplotlib.pyplot import *

# fname = 'Incoming_angles_list.txt'
# fname = 'TrajectoryListAll.txt'
# fname = 'TrajSkipped.txt'
# fname = 'TrajListOutAnalyzed.txt'
fname = 'Traj_cuts.txt'

endname='.txt'

cos = np.cos
sin = np.sin

# values of pixels for slits for the data set
slitrightx1 = 261.0
slitrighty1 = 287.0
slitleftx1 = 334.0
slitlefty1  = 291.0
numslitwidths = 2.0


with open(fname) as f:
    for cnt, line in enumerate(f,1):
        basename = line.rstrip('\n')
        if not os.path.isfile(basename):
            pass

            #data = loadtxt(basename+endname,unpack=True)
        else:
            if cnt < 1093:
                slitrightx = slitrightx1
                slitrighty = slitrighty1
                slitleftx =   slitleftx1
                slitlefty  = slitlefty1

            elif cnt == 1093:
                slitrightx = slitrightx1
                slitrighty = slitrighty1
                slitleftx  = slitleftx1
                slitlefty  = slitlefty1
                print("This is where we stop: {} {}".format(cnt, line))
                pass
            else:
                pass

            slitmidx = (slitrightx + slitleftx)/2.0
            slitmidy = (slitrighty + slitlefty)/2.0
            slit_slope = (slitlefty - slitrighty) / (slitleftx - slitrightx)
            slitangle = np.arctan(slit_slope)
            rot_angle = -slitangle + np.pi / 2.0

            slitrightxprime = slitrightx * cos(rot_angle) - slitrighty * sin(rot_angle)
            slitrightyprime = slitrightx * sin(rot_angle) + slitrighty * cos(rot_angle)

            slitleftxprime = slitleftx * cos(rot_angle) - slitlefty * sin(rot_angle)
            slitleftyprime = slitleftx * sin(rot_angle) + slitlefty * cos(rot_angle)
            slitwidth = slitleftyprime - slitrightyprime
            screenx = slitwidth*numslitwidths

            slitmidxprime = slitmidx * cos(rot_angle) - slitmidy * sin(rot_angle)
            slitmidyprime = slitmidx * sin(rot_angle) + slitmidy * cos(rot_angle)
```

```
            data = np.loadtxt(basename,unpack=True)
            data = loadtxt(basename,unpack=True)

        N = np.arange(len(data[0]))
        rot_data = np.zeros([2,len(data[0])])
        # ref_data = np.zeros([2,len(data[0])])

        for j in N:
            rot_data[0,j] = cos(rot_angle)*data[0,j] - sin(rot_angle)*data[1,j]
                            - slitmidxprime
            rot_data[1,j] = sin(rot_angle)*data[0,j] + cos(rot_angle)*data[1,j]
                            - slitmidyprime

        plot(rot_data[0],rot_data[1],'.k', markeredgecolor='black',markersize=1.2, alpha=0.4)

plot(slitrightxprime - slitmidxprime,slitrightyprime - slitmidyprime,'.r',markersize = 2)
plot(slitleftxprime - slitmidxprime,slitleftyprime - slitmidyprime,'.b',markersize = 2)
# plot(screenx+rot_data[0]*0,rot_data[1],'-g')

Figure()

ylim(-160,160)
xlim(-200,300)

#Comment
axes().set_aspect('equal', 'datalim')
# savefig(fname.rstrip('.txt')+'.png', dpi=600)
# savefig(fname.rstrip('.txt')+'.eps', dpi=600)

savefig(fname.rstrip('.txt')+'nogreen'+'.png', dpi=600)
savefig(fname.rstrip('.txt')+'nogreen'+'.eps', dpi=600)

clf()
```

Appendix E

Python Image Analysis Scripts

E.1 Compile.py

```python
import os
from struct import *
import numpy as np

# set bitmap dimensions
xwidth = 656
ywidth = 494
filtermin = 60
filtermax = 150
# initialize idata3, set up dummy floating array that will take all of the
# summed data because bytearrays can only accept inputs less than 256
idata3 = bytearray(1078+(ywidth - 1)*(xwidth)+(xwidth))
intdata = np.zeros(1078+(ywidth - 1)*(xwidth)+(xwidth),dtype=float)

directory = './'
testfname = 'bitmaptest.txt'
outname = 'test.bmp'

# check if output bmp file already exists
if os.path.isfile(outname):
        os.remove(outname)
        print "Old compiled image was deleted, huzzah!"


files = []
for filename in os.listdir(directory):
    if filename.endswith(".bmp"):
        files.append((os.path.join(directory, filename)))
        continue
    else:
        continue

for q in np.arange(0,len(files)-1):
        if q%50 == 0:
                print q
        else:
                pass

        file1 = files[q]
        file2 = files[q+1]

        with open(file1, 'rb') as f1:
                idata1 = bytearray(f1.read())
```

```python
        with open(file2, 'rb') as f2:
                idata2 = bytearray(f2.read())

        if q == 0:
                with open(testfname, 'w') as l:
                        for i in np.arange(0,11,1):
                                offset = i
                                a = unpack_from('<L',idata1,offset)
                                print >> l, i,a[0],idata1[i]

                # initialize header and data for idata3, the compiled image, to the
                # first read image
                for i in np.arange(0,1078,1):
                        idata3[i] = idata1[i]
                for i in np.arange(1078,1078+(ywidth - 1)*(xwidth)+(xwidth-1),1):
                        idata3[i] = 0
        else:
                pass

# take data from 2 consecutive bitmaps, do some appending, add filter
        for i in np.arange(1078,1078+(ywidth - 1)*(xwidth)+(xwidth-1),1):
                if idata1[i] > filtermin and idata1[i] < filtermax:
                        intdata[i] = intdata[i] + (idata1[i] + idata2[i])/2
                else:
                        intdata[i] = intdata[i] + (idata1[i] + idata2[i])/(2*len(files))


# preallocate the norm factor to get this going faster
intdatanorm = np.max(intdata)
for i in np.arange(1078,1078+(ywidth - 1)*(xwidth)+(xwidth-1),1):
        idata3[i] = int(255*(intdata[i]/intdatanorm))
with open(outname, 'wb') as h:
    h.write(idata3)

print "BMP1 closed is ", f1.closed
print "BMP2 closed is ", f2.closed
print "Compiled BMP closed", h.closed
```

E.2   Drop finding script

```python
import os
from struct import *
import numpy as np

#Instructions: Copy and paste this code into the file directory you want to analyze.
#We can get fancy and post it outside, but for now let's keep it simple.

#As written, the code reads from bitmaps sized 496x494. Values of "idatamin"
#and "idatamax" can be modified to adjust the threshold of how bright the pixels
#are. Try changing them!

#Edit the code in Notepad++ (and save changes) or edit from IDLE.
#This shouldn't break anything and is meant to be completely transparent.

#There are some bits that aren't so transparent, unfortunately. But
#that has to do with how bmp's represent their data. That value 1078, for example,
#is a special one and indicates where to look in our files for all of the color values.

#The output, bitmaptest.txt, will show line by line what shows up in actual bitmap files,
#give or take some padding spaces. See if you can make sense of it. For example, see if
#you can spot familiar numbers (file size = 246,102 bytes), width = 496, length = 494,
#offset = 1078, color values ranging from 0 to 255, etc.

#Author: Eric Jones and plenty of Googling, 2017-07-06

#this first step looks for every bitmap in the current directory,
#and then appends the file name to an array. '.' is used for current working directory.
#directory = 'Position1/drop1/traj1/'
directory = '.'
testfname = 'bitmaptest.txt'
outfname1 = 'x_ycoordinates_avg.txt'
outfname2 = 'x_ycoordinates_CM.txt'

# check if output files already exist, delete them
if os.path.isfile(testfname):
    os.remove(testfname)

if os.path.isfile(outfname1):
    os.remove(outfname1)

if os.path.isfile(outfname2):
    os.remove(outfname2)

files = []
for filename in os.listdir(directory):
    if filename.endswith(".bmp"):
        files.append((os.path.join(directory, filename)))
        continue
    else:
        continue

for q in np.arange(0,len(files)):
    file = files[q]

    with open(file, 'rb') as f:
        idata = bytearray(f.read())
    # 246099 lines for 496x494 bmp, 1078 is offset to get to pixel array
    if q == 0:
        with open(testfname, 'w') as l:
            for i in np.arange(0,246099,1):
                offset = i
                a = unpack_from('<L',idata,offset)
                print >> l, "{0:06d}".format(i),"{:12d}".format(a[0]),"{:4d}".format(idata[i])
    else:
        pass
```

```python
# Now, use idata array to find max pixel values
xmax = 0
ymax = 0
imax = []
idatamin = 100
idatamax = 256
for i in np.arange(1078,1078+493*496+495,1):
    if idata[i] > idatamin and idata[i] < idatamax:
        imax.append(i)

# avg of imax doesn't give a reasonable result, but here it is:
iavg = np.average(imax)

#Intensity center of mass calculations
#split imax into coordinates using fancy modulo functions % and //
#make a product array like x*Intensity
#take weighted average xCM = sum(x*Intensity)/sum(Intensity)

datamax = np.zeros(len(imax))
xmax = np.zeros(len(imax))
ymax = np.zeros(len(imax))
xprod = np.zeros(len(imax))
yprod = np.zeros(len(imax))

for i in np.arange(len(imax)):
    datamax[i] = idata[i]
    xmax[i] = ((imax[i].astype(int)-1078)  % 496)
    ymax[i] = ((imax[i].astype(int)-1078) // 496)
    xprod[i] = xmax[i]*idata[i]
    yprod[i] = ymax[i]*idata[i]

xavg = np.average(xmax)
yavg = np.average(ymax)
xCM = np.sum(xprod)/np.sum(datamax)
yCM = np.sum(yprod)/np.sum(datamax)

iAVG = 1078 + np.ceil(xavg) + np.ceil(yavg)*496
iCM = 1078 + np.ceil(xCM) + np.ceil(yCM)*496

#formatting the file output strings with spaces and padding zeros
sp="    "
avgdatastr="{0:04d}".format(q)+sp+"{0:.1f}".format(xavg)+sp+"{0:.1f}".format(yavg)
CMdatastr= "{0:04d}".format(q)+sp+"{0:.1f}".format(xCM)+sp+"{0:.1f}".format(yCM)

with open(outfname1, "a") as g:
    g.write(avgdatastr+"\n")

with open(outfname2, "a") as h:
    h.write(CMdatastr+"\n")

print file, "is analyzed: ", f.closed

print "avg txt is closed: ", g.closed
print "CM txt is closed: ", h.closed
```

E.3   Left-right trajectory script

```python
import os
from struct import *
import numpy as np

# Copy and paste this in the same directory as the textfile outputs.
# Run from the command prompt to see outputs if you like!

directory = '.'
fname1 = 'x_ycoordinates_avg.txt'
fname2 = 'x_ycoordinates_CM.txt'

outfname1 = 'x_avg_right.txt'
outfname2 = 'x_avg_left.txt'
outfname3 = 'x_CM_right.txt'
outfname4 = 'x_CM_left.txt'

# data1 = data1[i,j] where i is row, j is column.
data1 = np.loadtxt(fname1)
data2 = np.loadtxt(fname2)

x1 = data1[:,1]
x2 = data2[:,1]
iright1 = []
ileft1 = []
iright2 = []
ileft2 = []


for i in np.arange(1,len(data1)):
    deltax1 = x1[i] - x1[i-1]
    print i, deltax1

    if deltax1 > 0:
        iright1.append(i-1)

    elif deltax1 < 0:
        ileft1.append(i-1)

    else:
        pass

for i in np.arange(1,len(data2)):
    deltax2 = x2[i] - x2[i-1]

    if deltax2 > 0:
        iright2.append(i-1)

    elif deltax1 < 0:
        ileft2.append(i-1)

    else:
        pass

print "Total number of positions: ", len(x1)
print " "
print "Total number going right: ", len(iright1)
print " "
print "Total number going left: ", len(ileft1)
print " "
print "Total sum sanity check: ", len(iright1) + len(ileft1)

sp = "     "

with open(outfname1, "w") as g:
    for j in iright1:
```

```
        g.write("{0:04d}".format(int(data1[j,0]))+sp+"{0:.1f}".format(x1[j])+'\n')

with open(outfname2, "w") as h:
    for j in ileft1:
        h.write("{0:04d}".format(int(data1[j,0]))+sp+"{0:.1f}".format(x1[j])+'\n')

with open(outfname3, "w") as k:
    for j in iright2:
        k.write("{0:04d}".format(int(data2[j,0]))+sp+"{0:.1f}".format(x2[j])+'\n')

with open(outfname4, "w") as l:
    for j in ileft2:
        l.write("{0:04d}".format(int(data2[j,0]))+sp+"{0:.1f}".format(x2[j])+'\n')
```

E.4   CompileBright.py

```python
import os
from struct import *
import numpy as np

# set bitmap dimensions
xwidth = 656
ywidth = 494
# initialize idata3, set up dummy floating array that will take all of the
# summed data because bytearrays can only accept inputs less than 256
idata3 = bytearray(1078+(ywidth - 1)*(xwidth)+(xwidth))
intdata = np.zeros(1078+(ywidth - 1)*(xwidth)+(xwidth),dtype=float)

directory = './'
testfname = 'bitmaptest.txt'
outname = 'bright.bmp'

# check if output bmp file already exists
if os.path.isfile(outname):
        os.remove(outname)
        print "Old compiled image was deleted, huzzah!"


files = []
for filename in os.listdir(directory):
    if filename.endswith(".bmp"):
        files.append((os.path.join(directory, filename)))
        continue
    else:
        continue

# for q in np.arange(0,len(files)-1):
for q in np.arange(0,100):
        if q%5 == 0:
                print q
        else:
                pass

        file1 = files[q]
        file2 = files[q+1]

        with open(file1, 'rb') as f1:
                idata1 = bytearray(f1.read())
        with open(file2, 'rb') as f2:
                idata2 = bytearray(f2.read())

        if q == 0:
                with open(testfname, 'w') as l:
                        for i in np.arange(0,11,1):
                                offset = i
                                a = unpack_from('<L',idata1,offset)
                                print >> l, i,a[0],idata1[i]

                # initialize header and data for idata3, the compiled image, to the
                # first read image
                for i in np.arange(0,1078,1):
                        idata3[i] = idata1[i]
                for i in np.arange(1078,1078+(ywidth - 1)*(xwidth)+(xwidth-1),1):
                        idata3[i] = 0
        else:
                pass

# take data from 2 consecutive bitmaps, do some appending
        for i in np.arange(1078,1078+(ywidth - 1)*(xwidth)+(xwidth-1),1):
                intdata[i] = intdata[i] + np.absolute(idata2[i] - idata1[i])
```

```python
# preallocate the norm factor to get this going faster
intdatanorm = np.max(intdata)
for i in np.arange(1078,1078+(ywidth - 1)*(xwidth)+(xwidth-1),1):
        idata3[i] = int(255*(intdata[i]/intdatanorm))
with open(outname, 'wb') as h:
    h.write(idata3)

print "BMP1 closed is ", f1.closed
print "BMP2 closed is ", f2.closed
print "Compiled BMP closed", h.closed
```

Appendix F

Degenerate Electron Source Analysis Codes

F.1   Two-particle Gaussian Path Integral Fortran Code

```fortran
PROGRAM twopartgauss

IMPLICIT NONE
! Define real parameters and constants
REAL*8, PARAMETER :: Pi = 3.1415926535898d0, &
        Hbar = 1.05457173d-34, &
        m = 9.10938291d-31, &
        L = 2d-1, &
        Energy = 3d1, &
        elec = 1.60217662e-19,&
        eE = elec*Energy, &
        deltaE = 0.8*elec,&
        tsourcewidth = 5d-15,&
        tscreenwidth = 1.5d-8,&
        dt          = Hbar/(4d0*deltaE),& !50d-15,&
        tdelwidth = 15d-9

! Define complex parameter and constants (like, you know, I)
COMPLEX*16, PARAMETER :: I = (0d0, 1d0)

! Define numbers for arrays
INTEGER*8, PARAMETER :: Nsource = 1000,&
                        Nscreen = 1000,&
                        Ndelay = 100

! Define real arrays
REAL*8 :: tsource1(-Nsource:Nsource), &
        tsource2(-Nsource:Nsource), &
        tscreen(-Nscreen:Nscreen), &
        tdel(-Ndelay:Ndelay),&
        Phisource1plot(-Nsource:Nsource),&
        Phisource2plot(-Nsource:Nsource),&
        PDFsource1(-Nsource:Nsource), &
        PDFsource2(-Nsource:Nsource), &
        PDF11screen(-Nscreen:Nscreen),&
        PDF2part(-Nscreen:Nscreen),&
        PDF2partdel(-Ndelay:Ndelay)
! Define complex arrays
COMPLEX*16 :: Kscreen11pq,&
              Kscreen12pq,&
              Kscreen21pq,&
              Kscreen22pq,&
              Phisource1(-Nsource:Nsource),&
```

```fortran
                       Phisource2(-Nsource:Nsource),&
                       Phi11screen(-Nscreen:Nscreen),&
                       Phi12screen(-Nscreen:Nscreen),&
                       Phi21screen(-Nscreen:Nscreen),&
                       Phi22screen(-Nscreen:Nscreen),&
                       Phi2part(-Nscreen:Nscreen),&
                       ! PDF2part(-Nscreen:Nscreen),&
                       Phi2parttemp


        ! Define (real and complex) variables and looping integers
        REAL*8 :: v0, tflight, sigE, tsourcestep, tscreenstep, tdelaystep,&
                  PDF2partdeltemp
        COMPLEX*16 :: Phi11temp, Phi12temp, Phi21temp, Phi22temp
        INTEGER*8 :: p,q,r

        v0 = DSQRT(2d0*eE / m)
        tflight = L / v0
        sigE = deltaE*DSQRT(2d0)
        tsourcestep = tsourcewidth/(2d0*DFLOAT(Nsource)+1d0)

        PRINT*, 'Initializing all the things!'

        OPEN(UNIT=20, FILE="two_part_source1.txt")
        OPEN(UNIT=21, FILE="two_part_source2.txt")
        DO p = -Nsource, Nsource
             tsource1(p) = DFLOAT(p)*tsourcestep
             tsource2(p) = tsource1(p) + dt
             Phisource1(p) = DEXP(-(sigE/(DSQRT(2d0)*Hbar))**2d0 * tsource1(p)**2d0)&
                             *CDEXP(-I*eE*tsource1(p)/Hbar)
                             ! term for energy distribution centered at E0
             Phisource2(p) = DEXP(-(sigE/(DSQRT(2d0)*Hbar))**2d0 * (tsource2(p)-dt)**2d0)&
                             *CDEXP(-I*eE*(tsource2(p)-dt)/Hbar)
             Phisource1plot(p) = REALPART(Phisource1(p))
             Phisource2plot(p) = REALPART(Phisource2(p))
             PDFsource1(p) = REALPART(DCONJG(Phisource1(p))*Phisource1(p))
             PDFsource2(p) = REALPART(DCONJG(Phisource2(p))*Phisource2(p))
             ! WRITE(20,100) tsource(p),Phisource(p),PDFsource(p),p
             WRITE(20,100) tsource1(p),Phisource1plot(p),PDFsource1(p),p
             WRITE(21,100) tsource2(p),Phisource2plot(p),PDFsource2(p),p
        END DO
        CLOSE(20)
        CLOSE(21)

        tscreenstep = tscreenwidth/(2d0*DFLOAT(Nscreen)+1d0)
        DO q = -Nscreen, Nscreen
             tscreen(q) = DFLOAT(q)*tscreenstep + tflight
        END DO

        tdelaystep = tdelwidth/(2d0*DFLOAT(Ndelay)+1d0)
        DO r = -Ndelay, Ndelay
             tdel(r) = DFLOAT(r)*tdelaystep
        END DO

        PRINT*, 'Value of v0: ', v0
        PRINT*, 'Value of tflight: ', tflight
        PRINT*, 'Value of sigE: ', sigE
        PRINT*, 'Value of tsourcestep: ', tsourcestep

        PDF2partdel = 0d0
        ! OPEN(UNIT=30, FILE="two_part_screen.txt")
        OPEN(UNIT=31, FILE="two_part_delay.txt")
        ! OPEN(UNIT=32, FILE="two_part_test.txt")
        DO r = -Ndelay, Ndelay
             Phi11screen = COMPLEX(0d0,0d0)
             Phi12screen = COMPLEX(0d0,0d0)
```

```fortran
Phi21screen = COMPLEX(0d0,0d0)
Phi22screen = COMPLEX(0d0,0d0)
Phi2part    = COMPLEX(0d0,0d0)
PDF2part    = COMPLEX(0d0,0d0)
PDF2partdeltemp = 0d0
Phi2parttemp = COMPLEX(0d0,0d0)
DO q = -Nscreen, Nscreen
      Phi11temp = COMPLEX(0d0,0d0)
      Phi12temp = COMPLEX(0d0,0d0)
      Phi21temp = COMPLEX(0d0,0d0)
      Phi22temp = COMPLEX(0d0,0d0)
     DO p = -Nsource, Nsource
          Kscreen11pq = COMPLEX(0d0,0d0)
          Kscreen12pq = COMPLEX(0d0,0d0)
          Kscreen21pq = COMPLEX(0d0,0d0)
          Kscreen22pq = COMPLEX(0d0,0d0)

          Kscreen11pq = CDSQRT(m / (2*Pi*I*Hbar * (tscreen(q) - tsource1(p))))*&
                            ! CDEXP(-I*Pi/4d0)*&
                            CDEXP(I*m*L**2d0/(2d0*Hbar*&
                                (tscreen(q) - tsource1(p))))

          Kscreen12pq = CDSQRT(m / (2*Pi*I*Hbar * (tscreen(q) - tdel(r) - tsource1(p))))*&
                            ! CDEXP(-I*Pi/4d0)*&
                            CDEXP(I*m*L**2d0/(2d0*Hbar*&
                                (tscreen(q) - tdel(r) - tsource1(p))))

          Kscreen21pq = CDSQRT(m / (2*Pi*I*Hbar * (tscreen(q) - tsource2(p))))*&
                            ! CDEXP(-I*Pi/4d0)*&
                            CDEXP(I*m*L**2d0/(2d0*Hbar*&
                                (tscreen(q)  - tsource2(p))))

          Kscreen22pq = CDSQRT(m / (2*Pi*I*Hbar * (tscreen(q) - tdel(r) - tsource2(p))))*&
                            ! CDEXP(-I*Pi/4d0)*&
                            CDEXP(I*m*L**2d0/(2d0*Hbar*&
                                (tscreen(q) - tdel(r)- tsource2(p))))
          Phi11temp = Phi11temp + Kscreen11pq*Phisource1(p)
          Phi12temp = Phi12temp + Kscreen12pq*Phisource1(p)
          Phi21temp = Phi21temp + Kscreen21pq*Phisource2(p)
          Phi22temp = Phi22temp + Kscreen22pq*Phisource2(p)
     END DO ! source loop
     Phi11screen(q) = Phi11temp
     Phi12screen(q) = Phi12temp
     Phi21screen(q) = Phi21temp
     Phi22screen(q) = Phi22temp
     ! keep as a check
     ! IF (r == 1) THEN
         ! PDF11screen(q) = REALPART(DCONJG(Phi22screen(q))*Phi22screen(q))
         ! WRITE(30,101) tscreen(q),PDF11screen(q),q

         ! Phi2part(q) = (1d0/DSQRT(2d0)) * (Phi11screen(q)*Phi22screen(q) - &
                                            ! Phi21screen(q)*Phi12screen(q))
         ! PDF2part(q) = DCONJG(Phi2part(q))*Phi2part(q)
         ! WRITE(32,102) Phi11screen(q),Phi22screen(q),Phi21screen(q),Phi12screen(q)
     ! ELSE
     ! END IF
     Phi2part(q) = (1d0/DSQRT(2d0)) * (Phi11screen(q)*Phi22screen(q) - &
                                        Phi21screen(q)*Phi12screen(q))
     ! This is for conjugating before integrating
     PDF2part(q) = REALPART(DCONJG(Phi2part(q))*Phi2part(q))
     PDF2partdeltemp = PDF2partdeltemp + PDF2part(q)

     ! This is for summing before conjugating
     ! Phi2parttemp = Phi2parttemp + Phi2part(q)
END DO ! screen loop
```

```
        ! For conjugating before summing, take
        PDF2partdel(r) = PDF2partdeltemp

        ! For summing before conjugating, take
        !PDF2partdel(r) = REALPART(DCONJG(Phi2parttemp)*Phi2parttemp)
        WRITE(31,101) tdel(r), PDF2partdel(r), r
END DO        ! delay loop
CLOSE(30)
CLOSE(31)
 ! CLOSE(32)
PRINT*, 'Done with all the things!'

 100 FORMAT(E15.7E3,4x,E15.7E3,4x,E15.7E3,4x,I8)
 101 FORMAT(E15.7E3,4x,E15.7E3,4x,I8)
 ! 102 FORMAT(E15.7E3,4x,E15.7E3,4x,E15.7E3,4x,E15.7E3,4x,
               E15.7E3,4x,E15.7E3,4x,E15.7E3,4x,E15.7E3,4x)

ENDPROGRAM twopartgauss
```

F.2 Two-particle Temporal Slit Path Integral Fortran Code

```fortran
PROGRAM twopartslit

IMPLICIT NONE
! Define real parameters and constants
REAL*8, PARAMETER :: Pi = 3.1415926535898d0, &
        Hbar = 1.05457173d-34, &
        m = 9.10938291d-31, &
        L = 2d-1, &
        Energy = 3d1, &
        elec = 1.60217662e-19,&
        eE = elec*Energy, &
        deltaE = 0.8*elec,&
        ! tsourcewidth = 5d-14,&
        tscreenwidth = 8d-7,&
        dt          = 4.73*Hbar/(4d0*deltaE),& !50d-15,&
        tdelwidth = 60d-9

! Define complex parameter and constants (like, you know, I)
COMPLEX*16, PARAMETER :: I = (0d0, 1d0)

! Define numbers for arrays
INTEGER*8, PARAMETER :: Nsource = 3000,&
                        Nscreen = 10000,&
                        Ndelay = 300

! Define real arrays
REAL*8 :: tsource1(-Nsource:Nsource), &
          tsource2(-Nsource:Nsource), &
          tscreen(0:2*Nscreen), &
          tdel(-Ndelay:Ndelay),&
          Phisource1plot(-Nsource:Nsource),&
          Phisource2plot(-Nsource:Nsource),&
          PDFsource1(-Nsource:Nsource), &
          PDFsource2(-Nsource:Nsource), &
          PDF11screen(0:2*Nscreen),&
          PDF2part(0:2*Nscreen),&
          PDF2partdel(-Ndelay:Ndelay)
! Define complex arrays
COMPLEX*16 :: Kscreen11pq,&
              Kscreen12pq,&
              Kscreen21pq,&
              Kscreen22pq,&
              Phisource1(-Nsource:Nsource),&
              Phisource2(-Nsource:Nsource),&
              Phi11screen(0:2*Nscreen),&
              Phi12screen(0:2*Nscreen),&
              Phi21screen(0:2*Nscreen),&
              Phi22screen(0:2*Nscreen),&
              Phi2part(0:2*Nscreen),&
              ! PDF2part(-Nscreen:Nscreen),&
              Phi2parttemp


! Define (real and complex) variables and looping integers
REAL*8 :: v0, tflight, sigE, tsourcestep,tscreenstep,tdelaystep,&
          PDF2partdeltemp, tsourcewidth
COMPLEX*16 :: Phi11temp,Phi12temp,Phi21temp,Phi22temp
INTEGER*8 :: p,q,r

v0 = DSQRT(2d0*eE / m)
tflight = L / v0
sigE = deltaE*DSQRT(2d0)
tsourcewidth = 4.73*Hbar/(2d0*deltaE)
tsourcestep = tsourcewidth/(2d0*DFLOAT(Nsource)+1d0)
```

```fortran
      PRINT*, 'Initializing all the things!'

      OPEN(UNIT=20, FILE="tp_slitG_source1.txt")
      OPEN(UNIT=21, FILE="tp_slitG_source2.txt")
      DO p = -Nsource, Nsource
           tsource1(p) = DFLOAT(p)*tsourcestep
           tsource2(p) = tsource1(p) + dt
           Phisource1(p) = CDEXP(-I*eE*tsource1(p)/Hbar)  !*&
                        ! DEXP(-(sigE/(DSQRT(2d0)*Hbar))**2d0 * tsource1(p)**2d0)

                        ! term for energy distribution centered at E0
           Phisource2(p) = CDEXP(-I*eE*(tsource2(p)-dt)/Hbar)  !*&
                        ! DEXP(-(sigE/(DSQRT(2d0)*Hbar))**2d0 * (tsource2(p)-dt)**2d0)
           Phisource1plot(p) = REALPART(Phisource1(p))
           Phisource2plot(p) = REALPART(Phisource2(p))
           PDFsource1(p) = REALPART(DCONJG(Phisource1(p))*Phisource1(p))
           PDFsource2(p) = REALPART(DCONJG(Phisource2(p))*Phisource2(p))
           ! WRITE(20,100) tsource(p),Phisource(p),PDFsource(p),p
           WRITE(20,100) tsource1(p),Phisource1plot(p),PDFsource1(p),p
           WRITE(21,100) tsource2(p),Phisource2plot(p),PDFsource2(p),p
      END DO
      CLOSE(20)
      CLOSE(21)

      tscreenstep = tscreenwidth/(2*DFLOAT(Nscreen)+1)
      DO q = -Nscreen, Nscreen
           tscreen(q) = DFLOAT(q)*tscreenstep + 30.1d-9
      END DO

      tdelaystep = tdelwidth/(2d0*DFLOAT(Ndelay)+1d0)
      DO r = -Ndelay, Ndelay
           tdel(r) = DFLOAT(r)*tdelaystep
      END DO

      PRINT*, 'Value of v0: ', v0
      PRINT*, 'Value of tflight: ', tflight
      PRINT*, 'Value of sigE: ', sigE
      PRINT*, 'Value of tsourcestep: ', tsourcestep

      PDF2partdel = 0d0
      ! OPEN(UNIT=30, FILE="two_part_screen.txt")
      OPEN(UNIT=31, FILE="tp_slitG_delay.txt")
      ! OPEN(UNIT=32, FILE="two_part_test.txt")
      DO r = -Ndelay, Ndelay
           Phi11screen = COMPLEX(0d0,0d0)
           Phi12screen = COMPLEX(0d0,0d0)
           Phi21screen = COMPLEX(0d0,0d0)
           Phi22screen = COMPLEX(0d0,0d0)
           Phi2part    = COMPLEX(0d0,0d0)
           PDF2part    = COMPLEX(0d0,0d0)
           PDF2partdeltemp = 0d0
           Phi2parttemp = COMPLEX(0d0,0d0)
          DO q = -Nscreen, Nscreen
               Phi11temp = COMPLEX(0d0,0d0)
               Phi12temp = COMPLEX(0d0,0d0)
               Phi21temp = COMPLEX(0d0,0d0)
               Phi22temp = COMPLEX(0d0,0d0)
              DO p = -Nsource, Nsource
                    Kscreen11pq = COMPLEX(0d0,0d0)
                    Kscreen12pq = COMPLEX(0d0,0d0)
                    Kscreen21pq = COMPLEX(0d0,0d0)
                    Kscreen22pq = COMPLEX(0d0,0d0)

                    Kscreen11pq = CDSQRT(m / (2*Pi*I*Hbar * (tscreen(q) - tsource1(p))))*&
                                 ! CDEXP(-I*Pi/4d0)*&
```

```fortran
                                CDEXP(I*m*L**2d0/(2d0*Hbar*&
                                      (tscreen(q) - tsource1(p)))))

                Kscreen12pq = CDSQRT(m / (2*Pi*I*Hbar * (tscreen(q) - tdel(r) - tsource1(p))))*&
                                    ! CDEXP(-I*Pi/4d0)*&
                                    CDEXP(I*m*L**2d0/(2d0*Hbar*&
                                          (tscreen(q) - tdel(r) - tsource1(p)))))

                Kscreen21pq = CDSQRT(m / (2*Pi*I*Hbar * (tscreen(q) - tsource2(p))))*&
                                    ! CDEXP(-I*Pi/4d0)*&
                                    CDEXP(I*m*L**2d0/(2d0*Hbar*&
                                          (tscreen(q)  - tsource2(p)))))

                Kscreen22pq = CDSQRT(m / (2*Pi*I*Hbar * (tscreen(q) - tdel(r) - tsource2(p))))*&
                                    ! CDEXP(-I*Pi/4d0)*&
                                    CDEXP(I*m*L**2d0/(2d0*Hbar*&
                                          (tscreen(q) - tdel(r)- tsource2(p)))))
                Phi11temp = Phi11temp + Kscreen11pq*Phisource1(p)
                Phi12temp = Phi12temp + Kscreen12pq*Phisource1(p)
                Phi21temp = Phi21temp + Kscreen21pq*Phisource2(p)
                Phi22temp = Phi22temp + Kscreen22pq*Phisource2(p)
              END DO ! source loop
             Phi11screen(q) = Phi11temp
             Phi12screen(q) = Phi12temp
             Phi21screen(q) = Phi21temp
             Phi22screen(q) = Phi22temp

             ! keep as a check
             ! IF (r == 1) THEN
                 ! PDF11screen(q) = REALPART(DCONJG(Phi22screen(q))*Phi22screen(q))
                 ! WRITE(30,101) tscreen(q),PDF11screen(q),q

                 ! Phi2part(q) = (1d0/DSQRT(2d0)) * (Phi11screen(q)*Phi22screen(q) - &
                                                    ! Phi21screen(q)*Phi12screen(q))
                 ! PDF2part(q) = DCONJG(Phi2part(q))*Phi2part(q)
                 ! WRITE(32,102) Phi11screen(q),Phi22screen(q),Phi21screen(q),Phi12screen(q)
             ! ELSE
             ! END IF
             Phi2part(q) = (1d0/DSQRT(2d0)) * (Phi11screen(q)*Phi22screen(q) - &
                                               Phi21screen(q)*Phi12screen(q))
             ! This is for conjugating before integrating
             PDF2part(q) = REALPART(DCONJG(Phi2part(q))*Phi2part(q))
             PDF2partdeltemp = PDF2partdeltemp + PDF2part(q)

             ! This is for summing before conjugating
             ! Phi2parttemp = Phi2parttemp + Phi2part(q)
          END DO ! screen loop
          ! For conjugating before summing, take
          PDF2partdel(r) = PDF2partdeltemp

          ! For summing before conjugating, take
          !PDF2partdel(r) = REALPART(DCONJG(Phi2parttemp)*Phi2parttemp)
          WRITE(31,101) tdel(r), PDF2partdel(r), r
      END DO          ! delay loop
      ! CLOSE(30)
      CLOSE(31)
      ! CLOSE(32)
      PRINT*, 'Done with all the things!'

 100 FORMAT(E15.7E3,4x,E15.7E3,4x,E15.7E3,4x,I8)
 101 FORMAT(E15.7E3,4x,E15.7E3,4x,I8)
 ! 102 FORMAT(E15.7E3,4x,E15.7E3,4x,E15.7E3,4x,E15.7E3,4x,
              E15.7E3,4x,E15.7E3,4x,E15.7E3,4x,E15.7E3,4x)

ENDPROGRAM twopartslit
```

F.3 Two-particle Time-of-flight Matlab Script

```matlab
clc;

m = 9.10938356e-31; % electron mass in kilograms
hbar = 1.0545718e-34;% hbar in J.s
Evolt = 30; % tip voltage in V, strong dependence
E = Evolt*1.60217662e-19; % electron energy, in Joules
'velocity, in m/s'
v = sqrt(2*E/m)

L = 0.2;
deltaE = 0.8*1.60217662e-19; %1e-2*E;
tcoh = hbar/(2*deltaE); %4.73*hbar/(2*deltaE)
p0 = m*v;
tflight = L/v
% far field time condition
'far field condition, should be smaller than 1'
(E/hbar)*tcoh^2/tflight

tint = tflight;
deltat = tcoh; % with deltat = 4.5*tcoh, the width of sinc and gaussian are ~equal
deltatG = tcoh*4.73;
dt = deltat/2;
dtG = deltatG/2;


t     = tflight*linspace(0.1,2,100000)';
tdelt = tflight*linspace(-0.7,0,501)'; %(-0.5/100,0.5/100,1000)';

% transform energy dependence into time dependence
E11 = zeros(length(t), length(tdelt));
E21 = zeros(length(t), length(tdelt));
E12 = zeros(length(t), length(tdelt));
E22 = zeros(length(t), length(tdelt));

% transform energy dependence into time dependence
E11G = zeros(length(t), length(tdelt));
E21G = zeros(length(t), length(tdelt));
E12G = zeros(length(t), length(tdelt));
E22G = zeros(length(t), length(tdelt));


% substitution follows 2.8 of Barwick dissertation
for k=1:length(t);
    E11(k,:) = m*L^2./(2*t(k).^2)-E;
    E21(k,:) = m*L^2/(2*(t(k)-dt).^2)-E;
    E12(k,:) = m*L^2./(2*(t(k)+ -tdelt).^2)-E;
    E22(k,:) = m*L^2./(2*(t(k)-dt+ -tdelt).^2)-E;
end;

% substitution follows 2.8 of Barwick dissertation
for k=1:length(t);
    E11G(k,:) = m*L^2./(2*t(k).^2)-E;
    E21G(k,:) = m*L^2/(2*(t(k)-dtG).^2)-E;
    E12G(k,:) = m*L^2./(2*(t(k)+ -tdelt).^2)-E;
    E22G(k,:) = m*L^2./(2*(t(k)-dtG+ -tdelt).^2)-E;
end;

norm = sqrt(2/(hbar*deltat*pi));
phi11mat = norm*sin(E11*deltat/(2*hbar))./(E11/hbar);
phi22mat = norm*sin(E22*deltat/(2*hbar))./(E22/hbar);
phi12mat = norm*sin(E12*deltat/(2*hbar))./(E12/hbar);
phi21mat = norm*sin(E21*deltat/(2*hbar))./(E21/hbar);
```

```matlab
phi11matG = norm*sin(E11G*deltatG/(2*hbar))./(E11G/hbar);
phi22matG = norm*sin(E22G*deltatG/(2*hbar))./(E22G/hbar);
phi12matG = norm*sin(E12G*deltatG/(2*hbar))./(E12G/hbar);
phi21matG = norm*sin(E21G*deltatG/(2*hbar))./(E21G/hbar);

sigE = deltaE*sqrt(2);
gaussnorm = 1/sqrt(sqrt(pi)*sigE);

phi11gaus = gaussnorm*exp(-(E11/(sqrt(2)*sigE)).^2);
phi22gaus = gaussnorm*exp(-(E22/(sqrt(2)*sigE)).^2);
phi12gaus = gaussnorm*exp(-(E12/(sqrt(2)*sigE)).^2);
phi21gaus = gaussnorm*exp(-(E21/(sqrt(2)*sigE)).^2);

psi12mat = (1/sqrt(2))*(phi11mat.*phi22mat - phi21mat.*phi12mat);
prob12mat = psi12mat.*conj(psi12mat);
prob12 = real(nansum(prob12mat,1));

psi12matG = (1/sqrt(2))*(phi11matG.*phi22matG - phi21matG.*phi12matG);
prob12matG = psi12matG.*conj(psi12matG);
prob12slitG = real(sum(prob12matG,1));

psi12gaus = (1/sqrt(2))*(phi11gaus.*phi22gaus - phi21gaus.*phi12gaus);
prob12gaus = psi12gaus.*conj(psi12gaus);
prob12g = real(sum(prob12gaus,1));
figure(60);
plot(t,phi11mat.^2);
% ind = find(abs(prob12-max(prob12))<1e-6*max(prob12)  )
% tres = tdel(ind(2))-tdel(ind(1))
%%
figure(40);
plot(tdelt,prob12/max(prob12));
hold on;
plot(tdelt,prob12g/max(prob12g));
% plot(tdel(ind),prob12(ind),'xr');
hold off;
xlim([min(tdelt) max(tdelt)]);
% ylim([0  0.8]);
%%
```

Appendix G

GaAs Subadditivity Modeling Code

G.1   Subadditivity Modeling Fortran Code

```fortran
PROGRAM prog

IMPLICIT NONE
REAL*8, PARAMETER :: l = 1/(1d0), &
                     tw = 3.75d-1, &
                     tres = 2.5d3, &
                     alpha = 2.8d-1, &
                     tplot = 1d4

REAL*8     :: I1, I2, t, dt, tau, dtau, e1sum, e2sum, e12sum, &
              pop, subadd, e1summin, e2summin, e12summin, subaddmin,&
              E1, E2, I1sum, I2sum, I12sum, subaddI

REAL*8     :: condexp
INTEGER*8  :: i,j,Ndiv,Npoints

OPEN(UNIT=30,FILE='subaddOLD.dat')

Ndiv = 1000000
dt = 10d0*tplot/dfloat(Ndiv)
PRINT*, dt
Npoints = 1000
dtau = 1d0*tplot/dfloat(Npoints)
PRINT*, dtau

tau = 0d0
DO j = 1,Npoints
    t = -5d0*tplot
    e1sum = 0d0
    e2sum = 0d0
    e12sum = 0d0

    e1summin = 0d0
    e2summin = 0d0
    e12summin = 0d0

    I1sum = 0d0
    I2sum = 0d0
    I12sum = 0d0

    IF (tau.LT.8d0) THEN
        dtau = 1d-1
    ELSE
        dtau = 1d0*tplot/dfloat(Npoints)
```

```fortran
        END IF

        DO i = 1,Ndiv
            I1 = condexp((1/2)*l**2*tw**2-l*t)*&
                 derfc((l*tw**2-t)/(dsqrt(2d0)*tw))
            I2 = condexp((1/2)*l**2*t**2-l*(t-tau))*&
                 derfc((l*tw**2-(t-tau))/(dsqrt(2d0)*tw))
            E1 = sqrt(I1)
            E2 = sqrt(I2)
            pop = 1d0 - dexp(-tau/tres)*alpha
            ! e1sum = e1sum + I1**3
            ! e2sum = e2sum + I2**3
            ! e12sum = e12sum + (I1 + pop*I2)**3

            e1sum = e1sum + E1**6
            e2sum = e2sum + E2**6
            e12sum = e12sum + (E1 + sqrt(pop)*E2)**6

            e1summin = e1summin + E1**6
            e2summin = e2summin + E2**6
            e12summin = e12summin + (E1 - sqrt(pop)*E2)**6

            I1sum = I1sum + I1**3
            I2sum = I2sum + I2**3
            I12sum = I12sum + (I1 + pop*I2)**3

            !WRITE(30,101) t, I1, I2
            t = t + dt
        END DO
            subadd = (e12sum - e1sum - e2sum) / (e1sum + e2sum)
            subaddmin = (e12summin - e1summin - e2summin) / (e1summin + e2summin)
            subaddI = (I12sum - I1sum - I2sum) / (I1sum + I2sum)
            WRITE(30,100) tau, subadd, subaddmin, subaddI
            tau = tau + dtau
END DO

CLOSE(30)

100 FORMAT(E24.17E3,4x,E24.17E3,4x,E24.17E3,4x,E24.17E3)
! 101 FORMAT(E24.17,4x,E24.17,4x,E24.17)

ENDPROGRAM prog

FUNCTION condexp(x) result(ans)
    REAL*8, INTENT(IN) :: x
    REAL*8             ans

    IF (x.LT.7d2) THEN
        ans = dexp(x)
    ELSE
        ans = 0d0
    END IF

END FUNCTION
```

G.2   GaAsXcorrChirp.m

```
%%
% theory part
clc;
%import Evan's data
subaddGauss = importdata('subaddGauss.dat');
subaddArb = importdata('subaddArb.dat');

%%
clc;
I = sqrt(-1);
c = 3e8;
lambda = 800e-9;
omega = 2*pi*c/lambda;
b = 3.79e26;
sigt = 55e-15;  % pulse 1/e^2 width in fs

alpha = 0.134;
alpha2 = 1.11;
tres = 2.5e-10;
tw = 4.1e-1;
twfast = 40e-15;
twfast2 = 1180e-15;
taustart = 190e-15;
taustart2 = 2200e-15;

alpha2p2 = 0.66;
alphap2 = 0.0724;

% t = 1e-15*(-400:0.01:400)';
t   = 1e-15*(-200:0.01:200)';
tau = 1e-15*(0:1:1e6)';
% twfast adjusts slope of linear part of erfc for start of pop function
% taustart adjusts where pop turns on
% tres adjusts long-term exponential behavior
Iscale = 0.57;%0.57;
% poptest = alpha2*erfc((twfast2-(tau-taustart2))/(sqrt(2d0)*twfast2));
poptest = alpha2*exp(-((tau-taustart2)/twfast2).^2);
poptest2 = alpha2p2*exp(-((tau-taustart2)/twfast2).^2);
pop = 1d0 - (alpha)*(exp(-(tau)/tres).*erfc((twfast-(tau-taustart))/
      (sqrt(2d0)*twfast)) + poptest);
pop2 = 1d0 - (alphap2)*(exp(-(tau)/tres).*erfc((twfast-(tau-taustart))/
      (sqrt(2d0)*twfast)) + poptest2);

%%%%pop2 gets the job done with a scaled pulse 1 intensity!
e1sum = 1;
e2sum = 1;
e12sum = 1 + pop.^3;
subadd = (e12sum - e1sum - e2sum) / (e1sum + e2sum);

e1sum2 = Iscale^3;
e2sum2 = 1;
e12sum2 = Iscale^3 + pop2.^3;
subadd2 = (e12sum2 - e1sum2 - e2sum2) / (e1sum2 + e2sum2);


Igauss = exp(-t.^2/((sigt)^2));
Echirp = sqrt(Igauss).*exp(I*omega*t).*exp(I*b*t.^2);
Egauss = sqrt(Igauss).*cos(omega*t+b*t.^2);
% plot(t,Egauss)

E1 = Egauss;
E2 = sqrt(0.57)*Egauss;
```

```matlab
% generate 3rd order emission process terms,chirped
[ec60,lag60] = xcorr(E1.^6,E2.^0,0);
[ec51,lag51] = xcorr(E1.^5,E2.^1);
[ec42,lag42] = xcorr(E1.^4,E2.^2);
[ec33,lag33] = xcorr(E1.^3,E2.^3);
[ec24,lag24] = xcorr(E1.^2,E2.^4);
[ec15,lag15] = xcorr(E1.^1,E2.^5);
[ec06,lag06] = xcorr(E1.^0,E2.^6,0);

dt = t(2)-t(1);
tdelay = dt*lag33';

ecsigmax = ec60 + 6*ec51 + 15*ec42 + 20*ec33 + 15*ec24 + 6*ec15 + ec06;
bothsigmax = (ecsigmax);
refsig = ec60;
delsig = ec06;

ratiofitmaxGaAs = (bothsigmax-(refsig+delsig))/(refsig+delsig);

%%
% plot the non-subadditive, normal I^3 crosscorrelation
figure(1);
p1 =plot(tdelay*1e15,ratiofitmaxGaAs,'-r','Linewidth',1.5);
hold on;
p2 =  plot(AddRat(:,1),AddRat(:,2),'-k');
hold off;
xlim([-30 1.7e2]);
ylim([-1.2 26]);

legend([p2 p1],{'Data','$I^3$ Model'},'Location','northeast','Interpreter','latex');

xlabel('$\tau$ (fs)','Interpreter','latex');
ylabel('Additivity Ratio $\mathcal{R}(\tau)$','Interpreter','latex');
set(gca,'Fontsize',10,'FontName','Times New Roman','TickLabelInterpreter','latex',...
    'Linewidth',1);

fig = gcf;
fig.PaperUnits = 'inches';
% fig.PaperPosition = [0 0 3.4 2];
fig.PaperPosition = [0 0 6.5 4];
print('SubaddShort','-depsc');

%%
% plot the long-term subadditive behavior, semilog scale in time
figure(2);
p1 = semilogx(AddRat(:,1),AddRat(:,2),'-sk');
hold on;
p2 = plot(tdelay*1e15,ratiofitmaxGaAs,'-r','Linewidth',2);
plot(tau*1e15,subadd2,'-r','Linewidth',2);
plot((tau)*1e15-1e2,0*tau,'--k','Linewidth',1)
hold off;
xlim([1e2 1e6]);
ylim([-0.5 1.1]);

legend([p1 p2],{'Data','$I^3$ Model'},'Location','northeast','Interpreter','latex');

xlabel('$\tau$ (fs)','Interpreter','latex');
ylabel('Additivity Ratio $\mathcal{R}(\tau)$','Interpreter','latex');
set(gca,'Fontsize',10,'FontName','Times New Roman','TickLabelInterpreter','latex',...
    'Linewidth',1);

fig = gcf;
fig.PaperUnits = 'inches';
% fig.PaperPosition = [0 0 3.4 2];
fig.PaperPosition = [0 0 6.5 4];
```

```matlab
print('SubaddLong','-depsc');

%%%subadd starts at ~170fs, to 320fs, then sits and exponentially goes up
%%
figure(3);
oldchi = 1 - 0.28*exp(-tau/250e-12);

p1 = semilogx(tau*1e15,oldchi,'-k','Linewidth',2);
hold on;
p2 = semilogx(tau*1e15,pop,'-b','Linewidth',2);
p3 = semilogx(tau*1e15,pop2,'-r','Linewidth',2);
hold off;
xlim([1 1e6]);

% legend([p1 p2 p3],{'Old Model','New Model, $I_{1}=I_{2}$',
%                    'New Model, $I_{1} \neq I_{2}$'},
%                    'Location','southeast','Interpreter','latex');
% legend([p1 p2 p3],{'Old',
%                    'New, $I_{1}=I_{2}$',
%                    'New, $I_{1} \neq I_{2}$'},
%                    'Location','southeast','Interpreter','latex');


xlabel('$\tau$ (fs)','Interpreter','latex');
ylabel('Suppression $\chi(\tau)$','Interpreter','latex');
set(gca,'Fontsize',10,'FontName','Times New Roman','TickLabelInterpreter','latex',
        'Linewidth',1);

fig = gcf;
fig.PaperUnits = 'inches';
fig.PaperPosition = [0 0 3.4 2];
print('SuppFunc','-depsc');
%%
figure(4);

Echirp = sqrt(Igauss).*exp(I*omega*t).*exp(I*b*t.^2);
Egauss = sqrt(Igauss).*cos(omega*t+b*t.^2);

Ichirp = real(Echirp.*conj(Echirp));
%%%IFWHM = 91.58 fs

p1 = plot(t*1e15,real(Echirp),'-r','Linewidth',1);
hold on;
p2 = plot(t*1e15,Ichirp,'-g','Linewidth',2);
hold off;
xlim([-100 100]);
legend([p1 p2],{'$E(t)$','$I(t)$'},'Location','southeast','Interpreter','latex');


xlabel('$t$ (fs)','Interpreter','latex');
ylabel('E. Field/Intensity (arb.)','Interpreter','latex');
set(gca,'Fontsize',10,'FontName','Times New Roman','TickLabelInterpreter','latex',
        'Linewidth',1);

fig = gcf;
fig.PaperUnits = 'inches';
fig.PaperPosition = [0 0 3.4 2];
print('FieldInt','-depsc');
```

Appendix H

Comment statistics from *Quanta Magazine*

The impact of Wolchover's article in *Quanta Magazine* might be discussed by a statistical analysis of comments made to Physics articles around the time of publication. The *Quanta* article by Wolchover was the 2nd most commented article since its publication date in October, receiving 121 comments in the week or so after it was first published. The first most commented article since the October publication date, which received 340, discussed criticisms of the Many Worlds interpretation of quantum mechanics.[220] Considering then the 50 most recent articles, Wolchover's had the 4th highest number of comments. Including the highly commented article along with Wolchover's, the 50 articles received, on average, 31 comments, with a standard error of 8. Applying Chauvenet's criterion to remove the Many Worlds article from our sample, the average and standard error in comments for the most recent 49 articles drops to 25(5). Given that the median number of comments per article for this adjusted sample is 9, this suggests a significant skew from an ideal normal distribution of comments. A distribution of these 49 most recent articles is provided in Fig. H.1.
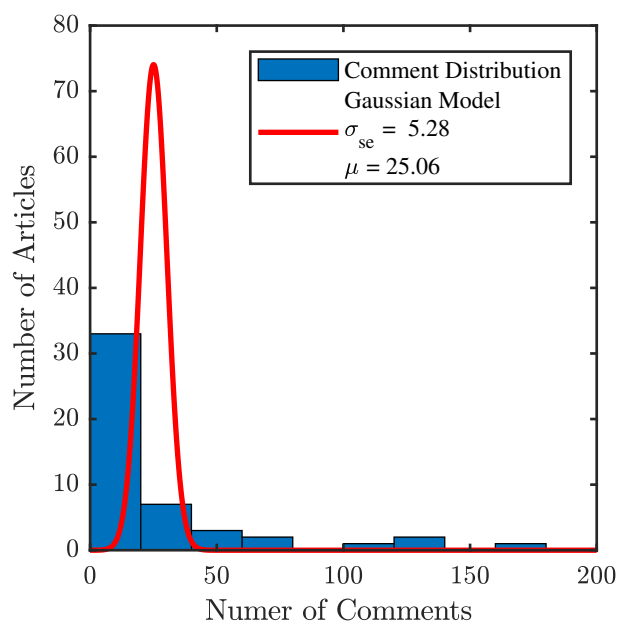
Figure H.1: Shown is a histogram of the number of comments posted to the 25 most recently published articles to *Quanta* in the category of physics. The histogram is modeled with a normal distribution that is normalized such that the areas under the comment histogram and the distribution PDF are equal. The distribution is plotted with an average $\mu = 25.06$ and the sample standard error, $\sigma = 5.28$. The median value of 9 of the comment distribution suggests a significant skew, indicating that the number of comments received by Wolchover's article is not typical.

From this skewed distribution, one can conclude that the discussion surrounding this article is not typical of other articles published around the same time. The oil droplet experiment, and discussions in quantum foundations in general, remain hotly debated topics.

References

[1]   C. Davisson and L. H. Germer, "Diffraction of electrons by a crystal of nickel," Phys. Rev. **30**, 705–740 (1927).

[2]   G. P. Thompson and A. Reid, "Diffraction of cathode rays by a thin film," Nature **119**, 890 (1927).

[3]   De Broglie, Louis, "Recherches sur la théorie des Quanta," Ann. Phys. **10**, 22–128 (1925).

[4]   P. Hommelhoff, Y. Sortais, A. Aghajani-Talesh, and M. A. Kasevich, "Field emission tip as a nanometer source of free electron femtosecond pulses," Phys. Rev. Lett. **96**, 077401 (2006).

[5]   B. Barwick, C. Corder, J. Strohaber, N. Chandler-Smith, C. Uiterwaal, and H. Batelaan, "Laser-induced ultrafast electron emission from a field emission tip," New J. Phys. **9**, 142 (2007).

[6]   C. Ropers, D. R. Solli, C. P. Schulz, C. Lienau, and T. Elsaesser, "Localized multiphoton emission of femtosecond electron pulses from metal nanotips," Phys. Rev. Lett. **98**, 043907 (2007).

[7]   A. H. Zewail, "4D ultrafast electron diffraction, crystallography, and microscopy," Annu. Rev. Phys. Chem. **57**, 65–103 (2006).

[8]   R. J. D. Miller, R. Ernstorfer, M. Harb, M. Gao, C. T. Hebeisen, H. Jean-Ruel, C. Lu, G. Moriena, and G. Sciaini, "'Making the molecular movie': first frames," Acta Crystallogr. A **66**, 137–156 (2010).

[9]   R. J. D. Miller, "Femtosecond crystallography with ultrabright electrons and x-rays: Capturing chemistry in action," Science **343**, 1108–1116 (2014).

[10]   E. T. J. Nibbering, "Low-energy electron diffraction at ultrafast speeds," Science **345**, 137–138 (2014).

[11]   M. Gulde, S. Schweda, G. Storeck, M. Maiti, H. K. Yu, A. M. Wodtke, S. Schäfer, and C. Ropers, "Ultrafast low-energy electron diffraction in transmission resolves polymer/graphene superstructure dynamics," Science **345**, 200–204 (2014).

[12]   V. A. Lobastov, R. Srinivasan, and A. H. Zewail, "Four-dimensional ultrafast electron microscopy," Proc. Natl. Acad. Sci. USA **102**, 7069–7073 (2005).

[13]   H. Batelaan and K. Uiterwaal, "Microscopy: Tip-top imaging," Nature **446**, 500–501 (2007).

[14]   B. Barwick, D. J. Flannigan, and A. H. Zewail, "Photon-induced near-field electron microscopy," Nature **462**, 902–906 (2009).

[15]   L. Piazza, T. T. A. Lummen, E. Quionez, Y. Murooka, B. W. Reed, B. Barwick, and F. Carbone, "Simultaneous observation of the quantization and the interference pattern of a plasmonic near-field," Nat. Commun. **6**, 6407 (2015).

[16]   A. Feist, K. E. Echternkamp, J. Schauss, S. V. Yalunin, S. Schfer, and C. Ropers, "Quantum coherent optical phase modulation in an ultrafast transmission electron microscope," Nature **521**, 200–203 (2015).

[17] M. T. Hassan, J. S. Baskin, B. Liao, and A. H. Zewail, "High-temporal-resolution electron microscopy for imaging ultrafast electron dynamics," Nat. Photonics **11**, 425 (2017).

[18] M. T. Hassan, "Attomicroscopy: from femtosecond to attosecond electron microscopy," J. Phys. B **51**, 032005 (2018).

[19] C. Kealhofer, S. M. Foreman, S. Gerlich, and M. A. Kasevich, "Ultrafast laser-triggered emission from hafnium carbide tips," Phys. Rev. B **86**, 035405 (2012).

[20] P. Hommelhoff, C. Kealhofer, A. Aghajani-Talesh, Y. R. Sortais, S. M. Foreman, and M. A. Kasevich, "Extreme localization of electrons in space and time," Ultramicroscopy **109**, 423 – 429 (2009), iFES 2008.

[21] A. Caprez, B. Barwick, and H. Batelaan, "Macroscopic test of the Aharonov-Bohm effect," Phys. Rev. Lett. **99**, 210401 (2007).

[22] M. Krüger, M. Schenk, and P. Hommelhoff, "Attosecond control of electrons emitted from a nanoscale metal tip," Nature **475**, 78–81 (2011).

[23] M. Krüger, M. Schenk, M. Förster, and P. Hommelhoff, "Attosecond physics in photoemission from a metal nanotip," J. Phys. B **45**, 074006 (2012).

[24] P. Lougovski and H. Batelaan, "Quantum description and properties of electrons emitted from pulsed nanotip electron sources," Phys. Rev. A **84**, 023417 (2011).

[25] E. Jones, M. Becker, J. Luiten, and H. Batelaan, "Laser control of electron matter waves," Laser Photonics Rev. **10**, 214–229 (2016).

[26]   B. N. Flanders, "Directed electrochemical nanowire assembly: Precise nanostructure assembly via dendritic solidification," Mod. Phys. Lett. B **26**, 1130001 (2012).

[27]   G. Basnet, K. R. Panta, P. S. Thapa, and B. N. Flanders, "Controlled electrochemical growth of ultra-long gold nanoribbons," Appl. Phys. Lett. **110**, 073106 (2017).

[28]   D. Roy, C. M. Williams, and K. Mingard, "Single-crystal gold tip for tip-enhanced Raman spectroscopy," J. Vac. Sci. Technol. B Nanotechnol. Microelectron. **28**, 631–634 (2010).

[29]   D. Gingery and P. Bühlmann, "Single-step electrochemical method for producing very sharp au scanning tunneling microscopy tips," Rev. Sci. Instrum. **78**, 113703 (2007).

[30]   L. Eligal, F. Culfaz, V. McCaughan, N. I. Cade, and D. Richards, "Etching gold tips suitable for tip-enhanced near-field optical microscopy," Rev. Sci. Instrum. **80**, 033701 (2009).

[31]   K. Yamaguchi and S. Tada, "Fabrication of GaAs microtips for scanning tunneling microscopy by wet etching," J. Electrochem. Soc. **143**, 2616–2619 (1996).

[32]   M. Kuwahara, T. Nakanishi, S. Okumi, M. Yamamoto, M. Miyamoto, N. Yamamoto, K. Yasui, T. Morino, R. Sakai, K. Tamagaki, and K. Yamaguchi, "Field emission of spin-polarized electrons extracted from photoexcited GaAs tip," Jpn. J. Appl Phys. **45**, 6245 (2006).

[33]   E. R. Jones, W. C. Huang, G. Basnet, B. N. Flanders, and H. Batelaan,

"Laser-induced electron emission from Au nanowires: A probe for orthogonal polarizations," Appl. Phys. Lett. **112**, 263104 (2018).

[34] E. Brunkow, E. R. Jones, H. Batelaan, and T. J. Gay, "Femtosecond-laser-induced spin-polarized electron emission from a GaAs tip," Appl. Phys. Lett. **114**, 073502 (2019).

[35] C. S. Adams, M. Sigel, and J. Mlynek, "Atom optics," Phys. Rep. **240**, 143–210 (1994).

[36] A. D. Cronin, J. Schmiedmayer, and D. E. Pritchard, "Optics and interferometry with atoms and molecules," Rev. Mod. Phys. **81**, 1051–1129 (2009).

[37] R. Bach, D. Pope, S.-H. Liou, and H. Batelaan, "Controlled double-slit electron diffraction," New J. Phys. **15**, 033018 (2013).

[38] R. E. Grisenti, W. Schöllkopf, J. P. Toennies, G. C. Hegerfeldt, and T. Köhler, "Determination of atom-surface van der Waals potentials from transmission-grating diffraction intensities," Phys. Rev. Lett. **83**, 1755–1758 (1999).

[39] S. Lepoutre, V. P. A. Lonij, H. Jelassi, G. Trénec, M. Büchner, A. D. Cronin, and J. Vigué, "Atom interferometry measurement of the atom-surface van der Waals interaction," Eur. Phys. J. D **62**, 309–325 (2011).

[40] B. Barwick, G. Gronniger, L. Yuan, S.-H. Liou, and H. Batelaan, "A measurement of electron-wall interactions using transmission diffraction from nanofabricated gratings," J. Appl. Phys. **100**, 074322 (2006).

[41] R. P. Feynman, *The Principle of Least Action in Quantum Mechanics*, Ph.D. thesis, Princeton University (1942).

[42] R. P. Feynman, "Space-time approach to non-relativistic quantum mechanics," Rev. Mod. Phys. **20**, 367–387 (1948).

[43] G. Gronniger, B. Barwick, H. Batelaan, T. Savas, D. Pritchard, and A. Cronin, "Electron diffraction from free-standing, metal-coated transmission gratings," Appl. Phys. Lett. **87**, 124104 (2005).

[44] G. Gronniger, B. Barwick, and H. Batelaan, "A three-grating electron interferometer," New J. Phys. **8**, 224–224 (2006).

[45] R. Bach, G. Gronniger, and H. Batelaan, "An electron talbot-lau interferometer and magnetic field sensing," Appl. Phys. Lett. **103**, 254102 (2013).

[46] Z. Chen, P. Beierle, and H. Batelaan, "Spatial correlation in matter-wave interference as a measure of decoherence, dephasing, and entropy," Phys. Rev. A **97**, 043608 (2018).

[47] P. J. Beierle, L. Zhang, and H. Batelaan, "Experimental test of decoherence theory using electron matter waves," New J. Phys. **20**, 113030 (2018).

[48] E. R. Jones, R. A. Bach, and H. Batelaan, "Path integrals, matter waves, and the double slit," Eur. J. Phys. **36**, 065048 (2015).

[49] T. Young, *A Course of Lectures on Natural Philosophy and the Mechanical Arts*, Vol. 1 (William Savage, London, 1807) pp. 464–468, 776–777, and 786–787.

[50] M. Faraday, "On a peculiar class of acoustical figures; and on certain forms assumed by groups of particles upon vibrating elastic surfaces," Philos. Trans. Royal Soc. **121**, 299–340 (1831).

[51] Y. Couder, E. Fort, C.-H. Gautier, and A. Boudaoud, "From bouncing to floating: Noncoalescence of drops on a fluid bath," Phys. Rev. Lett. **94**, 177801 (2005).

[52] Y. Couder, S. Protière, E. Fort, and A. Boudaoud, "Dynamical phenomena: Walking and orbiting droplets," Nature **437**, 208 (2005).

[53] E. Fort, A. Eddi, A. Boudaoud, J. Moukhtar, and Y. Couder, "Path-memory induced quantization of classical orbits," Proc. Natl. Acad. Sci. U.S.A. **107**, 17515–17520 (2010).

[54] Y. Couder, "A macroscopic-scale wave-particle duality: the role of a wave mediated path memory," (2011), colloquium, given at the Perimeter Institute.

[55] A. Eddi, E. Sultan, J. Moukhtar, E. Fort, M. Rossi, and Y. Couder, "Information stored in Faraday waves: the origin of a path memory," J. Fluid Mech. **674**, 433463 (2011).

[56] J. W. Bush, "Pilot-wave hydrodynamics," Annu. Rev. Fluid Mech. **47**, 269–292 (2015).

[57] Y. Couder and E. Fort, "Single-particle diffraction and interference at a macroscopic scale," Phys. Rev. Lett. **97**, 154101 (2006).

[58] G. Baym, "The physics of Hanbury Brown–Twiss intensity interferometry: from stars to nuclear collisions," arXiv preprint nucl-th/9804026 (1998).

[59] R. Hanbury Brown and R. Twiss, "Correlation between photons in two coherent beams of light," Nature **177**, 27–29 (1956).

[60] R. Glauber, in *Quantum Optics and Electronics*, edited by C. DeWitt, A. Blandin, and C. Cohen-Tannoudji (Gordon and Breach, New York, 1965) pp. 63–185.

[61] M. Henny, S. Oberholzer, C. Strunk, T. Heinzel, K. Ensslin, M. Holland, and C. Schönenberger, "The fermionic Hanbury Brown and Twiss experiment," Science **284**, 296–298 (1999).

[62] W. D. Oliver, J. Kim, R. C. Liu, and Y. Yamamoto, "Hanbury Brown and Twiss-type experiment with electrons," Science **284**, 299–301 (1999).

[63] T. Jeltes, J. M. McNamara, W. Hogervorst, W. Vassen, V. Krachmalnicoff, M. Schellekens, A. Perrin, H. Chang, D. Boiron, A. Aspect, and C. I. Westbrook, "Comparison of the Hanbury Brown–Twiss effect for bosons and fermions," Nature **445**, 402–405 (2007).

[64] R. Hanbury Brown and R. Twiss, "A new type of interferometer for use in radio astronomy," Philos. Mag. **45**, 663–682 (1954).

[65] R. Hanbury Brown and R. Twiss, "A test of a new type of stellar interferometer on Sirius," Nature **178**, 1046–1048 (1956).

[66] R. Hanbury Brown and R. Twiss, "The question of correlation between photons in coherent light rays," Nature **178**, 1447–1448 (1956).

[67] E. M. Purcell, "The question of correlation between photons in coherent light rays," Nature **178**, 1449–1450 (1956).

[68] U. Fano, "Quantum theory of interference effects in the mixing of light from phase-independent sources," Am. J. Phys. **29**, 539–545 (1961).

[69] G. Goldhaber, W. B. Fowler, S. Goldhaber, T. F. Hoang, T. E. Kalogeropoulos, and W. M. Powell, "Pion-pion correlations in antiproton annihilation events," Phys. Rev. Lett. **3**, 181–183 (1959).

[70] H. Kiesel, A. Renz, and F. Hasselbach, "Observation of Hanbury Brown-Twiss anticorrelations for free electrons," Nature **418**, 392 (2002).

[71] T. Kodama, N. Osakabe, and A. Tonomura, "Correlation in a coherent electron beam," Phys. Rev. A **83**, 063616 (2011).

[72] W. Schottky, "Über den Einfluß von Strukturwirkungen, besonders der Thomsonschen Bildkraft, auf die Elektronenemission der Metalle," Phys. Z. **15**, 872 (1914).

[73] O. W. Richardson, *The Emission of Electricity from Hot Bodies* (Longmans Green and Company, London, 1921).

[74] E. L. Murphy and R. H. Good, "Thermionic emission, field emission, and the transition region," Phys. Rev. **102**, 1464–1473 (1956).

[75] D. T. Pierce and F. Meier, "Photoemission of spin-polarized electrons from GaAs," Phys. Rev. B **13**, 5484–5500 (1976).

[76] R. Gomer, *Field Emission and Field Ionization* (Harvard University Press, Cambridge, MA, 1961) pp. 20–29.

[77] T. J. Gay, "Physics and technology of polarized electron scattering from atoms and molecules," Adv. At. Mol. Phys. **57**, 157–247 (2009).

[78] C. Ropers, C. C. Neacsu, T. Elsaesser, M. Albrecht, M. B. Raschke, and C. Lienau, "Grating-coupling of surface plasmons onto metallic tips: A nanoconfined light source," Nano Letters **7**, 2784–2788 (2007).

[79] J. Vogelsang, J. Robin, B. J. Nagy, P. Dombi, D. Rosenkranz, M. Schiek, P. Gro, and C. Lienau, "Ultrafast electron emission from a sharp metal nanotaper driven

by adiabatic nanofocusing of surface plasmons," Nano Lett. **15**, 4685–4691 (2015).

[80] M. Müller, V. Kravtsov, A. Paarmann, M. B. Raschke, and R. Ernstorfer, "Nanofocused plasmon-driven sub-10 fs electron point source," ACS Photonics **3**, 611–619 (2016).

[81] P. Klaer, F. Schertz, M. Lehr, G. Schönhense, and H. J. Elmers, "Spin-polarized photoelectrons resonantly excited by circularly polarized light from a fractional Ag film on GaAs(100)," Phys. Rev. B **88**, 214425 (2013).

[82] M. Schenk, M. Krüger, and P. Hommelhoff, "Strong-field above-threshold photoemission from sharp metal tips," Phys. Rev. Lett. **105**, 257601 (2010).

[83] B. Ozturk, B. N. Flanders, D. R. Grischkowsky, and T. D. Mishima, "Single-step growth and low resistance interconnecting of gold nanowires," Nanotechnology **18**, 175707 (2007).

[84] A. M. Summers, A. S. Ramm, G. Paneru, M. F. Kling, B. N. Flanders, and C. A. Trallero-Herrero, "Optical damage threshold of Au nanowires in strong femtosecond laser fields," Opt. Express **22**, 4235–4246 (2014).

[85] P. A. M. Dirac, "On the analogy between classical and quantum mechanics," Rev. Mod. Phys. **17**, 195–199 (1945).

[86] R. P. Feynman, A. R. Hibbs, and D. F. Styer, *Quantum Mechanics and Path Integrals, Emended ed.* (Dover Publications, Inc., Mineola, NY, 2010) pp. 26–43.

[87] D. C. Giancoli, *Physics: Principles with Applications*, 7th ed. (Pearson Education, Inc., New York, 2013) pp. 682–685 and 805–806.

[88] J. S. Walker, *Physics* (Prentice Hall, Upper Saddle River, NJ, 2002) pp. 916–920 and 995–1001.

[89] H. D. Young and R. A. Freedman, *Sear's and Zemansky's University Physics: with Modern Physics*, 13th ed. (Addison-Wesley, San Francisco, CA, 2012) pp. 1163–1173 and 1314–1315.

[90] K. Krane, *Modern Physics*, 3rd ed. (Wiley, Hoboken, NJ, 2012) pp. 72–73 and 107–110.

[91] H. C. Ohanian, *Modern Physics*, 2nd ed. (Prentice-Hall, Upper Saddle River, NJ, 1995) pp. 21 and 144–150.

[92] R. G. Marcley, "Apparatus drawings project. Report number 6. Bragg diffraction apparatus," Am. J. Phys. **28**, 415–417 (1960).

[93] Teachspin, Inc., "Two slit interference, one photon at a time," `https://www.teachspin.com/two-slit`, [Online; accessed 16-March-2019].

[94] Quantum Laser Pointers.com, "Quantum laser pointers," `http://www.quantumlaserpointers.com/`, [Online; accessed 16-March-2019].

[95] R. P. Feynman, R. B. Leighton, and M. L. Sands, *The Feynman Lectures on Physics*, Vol. 3 (Addison-Wesley, Reading, MA, 1965) pp. 1–6.

[96] S. Weinberg, *Lectures on Quantum Mechanics*, 2nd ed. (Cambridge University Press, 2015) pp. 86–102.

[97] G. Pucci, P. J. Senz, L. M. Faria, and J. W. M. Bush, "Non-specular reflection of walking droplets," J. Fluid Mech. **804**, R3 (2016).

[98] A. Eddi, E. Fort, F. Moisy, and Y. Couder, "Unpredictable tunneling of a classical wave-particle association," Phys. Rev. Lett. **102**, 240401 (2009).

[99] D. M. Harris, J. Moukhtar, E. Fort, Y. Couder, and J. W. M. Bush, "Wavelike statistics from pilot-wave dynamics in a circular corral," Phys. Rev. E **88**, 011001 (2013).

[100] A. Eddi, J. Moukhtar, S. Perrard, E. Fort, and Y. Couder, "Level splitting at macroscopic scale," Phys. Rev. Lett. **108**, 264503 (2012).

[101] S. Perrard, M. Labousse, M. Miskin, E. Fort, and Y. Couder, "Self-organization into quantized eigenstates of a classical wave-driven particle," Nat. Commun **5**, 3219 (2014).

[102] H. Batelaan, E. Jones, W. C.-W. Huang, and R. Bach, "Momentum exchange in the electron double-slit experiment," J. Phys.: Conf. Ser. **701**, 012007 (2016).

[103] A. Andersen, J. Madsen, C. Reichelt, S. Rosenlund Ahl, B. Lautrup, C. Ellegaard, M. T. Levinsen, and T. Bohr, "Double-slit experiment with single wave-driven particles and its relation to quantum mechanics," Phys. Rev. E **92**, 013006 (2015).

[104] G. Pucci, D. M. Harris, L. M. Faria, and J. W. M. Bush, "Walking droplets interacting with single and double slits," J. Fluid Mech. **835**, 11361156 (2018).

[105] N. Wolchover, "Famous experiment dooms alternative to quantum weirdness," Quanta Magazine (2018), online; posted 2018/10/11.

[106] D. Harris and J. W. Bush, "Generating uniaxial vibration with an electrodynamic shaker and external air bearing," J. Sound Vib. **334**, 255 – 269 (2015).

[107] E. Brannen and H. I. S. Ferguson, "The question of correlation between photons in coherent light rays," Nature **178**, 481–482 (1956).

[108] K. Shen, *Coulomb interactions in Hanbury Brown–Twiss Experiments with electrons*, Ph.D. thesis, University of Illinois at Urbana-Champaign (2009).

[109] G. Baym and K. Shen, "Hanbury Brown–Twiss interferometry with electrons: Coulomb vs. quantum statistics," in *In Memory of Akira Tonomura* (World Scientific, 2014) pp. 201–210.

[110] B. E. Barwick, *Coherent control of free electrons*, Ph.D. thesis, University of Nebraska-Lincoln (2007).

[111] B. Richards and E. Wolf, "Electromagnetic diffraction in optical systems, II. Structure of the image field in an aplanatic system," Proc. R. Soc. London, Ser. A **253**, 358–379 (1959).

[112] M. Lax, W. H. Louisell, and W. B. McKnight, "From Maxwell to paraxial wave optics," Phys. Rev. A **11**, 1365–1370 (1975).

[113] L. Cicchitelli, H. Hora, and R. Postle, "Longitudinal field components for laser beams in vacuum," Phys. Rev. A **41**, 3727–3732 (1990).

[114] R. Dorn, S. Quabis, and G. Leuchs, "The focus of lightlinear polarization breaks the rotational symmetry of the focal spot," J. Mod. Opt. **50**, 1917–1926 (2003).

[115] J. D. Jackson, *Classical Electrodynamics*, 3rd ed. (John Wiley and Sons, New York, 1999) pp. 361–362.

[116] H. Wang, L. Shi, B. Lukyanchuk, C. Sheppard, and C. T. Chong, "Creation of a needle of longitudinally polarized light in vacuum using binary optics," Nat. Photonics **2**, 501–505 (2008).

[117] A.-p. Yu, G. Chen, Z.-h. Zhang, Z.-q. Wen, L.-r. Dai, K. Zhang, S.-l. Jiang, Z.-x. Wu, Y.-y. Li, C.-t. Wang, and X.-g. Luo, "Creation of sub-diffraction longitudinally polarized spot by focusing radially polarized light with binary phase lens," Sci. Rep. **6**, 38859 (2016).

[118] K. Yoshiki, K. Ryosuke, M. Hashimoto, N. Hashimoto, and T. Araki, "Second-harmonic-generation microscope using eight-segment polarization-mode converter to observe three-dimensional molecular orientation," Opt. Lett. **32**, 1680–1682 (2007).

[119] G. Terakado, K. Watanabe, and H. Kano, "Scanning confocal total internal reflection fluorescence microscopy by using radial polarization in the illumination system," Appl. Opt. **48**, 1114–1118 (2009).

[120] W.-C. Kim, N.-C. Park, Y.-J. Yoon, H. Choi, and Y.-P. Park, "Investigation of near-field imaging characteristics of radial polarization for application to optical data storage," Opt. Rev. **14**, 236 (2007).

[121] Q. Zhan, "Trapping metallic Rayleigh particles with radial polarization," Opt. Express **12**, 3377–3382 (2004).

[122] Q. Zhan, "Trapping metallic Rayleigh particles with radial polarization: reply to comment," Opt. Express **20**, 6058–6059 (2012).

[123] D. N. Gupta, N. Kant, D. E. Kim, and H. Suk, "Electron acceleration to GeV energy by a radially polarized laser," Phys. Lett. A **368**, 402 – 407 (2007).

[124] C. Hnatovsky, V. Shvedov, W. Krolikowski, and A. Rode, "Revealing local field structure of focused ultrashort pulses," Phys. Rev. Lett. **106**, 123901 (2011).

[125] L. Novotny, M. R. Beversluis, K. S. Youngworth, and T. G. Brown, "Longitudinal field modes probed by single molecules," Phys. Rev. Lett. **86**, 5251–5254 (2001).

[126] Y. Gilbert, R. Bachelot, P. Royer, A. Bouhelier, G. P. Wiederrecht, and L. Novotny, "Longitudinal anisotropy of the photoinduced molecular migration in azobenzene polymer films," Opt. Lett. **31**, 613–615 (2006).

[127] D. Ehberger, J. Hammer, M. Eisele, M. Krüger, J. Noe, A. Högele, and P. Hommelhoff, "Highly coherent electron beam from a laser-triggered tungsten needle tip," Phys. Rev. Lett. **114**, 227601 (2015).

[128] G. Herink, L. Wimmer, and C. Ropers, "Field emission at terahertz frequencies: Ac-tunneling and ultrafast carrier dynamics," New J. Phys. **16**, 123005 (2014).

[129] M. Förster, T. Paschen, M. Krüger, C. Lemell, G. Wachter, F. Libisch, T. Madlener, J. Burgdörfer, and P. Hommelhoff, "Two-color coherent control of femtosecond above-threshold photoemission from a tungsten nanotip," Phys. Rev. Lett. **117**, 217601 (2016).

[130] W. C.-W. Huang, M. Becker, J. Beck, and H. Batelaan, "Two-color multiphoton emission from nanotips," New J. Phys. **19**, 023011 (2017).

[131] S. E. Irvine, A. Dechant, and A. Y. Elezzabi, "Generation of 0.4-keV femtosecond electron pulses using impulsively excited surface plasmons," Phys. Rev. Lett. **93**, 184801 (2004).

[132] P. Dombi, S. E. Irvine, P. Rácz, M. Lenner, N. Kroó, G. Farkas, A. Mitrofanov, A. Baltuška, T. Fuji, F. Krausz, and A. Y. Elezzabi, "Observation of few-cycle, strong-field phenomena in surface plasmon fields," Opt. Express **18**, 24206–24212 (2010).

[133] P. Rácz, Z. Pápa, I. Márton, J. Budai, P. Wróbel, T. Stefaniuk, C. Prietl, J. R. Krenn, and P. Dombi, "Measurement of nanoplasmonic field enhancement with ultrafast photoemission," Nano Lett. **17**, 1181–1186 (2017).

[134] R. Gomer, *Field Emission and Field Ionization* (Harvard University Press, Cambridge, MA, 1961) pp. 32–46.

[135] L. W. Nordheim and R. H. Fowler, "The effect of the image force on the emission and reflexion of electrons by metals," Proc. Royal Soc. Lond. A **121**, 626–639 (1928).

[136] R. E. Burgess, H. Kroemer, and J. M. Houston, "Corrected values of fowler-nordheim field emission functions $v(y)$ and $s(y)$," Phys. Rev. **90**, 515–515 (1953).

[137] M. Greiner and P. Kruse, "Recrystallization of tungsten wire for fabrication of sharp and stable nanoprobe and field-emitter tips," Rev. Sci. Instrum. **78**, 026104 (2007).

[138] A. D. Müller, F. Müller, M. Hietschold, F. Demming, J. Jersch, and K. Dickmann, "Characterization of electrochemically etched tungsten tips for scanning tunneling microscopy," Rev. Sci. Instrum. **70**, 3970–3972 (1999).

[139] H. B. Michaelson, "The work function of the elements and its periodicity," Journal of Applied Physics **48**, 4729–4733 (1977).

[140] J. R. Rumble, ed., "Electron Work Function of the Elements," in *CRC Handbook of Chemistry and Physics (Internet Version 2018)* (CRC Press, Boca Raton, FL, 2018) 98th ed.

[141] T. Young, "I. The Bakerian Lecture. Experiments and calculations relative to physical optics," Philos. Trans. Royal Soc. **94**, 1–16 (1804).

[142] E. Schrödinger, *Collected Papers on Wave Mechanics*, 3rd ed. (Chelsea Publishing Company, New York, 1982) pp. 102–104.

[143] A. I. Sabra, *Theories of light from Descartes to Newton* (Cambridge University Press, New York, 1981) pp. 136–158.

[144] R. P. Feynman, *QED: the strange theory of light and matter* (Princeton University Press, Princeton, NJ, 2006) pp. 36–76.

[145] M. Born and E. Wolf, *Principles of Optics*, sixth ed. (Pergamon Press, Tarrytown, NY, 1993) pp. 109–132.

[146] L. D. Landau and E. M. Lifshtiz, *The Classical Theory of Fields,* 4th revised English edition (Elsevier, Burlington, MA, 1975) pp. 140–143.

[147] D. J. Griffiths, *Introduction to Quantum Mechanics*, 2nd ed. (Prentice Hall, Upper Saddle River, NJ, 2005) pp. 59–67.

[148] D. Bohm, *Quantum Theory* (Dover Publications, Inc., Mineola, NY, 1989) pp. 59–66.

[149] A. O. Barut and S. Basri, "Path integrals and quantum interference," Am. J. Phys. **60**, 896–899 (1992).

[150] M. Beau, "Feynman path integral approach to electron diffraction for one and two slits: analytical results," Eur. J. Phys. **33**, 1023–1039 (2012).

[151] M. Beau and T. C. Dorlas, "Three-dimensional quantum slit diffraction and diffraction in time," Int. J. Theor. Phys. **54**, 1882–1907 (2015).

[152] M. Abramowitz and I. A. Stegun, *Handbook of Mathematical Functions with Formulas, Graphs, and Mathematical Tables*, 9th revised edition (Dover Publications, Inc., Mineola, NY, 1965) pp. 297–298.

[153] B. J. McMorran and A. D. Cronin, "An electron Talbot interferometer," New Journal of Physics **11**, 033021 (2009).

[154] C. Cohen-Tannoudji, B. Diu, and F. Laloë, *Quantum Mechanics*, 2nd ed., Vol. One (Wiley, New York, 2005) pp. 21–31 and 61–66.

[155] R. L. Liboff, *Introductory Quantum Mechanics*, 4th ed. (Addison-Wesley, San Francisco, CA, 2003) pp. 46–47, 82–84, and 156–157.

[156] S. M. Cohen, "Path integral for the quantum harmonic oscillator using elementary methods," Am. J. Phys. **66**, 537–540 (1998).

[157] E. F. Taylor, S. Vokos, J. M. O'Meara, and N. S. Thornber, "Teaching Feynman's sum-over-paths quantum theory," Computers in Physics **12**, 190–199 (1998).

[158] M. Malgieri, P. Onorato, and A. De Ambrosis, "Teaching quantum physics by the sum over paths approach and GeoGebra simulations," Eur. J. Phys. **35**, 055024 (2014).

[159] S. A. Hilbert and H. Batelaan, "Acoustic analog to quantum mechanical level splitting," Am. J. Phys. **75**, 1003–1008 (2007).

[160] M. D'Onofrio, M. Crum, S. A. Hilbert, H. Batelaan, T. Canalichio, and T. Bull, "An acoustic analog for a quantum mechanical level-splitting route to band formation," Am. J. Phys. **84**, 841–847 (2016).

[161] W. Newman, A. Skinner, and S. A. Hilbert, "An acoustic demonstration of an avoided crossing," Am. J. Phys. **85**, 844–849 (2017).

[162] I. Teachspin, "Quantum analogs," [Online; accessed 04-July-2018].

[163] A. Nachbin, P. A. Milewski, and J. W. M. Bush, "Tunneling with a hydrodynamic pilot-wave model," Phys. Rev. Fluids **2**, 034801 (2017).

[164] D. M. Harris and J. W. M. Bush, "Droplets walking in a rotating frame: from quantized orbits to multimodal statistics," J. Fluid Mech. **739**, 444464 (2014).

[165] K. Sayenga, "How Does the Universe Work?" (2011), *Through the Wormhole*, Season 2, Episode 7.

[166] S. Kocsis, B. Braverman, S. Ravets, M. J. Stevens, R. P. Mirin, L. K. Shalm, and A. M. Steinberg, "Observing the average trajectories of single photons in a two-slit interferometer," Science **332**, 1170–1173 (2011).

[167] G. Grössing, S. Fussy, J. M. Pascasio, and H. Schwabl, "An explanation of interference effects in the double slit experiment: Classical trajectories plus ballistic diffusion caused by zero-point fluctuations," Ann. Phys. (N. Y.) **327**, 421 – 437 (2012).

[168] Y. Aharonov, E. Cohen, F. Colombo, T. Landsberger, I. Sabadini, D. C. Struppa, and J. Tollaksen, "Finally making sense of the double-slit experiment," Proc. Natl. Acad. Sci. U.S.A. **114**, 6480–6485 (2017).

[169] W. S. Edwards and S. Fauve, "Patterns and quasi-patterns in the faraday experiment," J. Fluid Mech. **278**, 123148 (1994).

[170] D. M. Harris, J. Quintela, V. Prost, P.-T. Brun, and J. W. M. Bush, "Visualization of hydrodynamic pilot-wave phenomena," J. Vis. **20**, 13–15 (2017).

[171] B. Filoux, M. Hubert, P. Schlagheck, and N. Vandewalle, "Walking droplets in linear channels," Phys. Rev. Fluids **2**, 013601 (2017).

[172] R. Hanbury Brown, *The Intensity Interferometer, its Application to Astronomy* (Halsted, New York, 1974).

[173] C. Ropers and M. Kasevich, personal communication (11/30/2018), femtosecond degenerate electron sources are currently being explored at the University of Göttingen and at Stanford University.

[174] A. H. Zewail, "Four-dimensional electron microscopy," Science **328**, 187–193 (2010).

[175] R. Bormann, S. Strauch, S. Schäfer, and C. Ropers, "An ultrafast electron microscope gun driven by two-photon photoemission from a nanotip cathode," J. Appl. Phys. **118**, 173105 (2015).

[176] W. Wan, L. Yu, L. Zhu, X. Yang, Z. Wei, J. Z. Liu, J. Feng, K. Kunze, O. Schaff, R. Tromp, and W.-X. Tang, "Design and commissioning of an aberration-corrected ultrafast spin-polarized low energy electron microscope with multiple electron sources," Ultramicroscopy **174**, 89–96 (2017).

[177] M. Kuwahara, S. Kusunoki, X. G. Jin, T. Nakanishi, Y. Takeda, K. Saitoh, T. Ujihara, H. Asano, and N. Tanaka, "30-kV spin-polarized transmission electron microscope with GaAsGaAsp strained superlattice photocathode," Appl. Phys. Lett. **101**, 033102 (2012).

[178] M. Kuwahara, S. Kusunoki, Y. Nambo, K. Saitoh, X. Jin, T. Ujihara, H. Asano, Y. Takeda, and N. Tanaka, "Coherence of a spin-polarized electron beam emitted from a semiconductor photocathode in a transmission electron microscope," Appl. Phys. Lett. **105**, 193101 (2014).

[179] M. Kuwahara, Y. Nambo, K. Aoki, K. Sameshima, X. Jin, T. Ujihara, H. Asano, K. Saitoh, Y. Takeda, and N. Tanaka, "The Boersch effect in a picosecond pulsed electron beam emitted from a semiconductor photocathode," Appl. Phys. Lett. **109**, 013108 (2016).

[180] S. A. Hilbert, *Pulse Propagation of Sound, Light, and Electrons*, Ph.D. thesis, University of Nebraska-Lincoln (2009).

[181] M. P. Silverman, "On the feasibility of observing electron antibunching in a field-emission beam," Phys. Lett. A **120**, 442 – 446 (1987).

[182] M. P. Silverman, *More Than One Mystery: Explorations in Quantum Interference* (Springer-Verlag, New York, 1995) pp. 53–99.

[183] S. A. Hilbert, B. Barwick, M. Fabrikant, C. J. G. J. Uiterwaal, and H. Batelaan, "A high repetition rate time-of-flight electron energy analyzer," Appl. Phys. Lett. **91**, 173506 (2007).

[184] S. A. Hilbert, A. Neukirch, C. J. G. J. Uiterwaal, and H. Batelaan, "Exploring temporal and rate limits of laser-induced electron emission," J. Phys. B **42**, 141001 (2009).

[185] M. Moshinsky, "Diffraction in time," Phys. Rev. **88**, 625–631 (1952).

[186] P. Szriftgiser, D. Guéry-Odelin, M. Arndt, and J. Dalibard, "Atomic wave diffraction and interference using temporal slits," Phys. Rev. Lett. **77**, 4–7 (1996).

[187] C. Brukner and A. Zeilinger, "Diffraction of matter waves in space and in time," Phys. Rev. A **56**, 3804–3824 (1997).

[188] M. Moshinsky, "Diffraction in time and the timeenergy uncertainty relation," Am. J. Phys **44**, 1037–1042 (1976).

[189] W. Pauli, "Part 1: Prinzipien der Quantentheorie I," in *Handbuch der Physik*, Vol. 5, edited by S. Flügge (Springer, Berlin, 1958) p. 60.

[190] J. Kijowski, "On the time operator in quantum mechanics and the Heisenberg uncertainty relation for energy and time," Rep. Math. Phys. **6**, 361–386 (1974).

[191] G. Torres-Vega, "Energy-time representation for quantum systems," Phys. Rev. A **75**, 032112 (2007).

[192] J. Muga and C. Leavens, "Arrival time in quantum mechanics," Phys. Rep. **338**, 353 – 438 (2000).

[193] P. L. Muiño, "Introducing the uncertainty principle using diffraction of light waves," J. Chem. Educ. **77**, 1025 (2000).

[194] A. Goussev, "Diffraction in time: An exactly solvable model," Phys. Rev. A **87**, 053621 (2013).

[195] M. Krüger, M. Schenk, J. Breuer, M. Förster, J. Hammer, J. Hoffrogge, S. Thomas, and P. Hommelhoff, "From above-threshold photoemission to attosecond physics at nanometric tungsten tips," in *Progress in Ultrafast Intense Laser Science: Volume IX*, edited by K. Yamanouchi and K. Midorikawa (Springer Berlin Heidelberg, Berlin, Heidelberg, 2013) pp. 213–224.

[196] J. Eberly, J. Javanainen, and K. Rzażewski, "Above-threshold ionization," Phys. Rep. **204**, 331 – 383 (1991).

[197] N. B. Delone and V. P. Krainov, *Multiphoton Processes in Atoms* (Springer, Berlin, Heidelberg, New York, 2000).

[198] P. Hommelhoff, C. Kealhofer, and M. A. Kasevich, "Ultrafast electron pulses from a tungsten tip triggered by low-power femtosecond laser pulses," Phys. Rev. Lett. **97**, 247402 (2006).

[199] D. Androic, D. S. Armstrong, A. Asaturyan, T. Averett, J. Balewski, J. Beaufait, R. S. Beminiwattha, J. Benesch, F. Benmokhtar, J. Birchall, *et al.*, "First determination of the weak charge of the proton," Phys. Rev. Lett. **111**, 141803 (2013).

[200] F. Giebels, H. Gollisch, and R. Feder, "Electron pair emission from W(110): Response to a spin-polarized surface state," Phys. Rev. B **87**, 035124 (2013).

[201] K. Aulenbacher, J. Schuler, D. v. Harrach, E. Reichert, J. Rthgen, A. Subashev, V. Tioukine, and Y. Yashin, "Pulse response of thin III/V semiconductor photocathodes," J. Appl. Phys. **92**, 7536–7543 (2002).

[202] T. Irisawa, T. K. Yamada, and T. Mizoguchi, "Spin polarization vectors of field emitted electrons from Fe/W tips," New J. Phys. **11**, 113031 (2009).

[203] Y. Niu and M. Altman, "Spin polarized field emission from Fe and Co-coated W tips," Surf. Sci. **604**, 1055 – 1059 (2010).

[204] J. K. Bae, L. Cultrera, P. DiGiacomo, and I. Bazarov, "Rugged spin-polarized electron sources based on negative electron affinity GaAs photocathode with robust Cs_2Te coating," Appl. Phys. Lett. **112**, 154101 (2018).

[205] M. Pirbhai, J. Knepper, E. T. Litaker, D. Tupa, and T. J. Gay, "Optically pumped spin-exchange polarized-electron source," Phys. Rev. A **88**, 060701 (2013).

[206] N. B. Clayburn, E. Brunkow, S. J. Burtwistle, G. H. Rutherford, and T. J. Gay, "A cylindrically symmetric "micro-Mott" electron polarimeter," Rev. Sci. Instrum. **87**, 053302 (2016).

[207] M. W. J. Prins, R. Jansen, and H. van Kempen, "Spin-polarized tunneling with GaAs tips in scanning tunneling microscopy," Phys. Rev. B **53**, 8105–8113 (1996).

[208] F. V. Bunkin and M. V. Federov, "Cold emission of electrons from the surface of a metal in a strong radiation field," Sov. Phys. JETP **5**, 896.

[209] O. Schmidt, M. Bauer, C. Wiemann, R. Porath, M. Scharte, O. Andreyev, G. Schönhense, and M. Aeschlimann, "Time-resolved two photon photoemission electron microscopy," Appl. Phys. B **74**, 223–227 (2002).

[210] E. M. Brunkow, *Investigations of Novel Sources of Spin-Polarized Electrons*, Ph.D. thesis, University of Nebraska-Lincoln (2018).

[211] M. Beau, personal communication (04/29/2015).

[212] E. Fort, "Famous Experiment Dooms Alternative to Quantum Weirdness," (10/11/2018), In comments section, accessed on 2019/02/22.

[213] J. W. M. Bush, personal communication (02/20/2019).

[214] E. Brunkow, E. R. Jones, H. Batelaan, and T. J. Gay, "Fast spin-polarized electron source," (2019), U.S. Provisional Patent 62 769 356.

[215] L. Malikova, W. Krystek, F. H. Pollak, N. Dai, A. Cavus, and M. C. Tamargo, "Temperature dependence of the direct gaps of ZnSe and $Zn_{0.56}Cd_{0.44}Se$," Phys. Rev. B **54**, 1819–1824 (1996).

[216] D. Hägele, M. Oestreich, W. Rühle, J. Hoffmann, S. Wachter, H. Kalt, K. Ohkawa, and D. Hommel, "Relation between spin and momentum relaxation in ZnSe/Zn-MgSSe quantum wells," Physica B **272**, 338 – 340 (1999).

[217] M. J. Stevens, A. L. Smirl, R. D. R. Bhat, J. E. Sipe, and H. M. van Driel, "Coherent control of an optically injected ballistic spin-polarized current in bulk GaAs," J. Appl. Phys. **91**, 4382–4386 (2002).

[218] J. Hübner, W. W. Rühle, M. Klude, D. Hommel, R. D. R. Bhat, J. E. Sipe, and H. M. van Driel, "Direct observation of optically injected spin-polarized currents in semiconductors," Phys. Rev. Lett. **90**, 216601 (2003).

[219] I. Malajovich, J. J. Berry, N. Samarth, and D. D. Awschalom, "Persistent sourcing of coherent spins for multifunctional semiconductor spintronics," Nature **411**, 770–772 (2001).

[220] P. Ball, "Why the many-worlds interpretation has many problems," Quanta Magazine (2018), online; posted 2018/10/18.